Faculty of Science and Engineering
Department of Imaging and Applied Physics

# X-ray and neutron scattering of multiferroic LuFe$_2$O$_4$

Shane Michael Lawrence

This thesis is presented for the Degree of
Doctor of Philosophy
of
Curtin University

*August* 2011

To the best of my knowledge and belief this thesis contains no material previously published by any other person except where due acknowledgement has been made. This thesis contains no material which has been accepted for the award of any other degree or diploma in any university.

Signature: _____      Date: _____ / _____ / _____

# Abstract

Multiferroic materials have recently begun to attract significant scientific interest due to their potential applications in the design of modern electronic devices. Currently, the magnetic properties of materials form the basis of our electronic data storage and have the potential to enhance the logic operations performed in electronic devices (such as computers and sensors). Non-volatile magnetic memory is used in data storage devices, such as the hard drives found in personal computers, where data is encoded via the magnetisation state of magnetic domains in the device with one of two states: either up or down ($M \uparrow$ or $M \downarrow$); the state is determined or changed by interacting with the magnetic flux about the domain. Furthermore, in current computing and sensor technology, logic operations are performed with arrays of transistors; however, in *spintronics* ("spin transport electronics") the electric current itself is spin polarised and there is data encoded in the current itself. Circuit elements in such a system are magnetic devices that interact with the electron spin.

*Magnetoelectric multiferroics* are materials that have both a spontaneous ferroelectric polarisation ($P$) and magnetic magnetisation ($M$). Polarisation may be manipulated by an electric field and magnetisation by a magnetic field, hence the potential of multiferroics lies in the coupling between the two degrees of freedom and the manipulation of magnetisation by an applied electric field and vice versa. The properties of a magnetic device could be altered "on-the-fly" by applying an electric pulse, and in the context of the examples provided this would greatly diversify the logic elements in spintronic circuits. Furthermore, with both polarisation and magnetisation a multiferroic domain can take on one of four states ($M \uparrow P \uparrow$, $M \uparrow P \downarrow$, $M \downarrow P \uparrow$, or $M \downarrow P \downarrow$) dramatically increasing data storage density over the current binary system.

Lutetium ferrite ($LuFe_2O_4$) is a multiferroic material in which both the magnetisation and polarisation arise from the iron sites and with strong iron-iron

correlations the material is a promising candidate as a high temperature multi-ferroic. The material has a layered structure with bilayers of FeO separated by single layers of LuO on a hexagonal lattice. Frustrated 2D charge order exists below 550 K which transitions to 3D charge order below 330 K and simultaneously frustrated ferrimagnetic order exists in the multiferroic phase below 250 K. X-ray and neutron scattering experiments have been performed in order to characterise the ferroelectric and ferrimagnetic order and magnetoelectric coupling in this material.

Resonant x-ray scattering (RXS) was performed on the Material Science beamline of the Swiss Light Source where the energy dependence of the super-lattice reflections corresponding to the charge order was collected. Non-linear regression using a custom Levenberg-Marquadt algorithm was applied in order to extract the anomalous scattering factors which demonstrated the superlattice reflections were described by a charge order model. Furthermore, the chemical shift was shown to correspond to full $Fe^{2+}/Fe^{3+}$ charge disproportionation. The absence of any polarisation or azimuthal dependence, shown by resonant x-ray scattering data collected on the ID20 beamline of the European Synchrotron Radiation Facility, confirmed the prediction of Nagano *et al.* that the orbital moments of the $Fe^{2+}$-sites exist in a disordered glassy state.

X-ray absorption near edge structure (XANES) calculations were performed using the FDMNES program in order to assess the validity of the anomalous scattering factors obtained in the RXS experiment and to further test the charge order model. It was shown that the characteristic features of the experimentally determined functions can be qualitatively reproduced by calculations using the known charge order model. Furthermore, these functions were shown to reproduce the phase of the RXS data further demonstrating that the reflections result from a pure charge ordered phase.

Inelastic neutron scattering performed on the PUMA triple axis spectrometer of the FRMII demonstrated that magnetic critical scattering is observed at 250 K. A broad peak in the temperature dependence is observed rather than the characteristic divergence of a magnetic transition: this is attributed to broadening of the transition by the distribution of oxygen stoichiometry in the sample and ferroelectric fluctuations integrated into the data due to poor *c*-axis resolution. Pyroelectric current and magnetometry measurements demonstrate a peak in the magnetic susceptibility and a step in the polarisation at approximately 215 K, well below the magnetic transition. Elastic neutron scattering experi-

ments performed on the E2 flat cone diffractometer of the Helmholtz-Zentrum Berlin demonstrate these features correspond to a 2D-to-3D magnetic transition that has previously only been predicted by anomalies in other measurements.

An applied field study performed by neutron scattering on the E2 flat cone diffractometer of the Helmholtz-Zentrum Berlin and x-ray scattering on the PX1 protein crystallography beamline of the Australian synchrotron demonstrate the control of the magnetic domain population with an electric field, contrary to other recent reports on this topic. Furthermore, the observed magnetoelectric coupling is inconsistent with current models of the magnetic structure of this system. The x-ray measurements demonstrate a disorder-to-order effect by the applied electric field as 3D order is preferred with an increase in the intensity of all satellites.

Temperature dependent x-ray powder diffraction data collected on the Powder Diffraction (PD) beamline of the Australian Synchrotron has demonstrated anisotropic thermal expansion with negative thermal expansion of the $c$-axis in this material. Electron density mapping by Fourier analysis shows the disorder of the oxygen between the electrically static Lu ions and the neighbouring Fe ions, as electron hopping between $Fe^{2+}$ and $Fe^{3+}$ leading to a corresponding variation on the Fe-O bond length. Reversible structural distortions are observed indicating a piezoelectric effect in this material caused by the crushing during sample preparation. Furthermore, weak reflections in the x-ray patterns, corresponding to a monoclinic sublattice, suggest a monoclinic distortion of the oxygen sites which is supported by neutron powder diffraction collected on the ECHIDNA instrument of the OPAL reactor.

# Contents

# Chapter 1

# Introduction

Magnetism and electricity are important fundamental characteristics of our physical world. Iron and amber, examples of ferromagnetism and static electricity, have had a long history of use by many civilizations in history; therefore, it seems reasonable to assume that these phenomena have been observed and even applied long before attempts were made to understand them. Amber (preserved tree sap) is an insulator and collects charge which may be observed as a discharge of static electricity; it was widely used in jewellery and was of significance to many cultures. *Lodestone* (a naturally magnetised form of magnetite) was extracted from the earth and its magnetic properties observed due to its interaction with other lodestones and iron.

The early philosopher Thales of Miletus is considered to have made the first definitive statement on the nature of the lodestone. He concluded that as it caused the motion of iron the lodestone must have a soul. Later discourse by Greek philosophers attempted to move away from this explanation and rather proposed that a stream of particles were ejected from the lodestone creating a vacuum that drew the iron toward it, or alternatively that all materials eject these tiny particles and it was an affinity between the particle shapes and materials that caused these streams to lock together and the particle to move. However, it was acknowledged that these theories did not explain the observation that a piece of iron in contact with the lodestone would attract further pieces of iron to itself (the principle of magnetic induction). The methodology applied by these early theorists was based upon their understanding of the universe, which was strongly rooted in cultural beliefs.

A more rigorous "scientific method" was employed in the $16^{th}$ century by Gilbert who proposed that the earth itself was a magnet and developed apparatus for the study of electrical phenomena. He observed fundamental differences between electricity and magnetism: the electric force was isotropic about a charged object and therefore there were not electric poles about a charged object in the same way there were magnetic poles on a magnet. Additionally, he observed that the electric force could be blocked by a piece of paper unlike the magnetic force. Scientific research accelerated from the 17th through 19th centuries with the work of Guericke, Franklin, Priestley, Jefferson, Galvani, Volta, Faraday, Ampere, and Maxwell all empirically working to better understand electricity, magnetism, and the relationship between the two. The results of these centuries of work are best summarised in Maxwell's equations that describe the static and time-varying nature of electric and magnetic fields and their fundamental relationship.

Centuries had passed since the first discovery and use of the lodestone, yet despite a period of extensive scientific endeavour in this area, the fundamental origin of magnetism was still not understood. As it turned out, understanding magnetism required the results of Quantum Mechanics and the fundamental 'spin' possessed by all electrons that was described by Dirac in the $20^{th}$ century.

Research in the fields of magnetic and electric phenomena and related materials is still very active with many avenues to explore. There are a range of magnetic interactions and systems that currently attract attention, such as the RKKY and spin torque effects, geometrically frustrated and spin ice systems and the interaction between magnetism and superconductivity. Additionally, there exists a class of materials that have a spontaneous polarisation (electric poles) and the origin of these electric structures has also attracted much research. Due to the ongoing development and interest in spintronics, nanotechnology and the drive to develop better and smaller computer and data storage technologies, research in these areas plays a predominant role in shaping the world of tomorrow.

## 1.1 Multiferroicity

The term *multiferroic* does not appear in the literature prior to the year 2000: it refers to a material that exhibits two or more ferroic properties simultaneously. There are four ferroic properties: ferromagnetic, ferroelectric, ferroelastic and ferrotoroidal order. The "ferroic" classification indicates the ordering of a reversible

dipolar quantity into spatial domains that may be reversed by an external action. Ferromagnetism is the ordering of magnetic dipoles which may be oriented or reversed by a magnetic field, ferroelectricity is the ordering of electric dipoles which may be reversed by an electric field, ferroelasticity is the ordering of strain domains which may be reversed under an applied stress, and ferrotoroidal ordering is the ordering of toroidal moments which arise from spin vortices where the direction of the moment is the vector **curl** of the vortex. Ferrotoroidal ordering is an emerging field attracting a growing interest as it is the only ferroic ordering that is variant under both space and time reversal leading to unique magneto-electric properties [1], and the first direct observation of ferrotoroidal domains was reported in Nature in 2007 [2]. The focus of this work is on magnetoelectric multiferroics which have long range ferroelectric and magnetic order.

Materials that are both ferromagnetic and ferroelectric provide the potential for strong magnetoelectric coupling and therefore strong observable effects. For a long time though it was thought that these two properties were mutually exclusive, as the covalency of displacive ferroelectricity required empty orbitals to accept donor electron density and therefore form a highly covalent bond. On the other hand, transition metal magnetism relies upon the $3d$ electron density, hence it seemed that these two properties could not occur together [3].

These days there are multiple well-known mechanisms for ferroelectric polarisation to occur in transition metal oxides: lone-pair covalency in a magnetic material such as $BiFeO_3$ or $BiMnO_3$; geometric frustration of long range dipole-dipole interactions such as in $YMnO_3$; non-centrosymmetric charge ordering such as in $LuFe_2O_4$; and long range magnetic order in which the arrangement of magnetic dipoles has no reflection symmetry such as in $TbMnO_3$, $DyMnO_3$ or $TbMn_2O_4$ [4].

$LuFe_2O_4$ is a multiferroic ferrite that exhibits 3-dimensional charge order below 330 K and ferrimagnetic order below 250 K, and as the magnetism and ferroelectricity both arise from the same Fe sites strong correlates may lead to strong magnetoelectric coupling. The combination of a layered structure, geometrically frustrated order, and non-stoichiometric oxygen content make this material an interesting and unique example to study. An introduction to the magnetoelectric effect, magnetism, and ferroelectricity is provided in the following sections before returning to this material with an in-depth literature review of $LuFe_2O_4$ in Section 1.5 (page 21).

## 1.2   The magnetoelectric effect

The magnetoelectric (ME) effect describes the interaction between the electric properties of a material and an applied magnetic field, and conversely the interaction between the magnetic properties of a material and an applied electric field. This effect has been studied since its experimental discovery by Röntgen in 1888 and theoretical predictions on its nature by Curie in 1894. About 80 magnetoelectric compounds had been discovered by 1973; however, the strength of the interaction in these materials was very weak. A decline in interest in this field was observed through the 1970s and 1980s, but with the rapid growth of the electronics industry in the 1990s applications of materials with strong ME coupling in areas such as spintronics and high density data storage have become apparent, and a new fresh interest in understanding the nature of the interaction in this material has arisen. In the last few years research in this area has increased dramatically as demonstrated by the number of publications per year on the topic shown in Figure 1.1.

The magnetoelectric effect may be understood by expanding the free energy of a ME system with respect to the polarisation (**P**) and magnetisation (**M**) as a function of applied electric (**E**) and magnetic (**H**) fields [5]:

$$F\left(\mathbf{E}, \mathbf{H}\right) = F_0 - P_i^S E_i - M_i^S H_i - \frac{1}{2}\epsilon_0\epsilon_{ij}E_iE_j - \frac{1}{2}\mu_0\mu_{ij}H_iH_j - \alpha_{ij}E_iH_j$$
$$- \frac{1}{2}\beta_{ijk}E_iH_jH_k - \frac{1}{2}\gamma_{ijk}H_iE_jE_k \quad \ldots \tag{1.1}$$

where $\boldsymbol{\epsilon}$ is the electric permittivity, $\boldsymbol{\mu}$ is the magnetic permeability, and $\boldsymbol{\alpha}$, $\boldsymbol{\beta}$, and $\boldsymbol{\gamma}$ are the magnetoelectric parameters.
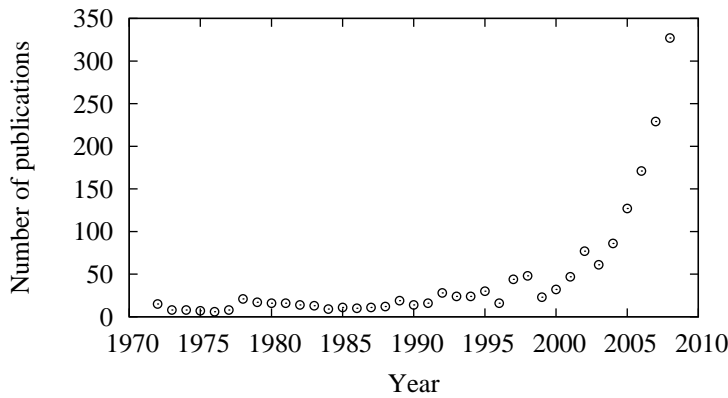


Figure 1.1: Publications per calendar year up to 2009. Statistics collected from Web of Science.

The polarisation and magnetisation may be written by differentiating the free energy with respect to the applied fields, yielding:

$$P_i\left(\mathbf{E}, \mathbf{H}\right) = -\frac{\partial F}{\partial E_i}$$
$$= P_i^S + \frac{1}{2}\epsilon_0\epsilon_{ij}E_j + \alpha_{ij}H_j + \frac{1}{2}\beta_{ijk}H_jH_k + \frac{1}{2}\gamma_{ijk}H_iE_j - \ldots \quad (1.2)$$

$$M_i\left(\mathbf{E}, \mathbf{H}\right) = -\frac{\partial F}{\partial H_i}$$
$$= M_i^S + \frac{1}{2}\mu_0\mu_{ij}H_j + \alpha_{ij}E_i + \frac{1}{2}\beta_{ijk}E_iH_j + \frac{1}{2}\gamma_{ijk}E_jE_k - \ldots$$
$$(1.3)$$

Inspection of Equations 1.2 and 1.3 with respect to the magnetoelectric parameters ($\boldsymbol{\alpha}$, $\boldsymbol{\beta}$ and $\boldsymbol{\gamma}$) shows that they correspond to contributions to the polarisation from an applied magnetic field, or conversely contributions to the magnetisation from an applied electric field. The contribution of $\boldsymbol{\alpha}$ is known as the *linear magnetoelectric effect* and is dominant, and as a result the term "magnetoelectric effect" is used almost exclusively to refer to this term. The *paramagnetoelectric effect*, described by $\boldsymbol{\beta}$, is the most investigated higher order magnetoelectric term and corresponds to a magnetoelectric effect induced by a magnetic field, and $\gamma$ corresponds to a magnetoelectric effect induced by an electric field.

Applications require materials with a strong magnetoelectric effect and $\alpha$ has been measured and calculated for many systems, but it is generally weak in magnetic materials which have normal dielectric properties. Furthermore, composites of dielectric and magnetic materials have been investigated where the magnetoelectric effect is mediated by strain at the material interface. A dielectric or magnetic material experiences small distortions due to strain in an electric or magnetic field respectively due to electro/magneto-striction. In a piezoelectric material an applied electric field leads to large distortions of the crystal lattice and this large strain may lead to a magnetoelectric effect through magnetostriction at an interface with a magnetic material. This effect may be further enhanced in low-dimensional magnetic systems such as thin-films where interface strain contributes significantly to the structure of the magnetic layer and strong effects on the spin structure and properties are observed.

It is expected that a material which has long-range magnetic order and a strong dielectric response may show a strong magnetoelectric effect. Ferroelec-

tric materials have a strong dielectric response due to the long-range ordering of electric dipoles, and so magnetoelectric multiferroic materials are promising candidates materials with a large magnetoelectric coupling.

## 1.3 Magnetism

Magnetism in transition metal compounds arises from the properties of $3d$ electrons. When an orbital is occupied by two electrons the electronic spin is compensated, as each electron has equal and opposite spin. Due to Coulomb repulsion there is an energy penalty for electrons to occupy the same orbital, and electrons will occupy the next orbital of lowest energy. As a result, the pairing of electrons and compensation of spin will only occur when the energy required to occupy the next unoccupied orbital is greater than the Coulomb penalty for the electrons to be paired. In an isolated atom the $3d$-orbitals are degenerate (they have the same energy) and therefore each of the five orbitals will be filled with a single electron and then should a sixth electron exist in the atom it will be paired with another $d$-electron rather than occupying an empty $4p$ orbital. In materials this degeneracy is lifted by solid state effects, known as *crystal field splitting*, due to the presence of neighbouring atoms and this must be considered when determining the spin configuration. The spin configuration is described by the spin number ($S$) which is the sum of the spin quantum numbers of the electrons, $S = \sum m_s$.

To illustrate this principle we consider the electronic configurations of the two iron ions $Fe^{2+}$, with 6 $3d$-electrons; and $Fe^{3+}$, with 5 $3d$-electrons. The degenerate spin configurations are presented in Figure 1.2; furthermore, the configurations of two octahedral $Fe^{3+}$ complexes, $[FeBr_6]^{3-}$ and $[Fe(NO_2)_6]^{3-}$, are shown in Figures 1.3 and 1.4.

Crystal field splitting (characterised by the splitting energy $\Delta$) may lead to
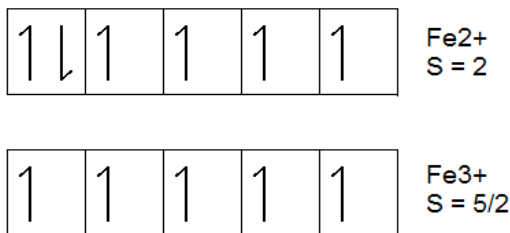


Figure 1.2: Degenerate spin configurations of $Fe^{2+}$ and $Fe^{3+}$.
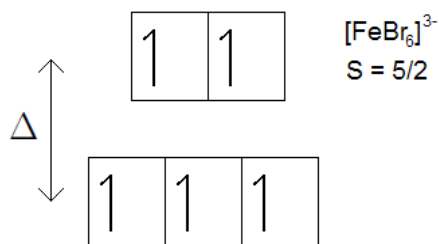
Figure 1.3: "High" spin configuration of octahedral $Fe^{3+}$ complex $[FeBr_6]^{3-}$.
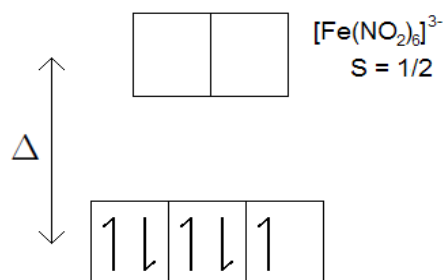
Figure 1.4: "Low" spin configuration of octahedral $Fe^{3+}$ complex $[Fe(NO_2)_6]^{3-}$.

two alternative cases where the compensation of electronic spin varies. The uncompensated case is referred to as the "high" spin configuration due to the maximum value of $S$, while the compensated case is referred to as the "low" spin configuration as it results in the minimum value of $S$. Crystal field splitting varies as a function of the geometry (in this case octahedral), effective bond length, and nature of the neighbouring atoms. In this example $NO_2^-$ is much more electronegative than $Br^-$, leading to a much stronger interaction and a greater crystal field splitting energy.

Due to the combined orbital motion and spin of the electron, the atomic moment is a magnetic dipole described by both the spin and orbital contributions of the electrons.

A magnetic field is described by the magnetic flux density ($\mathbf{B}$) and the magnetic field strength ($\mathbf{H}$). The net vector sum of all the dipole moments per unit volume within a material is the magnetisation ($\mathbf{M}$). The magnetic field within a material is expressed as:

$$\mathbf{B} = \mu\mathbf{H} + \mathbf{M} \tag{1.4}$$

where $\mu$ is the relative permeability.

An applied magnetic field will interact with the magnetic moments of the electrons in a material, altering the magnetisation. The relationship between the applied field $\mathbf{H}$ and $\mathbf{M}$ is given by:

$$\mathbf{M} = \chi\mu\mathbf{H} \tag{1.5}$$

where $\chi$ is a dimensionless quantity called the *magnetic susceptibility*.

The fundamental magnetic nature of a material determines the way by which it interacts with an external magnetic field, thus magnetic materials are classified by differences in their magnetic susceptibility. Materials may fundamentally be classified as either *diamagnetic*, *paramagnetic*, or *ferro/antiferro-magnetic* which are discussed in detail below.

### 1.3.1 Diamagnetism

In the example given earlier, the configuration of the $3d$ electrons of Fe was discussed and only uncompensated examples were shown; however, the magnetic properties of materials result from all the electrons and in the case where a material contains an even number of electrons complete spin compensation may occur.

If all electrons are paired then all spins are compensated and there is no atomic spin moment, $S = 0$. Materials where this is the case are *diamagnetic materials*. An example set of diamagnetic materials are the Nobel gases (He, Ne, Kr, Ar...) in which all electrons are paired.

Most materials are not mono-atomic and the electrons are involved in bonding. In diamagnetic materials, such as hydrogen gas ($H_2$), the energy difference between consecutive orbitals (the bonding and anti-bonding orbitals in $H_2$) is greater than the energy penalty to pair the two electrons, and so the result is that both electrons occupy the same orbital and the electron spin is completely compensated as shown in Figure 1.5.

A diamagnetic material has no net atomic spin, therefore there is no spin
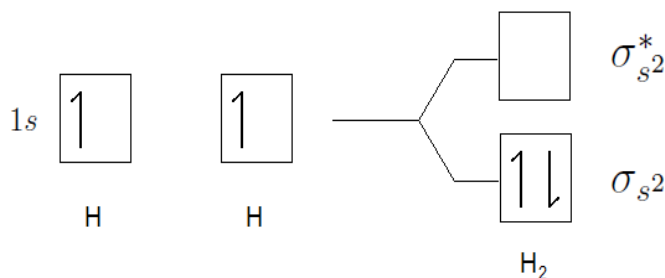


Figure 1.5: Orbital hybridisation and bonding in molecular $H_2$. Despite the electronic spin in atomic H being uncompensated, in the resulting molecule the two electrons are paired and the material is diamagnetic.

interaction with an applied magnetic field. Classically the orbital motion of electrons is analogous to a current carrying loop and it is well understood that when a magnetic field is applied to such a system a resulting magnetic field is established that opposes the direction of the applied field. Therefore a weak net magnetisation is induced in the sample opposing the applied field, or rather $\mathbf{M} \propto -\mathbf{H}$. As the moments are induced by the field the magnetisation returns to zero when the field is removed. Accordingly, diamagnetic materials may be characterised by a small *negative magnetic susceptibility*, $\chi < 0$.

As described previously in some materials crystal field splitting leads to a low spin configuration and for atoms with an even number of electrons this configuration may be diamagnetic (for example the low spin configuration of an octahedral $Fe^{2+}$ complex).

The process of covalent bonding always leads to the electrons occupying molecular bonding orbitals in pairs. Due to this, many covalently bonded materials with an even number of bonding electrons are diamagnetic, such a $H_2O$. On the other hand, a molecule with an odd number of bonding electrons such as CN will have uncompensated electronic spins and such a material is *paramagnetic*.

## 1.3.2 Paramagnetism

Paramagnetism results from uncompensated electronic spins within a material leading to permanent atomic moments. In a paramagnetic material there is no correlation between the atomic moment of an atom ($\mathbf{m}$) and that of its neighbour, and therefore the atomic moments are oriented in random directions and the net magnetisation is zero.

In the presence of an applied field there is an interaction between $\mathbf{H}$ and $\mathbf{m}$ and the atomic moments align in the direction of the applied field leading to a net magnetisation, $\mathbf{M} \propto \mathbf{H}$ (a saturation magnetisation is reached once all moments are aligned with $\mathbf{H}$). Therefore, paramagnetic materials are characterised by a *positive magnetic susceptibility*, $\chi > 0$.

The applied field will have a current loop effect following Lenz's law in all materials (this can be pictured by imagining a circular electron orbital path), therefore all materials are diamagnetic. In the case of paramagnetic materials

the permanent atomic moment is much greater than the weak induced opposing moment and the paramagnetism dominates. The preferred orientation of the atomic moments is induced by the field, thus when the field is removed the moments return to a randomly oriented state due to thermal fluctuations.

### 1.3.3 Ferromagnetism

Ferromagnetic (or antiferromagnetic) materials are materials in which permanent atomic moments exist due to the presence of unpaired electrons. Furthermore, strong correlations exist between one atomic moment and its neighbour leading to an energetically favorable ordering of atomic moments below a critical temperature. The parallel alignment of spins is called *ferromagnetism*, while anti-parallel alignment of spins is referred to as *antiferromagnetism*.

A ferromagnetic crystal (in which all spins are aligned along a single axis) will have a magnetisation per unit volume, and therefore create a stray magnetic field outside the sample. There is an energy penalty associated with this stray field and therefore it is thermodynamically favorable for regions of non-parallel spin (called *domains*) to exist [6]. Within a ferromagnetic domain all of the spins are ordered parallel, while in an adjacent domain the spins are ordered along a different axis. Between any two domains there exists a boundary known as the domain wall which has finite width where the spins have an orientation that varies across the wall from one orientation to the other. This minimises the energetically unfavourable effect of a sudden boundary where spins would be ordered anti-parallel. The presence of domain walls is also driven by crystal imperfections (such as defects or impurities) and the increase in entropy provided by the formation of domains. These are the primary reasons that despite the absence of a stray field from an antiferromagnetic sample, the formation of antiferromagnetic domains is observed.

The correlations between adjacent magnetic moments in these cases are the subject of extensive experimental and theoretical studies and are explained by quantum mechanics; they are characterised by a quantity called *exchange* ($J$) that determines both the strength and the preferred orientation of spins. Exchange correlations exist between all electrons, but it is only in particular cases that these correlations are strong enough that there exists a temperature below which thermal vibrations are insufficient to overcome their influence. A mathe-

matical treatment of exchange readily demonstrates that *direct exchange*, that is the exchange between electron spin on adjacent atoms where the direct overlap of electron density occurs, favours antiferromagnetic orderly where there is minimal to no overlap and/or the coulomb interaction is weak. Alternatively, ferromagnetic order is preferred with increasing overlap and coulomb interaction - which is the case in magnetic materials.

Direct exchange describes the spin correlations in materials where the magnetic atoms are adjacent to one another, for example metals. Yet, there are many magnetic materials where the magnetic ions are separate by an intermediate ion and direct exchange cannot apply, such is the case in transition metal oxides.

### 1.3.4 Exchange mechanisms in oxides

Direct exchange acts through the direct overlap of electron density; however, in transition metal oxides the magnetic $3d$ electron density of each metal ion overlaps with a lobe of a $2p$ orbital as demonstrated in Figure 1.6. Four electrons populate the overlapping orbitals and an exchange path from the electron of one metal ion through both oxygen electrons to the other metal ion may be considered. It can be shown that the lowest energy state in such a configuration is antiferromagnetic [6] by considering the "hopping" of an electron from metal site I to metal site II. This form of exchange is called *superexchange*.

Goodenough carefully investigated the crystal field and symmetry of the perovskite-type manganates [La, M(II)]MnO$_3$ [7] and the perovskite-type mixed crystals La$_{1-x}$Sr$_x$CoO$_{3-\lambda}$ [8] and determined rules for octahedrally coordinated magnetic cations that occupy sites on either side of an anion (180$^o$ bond) based upon the occupancy of the overlapping cation $3d$ and anion $2p$ orbitals. Superexchange mechanisms in oxides were proposed by multiple groups and Kanamori reviewed this work and further investigated these mechanisms from the point of view of the symmetry and occupancy of the specific orbitals involved in the bonding [9]. A set of rules not dissimilar to those proposed by Goodenough were put forward for not only the 180$^o$ case (Figure 1.6) but also the 90$^o$ case (Figure 1.7) and anions other than oxygen were considered. The results of this detailed study indicating the species, bonding and superexchange mechanisms are reproduced in Tables 1.1 and 1.2. Together, the results of Goodenough and Kanamori are formalised in the Goodenough-Kanamori rules for superexchange in oxides.
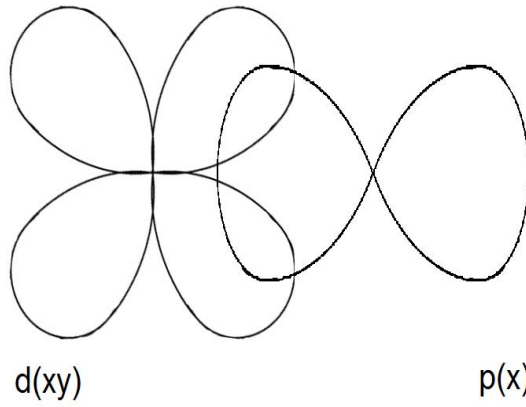
Figure 1.6: Overlap of the $3d$ and $2p$ orbitals of the magnetic cations and anion in a $180^o$ bond configuration.
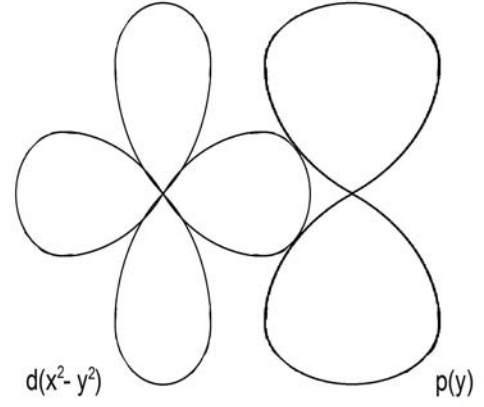


Figure 1.7: Overlap of the $3d$ and $2p$ orbitals of the magnetic cations and anion in a $90^o$ bond configuration.

Table 1.1: Investigation by Kanamori into superexchange mechanisms in transition metal oxides for the $180^o$ bond case [9].

| $N^o$. $3d$-electrons of interacting cations | Species of interacting cations | Relevant bond and mechanism | Resultant superexchange interaction | Total superexchange interaction |
|---|---|---|---|---|
| $d^3 - d^3$ | $Mn^{4+}$-Mn4+ $Cr^{3+}$-$Cr^{3+}$ | $\sigma$-bond and $\pi$-bond A, G, A-H, S | Antiferro. | Antiferro. |
| $d^8 - d^8$ | $Ni^{2+}$-$Ni^{2+}$ | $\sigma$-bond A, G, A-H, S | Antiferro. | Antiferro. |
| $d^5 - d^5$ | $Mn^{2+}$-$Mn^{2+}$ $Fe^{3+}$-$Fe^{3+}$ | $\sigma$-bond A, G, A-H, S $\pi$-bond G, A-H, S $\pi$-bond A | Antiferro. Antiferro. (weak) Uncertain (weak) | Antiferro. |
| $d^8 - d^3$ | $Ni^{2+}$-$V^{2+}$ | $\sigma$-bond and $\pi$-bond A, G, A-H, S | Ferro. | Ferro. |
| $d^5 - d^3$ | $Fe^{3+}$-$Cr^{3+}$ | $\sigma$-bond A, G, A-H, S $\pi$-bond G, A-H $\pi$-bond A, S | Ferro. Antiferro. (weak) Uncertain (weak) | Ferro. |
| $d^4 - d^4$ | $Mn^{3+}$-$Mn^{3+}$ | * | | |
| $d^6 - d^6$ | FeO ($Fe^{2+}$-$Fe^{2+}$) | $\sigma$-bond A, G, A-H, S $\pi$-bond | Antiferro. Uncertain (weak) | Antiferro. |
| $d^7 - d^7$ | CoO ($Co^{2+}$-$Co^{2+}$) | $\sigma$-bond A, G, A-H, S $\pi$-bond | Antiferro. † | Antiferro. |

*      Depends on the direction of the line of superexchange.

†      Weak, but dependent upon the line of superexchange.

Table 1.2: Investigation by Kanamori into superexchange mechanisms in transition metal oxides for the $90^o$ bond case [9].

| $N^o$. $3d$-electrons of interacting cations | Species of interacting cations | Relevant bond and mechanism | Resultant superexchange interaction | Total superexchange interaction |
|---|---|---|---|---|
| $d^8 - d^8$ | $Ni^{2+}$-$Ni^{2+}$ | $p\sigma$-d$\gamma$ bond<br>A, G<br>S<br>s-d$\gamma$ bond<br>A, G, A-H, S | Ferro.<br>Uncertain<br><br>Antiferro. | Ferro. |
| $d^5 - d^5$ | $Mn^{2+}$-$Mn^{2+}$<br>$Fe^{3+}$-$Fe^{3+}$ | | Uncertain | * |
| $d^3 - d^3$ | $Cr^{3+}$-$Cr^{3+}$ | p$\sigma$-d$\gamma$ and p$\sigma$-d$\epsilon'$<br>A, G, A-H, S<br>p$\pi$-d$\epsilon$ and s-d$\gamma$<br>A, G, A-H, S | Ferro.<br><br>Antiferro. (weak) | Ferro. |
| $d^8 - d^3$ | $Ni^{2+}$-$V^{2+}$ | p$\sigma$-d$\gamma$ and p$\sigma$-d$\epsilon'$<br>A, G, A-H<br>S<br>p$\pi$-d$\epsilon'$ and s-d$\gamma$,s-d$\gamma'$<br>A, G, A-H | Antiferro.<br>Uncertain (weak)<br><br>Ferro. (weak) | Antiferro. |

\*     Tendency toward antiferromagnetic interaction with decreasing number of 3d-electrons.

The Goodenough-Kanamori results state that:

(1) "whenever octahedral-site cations are located on opposite sides of a common anion, they interact antiferromagnetically if they have a half filled e$_g$ orbital (e.g. $Mn^{2+}$, $Fe^{2+}$, $Fe^{3+}$, $Co^{2+}$, $Co^{3+}$, $Co^{4+}$, $Ni^{2+}$)" [8]

(2) "any interaction between identical cations via and intervening, symmetrically bonded oxygen ion must, by symmetry, be antiferromagnetic" [8]

(3) "whenever octahedral-site cations are located on opposite sides of a common anion, they interact ferromagnetically if one cation has completely empty e$_g$ orbitals and the other has half filled e$_g$ orbitals" [8]; "for the $180^o$, we may say we expect generally antiferromagnetic interaction between cations of the same kind ... and ferromagnetic interaction between a cation with more-than-half-filled $d$-shell and a cation with less-than-half-filled $d$-shell." [9]

(4) in the $90^o$ case the interaction is generally ferromagnetic for cations of the same kind, and antiferromagnetic between a cation with more-than-half-filled $d$-shell and a cation with less-than-half-filled $d$-shell [9]

An alternative method of indirect exchange is that of *double exchange*. Many transition metals have multiple stable oxidation states and in some oxides both states may be simultaneously present; in these materials *double exchange* may dominate. The electron configuration of $M^{n+}$ and $M^{(n+1)+}$ are identical except

for a hole in the latter and it can be shown by derivation that the minimum energy spin configuration in this case is ferromagnetic [6], as the "hopping" of an electron from the first site to the second (or conduction of the hole in the reverse direction) results in the ground state configuration of each site only if parallel spin alignment is present.

### 1.3.5 Anisotropic exchange

The exchange present in a material may not be isotropic, with different exchange constants in different crystal directions that may even have different signs - leading to competing exchange interactions. Accordingly the orientation of the magnetic moment minimises the energy of the system and a preferred orientation of the magnetic moments on the lattice is a result of anisotropic exchange.

### 1.3.6 Geometric frustration

In a magnetically ordered system *geometric frustration* results when the spin on a lattice site cannot fully compensate the nearest neighbour exchange. For example, a network of antiferromagnetically coupled spins on a 2D triangular lattice has no well defined ground state as every third spin is *frustrated*, as shown in Figure 1.8.

Frustrated lattices exist in both 2- and 3-dimensions with the triangular and Kagome lattices in 2D, and the face centred cubic (FCC) and pyrochlore lattices in 3D [10]. The degeneracy of the ground states of these lattices may be lifted by extending the 2D lattices into 3D and thereby creating inequivalent exchange
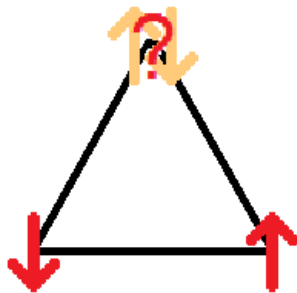


Figure 1.8: Geometric frustration of magnetic spins coupled by antiferromagnetic exchange on a triangular lattice.

paths. For example this may be achieved by layering the frustrated 2D lattices, or by the presence of lattice defects, vacancies, impurities or non-magnetic ions that interrupt the exchange paths and lift the geometric frustration.

### 1.3.7   Low dimensional magnetism

Low dimensional magnetic systems are interesting due to the unique physics present in these systems. In bulk materials the magnetic ions of these systems exist in ladders or chains for the 1D case, or planes in the 2D case that are isolated from each other in the alternative dimension(s) leading to the systems exhibiting low dimensional magnetic characteristics [11]. A statistical analysis investigating the disorder-to-order process for a 2D Ising magnetic was reported by Onsager [12]. In such systems the 1D or 2D exchange is significantly stronger than the exchange parallel to the alternative axes. However, as the material is inherently 3D often phase transitions to higher dimensionality are observed at sufficiently low temperatures.

These cross-over transitions are characterised by a variation in the critical exponent of the magnetic transition at the lower critical temperature [13], and a peak in the temperature dependent magnetic susceptibility at this point [14].

## 1.4   Ferroelectricity

Ferroelectricity is the phenomena of electric dipole ordering within a material, and specifically refers to systems where more than one equivalent orientation of dipoles exists (ferro/antiferro-electric domains) and an electric field may switch between the two configurations. The dipoles may order either parallel, ferroelectric ordering, or anti-parallel, antiferroelectric ordering. A system where electric dipoles order but orientable domains do not exist is not ferroelectric (it is *pyroelectric*). A summary of common structural transitions that involve the displacement of atoms and their behaviour under an applied electric field is provided as Figure 1.9. Electric dipole moments are aligned parallel in a pyroelectric crystal, and anti-parallel in an anti-polar crystal, yet in neither case does the polarisation swap under an applied electric field despite the presence of the dipole moment. In the case of a pyroelectric ferro/antiferro-electric or antipolar ferro/antiferro-

electric multiple polarisation states exist. Unlike the antiferromagnetic case, an antiferroelectric crystal swaps to a ferroelectric state with the application of an electric field.

A ferroelectric crystal may be *intrinsically* or *extrinsically* ferroelectric. The material is ferroelectric below a critical temperature that is referred to as the Curie temperature, and is either non-polar or paraelectric above this temperature, but if the melting point is below the Curie temperature the high temperature phase may never be observed. In the case of an intrinsic ferroelectric the primary order parameter of the phase transition at the Curie temperature is that of the ferroelectric ordering mechanism, whilst in an extrinsic ferroelectric the ferroelectric ordering is a secondary ordering parameter that is coupled to another ordering process.

In order to discuss the ferroelectric ordering process further it is first beneficial to understand the properties of the high temperature phase that exists above the Curie temperature, called the *ferroelectric prototype.*

### 1.4.1   Non-polar and paraelectric order

The ferroelectric prototype phase may be either *non-polar* or *paraelectric.* In a non-polar crystal there are no permanent electric dipoles in the material, and only temporary electric dipoles exist due to the instantaneous anisotropic distribution of electron density or thermal vibration of atoms (analagous to the diamagnetic state in magnetism). If an alternating ionic chain of cation A and anion B is considered then in this case the potential function of B relative to its position between two static A ions is plotted as Figure 1.10.

Alternatively, permanent electric dipoles may exist within the crystal structure where these dipoles are oriented randomly and no long range order exists (analogous to paramagnetic order). The potential energy diagram for the displacement of an anion in an alternating ionic chain in displacive paraelectric system is shown as Figure 1.11.

In this simple paraelectric example two energy minima exist with an energy barrier between the two. At $T_1$, thermal energy allows the anion to access both minima and within the crystal a disordered, fluctuating paraelectric distribution
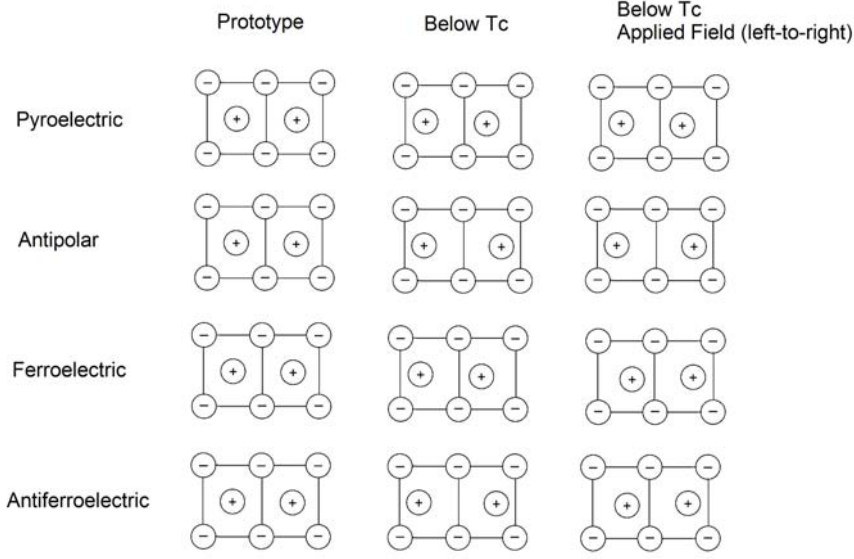
Figure 1.9: Example of the different electronic ordering motifs above and below the critical ordering temperature and under an applied field.
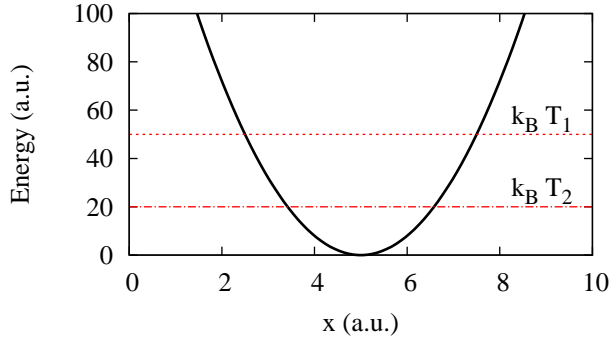


Figure 1.10: Potential energy function of anion $B_n$ as a function of its position between cations $A_n$ (located at $x = 0$) and $A_{n+1}$ (located at $x = 10$) in the case of a non-polar system. The thermal energy at temperatures $T_1$ and $T_2$ is indicated and discussed in text.
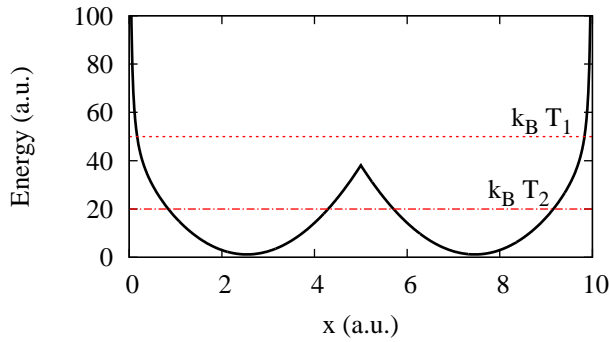


Figure 1.11: Potential energy function of anion $B_n$ as a function of its position between cations $A_n$ (located at $x = 0$) and $A_{n+1}$ (located at $x = 10$) in the case of a paraelectric system. The thermal energy at temperatures $T_1$ and $T_2$ is indicated and discussed in text.

of dipoles exists. On the other hand, at $T_2$ thermal energy is insufficient to overcome the barrier and and a disorder paraelectric state where the dipole orientation is fixed would be achieved, and if the application of an electric field leads to the two sites becoming inequivalent then the material is ferroelectric.

Non-polar and paraelectric crystals may be molecular, where the molecular electric dipole is the lattice dipole. In this case an example of a non-polar crystal would be dry ice, solid $CO_2$, and an example of a paraelectric crystal would be ice, solid $H_2O$.

In a purely ionic crystal the potential would be similar to that of Figure 1.10; however, all interatomic bonds have a degree of covalent character, that is electrons shared between the ions. Permanent electric dipoles may exist if the covalency about an ion is anisotropic and one interatomic bond has more electron density and is therefore shorter distorting the lattice.

In these ionic examples the electric dipole is produced due to the displacement of anions (or cations) leading to the centers of negative and positive charge of the lattice becoming inequivalent. In the case of a paraelectric system at a critical temperature between $T_1$ and $T_2$ the paraelectric dipoles may order as the energy minima shown in Figure 1.11 become inequivalent leading to a pyroelectric phase; this is referred to as an *order-disorder* transition. On the other hand, a material may have a high temperature non-polar configuration, but at a critical temperature the potential energy function changes leading to the presence of paraelectric dipoles. In this case a measurement at a high temperature $T_1$ would have the non-polar characteristics of Figure 1.10 whilst at a critical temperature the ions would displace and at the lower temperature $T_2$ the characteristics of Figure 1.11 with inequivalent minima would be observed and a pyroelectric phase would be observed. This sort of electric polarisation is said to be *displacive*. Not all electric dipoles in ionic systems are primarily displacive, if the distribution of positive and negative charge on the lattice sites of the crystal is not centrosymmetric then a net electric dipole will exist. It is not stable to group cations or anions together, but in a system where an element exists in different oxidation states, for example $M^n$ and $M^{n+1}$, then it is possible for these two states to order on the lattice in a non-centrosymmetric fashion leading to a net electric dipole. This is *charge ordering* and is an order-disorder transition associated with a decrease in electron hopping between the sites. In this case, the electric dipole may be enhanced by displacements of the ions that result from the charge order, but these displacements will be limited by the crystal structure and are secondary to the charge

ordering process.

A crystal in which hydrogen bonding exists may have permanent electric dipoles due to the distribution of the hydrogen bonds. There are cases where by symmetry there are multiple orientations of hydrogen bonds and an applied electric field alters these bond directions. These materials were the first discovered class of ferroelectric materials.

## 1.4.2   Ferroelectric order

A material with a polarisation per unit volume is pyroelectric, and as has been discussed, ferroelectrics are a subset of these materials where multiple equivalent orientations of the polarisation exist leading to the formation of ferroelectric domains. Temperature, pressure, crystal imperfections and crystal structure are all contributing factors as to whether other polarisation orientations exist and are thermally accessible and switchable with an applied electric field.

The pyroelectric phase of a crystal may be considered to be described by Figure 1.11 at $T_2$ with inequivalent minima, and in such a case there are two orientations of polarisation (each of the two wells). Assuming the energy barrier between the two states is not too high (and in the absence of quantum tunnelling) then an applied electric field may switch between the two polarisation states, changing the domain population, and the material is ferroelectric.

depending upon the extent of the asymmetry and the effective height of the energy barrier, as shown in Figure 1.12, then only one state may be populated and it may not be possible to switch to the other state with an applied electric field. Such a pyroelectric material is not ferroelectric. The application of pressure and the associated stress and strain, changing the temperature, the presence of crystal imperfections, and the local anisotropy of the material will vary the shape of the potential energy function.

Initially the order-disorder or displacive character of ferroelectric transitions was explained by individual microscopic models for each case as there seemed to be no relation between the different cases. These different mechanisms for the ionic instabilities in each case made it difficult to address ferroelectricity as a whole without a unified model. The displacements were explored from the point
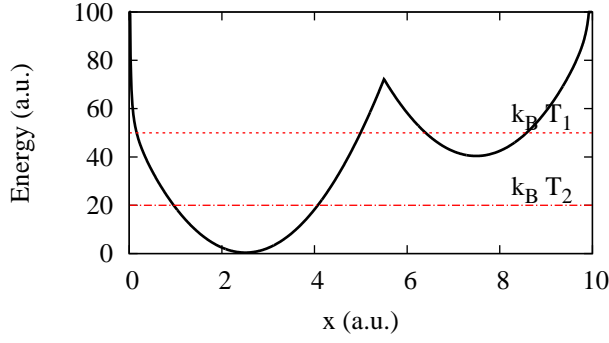
Figure 1.12: Potential energy function of anion $B_n$ as a function of its position between cations $A_n$ (located at $x = 0$) and $A_{n+1}$ (located at $x = 10$) in the case of an asymmetric potential, a potentially non-ferroelectric pyroelectric system. The thermal energy at temperatures $T_1$ and $T_2$ is indicated and discussed in text.

of view of lattice modes and it was found that the ferroelectric transitions may collectively be described by the condensation of a soft mode at the Brillouin zone centre. The condensation of a propagating mode corresponding to quasi-harmonic motion about the mean position characterises a displacive transition, while the condensation of a diffuse mode representative of thermal hopping between the two energy wells of a paraelectric state is characteristic of an order-disorder transition.

### 1.4.3   Phonons

Phonons are the quantised vibrational modes of a crystal lattice. A polar phonon is a vibrational mode of an ionic lattice where a dipole moment is created as the ions move away from their equilibrium positions. The ferroelectric displacements stabilised during the transition from a non-polar/paraelectric phase into the ferroelectric phase may correspond to the displacements associated with a polar phonon, in which case the transition may be described by the condensation of the polar phonon mode.

Phonons with displacements that are stabilised by the ferroelectric state will strain the lattice to a lesser extent in the ferroelectric phase than in the ferroelectric-prototype and therefore ferroelectric phase transitions are complemented by the softening of associated phonon modes.

## 1.5 Lutetium Ferrite

$LuFe_2O_4$ is a promising candidate for a strong magnetoelectric material as both the ferroelectricity and ferromagnetism result from the same Fe sites that are crystallographically equivalent in the ferroelectric prototype. $LuFe_2O_4$ and other isostructural $RFe_2O_4$ materials have been studied for nearly 35 years, and with a recent explosion in studies on this system there is an extensive range of literature to address.

A review of the literature is provided in the following sections and is divided into synthesis and structural characterisation, magnetic characterisation, electronic characterisation, and magnetoelectric characterisation.

There has been a reasonable amount of work devoted to studying doping in this system, that is either partial or complete substitution of the rare earth or Fe sites. Additionally the impact of high pressure on the crystal, magnetic, and electric properties of $LuFe_2O_4$ has been studied but this portion of the literature is outside the scope of this work.

### 1.5.1 Synthesis and characterisation

$LuFe_2O_4$ was first discovered as part of experimental investigations into the $Lu_2O_3/Fe_2O_3$ phase diagram, published in 1974. Independent of each other, the $RFe_2O_4$ ($R$ = rare earth) family of isostructural materials were discovered by researchers in France [15] and Japan [16]. Each group applied a different synthetic method: the French group combined $R_2O_3$ and $Fe_2O_3$ in a 1:2 ratio and reduced the mixture at $900^oC$ in a 23% $H_2$-$H_2O$ atmosphere for 24 hours prior to annealing at $900^oC$ under vacuum ($10^{-6}$ Torr), while the Japanese group combined $R_2O_3$ and $Fe_2O_3$ in a 1:2 ratio and reduced the mixture in air at $1200^oC$ for 3 days prior to equilibrating the oxygen content by annealing the sample at $1200^oC$ in a controlled $CO_2/H_2$ atmosphere.

The resulting powder samples were characterised by x-ray diffraction and determined to be layered oxides; both groups determined the structure to be trigonal corresponding to either R$\bar{3}$m, R3m or R32 [16,17] (the French group initially published a monoclinic solution [18], but a correction based upon further work quickly followed [17]). The discrepancy in the structural solutions proposed in Ref. [18]

and Ref. [16] was investigated by the Japanese group who confirmed the trigonal result with further single crystal refinement of the structure of $YbFe_2O_4$ [19], in agreement with Ref. [17]. The $LuFe_2O_4$ sample obtained was described as a black ferrimagnetic product with a Curie temperature of $237 \pm 2$ K and chemical analysis indicated the presence of both $Fe^{2+}$ and $Fe^{3+}$ [15]. A method for the controlled growth of large $YFe_2O_4$ single crystals was derived from the method of [16] where the oxygen partial pressure was controlled through the $CO_2$-$H_2$ system and the crystal growth performed by the floating zone method [20]. Large crystals of $LuFe_2O_4$, $LuFeCoO_4$ and $YbFeMgO_4$ were also reported as grown by the floating zone method with a $CO_2$-CO atmosphere due to the undesirable presence of $H_2O$ in the $CO_2$-$H_2$ environment [21]. The crystal structure of $LuFe_2O_4$ was determined by single crystal x-ray diffraction [22] and the resulting atomic structure is reproduced in Figure 1.13 with the structural parameters summarised in Table 1.3.

The synthesis method of the Japanese group equilibrated the oxygen content in a controlled oxygen atmosphere ($CO_2/H_2$) at high temperature [16]. Multiple $R$-Fe-O stable phases exist, therefore an understanding of the thermodynamics of this method is required to yield the desired product. The $Fe$-$Fe_2O_3$-$Y_2O_3$ [23] and $Fe$-$Fe_2O_3$-$Yb_2O_3$ [24] phase equilibrium was established at $1200^oC$ and the standard free energy of formation of $YFe_2O_{3.915}$, $YFeO_3$, and $Y_3Fe_5O_{12}$ and $YbFe_2O_4$, $Yb_2Fe_3O_7$, $YbFeO_3$, and $Yb_3Fe_5O_{12}$ were determined by this method of controlled oxygen partial pressure. These investigations revealed that multiple oxide phases are stable and that a range of oxygen content (deficient/excess) $RFe_2O_4$ samples may be synthesised. The Y-Fe-O system was equilibrated at $1100^oC$ and $YFe_2O_4$ was found to be unstable and did not form [25]. Alternatively, $LuFe_2O_4$ has been shown to form from an undercooled $LuFeO_3$ melt in a reduced oxygen partial pressure environment and the associated phase diagrams investigated [26].

The low temperature properties of stoichiometric $YFe_2O_4$ [27] have been shown to be very different to those demonstrated in the non-stoichiometric case [28]. Two discontinuities in the temperature dependent magnetisation were observed and powder x-ray diffraction indicated that the higher temperature discontinuity corresponded to a trigonal-monoclinic phase transformation where the *ab*-plane is distorted rectangularly, the *c*-axis tilts toward the *a*-axis, and the cell volume doubles. The second discontinuity was attributed to a further monoclinic-triclinic transition. No structural distortions have been observed in the non-stoichiometric case. Mössbauer spectroscopy indicated the transitions are first order due to distinct spectra observed for each phase. These transitions were attributed to
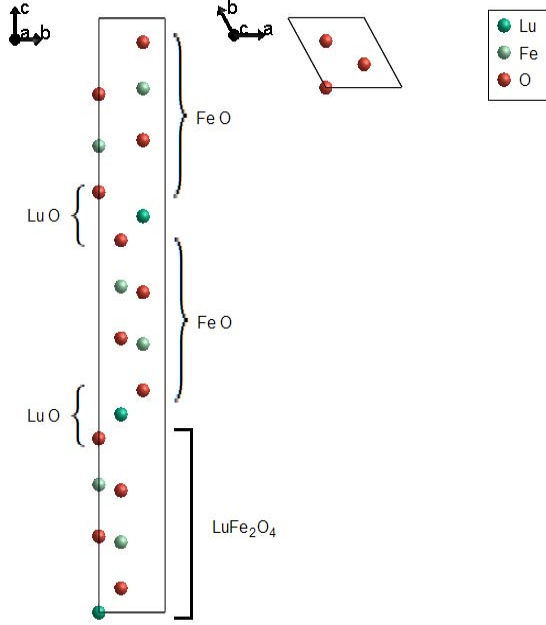
Figure 1.13: Atomic structure of LuFe$_2$O$_4$ determined by single crystal x-ray diffraction [22]. Structural parameters are summarised in Table 1.3.

Table 1.3: Summary of structural parameters of LuFe$_2$O$_4$ determined by single crystal x-ray diffraction [22] at 295 K. For all atoms $x = y = 0$, $U_{11} = U_{22} = 2U_{12}$ and $B_{eq} = \frac{8\pi^2}{3} \sum_i \sum_j U_{ij} a_i^* a_j^* \mathbf{a}_i \mathbf{a}_j$.

| Space Group | R$\bar{3}$m | (#166) | | |
|---|---|---|---|---|
| $Z$ | 3 | | | |
| $a$ | 3.4406(1) Å | $c$ | 25.28(1) Å | |
| Lu | z | 0 | O$_1$ z | 0.1281(3) |
| | U$_{11}$ | 0.0041(1) | U$_{11}$ | 0.019(1) |
| | U$_{33}$ | 0.0432(2) | U$_{33}$ | 0.047(4) |
| | B$_{eq}$ | 1.35(1) | B$_{eq}$ | 2.3(1) |
| Fe | z | 0.21518(3) | O$_2$ z | 0.2926(2) |
| | U$_{11}$ | 0.0100(1) | U$_{11}$ | 0.013(1) |
| | U$_{33}$ | 0.0090(2) | U$_{33}$ | 0.008(1) |
| | B$_{eq}$ | 0.76(1) | B$_{eq}$ | 0.9(1) |

magnetic and electric ordering and are discussed further in later sections.

Electron diffraction on $YFe_2O_4$ and $YbFe_2O_4$ revealed lattice distortions that break the 3-fold rotational symmetry of space group $R\bar{3}m$ due to extra super-structure reflections observed just above room temperature. Diffraction patterns of both stoichiometric and non-stoichiometric $YFe_2O_4$ were collected and super-lattice reflections with propagation vectors $\left(\frac{1}{3}\ \frac{1}{3}\ \frac{1}{2}\right)$ and $\left(\frac{1}{3}\ \frac{1}{3}\ \frac{3}{2}\right)$ were observed at room temperature in the stoichiometric case. The intensity of the superlattice reflections was found to decrease when the beam intensity was increased; this was attributed to ordered lattice distortions that are reversibly disordered by heating from the beam. On the other hand, in the non-stoichiometric case near-continuous twisted rods were observed with intensity modulated by the same propagation vectors; however, the observed variation in the superlattice intensity with variable beam intensity was not observed in the non-stoichiometric sample. A similar result was obtained for non-stoichiometric $YbFe_2O_4$.

The effect of oxygen stoichiometry on the properties of $YFe_2O_{4-x}$ where $x = 0.00, 0.095$, and $0.005$ have been investigated [29]. X-ray diffraction indicated that only the stoichiometric sample underwent the previously identified structural distortions as a function of temperature, and the non-stoichiometric samples remained trigonal even at 77 K. The non-stoichiometric samples showed an increase in the volume of the unit cell rather than the expected thermal contraction. The temperature dependence of resistivity and specific heat for powder and single crystal samples of these varying stoichiometries have been reported [30]. The specific heat change at both transition temperatures indicates the first order nature of the transitions.

A study on $YbFe_2O_{4+x}$ samples where $x = -0.027, -0.003, +0.015$ and $+0.03$ has been reported [31]. In no case was a structural distortion observed at any temperature despite the speculation that the $x = -0.003$ sample should have been sufficiently stoichiometric if $YbFe_2O_4$ were to be expected to behave in the same fashion as $YFe_2O_4$. It was therefore concluded that the choice of rare earth ion impacts the structural and magnetic properties of the $RFe_2O_4$ materials.

As it had been demonstrated that the nature of the rare earth cation influenced the stoichiometric dependence and properties of the $RFe_2O_4$ materials, a study was performed to classify the behaviour with respect to $R$ [32]. $Y_{1-t}Lu_tFe_2O_{4+x}$ ($t$=0.02,0.05,0.10,0.20,0.50), $Y_{1-t}Dy_tFe_2O_{4+x}$ ($t$=0.05,0.10,0.20), $ErFe_2O_{4+x}$ and $TmFe_2O_{4+x}$ were investigated and the results compiled with pre-

viously reported stoichiometric studies of $YFe_2O_{4+x}$, $YbFe_2O_{4+x}$ and $LuFe_2O_{4+x}$. Three types were identified:

(a) Exhibiting two successive transitions and a low temperature triclinic phase. Only stoichiometric $YFe_2O_4$ and $Y_{0.95}Dy_{0.04}Fe_2O_{4+x}$ ($x = 0.021$) belong to this type.

(b) Exhibiting only one structural transition to the monoclinic phase. A small magnetisation is observed at low temperatures after field cooling. $Y_{0.98}Lu_{0.02}Fe_2O_{4+x}$ ($x = -0.003$), $Y_{0.95}Lu_{0.05}Fe_2O_{4+x}$ ($x = -0.008$), $Y_{0.90}Lu_{0.10}Fe_2O_{4+x}$ ($x = -0.014$), and $Y_{0.90}Dy_{0.10}Fe_2O_{4+x}$ ($x = -0.040$) belong to this type.

(c) Exhibiting no structural distortions and a remarkable magnetisation is observed after field cooling. $Y_{0.80}Lu_{0.20}Fe_2O_{4+x}$ ($x = -0.007$), $Y_{0.50}Lu_{0.50}Fe_2O_{4+x}$ ($x = -0.003$), $Y_{0.80}Dy_{0.20}Fe_2O_{4+x}$ ($x = -0.061$), $ErFe_2O_{4+x}$ ($x = -0.085$) and $TmFe_2O_{4+x}$ ($x = -0.004$), all $LuFe_2O_{4+x}$, $YbFe_2O_{4+x}$ and non-stoichiometric $YFe_2O_4$ belong to this type.

It was concluded that the larger the ionic radius of $R^{3+}$, the greater the tendency for type (a), but this was countered by non-stoichiometry leading to a preference for type (b) or (c). Additionally, the better the stoichiometry the higher the temperature at which the transitions were observed.

Nearly stoichiometric $ErFe_2O_4$ showed a similar pair of transitions as stoichiometric $YFe_2O_4$ [33] in the magnetic susceptibility, crystal structure and electrical resistivity indicating a Verwey transition accompanied the lattice distortions.

High resolution neutron diffraction with polarisation analysis has been performed on stoichiometric $YFe_2O_4$ and determined the monoclinic phase is in fact triclinic at 225 K and the low temperature phase is another more complicated triclinic structure [34].

High resolution synchrotron powder x-ray diffraction was performed on nearly stoichiometric $YFe_2O_{4-\delta}$ where $\delta < 0.005$ [35] (previously the best sample was considered to have $\delta \approx 0.01$). Six temperature dependent structural phases were identified: between 225 and 250 K, $R\bar{3}m$ symmetry as described previously is observed; between 225 and 250 K, peaks split and superlattice peaks at $\left(\frac{h}{3} \frac{h}{3} \frac{3l}{2}\right)$ appear; between 150 and 225 K, additional peaks indexed as $\left(\frac{h}{2} \frac{k}{2} l\right)$ and $\left(\frac{h}{6} \frac{k}{6} l\right)$;

between 115 K and 150 K, a discontinuous jump in the peak positions and intensities is observed at around 150 K; between 60 K and 115 K, another discontinuity is observed at 60 K; below 60 K, further structural changes are observed below 60 K. Further complicating the structure, transmission electron microscopy revealed that the most common structural defect in $LuFe_2O_4$ is twinning along the *c*-axis [36].

## 1.5.2 Magnetic characterisation

In 1976, it was reported that non-stoichiometric $YFe_2O_{3.94}$ was prepared in powder form and both magnetometry and Mössbauer spectroscopy was performed between 77 and 300 K [37]. These measurements indicated that a weak magnetic moment of approximately 2 emu/g was induced below 240 K by magnetic field cooling from 300 to 77 K and an uniaxial anisotropy was also induced, whilst paramagnetism was observed above 300 K. Magnetisation measurements revealed antiferromagnetic ordering with a broad maximum in the magnetisation at approximately 185 K that increased with increasing applied field but was always weaker than the moment induced by field cooling. Mössbauer spectroscopy indicated an internal field characteristic of $Fe^{3+}$ and a chemical shift that was partway between that expected for high-spin configurations of $Fe^{2+}$ and $Fe^{3+}$. A single crystal study extending this work was reported in 1978 in which magnetisation, magnetic torque, Mössbauer spectroscopy and electrical conductivity measurements were performed [28]. Magnetic field cooling with the external field aligned in the *ab*-plane had little effect and a weak temperature dependence was reported; furthermore, no anisotropy in the *ab*-plane could be detected. On the other hand, strong temperature dependence was observed when the same process was applied with the external magnetic field parallel to the *c*-axis: magnetisation increased below 205 K and thermal hysteresis was evident below 140 K. The magnetisation was proportional to the applied field when applied in the *ab*-plane, and linear behaviour was observed when the field was parallel to the *c*-axis below 140 K and above 205 K. Non-linear behaviour was observed between these temperatures. The magnetic transition temperature was identified to be 205 K above which the sample was paramagnetic, and the magnetic susceptibility was shown to be ferromagnetic in character with strong anisotropy between the *c* and *a*-axes as demonstrated by an 80 K difference in the asymptotic Curie temperatures which was confirmed by magnetic torque measurements. The effective Bohr magneton was shown to be the average of $Fe^{2+}$ and $Fe^{3+}$. Below 120 K the magnetisation

was characterised as a weak ferromagnet and the magnetic susceptibility increased linearly with applied field. The residual moment was found to be proportional to the applied field above 0.6 T and unsaturated at the maximum field of 1.4 T, but non-linear between 0 and 0.6 T. The torque curves indicate the unidirectional nature of the magnetisation with little rotational hysteresis below 120 K and the easy axis parallel to the c-axis. Mössbauer spectroscopy also confirmed the large anisotropy and easy-axis parallel to the *c*-axis. A Jordan type after-effect was observed in the time dependence of magnetisation at 77 K, but the magnetisation was irreversible. Between 205 and 140 K the same non-linear behaviour described at low temperature was observed which disappeared at the Néel point. A large rotational hysteresis was observed in this temperature range by magnetic torque measurements. The electrical conductivity showed no anomalies between 120 and 300 K and could be described by a single activation energy. Anisotropy of the conductivity suggested the main process may be an electron hopping mechanism between $Fe^{2+}$ and $Fe^{3+}$. An inequivalent ordering of $Fe^{2+}$ and $Fe^{3+}$ was proposed based upon these observations as such ordering would lead to a magnetisation in addition to the ordinary one. Single crystal neutron diffraction performed on a similarly oxygen deficient sample revealed 2D magnetic order below 205 K [38] characterised by magnetic Bragg rods of scattering at $\left(\frac{1}{3} \frac{1}{3} L\right)$ and $\left(\frac{2}{3} \frac{2}{3} L\right)$ with no other magnetic scattering observed nor any magnetic contributions to nuclear scattering.

On the other hand, the magnetic properties of a stoichiometric sample of $YFe_2O_4$ were studied and found to be very different to those of the non-stoichiometric case [39]. The magnetisation was linear with applied external field at all field strengths and temperatures, and there was no remnant magnetisation induced by magnetic field cooling. The magnetic susceptibility had a maximum at about 240 K which was attributed to the antiferromagnetic ordering. Discontinuities in the magnetic susceptibility were noted at two temperatures which were approximately 10 K higher when measured during heating rather than cooling. These anomalies corresponded to the structural transitions noted in Section 1.5.1. The first was attributed to exchange-striction due to the antiferromagnetic ordering of spins and the second to the non-equivalent ordering of $Fe^{2+}$ and $Fe^{3+}$ on the lattice.

Mössbauer spectra were collected for the same stoichiometric powder of $YFe_2O_4$ [39] which revealed the same phase changes and associated thermal hysteresis as indicated by the previous x-ray diffraction and magnetisation study. The measured hyperfine field was similar to that cited for the non-stoichiometric case [37] and

disappeared at about 240 K confirming the Néel point. The temperature dependence of the hyperfine field was interpreted to indicate that the non-equivalent $Fe^{2+}/Fe^{3+}$ order enhanced the exchange coupling, consistent with [27]. The narrow line-width and well resolved spectra indicated the presence of distinct $Fe^{2+}$ and $Fe^{3+}$ species.

Mössbauer spectra of $YbFe_2O_4$, $TmFe_2O_4$, $ErFe_2O_4$, $HoFe_2O_4$, and $YFe_2O_4$ collected at 295 K indicate the presence of $Fe^{2+}$ and $Fe^{3+}$ and that the variation in the rare earth was observed through the compression of the s-electron density of $Fe^{2+}$ because as the radius of the rare earth is reduced (by varying $R$ from Ho→Yb) the *s*-electron density expands and the isomer shift increases [40]. At 77 K the hyperfine field of $Fe^{2+}$ was found to be 330 kOe in $YbFe_2O_4$ and 200 kOe in the other isostructural cases, and the hyperfine field of $Fe^{3+}$ was 470 kOe in $YbFe_2O_4$ and 450 kOe in the others. The observed splitting was similar in each case and consistent with the presence of magnetic relaxation processes. A paramagnetic doublet was observed and it was speculated this may be due to domain wall oscillations or the presence of superparamagnetic clusters. The slope of the log of resistivity plotted against $1/T$ was found to change at the Néel temperature. Refinement and analysis of Mössbauer spectroscopy of $YbFe_2O_4$ was reported which indicated ferrimagnetic order on a triangular lattice in agreement with previous work; furthermore, magnetic field cooling and measuring *in situ* allowed inequivalent $Fe^{2+}$ sites (and $Fe^{3+}$) within each antiferromagnetic spin sublattice to be observed [41]. Further Mössbauer spectroscopy measurements of $LuFe_2O_4$ and $YFe_2O_4$ allowed the $Fe^{2+}$ and $Fe^{3+}$ positions to be well separated and correlations between both charge and spin has been shown by modelling 3 inequivalent sublattices [42]. Later, Mössbauer spectroscopy of $LuFe_2O_4$ confirmed the ferrimagnetic ordering of Fe and that of the three inequivalent $Fe^{3+}$ sites two contribute to the minority spins and the other to the majority spin in a domain while all $Fe^{2+}$ contribute to the majority spin [43]. Mössbauer spectroscopy and magnetometry indicated a magnetic Curie temperature of 250 K [44, 45].

As the stoichiometry had a significant impact, the magnetisation and Mössbauer spectra of $YFe_2O_{4-x}$ where $x = 0.00, 0.095$ and $0.005$ were investigated [29]. Parasitic ferrimagnetism was observed in both non-stoichiometric cases but was absent in the stoichiometric case [27]; the magnetic transition temperature was also shown to be a function of stoichiometry. The Mössbauer spectra indicated that the more stoichiometric the sample material the sharper and more well defined the observed absorption. The parasitic ferrimagnetism was shown to appear between $x = 0.031$ and $0.040$ with the disappearance of the structural transition;

however, it is speculated the transition may still occur at $x = 0.040$ if the cooling rate is slow enough based upon the Mössbauer spectroscopy results.

The field and temperature dependence of the magnetisation as a function of stoichiometry of $YbFe_2O_{4+x}$ have been reported [31] and compared to the results obtained for $YFe_2O_4$. $YbFe_2O_{4+x}$ samples where $x$ = -0.027,-0.003,+0.015, and +0.03 displayed a field-cooled magnetisation in all cases, similar to the non-stoichiometric $YFe_2O_4$.

Neutron diffraction of $YFe_2O_4$ revealed the dimensionality of the magnetic order was stoichiometry dependent [46]. Three-dimensional magnetic order was demonstrated by the observation of magnetic satellite reflections at $\left(\frac{1}{3} \frac{1}{3} \frac{1}{2}\right)$ in the stoichiometry case, whilst only diffuse scattering along $\left(\frac{1}{3} \frac{1}{3} L\right)$ was observed in the non-stoichiometric case. Powder neutron diffraction of $ErFe_2O_4$ indicated it is similar to stoichiometric $YFe_2O_4$ with 2D magnetic order present while cooling until the magnetisation disappears at which point an incommensurate 3D magnetic structure was observed [47]. Neutron diffraction of $LuFe_2O_4$ revealed that 2D magnetic order existed and no 3D order was present down to low temperature [48]. The observed intensity was qualitatively explained by unequal exchange between three unique sublattices.

Polarised neutron analysis of the nuclear and magnetic contributions to scattering have been performed on single crystal $ErFe_2O_4$ [49, 50]. The correlation length of the nuclear component was about 2 lattice parameter lengths (about 50 Å), while the magnetic correlations extended 1/3 of a cell length (8 Å) along the *c*-axis (corresponding to one FeO bilayer) and 50 Å in the *ab*-plane. Furthermore, high resolution neutron diffraction with polarisation analysis was performed on stoichiometric $YFe_2O_4$ [34], but a magnetic structure could not be determined from the separated magnetic intensity.

As discussed in section 1.5.1, temperature dependent high resolution powder synchrotron x-ray diffraction revealed multiple phases in nearly stoichiometric $YFe_2O_4$ [35]. Anomalies in the derivative of the magnetic susceptibility of this sample at 60 and 130 K indicate strong spin-lattice coupling and variations in the magnetic structure at these transitions.

Anomalous thermomagnetisation curves for $LuFe_2O_4$ have been interpreted to indicate the existence of multiple magnetic phases [51]. Anomalous thermal hysteresis and field-cooled magnetisation between 130 and 200 K are observed and it

is hypothesised that unique, stable magnetic phases exist below 130 K and above 200 K and that a mixture of these phases exist in the intermediate temperature range. Single crystal magnetisation measurements have demonstrated the large anisotropy of the field-cooled magnetisation and a two step transition indicated in the magnetisation [52].

The ferrimagnetic spin arrangement in $LuFe_2O_4$ has been derived from high field magnetisation measurements. A moment of 2.8 $\mu_B$ extrapolated at 0 K [53] was observed which corresponds to a ferrimagnetic 2:1 spin arrangement on a triangular lattice with small ferromagnetic next nearest neighbour interactions. An irreversible decrease in field-cooled magnetisation was observed at low temperature similar to that reported previously [51] and it was speculated this may be due to thermally activated spin flip within each Fe-O layer. Furthermore, magnetisation jumps and saturation of the field-cooled magnetisation have been reported at applied fields greater than 10 T [54]. The same thermal hysteresis of the field-cooled magnetisation is observed when saturated with a field of 10 T.

Recently, neutron diffraction of a near stoichiometric sample of $LuFe_2O_4$ has revealed 3D magnetic order [55], in disagreement with previous reports. This difference was attributed to variations in stoichiometry between the two studies as stoichiometry has been shown to effect the dimensionality of the ordering in other $RFe_2O_4$ materials. Ferrimagnetic order is observed below 240 K with the appearance of magnetic satellite reflections at $\left(\frac{1}{3}\,\frac{1}{3}\,0\right)$ and $\left(\frac{1}{3}\,\frac{1}{3}\,\frac{3}{2}\right)$ type positions. The satellites at integer values of $L$ (considering a general index of $(H\,K\,L)$) are attributed to ferrimagnetic order of the Fe-sites with 2:1 spin ordering on the triangular lattice in the *ab*-plane and ferromagnetic correlations along the *c*-axis. The additional reflections at the half-integer $L$ positions are attributed to the magnetic texture produced by the 3D charge ordering and the resulting non-centrosymmetric distribution of $Fe^{2+}$ and $Fe^{3+}$ which have different magnetic moments yielding magnetic contrast. This magnetic phase is well crystallised and no diffuse magnetic scattering is reported. Whilst below 175 K the broadening of many reflections is observed and a new set of incommensurate satellites described by the propagation vector $\left(\frac{1}{3}\pm\delta\,\frac{1}{3}\pm\delta\,\frac{3L}{2}\right)$ (where $\delta \approx 0.027$) and a diffuse rod of magnetic scattering is observed along the $\left(\frac{1}{3}\,\frac{1}{3}\,L\right)$ direction. Furthermore, significant intensity variation in the $\left(\frac{1}{3}\,\frac{1}{3}\,0\right)$ type positions is observed through the transition. Three-dimensional correlations below the transition still exist, but have a shorter correlation length. In a later report the full magnetic scattering intensity has been reproduced with the charge order model proposed in [56], but with unexpectedly high magnetic contrast between the $Fe^{2+}$ and $Fe^{3+}$ moments.

Furthermore, it has been shown that the low temperature magnetic co-incides with a monoclinic structural distortion. The application of a magnetic field is able to drive this phase transition with the monoclinic phase distortion disappearing under an applied magnetic field of 1.2 T [57].

The low temperature magnetic coercivity of $LuFe_2O_4$ has been demonstrated to reach 9 T in single crystals. This is attributed to the low-dimensional, uni-axial anisotropy leading to the formation and freezing of pancake-like magnetic domains [58]. These domains have been characterised in detail by magnetic force microscopy (MFM) [59] and the magnetisation reversal demonstrated. Comparison of the MFM images of the magnetic domains and dark field TEM images of the charge ordered domains has demonstrated they have a similar morphology.

Direct current and alternating current measurements have revealed the presence of multiple transitions in $LuFe_2O_4$ and that the AC susceptibility is quantitatively fit by a cluster glass model [60]. An extensive AC susceptibility, DC magnetisation and specific heat investigation has determined the spin glass transition temperature to be 229 K and the dynamic scaling fitted by a cluster-glass model confirming the previously reported result [61]. Further work complimented by magnetocaloric measurements has lead to a complex magnetic phase diagram with multiple cluster glass states existing simultaneously with the reported long-range ferrimagnetic order [62].

A study of the effect of stoichiometry on the magnetic properties of $LuFe_2O_4$ has been reported where the temperature dependence of the field-cooled magnetisation as a function of the $CO_2$/CO ratio was measured [63]. The greatest field-cooled magnetisation was observed when $CO_2$:CO is 5:1 whilst the highest magnetic transition temperature was observed when $CO_2$:CO is 6:1. Furthermore, a magnetometry study of almost stoichiometric $LuFe_2O_{4-\delta}$ (where $\delta \approx 0.02$) has reported a residual moment at high temperature in both magnetically field cooled and zero field cooled cases [64]. This moment is attributed to short range 2D ferrimagnetic order that persists to high temperature in this sample as x-ray diffraction indicates no impurity phases.

Acoustic measurements on oxygen deficient $ErFe_2O_4$ [65] have demonstrated softening of the lattice along the *c*-axis at the magnetic transition temperature, and a large peak in the attenuation corresponding to the onset of 2D ferrimagnetic order.

### 1.5.3 Electric characterisation

Anomalies in the temperature dependent resistivity and specific heat for powder and single crystal samples of varying stoichiometries of $YFe_2O_{4+x}$ have been reported [30]. An anomaly in the resistivity is observed at both structural transition temperatures (for those samples that exhibit the transition) and this anomaly is shown to be anisotropic and only observed when measurements are made in the *ab*-plane. The resistivity measurements reinforce the Mössbauer spectroscopy interpretation that the low temperature structural transition in the stoichiometric case corresponds to the onset of charge ordering (Verwey transition), whilst the high temperature transition indicates the onset of magnetic order (Néel point).

The Seebeck coefficient characterises the electron transport properties of a material and has been reported for both stoichiometric and non-stoichiometric $YFe_2O_4$ [66]. In the stoichiometric case an abrupt change in the Seebeck coefficient is observed at the Verwey transition corresponding to the massive increase in resistivity and the onset of charge order. The form of the Seebeck coefficient below the transition is similar to that of magnetite. As temperature increases above the Verwey transition the Seebeck coefficient decreases, indicating an increase in electron-type transport. This in contrast to the coefficients of magnetite and $Na_{0.33}V_2O_5$ which are constant above the Verwey transition. The Seebeck coefficient above the Verwey transition was explained by electron hopping based upon the previously reported hopping observed in $LuFe_2O_4$. Further work was conducted to lower temperatures [67] and the temperature dependence of the hole and electron mobilities described by different temperature dependences of the spin flip-lattice interactions of $Fe^{2+}$ and $Fe^{3+}$. Further investigation and modelling are presented in Ref. [68].

Mössbauer spectroscopy studies of powdered samples of $RFe_2O_4$ ($R$ = Y, Ho, Er, Tm, Yb, Lu) have been reported [69] between 200 and 500 K and characterise the temperature dependence of electron transport. X-ray diffraction has shown that all Fe ions occupy the $6c$ site of the spacegroup $R\bar{3}m$; however, this is just a measured average and is only representative of the microscopic structure above the Verway transition. Local distortions in the charge ordered state are observed by broadening of the Mössbauer absorption bands. At high temperatures the absorption bands from the two species are merged, but at low temperatures, when the resonant frequency is higher than the hopping frequency, the $Fe^{2+}$ and $Fe^{3+}$ signals can be distinguished. The temperature dependence of the isomer

shift, quadrupole splitting and line width of each charge species for each of the $R\mathrm{Fe_2O_4}$ samples was reported. Further Mössbauer spectroscopy of $\mathrm{LuFe_2O_4}$ has been published where the data are shown to be fitted by 3 inequivalent $\mathrm{Fe^{3+}}$, but only one $\mathrm{Fe^{2+}}$; it is assumed that there are three inequivalent $\mathrm{Fe^{2+}}$ contributions, but that they may not be sufficiently resolved. These measurements indicate that the charge ordering begins to disappear at 320 K (the Verwey transition) and the ferroelectric Curie temperature is 350 K [44]. Alternative Mössbauer spectroscopy of powdered $\mathrm{LuFe_2O_4}$ determined the electric Curie temperature to be 370 K [45].

A dielectric constant and relaxation study of oxygen deficient $\mathrm{ErFe_2O_4}$ [70] has indicated a polarised state in the magnetic phase and a low-frequency dielectric response due to the motion of polarisation domain walls and anomalies at each Verwey transition. Single crystal measurements [71] show the dielectric response is anisotropic with greater dispersion in the *ab*-plane, but a higher frequency along the *c*-axis. The real ($\epsilon'$) and imaginary ($\epsilon''$) parts of the dielectric constant of $\mathrm{ErFe_2O_4}$ reveal two dielectric anomalies: a low temperature dispersion associated with the motion of pyroelectric domain boundaries corresponding to correlated electron hopping between $\mathrm{Fe^{2+}}$ and $\mathrm{Fe^{3+}}$ and a high temperature dispersion attributed to dipole glass behaviour [72]. Similar dispersion behaviour has been demonstrated at the Verwey transition in $\mathrm{TmFe_2O_4}$ [73], $\mathrm{LuFe_2O_4}$, $\mathrm{YFe_2O_4}$ and the rest of the $R\mathrm{Fe_2O_4}$ family. In the case of $\mathrm{HoFe_2O_4}$, dielectric characterisation has identified anomalies at high and low temperature, similar to those observed in other $R\mathrm{Fe_2O_4}$ materials. The high temperature anomaly is attributed to the onset of 3-dimensional charge order at 430 K while the origin of the low temperature step at 280 K is unknown. An activation energy of 0.24 eV was deduced from the loss tangent which is similar to the value of 0.3 eV quoted for other $R\mathrm{Fe_2O_4}$ oxides [74].

Glassy dielectric behaviour has been reported for $\mathrm{LuFe_2O_4}$ corresponding to short range charge order above the ferroelectric transition temperature. This behaviour is interpreted as the gradual freezing of polarisation and the dielectric response is attributed to electron transport between local regions of different polarisation [75]. Furthermore, the temperature dependence of the dielectric dispersion of $\mathrm{LuFe_2O_4}$ has been shown to vary with the oxygen stoichiometry [63]. The more stoichiometric samples have a greater activation energy indicating a longer charge order correlation length and more coherent domain wall motion. The maximum activation energy was measured for a sample synthesised with $\mathrm{CO_2}$:CO of 6:1.

Investigations into the charge ordering process [76, 77] by neutron, electron and x-ray diffraction have been reported. Superlattice reflections appear below the Verwey transition even though these techniques are not directly sensitive to the charge order, so it has been hypothesised that displacements induced by the charge order are observed and a charge density wave (CDW) model was proposed. Based upon these observations, it is shown that in the temperature range 330 to 500 K a 2D CDW state exists with geometric frustration on the hexagonal lattice leading to lines of undetermined charge where electron hopping is allowed. Below 330 K a 3D CDW structure exists with correlations between both Fe layers of an "isolated" bilayer and the geometric frustration is lifted completely. The satellites that describe the charge order are observed at $\left(\frac{1}{3}+\delta \; \frac{1}{3}+\delta \; \frac{3}{2}\right)$ type positions where a non-zero $\delta$ indicates the structure is incommensurate and a possible incommensurate model is proposed. Furthermore, resonant x-ray diffraction [78] performed on these incommensurate satellite reflections indicated they result from the ordering of iron due to observed resonance at the Fe K absorption edge. The experimentally obtained energy dependence of the spot intensity was shown to agree with that calculated by the proposed CDW model for charge order of $Fe^{2+}/Fe^{3+}$. The temperature dependence of a superlattice spot intensity and its energy dependence were reported and shown to increase below approximately 330 K [79].

Further resonant x-ray scattering of $LuFe_2O_4$ was reported and modelled by collecting x-ray absorption data of the isostructural material $LuCoFeO_4$ in which only $Fe^{3+}$ exists and taking the Kramers-Kronig transformation [80]; absorption measurements on $LuFe_2O_4$ were also taken. A chemical shift of 4 eV was determined from comparison of the absorption data and this offset used to calculate the pattern. Reproduction of the observed energy dependence indicated full $Fe^{2+}$ and $Fe^{3+}$ charge order exists in $LuFe_2O_4$.

In order to unambiguously confirm the valence of the ordered Fe species resonant x-ray scattering data of a charge order satellite reflection of $LuFe_2O_4$ was shown to have the same energy dependence as the anomalous scattering factor of $Fe^{2+}$ and $Fe^{3+}$, where the scattering factor was calculated from x-ray absorption data collected on isostructural $LuFeGaO_4$ and $LuFeCoO_4$ in which only $Fe^{2+}$ or $Fe^{3+}$ exist. This confirmed complete charge disproportionation of the $Fe^{2+}/Fe^{3+}$ charge order [81]. Furthermore, a detailed analysis of the previously reported scattering investigations of the highly stoichiometric $YFe_2O_4$ and $LuFe_2O_4$ has been presented and an antiferroelectric stacking of polarised bilayers proposed.

Non-centrosymmetric charge order leads to a polarisation per unit volume, and a switchable polarisation in $LuFe_2O_4$ has been demonstrated by pyroelectric current measurements [82]. Dielectric constant measurements show a low and high temperature dispersion similar to that previously reported for $ErFe_2O_4$ where the low temperature dispersion is attributed to movement of the ferroelectric domain (antiphase) boundary and the high temperature dispersion corresponds to glassy dipole behaviour. The polarisation hysteresis loop has been shown to deviate significantly from the standard square shape in near stoichiometric $LuFe_2O_{4-\delta}$ ($\delta \approx 0.02$) which is explained by large contributions of non-switching polarisation [64].

The polarisation of a classic ferroelectric arises from covalency between cations and anions and the $RFe_2O_4$ family of materials is not ferroelectric in the classic sense as the polarisation results from electron correlations between $Fe^{2+}$ and $Fe^{3+}$. Based upon analysis of the previously reported resonant x-ray and neutron scattering, pyroelectric current switching, dielectric dispersion, and Mössbauer results, $LuFe_2O_4$ was classified as an *electronic ferroelectric* [83].

The ground state charge order configuration of $LuFe_2O_4$ has been shown to have an antiferroelectric stacking of bilayers below the charge ordering transition temperature and a ferroelectric ordering above the transition temperature by single crystal x-ray diffraction and density functional theory calculations. Previously unreported satellites are also discussed, and there is an anomaly in the incommensurability of the charge order satellites at each magnetic transition temperature associated with the magnetoelectric coupling between the charge and magnetic order [56].

The complicated nature of nearly stoichiometric $YFe_2O_4$ was further demonstrated as high resolution synchrotron powder x-ray diffraction revealed multiple electronic phases with strong spin-lattice coupling [35]. Dielectric dispersion is noted at the 250 K transition similar to that previously observed for $ErFe_2O_4$ and $LuFe_2O_4$ and it is therefore believed that the phase between 225 and 250 K has the same 3D charge ordered structure. Transmission electron microscopy was performed on this nearly stoichiometric sample and electron diffraction employed to study the charge order structure in each phase [84]. It was concluded that at room temperature the charge order was 2D, while at 250 K 3D order is established described by $\left(\frac{n}{3} \frac{n}{3} 0\right)$ superlattice reflections. Below 250 K $\left(\frac{n}{2} \frac{n}{2} 0\right)$ superlattice peaks appear indicating a doubling of the CO unit cell in the *ab*-plane and the disappearance of a dielectric response was interpreted as the centrosymmetric charge

order in this phase. At 190 K superlattice peaks at $\left(\frac{n}{4}\,\frac{n}{4}\,0\right)$ appeared indicating a further quadrupling of the CO cell. At 140 K multiple sets of superlattice peaks were evident, at $\left(\frac{n}{2}\,\frac{n}{2}\,0\right)$, $\left(\frac{n}{3}\,\frac{n}{3}\,0\right)$ and $\left(\frac{n}{7}\,\frac{n}{7}\,0\right)$ indicating multiple CO structures in the *ab*-plane. Below 130 K commensurate satellites at $\left(\frac{n}{3}\,\frac{n}{3}\,\frac{m}{2}\right)$ were observed indicating a further 3D phase with doubling along the *c*-axis. Further electron diffraction results were reported [85] employing dark field imaging to explore the origin of the diffuse scattering. It was found that two types of domain structures are observed: one due to the charge order and another due to ordering of the oxygen vacancies.

Further electron diffraction and dark field imaging of the highly stoichiometric sample of $YFe_2O_{4-\delta}$ ($\delta < 0.005$) was reported in Ref. [86]. Commensurate superlattice reflections at $\left(\frac{1}{3}\,\frac{1}{3}\,0\right)$ type positions were found to exist in one part of the sample and incommensurate $\left(\frac{1}{3}+\delta\,\frac{1}{3}+\delta\,0\right)$ position in another. It was confirmed that the first arises from 2D charge order while the latter is due to ordering of oxygen vacancies.

Direct evidence that oxygen deficiencies in the lattice inhibit long range order along the *c*-axis has been observed by a study of the charge ordering in samples where the CO-$CO_2$ ratio has been varied. 2D charge order is observed by electron diffraction in oxygen deficient samples, while 3D order is only observed when the CO:$CO_2$ ratio is 2:3 [87]. The average size of a charge ordered domain in the *ab*-plane observed by dark field imaging was 20 nm. The nature of the satellite reflections and diffuse scattering has been shown to change with varying stoichiometry of $YFe_2O_4$ [88]. Oxygen deficiency is shown to decrease the *c*-axis charge correlations with a 3D-to-2D shift with decreasing oxygen content, but the superlattice periodicity in the *ab*-plane is invariant with changing stoichiometry.

Dark field imaging of $LuFe_2O_4$ has demonstrated a ferroelectric correlation length of approximately 10 nm in the *ab*-plane [89]. Similarly, high resolution imaging of the charge and oxygen vacancy ordering in nearly stoichiometric $YFe_2O_4$ confirmed the nano-size domains and the relationship to the observed dielectric anomalies [90]. Energy filtered dark field imaging has been reported for $YbFe_2O_4$ and indicates that while ferroelectric domains form, they remain less than 10 nm in size at all temperatures and it is assumed that it is the geometric frustration that prohibits long range charge ordering [91].

On the other hand, low temperature electron imaging and diffraction of $LuFe_2O_4$ has revealed that charge order is well crystallised in a charge-stripe phase where

the charge density wave behaves non-sinusoidally and ferroelectricity is established [92]. Furthermore, twinning of the ferroelectric domains at low temperature is observed.

Dielectric studies of $LuFe_2O_4$ under an applied electric field have revealed a giant dielectric tuneability effect. A significant decrease in the dielectric constant is observed with the application of small DC bias fields, up to 50 V/cm, where tens of kV/cm is usually required [93]. This reduction in the polarisability was found to be due to an insulator-metal transition caused by the applied electric field [94] believed to be due to the dielectric breakdown of the charge ordered state. Resistance hysteresis is observed as well as a temperature dependence that indicates thermal fluctuations assist the dielectric breakdown of the charge ordered phase due to the reduction in breakdown voltage with increasing temperature. Additionally, *in situ* transmission electron microscopy has demonstrated that the superlattice reflections attributed to the insulating charge ordered states disappear beyond the dielectric breakdown and reappear when the field is removed [95].

The charge ordered state of these materials has also been investigated extensively by theoretical calculations, and Monte Carlo simulations have been reported that study spin-charge-orbital structures in multiferroic $RFe_2O_4$ which agree with experimentally observed magnetic and electric frustration. Despite the fact that $Fe^{2+}$ is orbitally active, the calculations predict the absence of long range orbital order at low temperature, and a glassy orbital state is predicted [96]. Crystal field splitting calculations and further extensive calculations confirm this prediction of an orbital model that does not show conventional long-range order [97]. The temperature dependent role of thermal fluctuations and quantum zero point fluctuations in relieving the degeneracy is described. It is shown that the ground state wavefunction is well described by the linear combination of states where the honeycomb lattice is covered by nearest-neighbour pairs of orbitals with minimum bond energy [98].

Density functional theory calculations of $LuFe_2O_4$ have been reported and applied to describe the charge, magnetic and orbital order [99]. It is shown that the charge order model proposed by Ikeda is significantly more stable than that proposed by Subramanian, and that a third charge order phase exists which is only 20 meV per formula unit less stable than the Ikeda model. It is proposed that it is fluctuations between these two charge ordered states that lead to the large dielectric constant of $LuFe_2O_4$. Furthermore, the net polarisation per unit

volume for the ferroelectric structure is shown to be significantly greater than that observed experimentally whereas a proposed ferrielectric stacking agrees with the observed polarisation to within 6%.

A unified treatment of the charge and spin ordering in $LuFe_2O_4$ has been provided by Landau theory and symmetry considerations, and predicts that an applied electric field will favour a commensurate ferroelectric structure in order for a spontaneous polarisation to result [100].

Ferroelectric materials are characterised by the vibrational modes that correspond to the intrinsic connection between the polarisation and the lattice structure. Terahertz spectroscopy of $LuFe_2O_4$ has characterised the central mode associated with the electronic ferroelectric charge order as well as revealing a soft mode below 240 K demonstrating displacive ferroelectricity is also present in the multiferroic state [101].

### 1.5.4 Magnetoelectric characterisation

Magnetoelectric coupling has been demonstrated in the $RFe_2O_4$ materials; a large dielectric anomaly has been reported in $LuFe_2O_4$ when weak external magnetic fields are applied [102] at room temperature. At this temperature the material is charge ordered (but disordered magnetically) and the observed decrease in dielectric constant due to the applied field is explained due to the stronger interaction of $Fe^{3+}$ with the field than $Fe^{2+}$. This difference in interaction strength breaks the degeneracy of preferred polarisation directions and reduces the extent of domain wall motion that characterises the zero field dielectric dispersion. Density functional theory calculations have proposed that alternatively this large dielectric effect is due to the switching between two nearly equivalent ferroelectric configurations and that the applied magnetic field favours one configuration over the other, thereby reducing the dielectric constant as observed experimentally [99]. Additionally, an increase in the dielectric constant of $YFe_2O_4$ and $Y_{0.5}Lu_{0.5}Fe_2O_4$ at the magnetic transition temperature has been observed and this maximum shifts to higher temperature with the application of an external magnetic field [103].

Strong peaks in the pyroelectric current have been observed at the ferroelectric ordering and ferrimagnetic ordering temperature [64] of $LuFe_2O_4$. The former

is associated with the 3D charge ordering transition while the second is evidence of the magnetoelectric coupling between the polarisation and magnetisation. Furthermore, an anomaly is observed in the magnetisation at the ferroelectric ordering temperature which is attributed to further evidence of the magnetoelectric coupling in this material.

An extensive theoretical study into the spin, charge, and orbital structures in $R\text{Fe}_2\text{O}_4$ has been performed and the stability and degeneracy of different configurations discussed in detail and the influence of external fields investigated. Oxygen deficiency has also been discussed, and cross-correlation effects have been observed in the magnetic and electric field responses [104].

As discussed in Section 1.5.3, a soft mode has been identified in the multiferroic phase of $\text{LuFe}_2\text{O}_4$ [101] and an anomaly is observed at about 180 K that is attributed to magnetoelectron spin-charge coupling.

Magnetic field control of the charge ordering in $\text{LuFe}_2\text{O}_4$ has been demonstrated [105]. A charge order superlattice reflection was monitored and a magnetic field applied at 350 K in the 2D ordered phase, then the sample was cooled to 300 K in the magnetic field. No change of intensity is observed at 350 K, yet comparison of the zero field cooled and magnetic field cooled superlattice intensity indicates a definite change in intensity demonstrating a change in the charge order due to the applied magnetic field.

On the other hand, electric control of magnetisation has been demonstrated by switching of magnetisation states caused by an external electric field [106]. The field-cooled magnetisation has been shown to step down with the application of 22 V at 200 K (and 100 V at 100 K) while the magnetisation of a zero field cooled sample increased during the pulse in an external magnetic field. This effect is attributed to the dielectric breakdown previously reported destabilising the magnetic structure and causing it to change into a more stable state: either demagnetising a magnetised sample in zero field, or magnetisation a demagnetised sample in the presence of an applied magnetic field.

Elastic neutron diffraction has been performed as part of an applied electric field study where it is reported that an applied electric field at low temperature has no effect on the magnetic structure of $\text{LuFe}_2\text{O}_4$ [107]. Analysis of the sample temperature and resistivity indicate that an observed intensity reduction due to the field is caused by joule heating of the sample, and the previously reported

breakdown of the charge order and associated effects are attributed to local heating within the sample.

### 1.5.5   Summary

$LuFe_2O_4$ and the other rare earth substitutions of this material have been studied for 35 years. Prior to the recent exponential increase in research on this topic (particularly between 2007 and today) there were many open questions about the magnetic and charge ordered structures and the magnetoelectric effect had not been investigated in detail. The early work demonstrated that the rare earth influenced the electronic and magnetic order primarily through the effect on the interlayer spacing and compression of electron density due to the changing radius of the rare earth. It was determined that $LuFe_2O_4$ showed the least variation in properties with stoichiometry, with 2D magnetic order below 250 K and 3D charge order below 330 K.

Recent work has demonstrated that these earlier observations of stoichiometry invariance are incorrect, and the dimensionality of the magnetic order as well as correlation length and order parameters have been shown to be dependent upon the oxygen content of the sample. The magnetoelectric studies have demonstrated that a magnetic field may influence the charge order through the paramagnetic contrast of $Fe^{2+}$ and $Fe^{3+}$ as well as effect the polarisability of the sample. An applied electric field has been shown to switch the magnetisation state and it is believed this is mediated by the recently observed insulator-to-metal transition that is caused by an applied electric field.

Despite the recent explosion of research on this material there remain a number of outstanding questions. Anomalous behaviour such as the thermal hysteresis of the field-cooled magnetisation and magnetoelectric stepping of the magnetisation by an applied electric field have been shown to occur in a finite temperature range - despite all measurements so far indicating magnetic and electric order coexist to low temperature. Furthermore, despite multiple resonant x-ray scattering reports in the literature the orbital state of the $Fe^{2+}$ has yet to be fully addressed, and any magnetoelectric coupling in the multiferroic phase has yet to be demonstrated directly by scattering techniques.

## 1.6   Aims and objectives

The aim of this project is to characterise a sample of $LuFe_2O_4$ synthesised at the Paul Scherrer Institut, Switzerland. Two batches were synthesised and from the first a polished disk has been mounted for x-ray backscattered diffraction while two rods suitable for neutron scattering experiments were also cut. The second batch was determined to be too polycrystalline for single crystal experiments.

The objectives of this work are:

(a) to continue a resonant x-ray diffraction study that aims to confirm complete charge disproportionation between $Fe^{2+}$ and $Fe^{3+}$ by fitting an energy dependent structure factor using a non-linear refinement method and to investigate the orbital state of the $Fe^{2+}$ (Chapter 3),

(b) to perform XANES calculations to investigate the structure of the x-ray absorption associated with different charge order and structural schemes and attempt to extract further meaning from the energy dependence collected in the resonant x-ray scattering experiment (Chapter 4),

(c) to perform single crystal neutron diffraction experiments in an applied electric field to characterise the effect of electric field cooling on the magnetic structure (Chapter 6),

(d) to perform single crystal x-ray diffraction on a single piece of the crushed sample in order to investigate the crystal structure and the effect of electric field cooling on the charge ordered structure (Chapter 7),

(e) to crush the polycrystalline sample and perform powder neutron and x-ray diffraction experiments to study the lattice and magnetic structure (Chapter 8).

# Chapter 2

# Methods

Particle scattering is an invaluable tool for the study of the structure, dynamics, and properties of materials. It is possible to scatter a range of particles, such as x-rays, neutrons, or electrons, and the differing nature of these particles allow a range of material properties to be probed.

X-ray scattering results from the interaction of the x-ray with the electron density of the material, whereas neutron scattering results from the interaction of the neutron with the nucleus of atoms or the magnetic spin of electrons in the material. These differences make x-ray scattering well suited to study the structure of materials and properties based upon the variation in the electron density, while the neutron scattering cross section is sensitive to structure, structural dynamics, and magnetic order. Furthermore, x-ray scattering is proportional to the electron density and is therefore limited when it comes to light elements in the presence of heavy elements; however, the neutron scattering length arises from the nuclear interaction which is not proportional to the atomic number and therefore neutron scattering is also important in the study of systems containing light elements.

In this thesis neutron and x-ray scattering experiments have been performed in order to characterise the multiferroic properties of $LuFe_2O_4$. X-ray scattering experiments have been performed in order to study the structural and ferroelectric order as well as its response to an applied electric field. Neutron scattering experiments have been performed to characterise the structural and magnetic dynamics, magnetoelectric response of the magnetic order to an applied electric field, and structural order.

This chapter establishes the theoretical background of the relevant scattering techniques by first establishing the general scattering relations before moving onto elastic diffraction from crystals, followed by the technical aspects of both x-ray and neutron scattering, and finally the theoretical methods applied to the data to obtain structural and materials properties.

## 2.1 Scattering Principles

Any scattering process leads to a change in the propagation direction and/or energy of the incoming particle or wave. For an incoming wavevector $\mathbf{k}_i$ and an outgoing wavevector $\mathbf{k}_f$ this change is summarised by the *scattering vector* $\mathbf{Q}$:

$$\mathbf{Q} = \mathbf{k}_f - \mathbf{k}_i \tag{2.1}$$

In a scattering experiment the cross-section that is measured is a function of $\mathbf{Q}$, the nature of the material, and the nature of the scattering particle or wave. These relationships are best summarised by the correlation functions of a scattering system.

### 2.1.1 The Born Approximation

The Born approximation assumes that the scattering from any particular scatterer varies in magnitude depending upon the nature of the scatterer, but that the waveforms interfere identically. That is to say that the incoming wave is not distorted by the potential of the scatterer. This approximation is valid for bound states which is sufficiently true for non-resonant x-ray scattering and neutron scattering, but in the case of resonant x-ray scattering this approximation may break down as the photon energy corresponds to the absorption edge energy leading to excitation of the scatterer to continuum states which may distort the incoming wavefunction. The resonant scattering work presented in Chapter 3 treats the scattering intensities in a relative fashion and therefore small inconsistencies due to this effect are absorbed by scaling factors used in the data processing.

## 2.1.2 Correlation functions

The following treatment is based upon that of Squires [108].

For a system containing many identical scatterers, it can be shown that the general coherent and incoherent scattering cross-sections may be written as:

$$\left(\frac{d^2\sigma}{d\Omega dE'}\right)_{\text{coh}} = \frac{\sigma_{\text{coh}}}{4\pi}\frac{|\mathbf{k}_f|}{|\mathbf{k}_i|}\frac{1}{2\pi\hbar}\sum_{jj'}\int_{-\infty}^{\infty}\langle\exp(-i\mathbf{Q}\cdot\mathbf{R}_{j'}(0))\exp(i\mathbf{Q}\cdot\mathbf{R}_j(t))\rangle$$
$$\times \exp(-i\omega t)dt \tag{2.2}$$

$$\left(\frac{d^2\sigma}{d\Omega dE'}\right)_{\text{inc}} = \frac{\sigma_{\text{inc}}}{4\pi}\frac{k'}{k}\frac{1}{2\pi\hbar}\sum_{j}\int_{-\infty}^{\infty}\langle\exp\left(-i\boldsymbol{\kappa}\cdot\mathbf{R}_j(0)\right)\exp\left(i\boldsymbol{\kappa}\cdot\mathbf{R}_j(t)\right)\rangle$$
$$\times \exp\left(-i\omega t\right)dt \tag{2.3}$$

where the change of energy of the system due to the scattering event is $\hbar\omega$, $\mathbf{R}_j(t)$ is the position vector of scatterer $j$ at time $t$, $\sigma_{\text{coh}}$ and $\sigma_{\text{inc}}$ are a probe-dependent function of the nature of the scatterer, and $\langle\ldots\rangle$ represents a thermal average.

The scattering cross-sections are functions of thermal averages which may be expressed as *correlation functions*. The correlation functions $I(\mathbf{Q},t)$, $G(\mathbf{r},t)$, $S(\mathbf{Q},\omega)$, $I_s(\mathbf{Q},t)$, $G_s(\mathbf{r},t)$, and $S_i(\mathbf{Q},\omega)$ (outlined below) are used to describe the relationship between the cross-section and the properties of the material under study.

The *intermediate function*, $I(\mathbf{Q},t)$, is defined to replace the thermal average in Equation 2.2, while the *scattering function*, $S(\mathbf{Q},\omega)$, is the Fourier transform of the intermediate function in time. These functions are written as:

$$I(\mathbf{Q},t) = \frac{1}{N}\sum_{jj'}\langle\exp\{-i\mathbf{Q}\cdot\mathbf{R}_{j'}(0)\}\exp\{i\mathbf{Q}\cdot\mathbf{R}_j(t)\}\rangle \tag{2.4}$$

$$S(\mathbf{Q},\omega) = \frac{1}{2\pi\hbar}\int I(\mathbf{Q},t)\exp\left(-i\omega t\right)dt \tag{2.5}$$

Combining Equations 2.2, 2.4, and 2.5 allows the coherent scattering cross-section to be re-written as:

$$\left(\frac{d^2\sigma}{d\Omega dE'}\right)_{\text{coh}} = \frac{\sigma_{\text{coh}}}{4\pi}\frac{|\mathbf{k}_f|}{|\mathbf{k}_i|}N\,S(\mathbf{Q},\omega) \tag{2.6}$$

In a scattering experiment it is $S(\mathbf{Q},\omega)$ that is measured.

In order to use the measured cross-section to interpret physical information about the sample $S(\mathbf{Q}, \omega)$ needs to be described in $\mathbf{r}$-space. The *time-dependent pair-correlation function*, $G(\mathbf{r}, t)$, is related to the time-dependent density of the scattering system and has a Fourier-relationship to $I(\mathbf{Q}, t)$ and $S(\mathbf{Q}, \omega)$.

$$G(\mathbf{r}, t) = \frac{1}{(2\pi)^3} \int I(\mathbf{Q}, t) \exp\left(-\mathbf{Q} \cdot \mathbf{r}\right) d\mathbf{Q} \tag{2.7}$$

$$G(\mathbf{r}, t) = \frac{\hbar}{(2\pi)^3} \int S(\mathbf{Q}, \omega) \exp\left\{-i(\mathbf{Q} \cdot \mathbf{r} - \omega t)\right\} d\mathbf{Q} d\omega \tag{2.8}$$

Equation 2.8 demonstrates that $S(\mathbf{Q}, \omega)$ is the Fourier transform of $G(\mathbf{r}, t)$ in space and time, and therefore the aim of the scattering experiment is to obtain a model for the physical system from $G(\mathbf{r}, t)$.

The incoherent scattering cross-section may be represented by the *self intermediate function*, $I_s(\mathbf{Q}, t)$, *self time-dependent pair correlation function*, $G_s(\mathbf{r}, t)$, and *incoherent scattering function* , $S_i(\mathbf{Q}, \omega)$ in a similar fashion. The self intermediate function is designed to replace the thermal average in Equation 2.3 as shown in Equation 2.9 and thus to allow Equation 2.3 to be rewritten as Equation 2.10 in terms of the incoherent scattering function.

$$I_s\left(\mathbf{Q}, t\right) = \frac{1}{N} \sum_j \left\langle \exp\left\{-i\mathbf{Q} \cdot \mathbf{R}_j(0)\right\} \exp\left\{i\mathbf{Q} \cdot \mathbf{R}_j(t)\right\} \right\rangle \tag{2.9}$$

$$\left(\frac{d^2\sigma}{d\Omega dE'}\right)_{\text{inc}} = \frac{\sigma_{\text{inc}}}{4\pi} \frac{k'}{k} N S_i(\mathbf{Q}, \omega) \tag{2.10}$$

The same relationships exist between $I_s(\mathbf{Q}, t)$, $G_s(\mathbf{r}, t)$, and $S_i(\mathbf{Q}, \omega)$ as have already been presented for the coherent equivalents.

A number of important results are obtained by considering the analytical results and limits of these functions. The *principle of detailed balance* stated as Equation 2.11 describes the relationship between the observed intensities for excitations symmetric about $(\mathbf{Q} = 0, \omega = 0)$. This relationship demonstrates that the probability of the system being in an excited state and transferring energy to the scattering particle is less than that of the system being in the ground state (or a lower excited state) and becoming excited due to the scattering event and the scattering functions (and therefore observed intensities) vary accordingly.

$$S(-\mathbf{Q}, -\omega) = \exp\left(-\hbar\omega\beta\right) S(\mathbf{Q}, \omega) \tag{2.11}$$

Where $\beta = \frac{1}{k_B T}$.

In the $t \to \infty$ limit $\omega = 0$ and the scattering is *elastic* with no change in energy; in this case the principle of detailed balance states that $S(\mathbf{Q}, 0) = S(-\mathbf{Q}, 0)$ which indicates that the elastic coherent cross-section is distributed symmetrically in space. This is known as *Friedel's law* and the pair $\mathbf{Q}$ and $-\mathbf{Q}$ are known as a Friedel pair.

In the elastic limit as $t$ approaches infinity, the scatterer-scatterer correlations become independent of time. In this case the time integral in the scattering function becomes unity when the cross-section is integrated with respect to energy, and the thermal averages in the intermediate function become independent of time. Based upon these results, it can be derived that the coherent elastic cross-section is a direct function of the intermediate function as shown in Equation 2.12.

$$\left(\frac{d\sigma}{d\Omega}\right)_{\text{coh. el.}} = \frac{\sigma_{\text{coh}}}{4\pi} N I(\mathbf{Q}, \infty) \tag{2.12}$$

$G(\mathbf{r}, \infty)$ becomes the direct spatial Fourier transform of the observed coherent elastic cross-section and is known as the *Patterson function* as described by Equation 2.13. As shown, the Patterson function is a function of the thermally averaged scatterer density in real-space and plays an important role in solving structures from diffraction data. This is addressed further in Section 2.5.

$$G(\mathbf{r}, \infty) = \frac{1}{N} \int \langle \rho(\mathbf{r}') \rangle \langle \rho(\mathbf{r}' + \mathbf{r}) \rangle d\mathbf{r}' \tag{2.13}$$

Both the coherent and incoherent cross-sections may be simplified in the elastic limit as shown in Equations 2.14 and 2.15.

$$\left(\frac{d\sigma}{d\Omega}\right)_{\text{coh. el.}} = \frac{\sigma_{\text{coh}}}{4\pi} N I(\mathbf{Q}, \infty)$$

$$= \frac{\sigma_{\text{coh}}}{4\pi} \left| \int \langle \rho(\mathbf{r}) \rangle \exp(i\mathbf{Q} \cdot \mathbf{r}) d\mathbf{r} \right|^2 \tag{2.14}$$

$$\left(\frac{d\sigma}{d\Omega}\right)_{\text{inc. el.}} = \frac{\sigma_{\text{inc}}}{4\pi} N I_s(\mathbf{Q}, \infty)$$

$$= \frac{\sigma_{\text{inc}}}{4\pi} \sum_j \langle \exp(-i\mathbf{Q} \cdot \mathbf{R}_j) \rangle \langle \exp(i\mathbf{Q} \cdot \mathbf{R}_j) \rangle \tag{2.15}$$

$$= \frac{\sigma_{\text{inc}}}{4\pi} \int G_s(\mathbf{r}, \infty) \exp(i\mathbf{Q} \cdot \mathbf{r}) d\mathbf{r} \tag{2.16}$$

The *Debye-Waller factor* is a term that accounts for the reduction in the observed intensity due to the thermal motion of atoms about their equilibrium positions. It can be shown that the Debye-Waller factor is equivalent to $I_s(\mathbf{Q}, \infty)$ and written as the sum shown in Equation 2.15, and from Equation 2.16 it may be noted that the Debye-Waller factor is the Fourier transform of $G_s(\mathbf{r}, \infty)$.

These results are based upon a scattering system with a mono-atomic basis; but, they may be extended to the general case of a system made up of differing scattering lengths. In such a case, every scatterer's contribution to $S(\mathbf{Q}, \omega)$ is weighted by the scattering length, modulating $G(\mathbf{r}, t)$ as a result.

The special case where the scatterers are arranged on a regular lattice for a generalised atomic basis in the elastic limit is addressed in the next section. Equation 2.14 is re-expressed in terms of what is known as the *structure factor* for crystalline systems.

### 2.1.3   Diffraction and the Reciprocal Lattice

A crystalline material possesses a well-ordered, uniform arrangement of atoms for which there exists a subset of atoms that when repeatedly translated the entire crystal lattice may be constructed; this repeating unit is called the *unit cell*. Any arbitrarily large group of atoms may be chosen that possesses the translational symmetry of the unit cell; however, due to the stacking arrangement of the atoms/molecules and the associated occupancy of lattice sites there will be a minimum set of atoms that can be used to construct the crystal structure and the unit cell is selected to be this cell of minimum volume.

Depending upon the arrangement of atoms, there are symmetry operators that relate atoms within the unit cell to one another. There are 14 Bravais lattices, which represent the fundamentally different symmetries possible for the unit cell, and 180 crystallographic point groups that describe symmetry operations about a point. Combining the 180 point groups with the 14 Bravais lattices yields 230 space groups, therefore the unit cell may be described by a smaller basis set of atoms combined with the symmetry operations of one of the 230 space groups.

Considering only elastic scattering, each atom in the lattice re-emits the scattered particle coherently and the overall periodic system may be addressed with

Fourier analysis as outlined in [109] and the Fourier relations presented in Section 2.1.2. As there is a well defined periodicity in real space ($G(\mathbf{r}, \infty)$) the Fourier transform ($S(\mathbf{Q}, 0)$) will be made up of discrete points corresponding to each unique lattice spacing. This Fourier space is known as *reciprocal space* and the lattice of points as the *reciprocal lattice*. The *reciprocal unit cell* is the volume of which the edges are the reciprocal translation vectors, a linear combination of which may produce any reciprocal lattice point. As $S(\mathbf{Q}, 0)$ relates directly to the measured cross-section portions of reciprocal space are mapped by elastic diffraction experiments.

If the real-space crystal lattice is described by the three translation vectors $\mathbf{a}_1, \mathbf{a}_2$, and $\mathbf{a}_3$ then the translation vectors of the reciprocal unit cell are described by Equations 2.17, 2.18, and 2.19.

$$\mathbf{b}_1 = 2\pi \frac{\mathbf{a}_2 \times \mathbf{a}_3}{\mathbf{a}_1 \cdot \mathbf{a}_2 \times \mathbf{a}_3} \tag{2.17}$$

$$\mathbf{b}_2 = 2\pi \frac{\mathbf{a}_3 \times \mathbf{a}_1}{\mathbf{a}_1 \cdot \mathbf{a}_2 \times \mathbf{a}_3} \tag{2.18}$$

$$\mathbf{b}_3 = 2\pi \frac{\mathbf{a}_1 \times \mathbf{a}_2}{\mathbf{a}_1 \cdot \mathbf{a}_2 \times \mathbf{a}_3} \tag{2.19}$$

Any reciprocal space point, $\mathbf{G}$, may be obtained by a linear combination of these vectors. The scattering vector, $\mathbf{Q}$, corresponds to a coordinate in reciprocal space as described in Equation 2.20.

$$\mathbf{Q} = h\mathbf{b}_1 + k\mathbf{b}_2 + l\mathbf{b}_3 \tag{2.20}$$

For any integer values of $h$, $k$, and $l$ the scattering vector is equivalent to a reciprocal lattice point, and the crystal orientation relative to the beam meets Bragg's Law for the corresponding interplanar spacing of the crystal. Accordingly, diffracted intensity may be measured.

As shown in Equation 2.14, the elastic cross-section is equal to the integrated contribution of a continuous distribution of scatterers. Extending this result to multiple scatterers simply leads to the scattering length being moved into the integral, and given $\sigma_{\mathrm{coh}} = 4\pi(f_{\mathrm{coh}})^2$ where $f$ is the scattering length (which is the ratio of the outgoing wave to the incoming wave in the scattering process) of the

scatterer. This may be re-expressed as Equation 2.21.

$$\left(\frac{d\sigma}{d\Omega}\right)_{\text{coh. el.}} = \left| \int f(\mathbf{r}) \langle \rho(\mathbf{r}) \rangle \exp(-i\mathbf{Q} \cdot \mathbf{r}) d\mathbf{r} \right|^2 \qquad (2.21)$$

Given a discrete distribution occupying a lattice the continuous density present in Equation 2.21 may be expressed as a series of delta-functions allowing the integral to be re-written as a discrete sum as presented in Equation 2.22.

$$\left(\frac{d\sigma}{d\Omega}\right)_{\text{coh. el.}} = N \left| \sum_j f_j \exp(-i\mathbf{Q} \cdot \mathbf{R}_j) \right|^2 \qquad (2.22)$$

Where $N$ is the number of unit cells in the sample volume and $f_j$ is the scattering length of the $j^{\text{th}}$ scatterer.

As the expression within the sum is not necessarily real this may be further simplified as shown in Equation 2.23.

$$\left(\frac{d\sigma}{d\Omega}\right)_{\text{coh. el.}} = NF^*(\mathbf{Q})F(\mathbf{Q}) \qquad (2.23)$$

Where $F(\mathbf{Q}) = \sum_j f_j \exp(-i\mathbf{Q} \cdot \mathbf{R}_j)$.

$F(\mathbf{Q})$ is known as the *structure factor* and is used to calculate the diffracted intensity for a given $\mathbf{Q}$ as the intensity is proportional to $F^*F$, where $F^*(\mathbf{Q})$ is the complex conjugate of $F(\mathbf{Q})$. Reflections forbidden by symmetry have a structure factor of zero.

This result demonstrates that by measuring a series of $S(\mathbf{Q}, 0)$ the structure of a crystalline material may be solved by inverse solution methods applied to the structure factor.

## 2.2   X-ray Scattering

The interaction of x-rays with matter is predominantly determined through the interaction of the electromagnetic radiation with the electrons of the material. Classically, the x-ray electron scattering process is described by the acceleration of the electron due to the electric field of the incoming radiation. The electron

oscillates in the presence of the alternating electric field, and it emits spherical wavefronts of a dipole amplitude distribution that are 180° out of phase with the incoming radiation. This is known as Thomson scattering and is characterised by the Thomson scattering length or classical electron radius $r_0 = \frac{e^2}{4\pi\epsilon_0 mc^2}$.

The observed intensity at a point located away from the scattering event, normalised with respect to the cross-sectional area of the incoming beam and the solid angle of the detector, is:

$$\frac{d\sigma}{d\Omega} = \left(r_0\hat{\boldsymbol{\epsilon}} \cdot \hat{\boldsymbol{k}_f}\right)^2 \tag{2.24}$$

where $\hat{\boldsymbol{\epsilon}}$ and $\mathbf{k_f}$ are unit vectors in the direction of the x-ray polarisation and scattered beam respectively.

Scattering from a multi-electron system requires the phase difference between the different volume elements be included in the calculated intensity. The phase difference between the scattered waves from a volume element at the origin and another described by the position vector $\mathbf{r}$ is $\mathbf{Q} \cdot \mathbf{r}$. This phase difference is accounted for by the *atomic form factor* which is provided as Equation 2.25.

For an elastic, i.e. recoil free, process the total scattering length of the atom is $-r_0 f^0$, where:

$$f^0\left(\mathbf{Q}\right) = \int \rho\left(\mathbf{r}\right)\exp\left(i\mathbf{Q} \cdot \mathbf{r}\right)d\mathbf{r} \tag{2.25}$$

This term is known as the Thomson scattering factor. In the forward direction ($\mathbf{Q} = 0$) the atomic form factor of the element is the atomic number, $Z$.

Atomic electrons are bound, and as such will not respond to the electric field of the x-ray in the same way as a free electron. In fact, this system may be treated as a damped harmonic oscillator, and thus the Thomson scattering factor must be corrected for both this reduction in amplitude and a phase-lag between the oscillatory motion and the driving field. At x-ray energies corresponding to the binding energy of the electrons additional processes due to photon absorption occur, and these corrections to the scattering factor exhibit resonant behaviour.

Including these corrections the atomic scattering length, also known as the atomic scattering factor, is written as:

$$f\left(\mathbf{Q}, E\right) = f^0\left(\mathbf{Q}\right) + f'\left(E\right) + if''\left(E\right) \tag{2.26}$$

where $E = \hbar\omega$ is the x-ray energy and the complex number $f'(E) + if''(E)$ is known as the anomalous scattering factor.

Solving the equation of motion of the electron in the presence of the driving field of the x-ray as a single oscillator with resonant frequency $\omega_s$, damping constant $\Gamma$ and driving frequency $\omega$ yields expressions for the real and imaginary parts of the anomalous scattering factor.

$$f'(\omega) = \frac{\omega_s^2 (\omega^2 - \omega_s^2)}{(\omega^2 - \omega_s^2)^2 + (\omega\Gamma)^2} \tag{2.27}$$

$$f''(\omega) = \frac{\omega_s^2 \omega\Gamma}{(\omega^2 - \omega_s^2)^2 + (\omega\Gamma)^2} \tag{2.28}$$

These functions are related through the Kramers-Kronig (KK) dispersion relationship:

$$f'(\omega) = \frac{2}{\pi} P \int_0^\infty \frac{\omega' f''(\omega')}{\omega'^2 - \omega^2} d\omega' \tag{2.29}$$

$$f''(\omega) = -\frac{2\omega}{\pi} P \int_0^\infty \frac{f'(\omega')}{\omega'^2 - \omega^2} d\omega' \tag{2.30}$$

where P is the Cauchy principle value of the integral shown.

The resonance behaviour of equations 2.27 and 2.28 is presented as Figure 2.1.

The frequency dependence shown in Figure 2.1 demonstrates the shape of these functions, but in order to adequately describe the anomalous scattering the nature of this resonance must be better described.

The electrons in atoms are bound in discrete energy levels described by their principle quantum number (n = 1,2,3 ... ) or the corresponding alphabetic label (K, L, M ... ). When the incident photon has energy equal to or greater than the binding energy of that shell an electron in that shell may be excited leaving a hole in the core state. This is the process of photoelectric absorption, and there is a significant drop in x-ray transmission at (and above) these energies leading to steps in the absorption profile which are referred to as absorption edges. These excitations have a finite lifetime as the resulting hole may be filled by an electron transitioning from a higher energy shell resulting in the emission of an x-ray, this process is known as fluorescence. Furthermore, the electron may be excited into not only a single final state, but rather a continuum of states and a weighted distribution of oscillators is required to describe the edge.
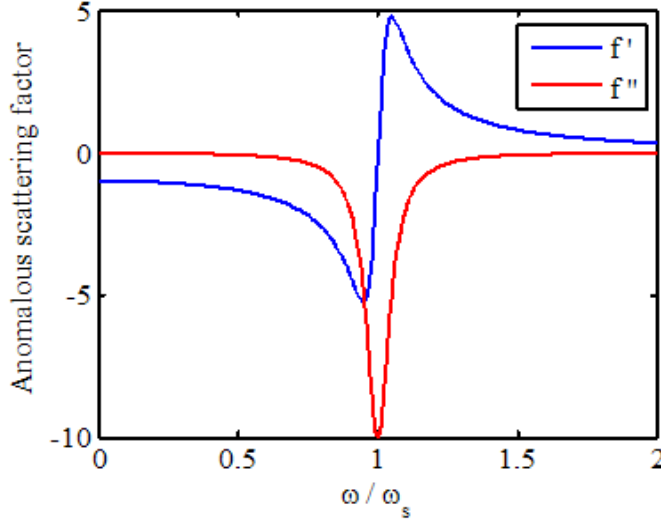
Figure 2.1: The frequency dependence of the real ($f'$) and imaginary ($f''$) parts of the anomalous scattering factor. The damping constant is $0.1\omega_s$.

Photoelectric absorption is the mode through which power is dissipated into the system, and as such the anomalous scattering factor relates to the absorption cross-section. The optical theorem expresses this relationship and given the speed of light, $c$, and the atomic absorption cross section, $\sigma_a$, then:

$$f''(\omega) = -\frac{\omega}{4\pi r_0 c}\sigma_a(\omega) \tag{2.31}$$

Considering this relation to the absorption process and the distribution of oscillators, obtaining reasonable values for the anomalous scattering factors of any element requires a proper *ab initio* method which is in itself non-trivial; however, a preferred method is that of Cromer and Liberman [110, 111]. Using this method, values of $f'$ and $f''$ have been calculated for every element and tabulated in the Cromer-Liberman (CL) tables that are widely available in references such as the International Tables for Crystallography [112] and programs such as Hephaestus from the IFEFFIT package [113, 114].

The CL values (obtained from Hephaestus [113]) of the real and imaginary parts of the anomalous scattering factor for iron are shown in Figure 2.2 and for the case of an isolated atom these values are accurate. Practically, the photoelectric absorption process is influenced by the chemical environment of the absorbing atom, leading to variations in $f'(\omega)$ and $f''(\omega)$ as per the optical theorem (equation 2.31). The photoelectron (PE) is backscattered from the surrounding atoms and interferes with the outgoing PE wave perturbing the final state. The interference is a function of the wavelength of the PE, the distance between the absorbing
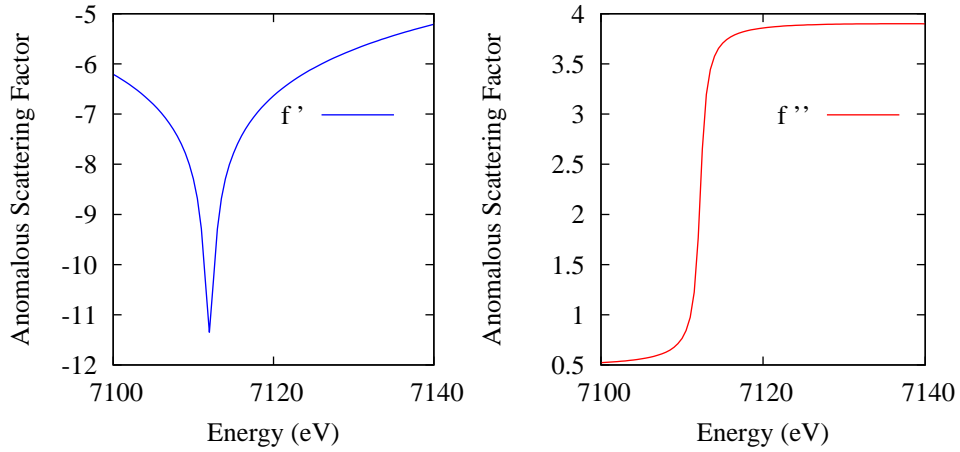
Figure 2.2: The Cromer-Liberman values of the real ($f'$) and imaginary ($f''$) part of the anomalous scattering factor. The K-edge of Fe is at 7112 eV.

atom and the backscattering neighbour, and the scattering power of the neighbouring atom. The interference will vary with x-ray energy, as the kinetic energy of the PE is the difference between the energy of the incoming photon and the binding energy of the electron. Thus, the absorption cross-section is expected to oscillate about the theoretical value of an isolated atom, and through the optical theorem and the KK transformation the anomalous scattering factor will oscillate about the CL values. This is demonstrated in Figure 2.3 where the theoretically calculated $f'$ and $f''$ for magnetite are shown.

### 2.2.1 The Kramers-Kronig relation

The KK transformations described by equations 2.29 and 2.30 are what may be referred to as *non-local* integrals, in that the value at each frequency, $\omega$, of one function is equal to an integral of the other function with respect to frequency, $\omega'$, for all possible values (from zero to infinity). As demonstrated in Figure 2.2 both $f'(\omega)$ and $f''(\omega)$ are non-zero over this range, and thus in order to perform these integrals values of these functions must be obtained for all frequencies. In an experiment this is not possible, but by making use of the oscillatory nature of these functions as shown in Figure 2.3(b) a solution to this problem may be obtained as demonstrated below.

Consider the KK transformation of the imaginary part of the anomalous scat-
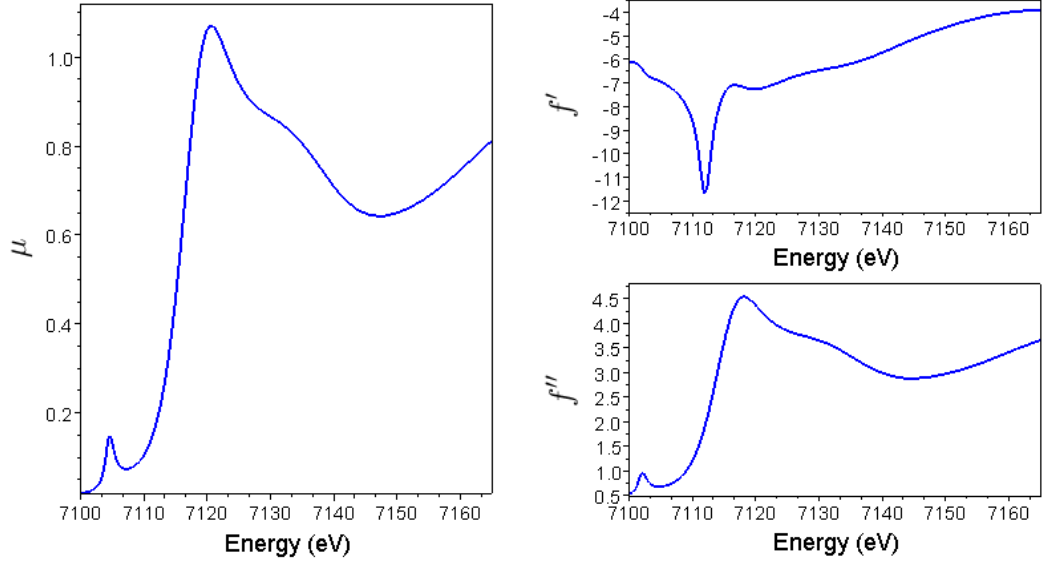
Figure 2.3: (a) The absorption at the Fe-edge calculated for magnetite using FDMNES, and (b) the real ($f'$) and imaginary ($f''$) parts of the anomalous scattering factor determined from (a).

tering factor from equation 2.29:

$$f'(\omega) = \frac{2}{\pi} P \int_0^\infty \frac{\omega' f''(\omega')}{\omega'^2 - \omega^2} d\omega'$$

Next, apply the relationship demonstrated in Figure 2.3(b) and simplify:

$$f'(\omega) = \frac{2}{\pi} P \int_0^\infty \frac{\omega' [f''(\omega') - f''_{CL}(\omega') + f''_{CL}(\omega')]}{\omega'^2 - \omega 2} d\omega'$$

$$f'(\omega) = \frac{2}{\pi} P \int_0^\infty \frac{\omega' [f''(\omega') - f''_{CL}(\omega')]}{\omega'^2 - \omega 2} d\omega' + \frac{2}{\pi} P \int_0^\infty \frac{\omega' f''_{CL}(\omega')}{\omega'^2 - \omega^2} d\omega'$$

Finally, applying equation 2.29, the second term may be rewritten:

$$f'(\omega) = \frac{2}{\pi} P \int_0^\infty \frac{\omega' [f''(\omega') - f''_{CL}(\omega')]}{\omega'^2 - \omega^2} d\omega' + f'_{CL}(\omega) \tag{2.32}$$

The values of the second term can be obtained from tabulated data, and the first term is now the KK-transformation of the difference between the CL-value and the true value which as shown in Figure 2.3(b) is the amplitude of the oscillations. These oscillations decay away from the absorption edge, so the difference becomes a zero-valued function outside a finite frequency range. This method is the *difference Kramers-Kronig* transformation. Thus in an experiment, measurements need only be taken from an energy below the edge to an energy above the edge such that the amplitude of the oscillations has sufficiently decayed.

There are many numeric methods to perform the KK transformation, and a detailed discussion of the differences of optimisations of each method is available [115]. Programs that implement the transformation are also available, for example two that were investigated are: DIFFKK [116] implements the difference Kramers-Kronig method, which offers little control over how the CL values are fitted to the experimental data; and the MATLAB code of Valerio Lucarini [117] that purely evaluates the KK transformation, allowing for the implementation of the further steps required by the difference KK transformation to be coded by the user.

### 2.2.2 The anomalous structure factor

As discussed in Section 2.1 the structure factor of a crystalline material allows the theoretical intensity of diffraction peaks to be calculated and extinctions due to symmetry to be predicted. Previously (Equation 2.22) this has been expressed for a generic scattering length, and this expression may be re-written to include the anomalous scattering factors:

$$F\left(\mathbf{Q}\right) = \sum_j \left(f_0\left(\mathbf{Q}\right) + f'\left(E\right) + if''\left(E\right)\right) \exp\left(i\mathbf{Q}\cdot\mathbf{R}\right)$$

$$F\left(\mathbf{Q}\right) = \sum_j \left(f_0\left(\mathbf{Q}\right) + f'\left(E\right) + if''\left(E\right)\right) \exp\left(2\pi i\left(hx + ky + lz\right)\right) \quad (2.33)$$

Where the dot product is expanded in Equation 2.33 assuming orthogonal axes.

For the $R\bar{3}m$ symmetry of $LuFe_2O_4$ the complex terms of the allowed reflections cancel when summed across the lattice sites leading to a real-valued structure factor.

### 2.2.3 Anisotropic anomalous scattering

The atomic scattering factor (equation 2.26) written above is isotropic; it may be considered a rank 1 tensor. Isotropic scattering will occur in materials with spherically symmetric electron densities, such as metallic systems, where the electrons are delocalised in the conduction band; or strongly ionic systems, where

the electrons are localised at the atomic site. Anisotropic electron densities may be present in materials where strong covalent bonding is present, leading to bond centred electron density; where a local or long range electric field leads to the distortion of the electron cloud; or where effects such as magnetostriction, electrostriction or piezoelectricity cause anisotropic displacements of the crystal structure and differential covalency of the nearest neighbour bonds. The isotropic approximation has been shown experimentally to be valid for most cases at energies far away from absorption edges, where the majority of the x-ray electron interaction volume is site centred due to the weak interaction of excited photo-electrons with lattice; however, at energies around absorption edges the x-ray scattering intensity depends strongly on the interaction of the excited photoelectron and the local electronic density and the approximation is invalid. Under these conditions lattice sites occupied by atoms of the same element will have different atomic scattering factors that are a function of the local point symmetry of the site and the orientation of the local electron density with respect to the incoming beam. This effect causes usually forbidden reflections to be observable, and both a polarisation and azimuthal angle (a rotation about $\mathbf{Q}$) dependence may be observed in the intensity of Bragg peaks where these atoms contribute significantly. The relevance of this effect must be considered for all lattices with symmetry lower than cubic.

The x-ray photons also interact with the magnetic moments present in magnetic materials leading to scattering from the sites occupied by magnetic atoms. This scattering is weak at energies away from absorption edges, but when measured about absorption edges corresponding to transitions into the orbitals associated with the magnetic moment (the L edge corresponding to 3d orbitals in the case of transition metals) a significant increase in the magnetic scattering is observed. The magnetic moment is anisotropic and magnetic scattering will have a distinct polarisation and azimuthal dependence.

Orbital order (OO) leads to the site-centred regular arrangement of anisotropic electron density, and therefore Bragg peaks arising from OO will also demonstrate a characteristic polarisation and azimuthal dependence.

## 2.2.4  Resonant X-ray Scattering

Resonant x-ray scattering (RXS) is an experimental technique where the x-ray scattering intensity for a fixed value of $\mathbf{Q}$ is measured as a function of energy through an absorption edge of an element under study. This method provides access to the anomalous scattering functions discussed previously, as well as electronic transitions that occur around the absorption edge. This technique provides both $\mathbf{Q}$ and element selectivity allowing specific sublattices of an ordered structure to be investigated. Selection of the L- or M-edges also provides greater sensitivity to the orbital and magnetic order of a sample, and by measuring with different x-ray polarisations and azimuthal angles the electronic ordering of the sublattice can be fully characterised.

## 2.2.5  Measuring the polarisation and azimuthal dependence

The polarisation of the x-ray beam is described as $\pi$ polarised when the polarisation vector lies in the plane of the synchrotron ring, and $\sigma$ polarised when the polarisation vector is perpendicular to the plane of the synchrotron ring. The Poincaré vector provides a good summary of the incident polarisation as it is +1 for $\sigma$ and -1 for $\pi$ polarised light. Due to the anisotropic nature of the electron density associated with orbital order and the anisotropic magnetic spin, a dependence on the polarisation of the incoming beam is expected where magnetic and/or orbital order exists.

Rotation about the scattering vector, $\mathbf{Q}$, does not change the scattering profile, and no dependence on this azimuthal angle is expected in a spherically symmetric case. The anisotropy introduced by orbital or magnetic order may lead to an azimuthal dependence and therefore measuring the scattering intensity as a function of azimuthal angle will reveal orbital ordering, and allow the symmetry of the order to be characterised.

## 2.3   X-ray Absorption Spectroscopy

X-ray absorption spectroscopy is the study of the energy dependence of the x-ray absorption cross-section. The cross-section is a result of the photoelectric absorption process, introduced in Section 2.2, during which inner-shell electrons (K, L, M . . . ) are excited into unbound states. The optical theorem states there is a direct relationship between the observed absorption cross-section and the imaginary part of the anomalous scattering factor ($f''$). In the case of a single isolated atom the photoelectron is ionised and a smooth absorption cross-section with steps corresponding to the progressive ionisation energies is expected as shown in Figure 2.2 where the anomalous scattering factors for such a system are plotted. Alternatively in a multi-atomic system the photoelectron travels outward from the excited atom, but is backscattered by the other atoms leading to interference of the outgoing and incoming wavefunctions. As the x-ray energy is varied the wavelength of the outgoing and incoming waves changes accordingly resulting in a different interference effect and therefore an increased or decreased absorption cross-section as the final state is perturbed. The result is smooth oscillations of the absorption cross-section as shown in the anomalous scattering factors presented in Figure 2.3.

The post-edge absorption cross-section is divided into two regions: the x-ray absorption near edge structure (XANES) and the extended x-ray absorption fine structure (EXAFS). Generally, the XANES region is considered to be the structure up to 50 eV above the edge and EXAFS beyond this. The physics in these regions differs as in the EXAFS region the observed cross-section is a function of the interference of the outgoing wave and backscattered wavefronts from neighbouring atoms, whilst in the XANES region multiple scattering contributes significantly where the photoelectric scatters more than once leading to more complicated interference at the position of the absorbing atom.

X-ray absorption spectra are most commonly measured in transmission where the sample is put in the direct beam and the transmission measured, from which the absorption is readily calculated. Practically these spectra are used to fingerprint unknown materials with known standards, to determine the anomalous scattering factors via the optical theorem and Kramers-Kronig transformations, to understand the local chemical environment by the direct Fourier transform of the oscillations, or as the reference for calculations to understand the chemical and electronic structure of the material.

The diffraction anomalous fine structure (DAFS) technique combines elastic diffraction the electronic information of x-ray absorption spectroscopy by measuring the Bragg intensity as a function of x-ray energy. Through an understanding of the elastic scattering cross-section both the real and imaginary part of the anomalous scattering factor may be extracted from the data. In this way DAFS is practically similar to RXS (introduced in Section 2.2); however, RXS is generalised to include contributions to the Bragg intensity that originate from sources other than the anomalous scattering factor such as transitions into bound states and orbital and magnetic order.

### 2.3.1   Modelling the isolated atom

The first stage of modelling the x-ray absorption cross-section of multi-atom systems is to investigate the calculation of the cross-section for isolated atoms.

The detailed procedure is beyond the scope of this work and the reader is directed to texts such as Als-Nielsen and McMorrow [118] where the calculations are introduced in detail and further reading is indicated. The main results are presented and discussed briefly here.

The starting point, which comes directly from first order perturbation theory, is the general equation for the atomic absorption cross-section in terms of the ejection of a photoelectron in angular coordinates that relate the wavevector of the photoelectric to the polarisation and wavevector of the incident photon. The Hamiltonian is expressed in terms of the vector potential of the incident photon field and the bound wavefunction is taken to be that of the $1s$ state of the hydrogen atom, and it is shown that neglecting the coulomb interaction between the photoelectron and the resulting ion does not lead to a sufficiently accurate result.

A correction factor, $f(\zeta)$ was introduced and the resulting expression for the atomic absorption cross-section ($\sigma_A$) of the K-edge is provided as Equation 2.34, where $\omega$ is the angular frequency, $\omega_K$ is the angular frequency of the K-edge, $\hbar\omega_c = 2mc^2$, $\hbar\omega_A = Z\hbar c/a_0$ (where $a_0$ is the Bohr radius), $\lambda$ is the wavelength,

and $r_0$ is the Thompson scattering length introduced in Section 2.2.

$$\sigma_a(\omega) = 32\lambda r_0 \left(\frac{4}{3}\right) \left[\frac{\omega_A^2}{\omega\omega_c}\right]^{\frac{5}{2}} f(\zeta) \tag{2.34}$$

$$f(\zeta) = 2\pi\sqrt{\frac{\omega_K}{\omega}} \left(\frac{\exp\left(-4\zeta\operatorname{arccot}\zeta\right)}{1 - \exp\left(-2\pi\zeta\right)}\right) \tag{2.35}$$

$$\zeta = \sqrt{\frac{\omega_K}{\omega - \omega_K}} \tag{2.36}$$

Equation 2.34 is simplified for the two limits $\omega \gg \omega_K$ and $\omega \to \omega_K$. In the first case the correction becomes unity and the free-electron approximation becomes valid due to the high energy of the resulting photoelectron. In the second case, approaching the edge from the positive side the correction becomes a constant predicting a discrete step in the absorption cross-section at $\omega_K$.

Simplifying this result further by assuming a hydrogen-like atom then $\hbar\omega_K = Z^2 e^2/(4\pi\epsilon_0 2a_0)$ (where $\epsilon_0$ is the permittivity of free space) and the ratio $\omega_A^2/(\omega_K\omega_c)$ becomes independent of $Z$. Accordingly the step at the absorption edge may be written as shown in Equation 2.37 and the absorption cross-section as shown in Equation 2.38.

$$\sigma_a(\omega_k) \approx 32\lambda_k r_0 \left(\frac{4}{3}\right) \left(\frac{2\pi}{e^4}\right) \tag{2.37}$$

$$\sigma_a(\omega) \approx 32\lambda r_0 \left(\frac{4}{3}\right) \left[\frac{\omega_K}{\omega}\right]^{\frac{5}{2}} f(\zeta) \tag{2.38}$$

Where $\lambda_K$ is the wavelength corresponding to the angular frequency $\omega_K$.

These equations are based upon hydrogen-like atoms therefore they are expected to become less accurate as $Z$ increases. This model has been shown to be most accurate when $\omega_K$ is determined from experimental results with decreasing accuracy at high atomic number for an inert gas series.

In practice, modern self-consistent *ab initio* methods are used to calculate the isolated atom cross-section following the same principles as the calculation of the Cromer-Liberman values of the anomalous scattering factors introduced in Section 2.2.

## 2.3.2 Modelling EXAFS

The extended x-ray absorption fine structure (EXAFS) region is the high energy portion of the x-ray absorption spectrum where the photoelectron kinetic energy is greater than 50 eV. In this region the interaction between the photoelectron and the ion has little impact due to the high kinetic energy, and the oscillations become a function of the interference of the incoming and outgoing waves. The oscillations are defined as shown in Equation 2.39 therefore it is the function $\chi(q(E))$ that is under investigation.

$$\chi(q(E)) = \frac{\mu_\chi(E) - \mu_0(E)}{\mu_0(E)} \tag{2.39}$$

Where $\mu_0$ is the absorption coefficient of the isolated atom and $\mu_\chi$ is the absorption coefficient of the condensed matter system.

The initial state of the problem is similar to that of the isolated atom except that the neighbouring atoms perturb the final state. The initial state wavefunction for the excitation of the photoelectron is localised to the atom and as such is approximated by a delta function, and the outgoing and incoming waves are represented by spherical wavefronts. The interference at the origin between backscattered wave $q_j$ from atom $j$ will be a function of the path difference between the two functions which is a function of the wavelength and interatomic distance. A phase shift must be introduced to account for both the phase shift due to the interaction of the negative photoelectron and the positive ions of the lattice and due to the absorbing atom. The sum of these effects is denoted $\delta_j(q)$ and is either modelled or fitted from experimental data. Furthermore the hole left due to the excitation of the photoelectric has a finite lifetime and therefore a mean free path of the photoelectron, $\Lambda$, is introduced.

The result for the amplitude of the XAFS oscillations is shown as Equation 2.40, but the derivation is beyond the scope of this work. The reader is directed to texts on this topic such as Koningsberger and Prins [119] or Als-Neilsen and McMorrow [118] for more information.

$$q\chi(q) \propto \sum_j N_j \frac{t_j(q)sin(2qR_j + \delta_j(q))}{R_j^2} \exp(-2(q\sigma_j)^2) \exp(-2R_j/\Lambda) \tag{2.40}$$

### 2.3.3 Modelling XANES

The x-ray absorption near edge structure (XANES) is the complex oscillating structure that occurs from the absorption edge up to about 50 eV above the edge. In this region the interaction between the photoelectron and the excited ion plays an important role due to the low kinetic energy of the photoelectron, and similarly multiple scattering effects may significantly impact the observed absorption cross-section.

While in the EXAFS region the photoelectron interaction was so weak the result was the interference of wavefronts, in the XANES region the photoelectron is excited into continuum of states including those just above the Fermi level that relate directly to the bonding and electronic configuration of the material. The photoelectron may directly probe unoccupied bonding states just above the Fermi level, but the multiple scattering process also conveys information on bond angles and electronic anisotropy. Therefore the most interesting information is summarised in the XANES oscillations, but this makes them significantly more difficult to model.

Practically this means solving the Schrödinger equation on a grid within a particular radius of the absorbing atom for energies ranging from the strongly interacting photoelectrons produced near the edge to the weaker interactions of those photoelectrons just prior to the EXAFS region. Furthermore, the potential varies rapidly about atom cores while it is more constant in the interstitial zone between atoms.

Due to the highly specific nature of the information in the XANES region there exist no general representations such as Equation 2.40 for $\chi(q(E))$ and even the simplified calculations presented in texts (for example Koningsberger and Prins [119]) are beyond the scope of this work.

An important approximation which is dealt with differently in the two programs utilised in this work is the *muffin tin approximation*. The potential varies rapidly about the atom cores, but the gradient is much smaller in the interstitial regions between sites. The muffin-tin approximation defines a spherical region about each atomic site within which the potential is calculated for the atom, while outside this region the potential is fixed to a constant value.

### 2.3.4 FDMNES and FEFF

FDMNES [120] and FEFF8 [121] are the two XANES calculation programs that were employed in this work. Both codes can perform the calculation using the muffin-tin approximation with a number of different formalisms for the potentials available to the user. A self consistent calculation of the electronic configuration of a small sub-cluster is implemented in both programs and the overall calculation is performed based upon contributions from atomic sites within a radius defined by the user.

FDMNES provides the capability to input molecules or structures that take advantage of symmetry. In this way the pattern may be calculated for different inequivalent sites of a lattice. Furthermore a starting electron configuration may be input prior to the self consistent calculation.

The muffin-tin approximation has been shown to produce results in good agreement with those measured experimentally; however, FDMNES goes beyond this approximation with the implementation of the finite difference method [120]. A discretised version of the Schrödinger wave equation is solved on a grid where the finite difference method is applied. The potential at the interface between regions is required to be equal and the potential at each point is determined in a self consistent fashion from the potential of neighbouring points. The finite difference method has been shown to agree well with experimental results particularly for more complicated structures where the muffin-tin potential does not replicate the experimental pattern.

## 2.4 Neutron Scattering

Neutrons are an excellent probe for condensed matter studies as they carry no charge and therefore penetrate deep, and are often transmitted through the sample. With the same mass as a hydrogen nucleus, neutrons have a large interaction cross-section with the nucleus of atoms, but unlike the Thompson scattering of x-rays the scattering length of the neutron is not directly proportional to Z and in fact may be negative. The neutron scattering length, $b$, depends upon the isotope of the nucleus and combined spin of the nucleus-neutron system. Values of $b$ for select elements are provided in in Table 2.1.

Table 2.1: Neutron scattering length, $b$, for selected elements. Data reproduced from Squires [108].

| Nuclide | Combined spin | b (fm) | Nuclide | Combined spin | b (fm) |
|---------|---------------|--------|---------|---------------|--------|
| $^1$H | 1 | 10.85 | $^{23}$Na | 2 | 6.3 |
| | 0 | -47.50 | | 1 | -0.9 |
| $^2$H | $\frac{3}{2}$ | 9.53 | $^{59}$Co | 4 | -2.78 |
| | $\frac{1}{2}$ | 0.98 | | 3 | 9.91 |

As demonstrated in Section 2.1.2 the observed scattering cross-section is directly related to $S(\mathbf{Q}, \omega)$ which is the weighted sum of the time-dependent spatial correlations of the atoms in the material. In the case of neutron scattering $b$ may be positive or negative, and the weighting due to the differing scattering lengths will lead to contrast effects between lattice sites due to the varying sign of $b$.

In a sample not all atoms of the same element will have the same value of $b$ due to different nuclear spin states and the abundance of different isotopes. It can be shown that for a system containing a large number of scattering sites the observed scattering may be expressed as the average scattering length for similar sites. In the case of both unpolarised neutrons and nuclear spins there will be $4I + 2$ states of the nucleus-neutron spin system, where $I$ is the nuclear spin, each with a different scattering length.

Consider a series of scattering systems each identical with respect to the number, position and motion of each scatterer, but where each has a different distribution of $b$ between the occupied sites. In such a case where $b_j$ is the scattering length of site $j$ then the mean products will be:

$$\overline{b_{j'}b_j} = (\bar{b})^2$$
$$\overline{b_j b_j} = \overline{b^2}$$

As a result, the incoherent scattering length is non-zero corresponding to scattering due to the distribution of $b$ values between the sites. The incoherent scattering length is equal to $\overline{b^2} - (\bar{b})^2$.

The incoherent scattering intensity arises from the distribution of $b_j$ and the self-correlations of the nuclei with respect to time. The former indicates that a large incoherent cross-section is expected for elements with a distributed population of isotopes, while the latter predicts a large incoherent cross-section from very mobile nuclei. Hydrogen is the only isotope where its light weight and

mobility contribute significantly to a large incoherent cross-section. With the same mass as a neutron, the momentum transfer in the scattering process will result in a large change in velocity of a hydrogen nuclei leading to significant self-correlations at all temperature. Furthermore, thermal vibrations and the degrees of freedom of bond rotation in organic molecules contribute to these time dependent self-correlations. As shown in Table 2.2 deuterium which has twice the mass of hydrogen has a significantly reduced incoherent cross-section due to the reduction in velocity. Table 2.2 also demonstrates the incoherent scattering from the distribution of isotopes and nuclear spin states with a large cross-section observed for V, Co, and Ni.

In addition to scattering from the nucleus there is a non-zero cross-section for neutron-electron scattering due to the spin-spin interaction between the two particles. A detailed derivation is provided by Squires [108] and the result is written as:

$$\left(\frac{d^2\sigma}{d\Omega dE'}\right)_{s\lambda \to s'\lambda'} = (\gamma r_0)^2 \frac{|\mathbf{k'}|}{|\mathbf{k}|} \left|\langle s'\lambda'|\mathbf{s}\cdot\mathbf{M}_\perp|s\lambda\rangle\right|^2 \delta(E_\lambda - E_{\lambda'} + \hbar\omega) \quad (2.41)$$

where $s$ is the spin-state operator of the neutron, and $\mathbf{M}_\perp$ is the component of magnetisation perpendicular to the scattering vector $\mathbf{Q}$.

The Thompson scattering length, $r_0$, introduced in Section 2.2 appears as the scattering length arises from the unpaired electron density rather than the nuclear spin. The dot-product in the expectation value demonstrates that the cross-section is only sensitive to the component of magnetisation perpendicular to the scattering vector.

Table 2.2: Coherent and incoherent scattering cross-sections for select elements. Reproduced from [108] without permission.

| Element or nuclide | Z | $\sigma_{\mathrm{coh}}$ | $\sigma_{\mathrm{inc}}$ | Element | Z | $\sigma_{\mathrm{coh}}$ | $\sigma_{\mathrm{inc}}$ |
|---|---|---|---|---|---|---|---|
| $^1$H | 1 | 1.8 | 80.2 | V | 23 | 0.02 | 5.0 |
| $^2$H | 1 | 5.6 | 2.0 | Fe | 26 | 11.5 | 0.4 |
| C | 6 | 5.6 | 0.0 | Co | 27 | 1.0 | .2 |
| O | 8 | 4.2 | 0.0 | Ni | 28 | 13.4 | 5.0 |
| Mg | 12 | 3.6 | 0.1 | Cu | 29 | 7.5 | 0.5 |
| Al | 13 | 1.5 | 0.0 | Zn | 30 | 4.1 | 0.1 |

## 2.4.1 Elastic nuclear and magnetic scattering

The diffracted intensity measured from a lattice of nuclei or spins is a function of the nuclear or magnetic structure factor (the structure factor was introduced as Equation 2.23 of Section 2.1).

For a set of $j$ symmetry inequivalent atoms arranged on the sites of a non-Bravais lattice described by the set of position vectors $\mathbf{R}_j$ the coherent elastic cross section may be written as a function of the nuclear structure factor as shown in 2.43 which is non-zero when the lattice is in the Bragg condition.

$$\left(\frac{d\sigma}{d\Omega}\right)_{\text{coh. el.}} = N\frac{(2\pi)^3}{v_0}\sum_{\mathbf{Q}}\delta(\mathbf{Q} - \mathbf{G}_N)\left|F_N(\mathbf{Q})\right|^2 \tag{2.42}$$

$$F_N(\mathbf{Q}) = \sum_j \bar{b}_j \exp(i\mathbf{Q}\cdot\mathbf{R}_j)\exp(-W_j) \tag{2.43}$$

where $\mathbf{G}_N$ is reciprocal lattice vector corresponding to a nuclear Bragg peak, $\bar{b}_j$ is the coherent scattering length of atom $j$, N is the number of unit cells contributing to the structure, $v_0$ is the volume of the unit cell, and $\exp(-W_j)$ is the Debye-Waller term that accounts for the reduction of intensity due to thermal fluctuations.

In the case of an ordered magnetic system the same principle applies; however, instead the spins occupy the lattice sites and the coherent scattering length is replaced by a function of the spin magnitude, direction, and as the scattering is from an electron density a form factor known as the magnetic form factor is required (similar to the atomic form factor discussed in Section 2.2) to account for the difference in phase between each electron as the scatterer is a multi-electron system. This is shown in Equation 2.44 which is non-zero when the spin-lattice is in the Bragg condition.

$$\left(\frac{d\sigma}{d\Omega}\right)_{\text{mag. el.}} = (\gamma r_0)^2 N_m \frac{(2\pi)^3}{v_{0m}}\sum_{\mathbf{Q}}\left|F_M(\mathbf{Q})\right|^2 \exp(-2W)\left[1 - \left(\hat{\mathbf{Q}}\cdot\hat{\boldsymbol{\eta}}\right)^2\right]$$
$$\times\,\delta\left(\mathbf{Q} - \mathbf{G}_m\right) \tag{2.44}$$

$$F_M(\mathbf{Q}) = \frac{1}{2}g\left\langle S^\eta\right\rangle\sum_j F_j(\mathbf{Q})\,exp\left(i\mathbf{Q}\cdot\mathbf{R}_j\right)$$

where $\mathbf{G}_m$ is a reciprocal lattice vector corresponding to a magnetic Bragg peak, $v_{0m}$ the the volume of the magnetic unit cell, $\left\langle S^\eta\right\rangle$ is the time-average spin magnitude with easy axis $\boldsymbol{\eta}$, $g$ is the g-factor, $F_j(\mathbf{Q})$ is the magnetic form factor of

spin $j$, and $\mathbf{R}_j$ is the position vector of spin $j$.

For the case of a general ferrimagnet each spin on the lattice may have a unique direction, and the magnitude of the spin may change from site to site. Based upon this, Equation 2.44 may be generalised as:

$$\left(\frac{d\sigma}{d\Omega}\right)_{\text{mag. el.}} = (\gamma r_0)^2 \, N_m \frac{(2\pi)^3}{v_{0m}} \sum_{\mathbf{Q}} |F_M(\mathbf{Q})|^2 \exp(-2W) \left[1 - \left(\hat{\mathbf{Q}} \cdot \hat{\boldsymbol{\eta}}\right)^2\right]$$

$$\times \, \delta\left(\mathbf{Q} - \mathbf{G}_m\right) \tag{2.45}$$

$$F_M(\boldsymbol{Q}) = \frac{1}{2}g \sum_j \sigma_j F_j(\mathbf{Q}) \langle S^\eta \rangle \exp(i\mathbf{Q} \cdot \mathbf{R}_j)$$

where $\left\langle S_j^\eta \right\rangle$ is the mean spin magnitude and $\sigma_j$ is the spin orientation ($= \pm 1$) of spin $j$.

Furthermore, for an Ising system:

$$\left\langle S_j^\eta \right\rangle = \left\langle S_j^z \right\rangle$$

$$\hat{\boldsymbol{\eta}} = <0, 0, 1>$$

$$\left[1 - \left(\hat{\mathbf{Q}} \cdot \hat{\boldsymbol{\eta}}\right)^2\right] = \left[1 - \hat{\mathbf{Q}}^z\right]$$

Given these equalities and that $gS = \mu$, the observed magnetic neutron diffraction intensity of a Ising ferrimagnet can be written as:

$$I = K \, |F_M(\mathbf{Q})|^2 \left[1 - (Q^z)^2\right] \tag{2.46}$$

$$F_M(\mathbf{q}_m) = \sum_j \sigma_j F_j(\mathbf{Q}) \, \mu_j \exp(i\mathbf{Q} \cdot \mathbf{R}_j)$$

where $Q^z$ is the z-component of the scattering vector and $\mu_j$ is the magnetic moment of the $j^{\text{th}}$ spin.

As the scattering cross-section results from the spin-spin neutron-electron interaction a non-zero cross-section is observed in the magnetically disordered (paramagnetic) phase.

## 2.4.2  Paramagnetic scattering

In the magnetically disordered paramagnetic state neutron scattering from magnetic spins still occurs: for a 3D isotropic magnetic system the paramagnetic scattering occurs uniformly across $4\pi$ steradians. On the other hand, for an anisotropic spin system the intensity will become accordingly anisotropically distributed. For an Ising spin system the intensity will drop off as the scattering rotates out of the plane perpendicular to the spin-axis, and fall off within the plane as a function of the magnetic form factor.

Furthermore, in the case of $LuFe_2O_4$ the non-centrosymmetric ordering of $Fe^{2+}/Fe^{3+}$ in the paramagnetic phase due to the ferroelectric order will lead to spin contrast that will modulate the paramagnetic scattering with the same $\left(\frac{1}{3} \, \frac{1}{3}\right)$ propagation vector. This modulation should lead to diffuse rods perpendicular to the xy-plane that decay as $(1 - q_z^2)$. The large orbital moment reported by Ko *et al.* [122] and independently verified by Kuepper *et al.* [123] significantly reduces the contrast between the two Fe sites reducing the intensity of the paramagnetic scattering in the $\left(\frac{1}{3} \, \frac{1}{3} \, L\right)$-type diffraction rods.

## 2.4.3  The inelastic scattering cross-section

The inelastic neutron scattering cross-section is important in the study of condensed matter systems as the energy of thermal neutrons is of the same order of magnitude as structural and magnetic excitations.

Phonons and magnons correspond to propagating structural and spin modes respectively. $S(\mathbf{Q}, \omega)$ for inelastic scattering ($\omega \neq 0$) is equal to the sum of contributions from the dispersion of phonons and magnons, quasi-elastic scattering, and critical scattering.

Quasi-elastic and critical scattering correspond to structural or spin fluctuations that correspond directly to the spatial order and time-correlations of that order and are therefore tails that extend into inelastic space from elastic Bragg peaks.

The dispersion of phonon/magnon modes extends out into $\mathbf{Q}$-$\omega$ space and mapping $S(\mathbf{Q}, \omega)$ space allows the dispersion of the modes to be well charac-

terised.

Inelastic neutron scattering may be performed using either a time-of-flight or monochromatic triple axis instrument. Multiple regions in **Q**-$\omega$ space are measured in each data collection by time-of-flight instruments, but separating this information out to prepare a **Q**-$\omega$ map may be very time consuming. On the other hand, a single line-segment (parallel to **Q**) is collected in each measurement of a triple axis instrument using an area detector. In fact, if a point detector is used only a single point of **Q**-$\omega$ space is collected per measurement.

In this work inelastic neutron scattering was performed using a triple axis spectrometer; however, due to instrumental and sample effects the measured intensity map does not correspond directly to $S(\mathbf{Q}, \omega)$ and the resolution of the measurement in **Q**-$\omega$ space must be taken into account.

### 2.4.4 The resolution function

The resolution function of a triple-axis spectrometer accounts for the distribution of neutrons measured on the detector for any particular instrument configuration. In practice, the neutron flux is not perfectly parallel (beam divergence) even after collimation, and the monochromator and analyser diffract a small range of wavelengths (crystal mosaic). The combination of these effects mean that instead of investigating a single position in Q-E space described by the scattering function $S(Q, \omega)$, a convolution of the scattering function and the resolution function is observed. The general form of the resolution function is presented as Equation 2.47.

$$R\left(\omega, \mathbf{Q}\right) = \frac{\hbar^2}{m_n} \int d\mathbf{k}_i d\mathbf{k}_f P_i\left(\mathbf{k}_i\right) P_f\left(\mathbf{k}_f\right) \delta\left(\mathbf{Q} - \mathbf{k}_f + \mathbf{k}_i\right)$$
$$\times \left[\omega - \frac{\hbar}{2m_n}\left(k_i^2 - k_f^2\right)\right] \tag{2.47}$$

Where $m_n$ is the rest mass of the neutron, $\mathbf{k}_i$ and $\mathbf{k}_f$ are the wavevectors of the incoming and scattered neutron, $P_i$ is the probability that an incoming neutron has a particular wavevector, $P_f$ is the probability that a neutron with a particular wavevector is detected, **Q** is the scattering vector, and $\omega$ is the angular momentum corresponding to the energy transfer $\hbar\omega$.

If the distribution is approximated to be Gaussian then the resolution function

can be calculated analytically [124] as expressed in Equation 2.48.

$$R\left(\omega - \omega_0, \mathbf{Q} - \mathbf{Q}_0\right) = R_0 \exp\left(-\frac{1}{2}\Delta\zeta M \Delta\zeta\right) \tag{2.48}$$

Where $\zeta$ is the 4D vector $\left(\frac{m_n}{\hbar Q_0}\omega, Q_\parallel, Q_\perp, Q_z\right)$ so, $\Delta\zeta = \left(\frac{m_n}{\hbar Q_0}\left(\omega - \omega_0\right), Q_\parallel - Q_0, Q_\perp, Q_z\right)$ and M is a 4x4 matrix calculated from instrument parameters as described in [124].

In practice, in order to obtain $S(\mathbf{Q}, \omega)$ the resolution function must be calculated and the observations corrected for this effect.

## 2.5 Structural Characterisation and Refinement

Structural refinement and characterisation of materials properties is a key application of scattering techniques. In this work elastic single crystal x-ray diffraction and x-ray and neutron powder diffraction has been performed in order to investigate the structure and material properties associated with the electronic ordering in $LuFe_2O_4$.

In this section the methods and key programs utilised in Chapters 7 and 8 are introduced.

### 2.5.1 Single crystal data reduction

The Fourier relationship between the observed intensity and functions related to the structure was introduced in Section 2.1.2, and in order to calculate these transformations and make use of the Fourier relations as many reflections as possible need to be collected.

Modern single crystal diffractometers provide one or more degrees of freedom of sample rotation and a 2-dimensional CD detector. In this work the experiment setup provided one degree of freedom with the axis of rotation in the horizontal plane and perpendicular to the incident beam.

XDS is a program that is free for academic use and has the capacity to index,

integrate, and correct the spot intensities recorded on a 2D detector. The recorded reflections are located by image processing where the centroid of the spot is fitted on and between detector frames, after which a reciprocal space vector is calculated for each spot. This large set of reciprocal space points is reduced by generating a histogram of the distances between each pair of points. A list of the most populated difference vectors is produced, and a 3-vector basis is selected such that the greatest number of spots may be explained by near-integer multiples of these vectors. Once a suitable set of basis vectors has been identified every reciprocal lattice vector is indexed by an implementation of the *local indexing method*. Beyond this stage the Bravais lattice is determined from the indexing results, and the intensity profiles are extracted by fitting in three dimensions. XDS is then able to partially correct the data for radiation damage and absorption effects. This process is completely automated in the code following instructions provided in an input file [125].

The indexing method implemented in XDS is unable to handle twinned or incommensurate data; alternatively, the program DIRAX is able to identify these lattices. The method implemented in DIRAX operates on the principle of *triplets* in reciprocal space. If a triplet is defined as the triangle with vertices corresponding to three reciprocal lattice vectors, then the normal of this plane will be a direct lattice vector if the three points belong to the same reciprocal lattice. Using this principle, a histogram of possible direct lattice vectors derived from triplets chosen at random is produced and those vectors with the highest population are tested as possible direct lattice vectors. For each possible unit cell each observed reflection is indexed and the solution assessed for agreement with integer indices, or related to integer indice reflections by incommensurate propagation vectors. DIRAX allows for fitting reflections to be refit without non-fitting reflections in order for the accurate solution to be obtained, as the non-fitting "outliers" will have impacted the assessment of each solution. Different solutions can be saved and compared, and twins, domains and incommensurate lattices can accordingly be identified.

## 2.5.2   Patterson and Direct Methods

Following the determination of the space group and indexing the diffraction pattern structural determination is performed. *Ab initio* methods or *direct methods* apply the Fourier relations introduced in Section 2.1.2 in order to solve the struc-

ture.

A Fourier map may be produced by the direct Fourier transform of the structure factor calculated from the square root of the observed intensities; however, the phase of the structure factor depends upon the atomic position and presence of an inversion centre which are initially unknown.

The Patterson function, Equation 2.13, is an important tool in identifying the atomic positions and thus solving the phase of the structure factor. As shown in Equation 2.8 the Patterson function, $G(\mathbf{r}, \infty)$, is the spatial Fourier transform of the elastic scattering function, $S(\mathbf{Q}, 0)$, which is calculated directly from the observed intensities. This may be expressed as the convolution of $\rho(\mathbf{r}')$ and $\rho(\mathbf{r}' + \mathbf{r})$ as shown in Equation 2.13 where $\rho$ is the density of the scattering, which in the case of x-ray scattering is the electron density.

The Patterson function will therefore have peaks at values of $\mathbf{r}$ where $\rho(\mathbf{r}')$ and $\rho(\mathbf{r}' + \mathbf{r})$ are both non-zero. These values of $\mathbf{r}$ correspond to interatomic spacings, therefore a maximum is observed at the origin corresponding to the sum of all the atoms translated onto themselves and maxima are observed at $\mathbf{r}$ with the direction and distance corresponding to an interatomic spacing and magnitude weighted by the products of the scattering density of the pair of atoms. In the case of x-rays this weighting factor is the atomic number, $Z$.

Model structures may be constructed using the symmetry information obtained from indexing and the interatomic distances and directions obtained from analysis of the Patterson map. Fourier maps calculated from the square root of the observed intensities can then be compared to Fourier maps calculated from the structural models and the models varied until the difference map is zero. The difference map is defined as shown in Equation 2.49 with positive density corresponding to insufficient electron density and negative density corresponding to excess electron density in the model.

$$F_\Delta = F_{\text{obs}} - F_{\text{calc}} \tag{2.49}$$

where $F_{\text{obs}}$ is the Fourier map calculated from the square root of the observed intensities, and $F_{\text{calc}}$ is the Fourier map calculated from the proposed model.

A number of techniques exist to solve the phase problem outlined earlier, such as charge flipping or the use of anomalous scattering data, but a detailed

discussion of these methods is beyond the scope of this work.

### 2.5.3 Powder Data: Rietveld Method

The Rietveld method, first described by Hugo Rietveld, fits powder diffraction patterns in order to determine structural and phase composition information using a least squares algorithm as shown in Equation 2.50.

$$\chi^2 = \sum_{i=1}^{N} w_i \left\{ y_i(\theta_i) - y_c(\theta_i) \right\}^2 \tag{2.50}$$

Where $w_i$ is $1/\sigma^2$ with $\sigma$ representing the standard deviation of the $i$th measurement, $y_i$ is the observed value of the $i$th measurement collected at $\theta_i$, and $y_c$ is the calculated value for position $i$.

The calculated intensity at each point is the sum of the contribution from each observed reflection of each phase as indicated in Equation 2.51, where $S_\phi$ is the scale factor of phase $\phi$, $I_{\phi,\mathbf{h}}$ is the predicted intensity for reflection $\mathbf{h}$ of phase $\phi$, $\Omega$ is the peak profile function that describes the intensity distribution of reflection $\mathbf{h}$ with respect to the diffraction coordinate system $\theta$, and $b_i$ is the background at $\theta_i$.

$$y_c(\theta_i) = \sum_{\phi} S_\phi \sum_{\mathbf{h}} I_{\phi,\mathbf{h}} \, \Omega \left( \theta_i - \theta_{\phi,\mathbf{h}} \right) + b_i \tag{2.51}$$

The peak profile function and background function are selected from a number of options within the chosen software package, which yield a series of potentially refineable parameters that describe the background and peak profile as a function of $\theta$.

The intensity of reflection $\mathbf{h}$ is calculated from the structure factor (introduced in Section 2.1.3) and corrected for the Lorentz and polarisation factors, multiplicity, absorption, and preferred orientation as shown in Equation 2.52.

$$I_{\phi,\mathbf{h}} = L_{\phi,\mathbf{h}} \, A_{\phi,\mathbf{h}} \, P_{\phi,\mathbf{h}} \, F_{\phi,\mathbf{h}}^2 \tag{2.52}$$

Where $L$ is the Lorentz-polarisation correction, $A$ is the absorption correction, $P$ is the preferred orientation correct, and $F$ is the structure factor.

Combining the background, profile, and phase parameters and intensity corrections yields a large set of variables to fit the pattern and understand the structure, material properties, and phase composition.

The method is generalised to all powder diffraction data where $\theta_i$ may be in angular diffraction coordinates such as $2\theta$ for monochromatic diffractometers, or time a s is the case for time-of-flight diffractometers.

FULLPROF and GSAS are the two Rietveld refinement packages utilised in this work.

## 2.5.4   Powder Data: Le Bail Fitting

Le Bail fitting, also known as *whole pattern decomposition*, extracts the observed intensities of the reflections individually. This allows the intensities to be applied in the same fashion as single crystal diffraction data.

The aim is to obtain the set $I_{\mathbf{h}}$ by fitting each individual peak. Peak profile and background parameters are required, and a basic description of the unit cell is needed to calculate the position of the reflections. Equation 2.53 is fitted to each reflection.

$$y_c(\mathbf{h}) = I_{\mathbf{h}} \ \Omega \left(\theta - \theta_{\mathbf{h}}\right) + b_{\mathbf{h}}(\theta) \tag{2.53}$$

Cell parameters and a space group are used to calculate the positions of $N$ allowed reflections and they are iteratively processed to obtain $I_{\mathbf{h}}$.

Le Bail fitting is implemented in both FULLPROF and GSAS; however, the *direct methods* implementation that was chosen was that of GSAS as it was easier to use, had a larger toolset, and the density files are compatible with the MARCHING CUBES visualisation program.

# Chapter 3

# Resonant X-ray Diffraction

## 3.1  Introduction

LuFe$_2$O$_4$ is a complex material, as discussed in Section 1.5, with both long range charge and magnetic order in the multiferroic phase. Unlike many other multiferroic materials the high temperature phase is the ferroelectric phase, and it is important to fully characterise the charge ordered state of the material in order to understand what happens when the material becomes multiferroic below 255 K. Mössbauer spectroscopy [44, 45, 69] and resonant x-ray scattering (RXS) [79–81] have indicated that complete charge disproportionation is present between the iron sites (i.e. Fe$^{2+}$/Fe$^{3+}$ charge order) by the measured chemical shifts and observed interference in the measured energy dependence.

The RXS studies previously reported determine this charge disproportionation by fitting the data with anomalous scattering factors obtained by measuring the absorption cross-section of isostructural materials [81]. Theoretical work has demonstrated that an orbital degree of freedom is active on the Fe$^{2+}$ sites of this material [97] and predict a disordered orbital state. RXS is an excellent tool for investigating orbital ordering due to the polarisation and azimuthal dependence that is observed for the ordered case; however, RXS studies reported in the literature fail to address this point.

In this chapter a RXS study is presented that attempts to extract the anomalous form factors from the resonant data in a self-consistent fashion and inves-

tigates orbital order in $LuFe_2O_4$. Introductory material to x-ray scattering was presented in Chapter 2, an outline of the experimental method is provided as Section 3.2, data processing and analysis are provided in Section 3.3, and finally the discussion and conclusions are presented in Section 3.4.

## 3.2 Experimental

Resonant x-ray scattering was performed on the 5-circle surface diffraction end-station of the material science X04SA beamline at the Swiss Light Source. A large single crystal ingot of $LuFe_2O_4$ was prepared by Pomjakushina and Conder and a thin piece cut, oriented with the surface normal parallel to the proposed c-axis. The sample was mounted on the 'hexapod' in the vertical position (as shown in Figure 3.1) and the surface reflectivity used as a guide to adjust the hexapod such that the surface normal was in the horizontal plane of the beam. The beam energy was tuned to 7112 eV, the iron K-edge.

The diffractometer was operated such that the angle of incidence of the x-ray beam ($\alpha$) was kept constant whilst the rotation about the sample normal ($\omega$) was used to explore reciprocal space. The vertical circle ($\delta$) and horizontal circle ($\gamma$) of the detector were allowed to vary fully within the range of motion limited only by motor mechanics and potential collisions. The Pilatus II pixel detector was utilised and the rotation about the normal to the imaging plane ($\nu$) was kept constant throughout the experiment.

The orientation (UB) matrix was determined by indexing multiple (minimum of three) non-coplanar reflections and the beamline operation software SPEC calculated and stored the orientation matrix. Multiple crystallites within the sample volume caused some difficulty as initially it was not possible to separate the reflections from the individual crystals; however, the observed reflections were processed systematically until a consistent UB-matrix for a single crystallite was obtained.

A SPEC routine was written for this experiment that shifted the beam energy below the K-edge then increased it in successive increments such that an energy scan was performed from 7012 to 7312 eV. This routine was copied and steps added that calculated the motor positions for each x-ray energy and executed the move command such that the diffractometer remained aligned on a fixed point in
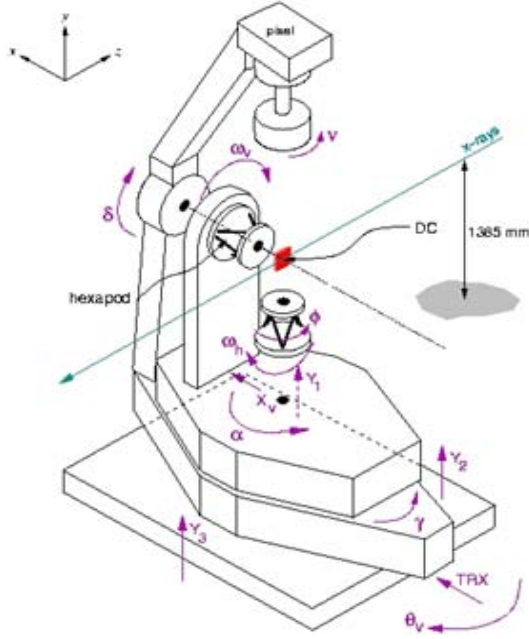
Figure 3.1: Schematic diagram of the 5-circle Surface Diffraction endstation of the MS beamline at the Swiss Light Source.

reciprocal space (this will be referred to as an *EfixQ scan*).

EfixQ scans were collected for a number of charge peaks from the $R\bar{3}m$ structure and charge ordered satellite reflections at room temperature. The Be-dome was then mounted and the He refrigeration system activated to cool the sample to approximately 15 K. The sample was realigned and EfixQ scans collected for multiple series of $R\bar{3}m$ structural and superlattice satellite peaks.

Once these scans were complete the sample was returned to room temperature and the cooling system removed, with the sample remounted on a heating mount. The intensity of the $\left(\frac{1}{3} \; \text{-}\frac{2}{3} \; \frac{7}{2}\right)$ reflection was recorded by taking single detector images as a function of temperature between 297 and 390 K. The sample alignment was not varied during this process.

## 3.3 Data Reduction

Data reduction and analysis was performed using SCILAB. MATLAB code provided by the beamline to read the image files, and the MATLAB KK-routines [117] introduced in Section 2.2.1 have been rewritten in SCILAB syntax and further code written to analyse the data as discussed in this section.

### 3.3.1   Data correction and selection

Fluorescence, caused by photoelectric absorption, is the primary source of background in these measurements. The x-ray energy is well above the energy of the L and M absorption edges so the fluorescence caused by the decay of electrons into the holes created in these shells is observed. Due to the trigonal symmetry the absorption cross-section is anisotropic with respect to the sample orientation; thus, the fluorescence is also expected to be anisotropic. For this experiment the extent of the anisotropy with respect to the solid angle of the detector is relevant, and a frame from a fluorescence scan is provided as Figure 3.2.

The profiles presented in Figure 3.2(b) show that the fluorescent background varies continuously across the detector.

As the x-ray energy is scanned through the K-edge a step in the absorption cross-section occurs, and a corresponding step in the fluorescence is expected; this is demonstrated in the observed energy dependence presented as Figure 3.3.

Two methods were investigated in order to obtain the integrated intensity of each frame and correct the EfixQ scans for this experimental background. Firstly, a sample detector image of each scan was examined and a region-of-interest (ROI) about the diffraction spot was integrated to obtain the integrated intensity. Following this, multiple rectangular regions about the detector were selected and the average pixel intensity multiplied by the number of pixels in the ROI to determine the background, which was then subtracted. An example using the $\left(\frac{2}{3} \text{-} \frac{1}{3} \, \frac{7}{2}\right)$ reflection is provided as Figure 3.4, where the sample frame, integrated intensity, background subtracted integrated intensity and fluorescent
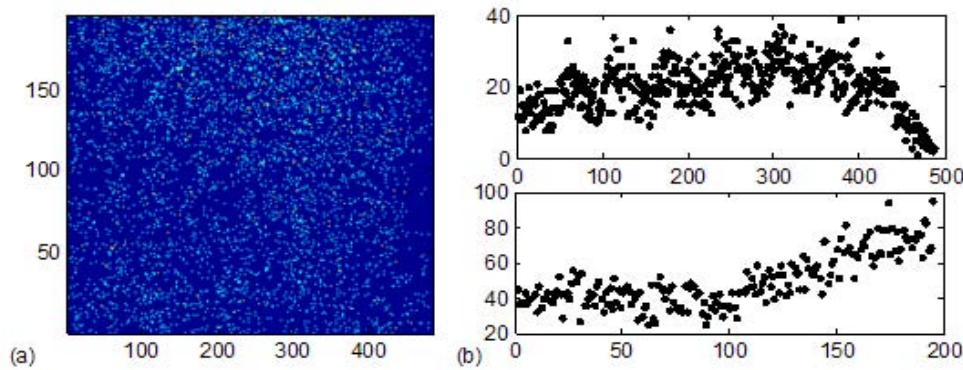


Figure 3.2: (a) A sample frame from a fluorescence scan with, (b) the integrated profiles of the frame along the two orthogonal axes of the detector.
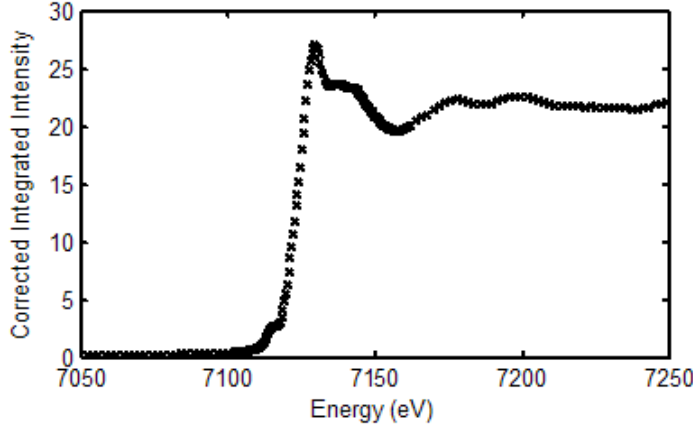
Figure 3.3: A fluorescence scan collected at 15 K. An EfixQ scan (as outlined in the experimental section) was collected at a wavevector transfer that does not correspond to a diffraction spot of the sample.

background are shown.

Alternatively, the integrated profile of the camera with respect to each of its two orthogonal axes were calculated and fitted with a Lorentzian peak profile function on a linear background by an automated method. As each scan is made up of hundreds of frames an early frame was fitted and then those parameters minimised against the first frame; these optimised parameters were then passed on and used as the basis to fit the second frame, and so on. The integrated area of the Lorentzian function is used to determine the peak intensity. A fit of the $\left(\frac{2}{3} \text{-}\frac{1}{3} \frac{7}{2}\right)$ reflection and comparison of the energy dependence determined by each of these methods is presented in Figure 3.5. Figure 3.5(b) shows a constant offset between the functions determined by the two methods, which may be explained by a slight difference in the background correction methods as the fitting method accounts for the full frame background, whilst the ROI method takes an average. The ROI method is only accurate if the background is completely uniform; however, as shown in the line profile the background is sloped. The magnitude will scale with the absorption function, but so too will the slope leading to an effectively constant offset. As there is a constant offset between the two methods the ROI method was used as it was faster to implement across the large number of frames collected.

Further to background correcting the data, an absorption correction process must be carried out. The measured fluorescence was used to absorption correct the data, but the step-size was found to be insufficient, indicating the collected fluorescence is not a direct indicator of the sample absorption. Rather, the energy dependence of the $R\bar{3}m$ symmetry Bragg peaks was used to obtain an absorption
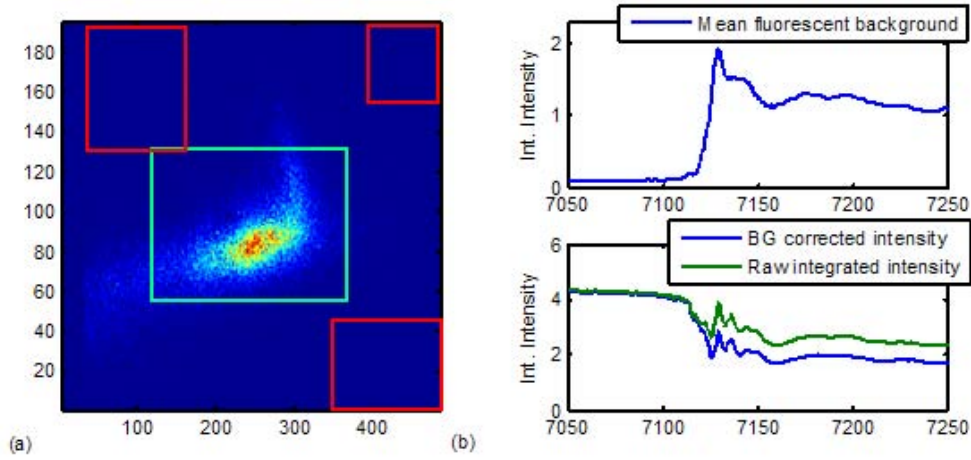
Figure 3.4: (a) A sample frame from the $\left(\frac{2}{3} \text{-} \frac{1}{3} \frac{7}{2}\right)$ reflection collected at approximately 15 K where the green box indicates the region used to determine the integrated intensity and the red boxes indicate the regions used to determine the fluorescent background, and (b) top: the mean fluorescent background determined from the red regions of (a), and bottom: the raw integrated intensity determined from the green region of (a) and the background corrected intensity.
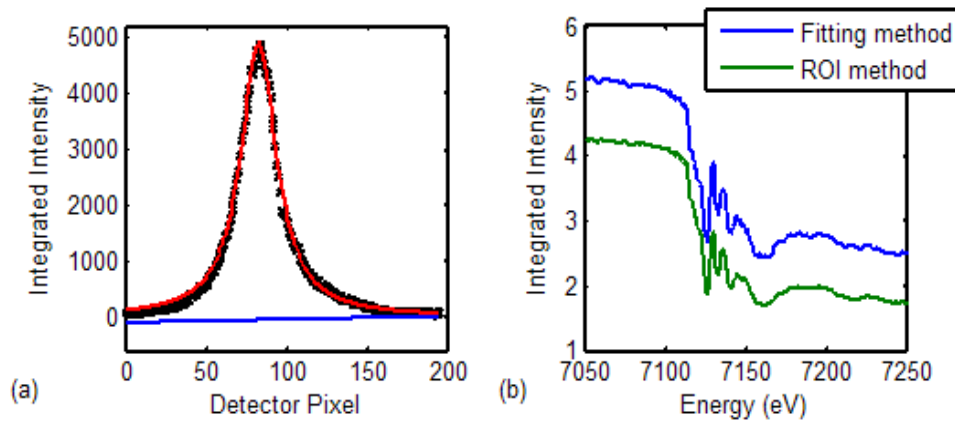


Figure 3.5: (a) The line profile of the detector image shown as Figure 3.4(a) integrated along the x-axis; fitted with a Lorentzian peak shape and linear background, and (b) Comparison of the energy dependence determined by each method.

function.

Each $R\bar{3}m$ reflection that was collected was used to calculate an absorption function ($\mu$) from the observed data ($RXS$). Then, the energy dependent structure factor was calculated using the known $R\bar{3}m$ structural information and the CL-values for the anomalous scattering factor via the relation shown in Equation 3.1.

$$
\begin{aligned}
F(\mathbf{Q}, E) &= \sum_j (f_0(\mathbf{Q}) + f'(E) + if''(E)) \exp\left(i\mathbf{Q} \cdot \mathbf{R}\right) \\
&= RXS(\mathbf{Q}, E) \times \mu(E)
\end{aligned}
\tag{3.1}
$$

The $(0\,0\,6)$ reflection was found to yield the best result and an iterative process was applied to obtain the final absorption correction. At each stage, the value of $\mu$ owas used to produce the anomalous scattering factor and then these new values were used to yield a new $\mu$. This process converged quickly, and the best L-series that remained after this correction was applied is shown as Figure 3.6. The oscillations about a constant pre- and post-edge value indicates these reflections are a result of charge ordering as a difference pattern is observed.

## 3.3.2 Implementing the anomalous structure factor

As shown in Equation 2.33 the x-ray structure factor is the sum of complex exponential functions, one for each atom of the basis, and therefore each atom may be thought of as a vector in the Argand plane with a magnitude at a particular $\mathbf{Q}$ and $E$ of the anomalous atomic form factor for that element. At any point where the structure factor is zero it means that the sum over all atoms is zero, and therefore for every vector in the Argand plane there exists one of equal magnitude and opposite direction. As the anomalous atomic form factor is different for each element this means that *every atom is out of phase with an atom of the same type.*

The $\left(\frac{1}{3}\,\frac{1}{3}\,\frac{3}{2}\right)$-type superlattice reflections recorded in this experiment are not allowed by the symmetry of the ferroelectric prototype for $LuFe_2O_4$. This means that no Bragg peak can be observed if the atoms have the atomic coordinates and type as described by this phase. However, if the iron sites are modulated with $Fe^{2+}/Fe^{3+}$ as reported in the literature, then the Fe sites on the lattice are no

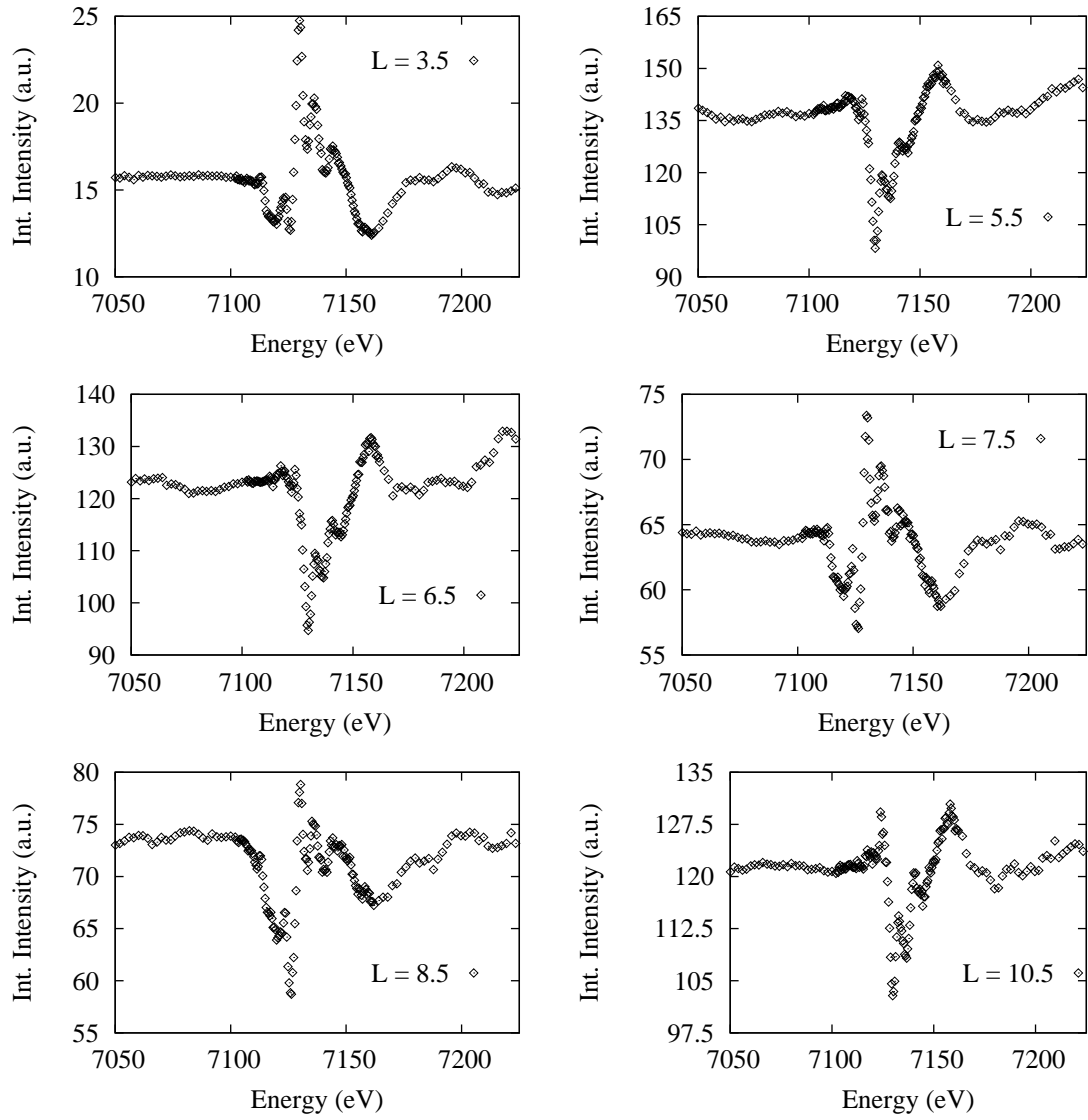Figure 3.6: EfixQ scans collected for a series of $\left(\frac{2}{3}\,\text{-}\frac{1}{3}\,L\right)$ reflections after a background correction and absorption correction has been applied. Data processing was performed in SCILAB.

longer equivalent as the anomalous atomic form factors for the two ionic species are different. Even though the **Q**-dependent Thompson scattering factor is very similar (as the number of electrons only varies by 1), the anomalous scattering factor is different due to the chemical shift of the x-ray absorption edge and variations in the fine structure due to differences in the chemical environment. If this modulation occurs in such a fashion that pairs of iron that are $180^o$ out-of-phase in the structure factor are no longer equivalent then the structure factor becomes non-zero. In fact, if this is the case, constant intensity corresponding to Thompson scattering is expected before and after the absorption edge, and an intensity that oscillates about this value as a function of the difference between the anomalous scattering factors is expected through the edge. This is consistent with the observed energy dependence shown in Figure 3.6.

A model structure factor may be written assuming this modulation of the $Fe^{2+}/Fe^{3+}$ occurs in the fashion described above, and that non-resonant intensity is contributed to by structural distortions of the lattice due to this charge ordering. Such a model is shown as Equation 3.2, where the structure factor has been rotated such that the difference vector of the real anomalous scattering factor is parallel to the *Re* axis, and the difference vector for the imaginary part is parallel to the *Im* axis.

$$\begin{aligned}
F(\mathbf{Q}, E) = K_{\text{Lu}}(\mathbf{Q}) + K_{\text{O}}(\mathbf{Q}) + K_{\text{Fe}}(\mathbf{Q}) + f'_{\text{Fe1}}(E) - f'_{\text{Fe2}}(E) \\
+ i\left(f''_{\text{Fe1}}(E) - f''_{\text{Fe2}}(E)\right)
\end{aligned} \tag{3.2}$$

where $K_{\text{j}}$ are the complex-valued contributions to the structure factor due to the structural distortion of atom $j$, and $f'_j$ and $f''_j$ are the real-valued anomalous scattering factors for atom $j$.

In order to simplify the evaluation of this expression the real and imaginary part of the structure factor are separated and expressed as the real constants $A$ and $B$ as demonstrated in Equation 3.3, and from this a model may be written for the observed intensity as described by Equation 3.4.

$$F(\mathbf{Q}, E) = A(\mathbf{Q}) + \Delta f'(E) + i\left(B(\mathbf{Q}) + \Delta f''(E)\right) \tag{3.3}$$

$$I(\mathbf{Q}, E) = C.\left((A(\mathbf{Q}) + \Delta f'(E))^2 + (B(\mathbf{Q}) + \Delta f''(E))^2\right) \tag{3.4}$$

Each reflection presented in Figure 3.6 represents a different **Q** and therefore every data point of every scan may be expressed as Equation 3.4. If we allocate

an energy grid of 180 points this means across the 6 datasets there are 1080 equations with 378 unknowns. The solution space of this over-determined system can be explored by progressive non-linear refinement.

### 3.3.3 Progressive non-linear refinement

In order to extract the two pairs of anomalous scattering factors for the two sites a progressive non-linear method was employed. The relative error calculated from the difference between the calculated intensity ($\mathbf{I}_{\text{calc}}$) using Equation 3.4 and the observed intensity ($\mathbf{I}_{\text{obs}}$) was established as the main error function with the four anomalous scattering factors expressed individually in the error function.

The Jacobian (the derivative of the error function with respect to the full parameter space) was calculated using the `derivative` built-in function of SCILAB. If $\mathbf{x}_0$ is the column of the values of the two imaginary anomalous scattering factors then the next "step" of each parameter is calculated such that $\mathbf{x} = \mathbf{x}_0 - \boldsymbol{\delta}$. The method to calculate the values of $\boldsymbol{\delta}$ was derived from the Levenberg-Marquadt algorithm as shown in Equation 3.5.

$$\left(\mathbf{J^T J} + \lambda.\mathbf{diag}\left(\mathbf{J^T J}\right)\right)\boldsymbol{\delta} = \mathbf{J^T}\left[\mathbf{I}_{\text{obs}} - \mathbf{I}_{\text{calc}}\right] \tag{3.5}$$

Where $\mathbf{J}$ is the Jacobian, $\lambda$ is a damping constant, $\mathbf{I}_{\text{obs}}$ is the measured intensity, and $\mathbf{I}_{\text{calc}}$ is the intensity calculated by Equation 3.4.

From the optical theorem it was assumed that the absorption calculated from the $(0\,0\,6)$ reflection can be transformed to $f''_{\text{sum}}$, where $f''_{\text{sum}} = f''_{\text{Fe1}} + f''_{\text{Fe2}}$. With this as a starting point, initial values of the anomalous scattering factors were determined by solving the quadratic form of Equation 3.4 assuming $A = 0, B = -18$, and $C = \frac{73}{18^2}$ on a point by point basis using the $\left(\frac{2}{3}\,\text{-}\frac{1}{3}\,\frac{17}{2}\right)$ reflection data, neglecting the $(\Delta f')^2$ term. The imaginary anomalous functions obtained by this method are provided as Figure 3.7, and the fit of these functions to the full form of Equation 3.4 is shown as Figure 3.8.

These anomalous functions were then fitted to the $L = \frac{7}{2}$ and $\frac{17}{2}$ RXS data to obtain values for the constant A, B and C. In addition to the difference between observed and predicted RXS intensity, a penalty for deviation from $f''_{\text{sum}}$ was introduced into the error function. The two error functions used in this work are
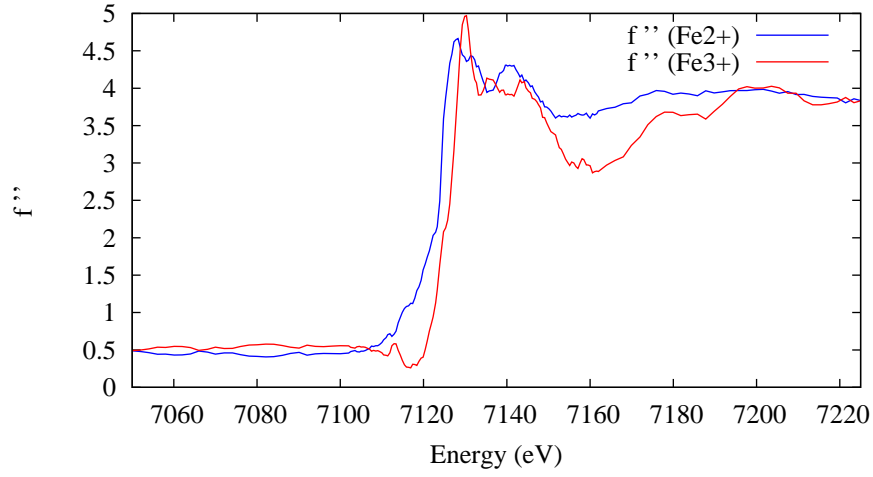
Figure 3.7: The imaginary part of the anomalous scattering factors of the two Fe sites calculated on a point-by-point basis from the $L = \frac{17}{2}$ RXS data using the quadratic form of Equation 3.4 and neglecting the $(\Delta f')^2$ term.
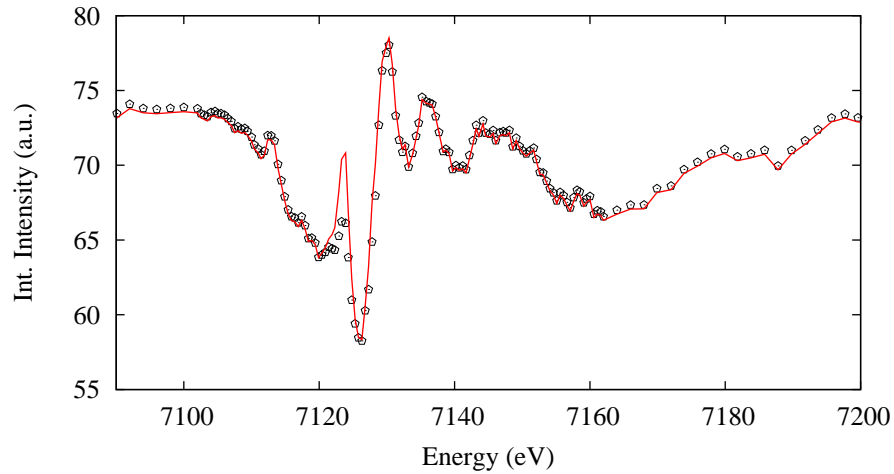


Figure 3.8: Fit of the $L = \frac{17}{2}$ RXS data using the anomalous functions shown in Figure 3.7 and the full form of Equation 3.4. The KK-transformation and fitting were performed using SCILAB.

provided as Equations 3.6 and 3.7.

$$\mathbf{E} = \frac{\mathbf{I}_{\text{obs}} - \mathbf{I}_{\text{calc}}}{\mathbf{I}_{\text{obs}}} \tag{3.6}$$

$$\mathbf{E} = \frac{\mathbf{I}_{\text{obs}} - \mathbf{I}_{\text{calc}}}{\mathbf{I}_{\text{obs}}} + \frac{f''_{\text{sum}} - (f'_{\text{Fe1}} + f'_{\text{Fe2}})}{f''_{\text{sum}}} \tag{3.7}$$

Using the fitted values for the constants A, B, and C, the incremental step ($\delta$) for the values of the imaginary anomalous scattering factors was calculated by Equation 3.5 using error function Equation 3.7 with $\lambda$ adjusted to produce a suitable change in the functions. At every step the difference KK transformation was performed in order to obtain the real component of the anomalous scattering factor and the point at which the CL-values were centred was automated within the code to be the half-height value of the step in the imaginary function.

Using this method the functions shown in Figure 3.9 were obtained. The fitting of these functions (and their KK-transforms) to the data presented in Figure 3.6 is shown in Figure 3.10 while the inset shows the measured temperature dependence of the satellite intensity. Each function has a similar shape with a well defined pre-edge feature in both cases (feature A), and a series of post-edge oscillations (B-E). The two functions are very similar and it appears that a constant value may be added to the energy position of either function to align all the points of equivalent phase. Despite the similarities, the differences in the amplitude of the oscillations in the two functions relate to the difference in the PE wave interference at the $Fe^{2+}$ and $Fe^{3+}$ sites and contain information about the local chemical environments of the two species. The differences between the two functions, for example the difference in the absorption peak intensity (B) or the absence of the trough (E) in the case of $Fe^{2+}$, are further investigated in Chapter 4.

## 3.4 Discussion & Summary

The final values of the imaginary part of the anomalous scattering factor obtained from the fitting method described in Section 3.3.3 by are shown in Figure 3.9 and the observed chemical shift was found to be 4.0 eV.

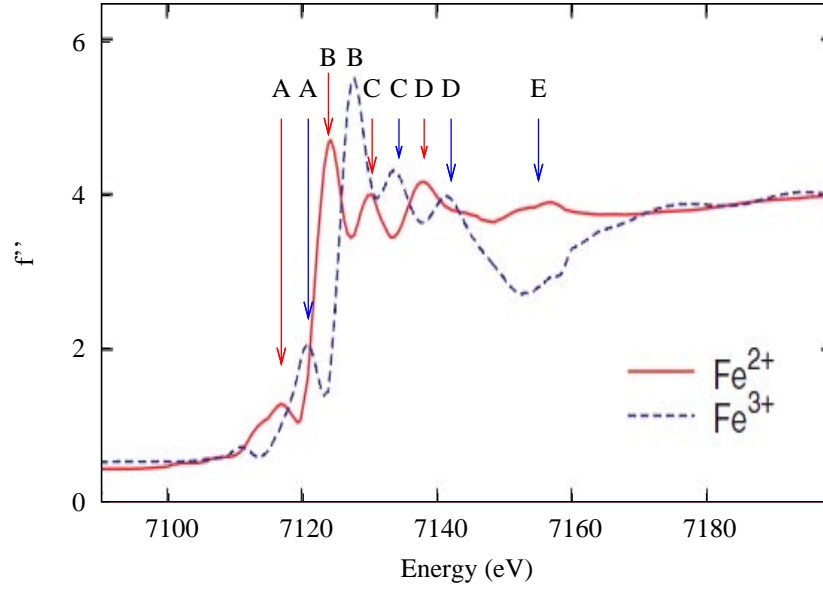The chemical shift has been reported to be 4.3 eV from $Fe_2O_3$ and FeO octa-

Figure 3.9: The imaginary part of the anomalous scattering factor for the two iron sites [126].
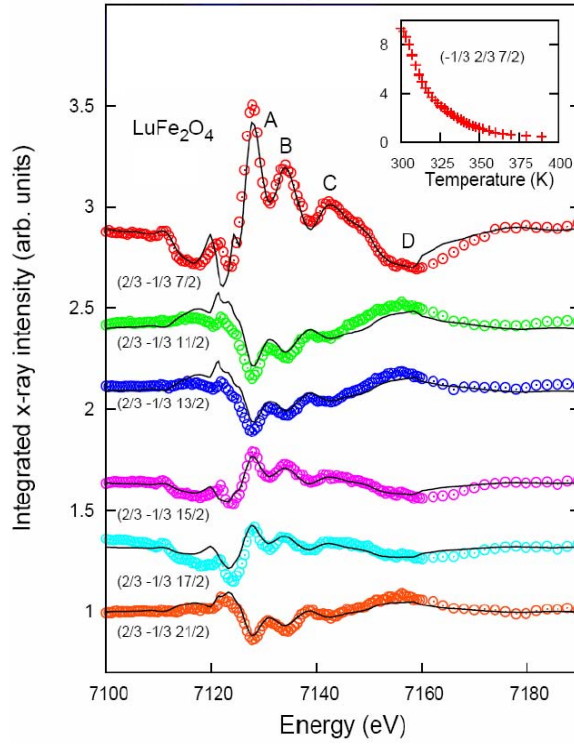


Figure 3.10: Fits of Equation 3.4 to each of the L-series datasets using the imaginary part of the anomalous scattering functions presented in Figure 3.9 and their KK-transforms [126].

hedrally coordinated reference materials [127] and 4.5 eV from XANES spectra of $Fe^{2+}/Fe^{2+}$ aqua-complexes [128]. Accordingly, the observed value is attributed to complete $Fe^{2+}/Fe^{3+}$ charge-order.

In addition to investigating the chemical shift, orbital order was investigated by analysing the azimuthal and polarisation dependence of the collected energy scans. The polarisation of the synchrotron radiation with respect to the instrument was horizontal, therefore the $\pi$ radiation was incident when the scattering plane was in the plane of the synchrotron ring. However, as soon as the scattering plane was not horizontal (characterised by a non-zero value of $\delta$) a component of $\sigma$ polarisation was introduced. Due to the anisotropic nature of the electron density associated with orbital order the polarisation of the incident radiation should influence the observed intensity in the presence of orbital order. As shown in the final column of Table 3.1 the polarisation varies significantly across the six reflections fitted by the anomalous scattering model. The model described by Equation 3.4 does not include any polarisation dependent terms, and therefore this model should fail to fit the data in the presence of orbital order. Furthermore, the six symmetry equivalent reflections including the $\left(\frac{2}{3} \text{-}\frac{1}{3} \frac{7}{2}\right)$ represent the same reflection from slightly different azimuthal angles. As shown in Figure 3.11 the energy dependence of these reflections are almost identical and there does not appear to be any change that is a function of this small change in azimuthal angle.

These observations indicated a full polarisation and azimuthal dependence study was in order and as shown in Figure 3.12, Scagnoli and Mazzoli measured the azimuthal dependence of the $\left(\frac{1}{3} \frac{1}{3} \frac{31}{2}\right)$ reflection at 300 K and the polari-
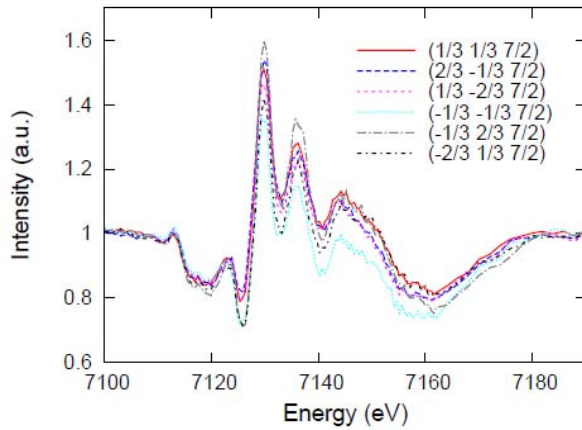


Figure 3.11: Resonant x-ray scattering profile of 6 hexagonally equivalent charge order satellites.

Table 3.1: Summary of the instrument angles (described in Section 3.2) for selected reflections and the Poincaré vector which indicates the incident polarisation for that measurement; the Poincaré vector is $+(-)1$ for $\sigma(\pi)$ polarisation.

| Miller Index | $\alpha$ | $\omega_v$ | $\gamma$ | $\delta$ | $\mathbf{P}_\zeta$ |
|---|---|---|---|---|---|
| $\left(\frac{1}{3}\ \frac{1}{3}\ \frac{7}{2}\right)$ | 10 | 66.29 | 14.09 | 19.73 | 0.37 |
| $\left(\frac{1}{3}\ \text{-}\frac{2}{3}\ \frac{7}{2}\right)$ | 10 | -48.32 | 12.97 | 20.31 | 0.46 |
| $\left(\text{-}\frac{1}{3}\ \text{-}\frac{1}{3}\ \frac{7}{2}\right)$ | 10 | -106.19 | 14.39 | 19.29 | 0.33 |
| $\left(\text{-}\frac{1}{3}\ \frac{2}{3}\ \frac{7}{2}\right)$ | 10 | 127.84 | 15.70 | 18.44 | 0.21 |
| $\left(\text{-}\frac{2}{3}\ \text{-}\frac{1}{3}\ \frac{7}{2}\right)$ | 10 | -169.65 | 15.48 | 18.27 | 0.21 |
| $\left(\frac{2}{3}\ \text{-}\frac{1}{3}\ \frac{7}{2}\right)$ | 10 | 10.06 | 12.69 | 20.49 | 0.49 |
| $\left(\frac{2}{3}\ \text{-}\frac{1}{3}\ \frac{11}{2}\right)$ | 10 | 11.39 | 21.03 | 20.99 | 0.07 |
| $\left(\frac{2}{3}\ \text{-}\frac{1}{3}\ \frac{13}{2}\right)$ | 10 | 14.56 | 25.27 | 21.05 | -0.10 |
| $\left(\frac{2}{3}\ \text{-}\frac{1}{3}\ \frac{15}{2}\right)$ | 10 | 17.15 | 29.75 | 21.43 | -0.23 |
| $\left(\frac{2}{3}\ \text{-}\frac{1}{3}\ \frac{17}{2}\right)$ | 10 | 20.69 | 34.61 | 20.83 | -0.38 |
| $\left(\frac{2}{3}\ \text{-}\frac{1}{3}\ \frac{21}{2}\right)$ | 10 | 30.45 | 43.68 | 20.01 | -0.56 |

sation dependence of the $\left(\frac{1}{3}\ \frac{1}{3}\ \frac{3}{2}\right)$ reflection at 10 K. No azimuthal dependence is observed, and no rotation of the polarisation is observed as the scattering is demonstrated to be purely $\sigma - \sigma$ in type. These results demonstrate that no orbital order is observed in agreement with the theoretical predictions of Nagano *et al.* [97].
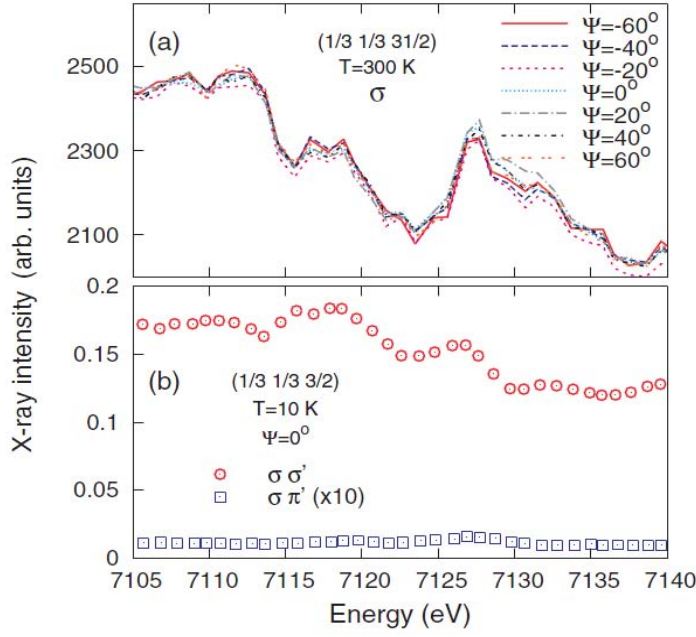
Figure 3.12: (a) the azimuthal ($\Psi$) dependence of the $\left( \frac{1}{3} \frac{1}{3} \frac{31}{2} \right)$ reflection collected at 30 K, and (b) the polarisation dependence of the $\left( \frac{1}{3} \frac{1}{3} \frac{3}{2} \right)$ reflection collected at 10 K.

The imaginary part of the anomalous scattering factor obtained for each site shows unique features corresponding to the local chemical environment of the respective ion. These differences may be investigated directly by taking the Fourier transform to yield the real space pair distribution function or by attempting to model these results using available codes. The usefulness of each of these methods of investigation with respect to the results presented here is outlined in Chapter 4.

# Chapter 4

# X-ray absorption spectroscopy: calculations

## 4.1 Introduction

The polarisation in ferroelectric oxides is usually caused by the displacement of cations or anions due to increased covalency. $LuFe_2O_4$ has been shown to be an exception to this rule as it is an *electronic ferroelectric* where the ferroelectric polarisation results from the anisotropic ordering of $Fe^{2+}/Fe^{3+}$ ions. Even though the polarisation does not result from ionic displacements there will be a coupling between the anisotropic charge distribution and the lattice, leading to lattice distortions with the same propagation vector as the charge ordering.

As demonstrated in Chapter 3, the imaginary part of the anomalous scattering factor is a direct transformation of the x-ray absorption spectra of a material. The shape of these functions is a result of the interference of photoelectron (PE) wavefronts excited by the x-ray absorption process and the magnitude and frequency of these oscillations describes the local chemical environment of the excited species. The imaginary parts of the anomalous scattering factors of $Fe^{2+}$ and $Fe^{3+}$ were separated by the iterative analysis procedure outlined in Chapter 3 and the functions obtained were provided in Figure 3.9. As demonstrated in this plot, the two functions are similar but have distinct differences in the amplitude of the corresponding features.

In this chapter the origin of these functions has been investigated by modelling the absorption spectra of the Fe-sites of $LuFe_2O_4$ using the software FDMNES and FEFF. An introduction to the x-ray absorption process and a discussion of modelling the extended x-ray absorption fine structure (EXAFS) and x-ray absorption near edge structure (XANES) regions was provided in Chapter 2 along with a brief introduction to the software packages used in this study.

The extent to which useful information can be extracted by a direct Fourier transform is investigated in Section 4.2 followed by a detailed series of calculations that investigate the effect of the charge distribution and lattice distortions on the absorption cross-section presented in Section 4.3. Finally, a discussion of the results is provided in Section 4.4.

## 4.2 The inverse Fourier transform

The oscillations above the edge in an x-ray absorption spectrum are due to the interference of photoelectron wavefronts and are described by the function $\chi(k)$ which is related to the observed absorption coefficient as presented in Equation 2.39 of Section 2.3.2.

The values of $\chi(k)$ may be obtained from the imaginary part of the anomalous scattering factor obtained in Chapter 3 by subtracting the Cromer-Lieberman values. The energy scale is converted into the photoelectron wavenumber by fitting the edge position, and the resulting $\chi(k)$ functions for the $Fe^{2+}$ (labelled $Fe_1$) and $Fe^{3+}$ (labelled $Fe_2$) site are shown in Figure 4.1. A pair distribution function (PDF) was obtained for each of these functions by taking the Fourier transform of $\chi(k)$ using the IFEFFIT toolpack. Peaks corresponding to known atomic position were observed in the PDF; however, other broad contributions were noted.

In Chapter 3, the resonant scattering intensity was measured as a function of energy out to approximately 7300 eV which is around 176 eV above the K-edge; however, the beamline energy was varied in such a way that the optics were aligned at 7112 eV and as the energy was scanned the instrument configuration became less optimal. As a result of this, only the intensity measured out to 7200 eV was found to behave reasonably with regard to the expected non-resonant energy dependence. Therefore the majority of the x-ray absorption coefficient that
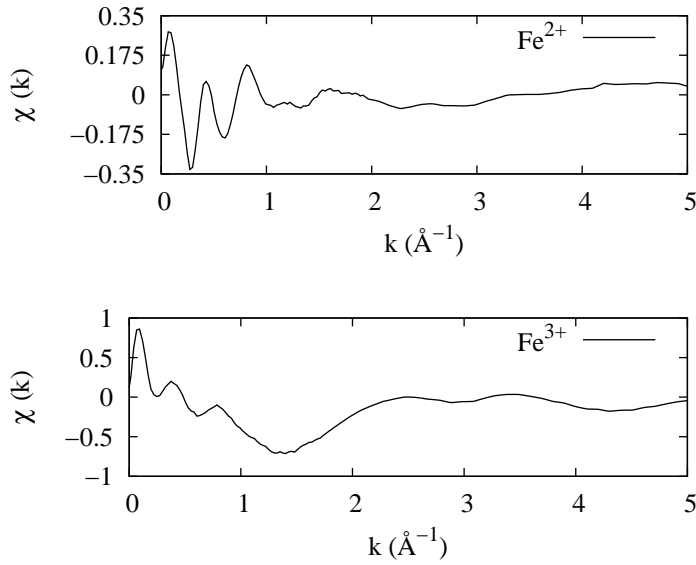
Figure 4.1: The difference between the refined imaginary part of the anomalous scattering factor for (a) $Fe^{2+}$ and (b) $Fe^{3+}$ and the CL-values ($\chi$) plotted as function of photoelectron wavenumber.

was calculated from the anomalous scattering factor corresponds to the XANES region.

Within the XANES region the photoelectron interacts strongly with the ion cores and electron density of the material and multiple scattering plays a dominant role. The observed oscillations are not simply a result of the geometric arrangement of neighbouring atoms and as such the maxima in the Fourier transform do not correspond only to the interatomic spacings as is the case in the XAFS region. Rather, these contributions from multiple scattering must be modelled in order to understand $\chi(k)$ and its Fourier transform over this energy range. Furthermore, $\chi(k)$ is weighted by the photoelectron wavenumber during the Fourier transform process and a plot of $k\chi(k)$ for each site is provided as Figure 4.2. The oscillations reduce rapidly in Figure 4.1; however, as shown here the deviations from zero at high $k$ contribute significantly to the Fourier transform. The lack of high energy data from the RXS experiment also produces a greater uncertainty in the slope of the anomalous scattering factor prior to the subtraction of the Cromer-Lieberman values. A number of different subtractions were shown to result in what appeared to be slightly different $\chi(k)$ functions, yet due to the weighting shown in Figure 4.2 had a dramatic impact on the Fourier transform.

Further experimental work is required before meaningful results can be obtained from the direct Fourier transform of the anomalous scattering factors due
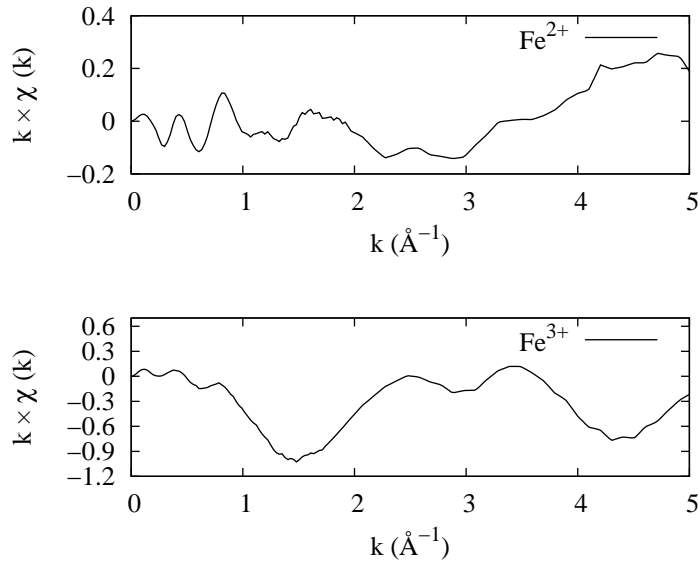
Figure 4.2: The $\chi(k)$ function for (a) $Fe^{2+}$ and (b) $Fe^{3+}$ weighted by the photoelectron wavenumber.

to the contributions from multiple scattering and the uncertainty introduced by the lack of high energy data.

## 4.3 Calculation refinement and analysis

XANES calculations were performed using the FEFF8 [121] and FDMNES [120] programs. The results for the Greens function muffin-tin calculations of both programs were found to be very similar, so the discussion presented here focuses on the results obtained from FDMNES.

The Fe in $LuFe_2O_4$ has a coordination number of 5 with three oxygen atoms located in the *ab*-plane and one above and one below along the *c*-axis. It might be expected that the Fe occupied a site at the centre of the bipyramid of which the O atoms form the vertices, yet the structural determination reported in the literature [22] indicated that in each bilayer the Fe of one layer sits above the plane occupied by the oxygen and in the other layer they sit below the plane such that the Fe-Fe distance is maximised.

The XANES spectra for both molecular and periodic systems may be investigated with FDMNES. The value of the Fermi energy plays an important role as it determines the level at which the electronic occupancy is not full and transi-

tions are allowed. The code implements a self consistent method to determine the Fermi level whereby convergence is sought over a number of iterations which may be enabled in the input file with the keyword "SCF", or alternatively skipped with the keyword "No_fermi". Omitting both of these keywords causes the program to perform a single iteration. These three scenerios are investigated in addition to the charge and geometric order of the Fe-sites.

Initially, the XANES spectra for different electronic and structural configurations of an $FeO_5$ molecule were investigated. The calculations were performed with a cluster radius of 5 Å and quadrupole scattering was considered in addition to the dipole interaction.

A series of calculations was performed where the charge on the Fe site was increased by shifting electrons from the $3d$ orbitals into the $4p$ orbitals. The resulting series is shown in Figure 4.3 where a single step of the self consistent method was performed, in Figure 4.4 where the calculation of the Fermi level was skipped, and in Figure 4.5 where the Fermi level was determined by convergence over many iterations.

In the first case, a progressive shift to lower energy is observed with increasing charge state and a steady increase in the intensity of the pre-edge feature. In the final case a dramatic increase in the intensity of the peak is observed which is inconsistent with the other calculations as a continuous increase is expected. Due to the single step of the SCF-process performed in these calculations the absolute electronic configuration at each stage is not necessarily related consistently to the other members of the series and this is the most likely cause of this effect. In the second case, where the calculation of the Fermi level was skipped, both a continuous shift to lower energy and an increase in the absorption peak are observed with increasing charge state. The progressive movement of charge from the $3d$ to $4p$ state leads to an increasing population of unoccupied $3d$ states just above the Fermi level and accordingly the intensity of the absorption peak just above the edge increases continuously. Finally in the third case the Fermi energy was determined by convergence over a number of cycles. The results are similar to the previous case with a gradual shift in the position of the edge until the high charge state where a different minimum is reached by the convergence process. The pre-edge feature shows the greatest variation in intensity, but no systematic behavior is observed.

The only series that demonstrated expected behavior was the series for which

Figure 4.3: XANES spectra calculated using FDMNES for an $FeO_5$ molecule where the Fe atom is progressively excited by moving electron density into the $4p$ orbitals. The Greens function method with the muffin-tin potential is shown and quadrupole contributions were included. A single step of the self consistent method was performed. The legend shows the number of electrons excited to the $4p$ state.



Figure 4.4: XANES spectra calculated using FDMNES for an $FeO_5$ molecule where the Fe atom is progressively excited by moving electron density into the $4p$ orbitals. The Greens function method with the muffin-tin potential is shown and quadrupole contributions were included. The calculation of the Fermi level was skipped. The legend shows the number of electrons excited to the $4p$ state.
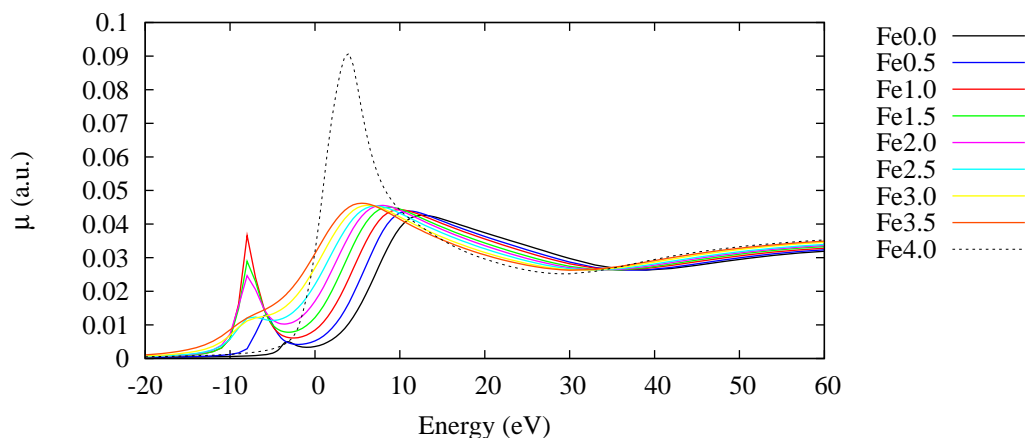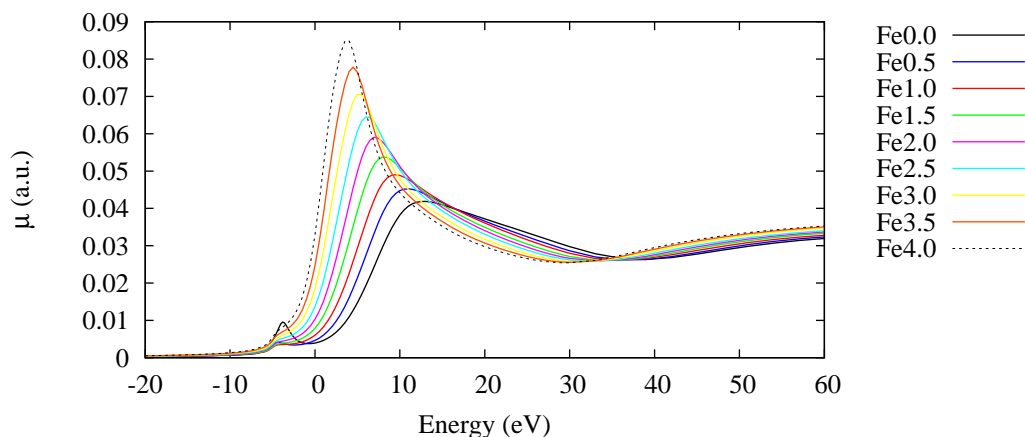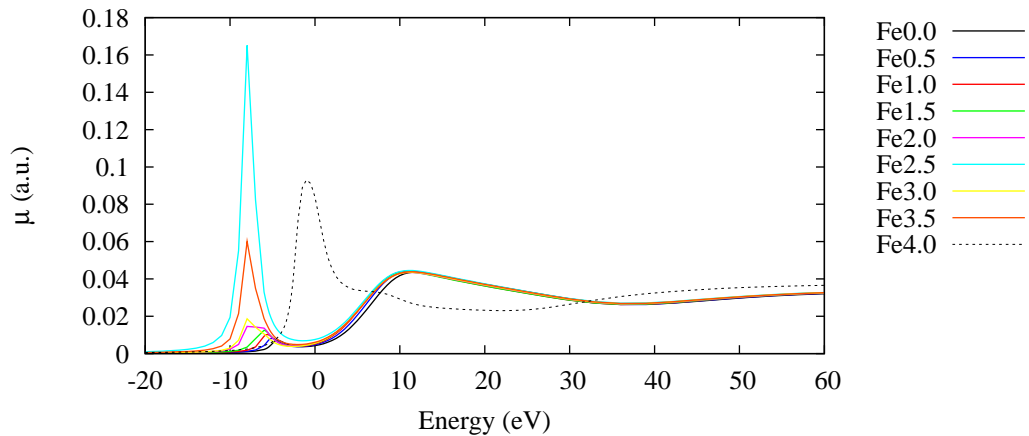
Figure 4.5: XANES spectra calculated using FDMNES for an $FeO_5$ molecule where the Fe atom is progressively excited by moving electron density into the $4p$ orbitals. The Greens function method with the muffin-tin potential is shown and quadrupole contributions were included. The self consistent iterative calculation of the Fermi level was turned on. The legend shows the number of electrons excited to the $4p$ state.

the calculation of the Fermi level was skipped. The self consistent process varies the electronic configuration in order to converge the system energy and as a result the relationship between the electronic configurations is the series also changes. Accordingly, these results demonstrate that the best option for the investigation of the charge state is to skip the initial calculation of the Fermi level.

The effect of isotropic expansion and contraction of the surrounding oxygen atoms was investigated. A neutral charge state ($Fe^0$) was used on the iron and the calculation of the Fermi level was skipped. The resulting XANES spectra are plotted in Figure 4.6. Qualitatively, expansion leads to a decrease in the intensity of the absorption peak and the XANES oscillations. Conversely, contraction leads to an increase in the intensity of the absorption peak and the oscillations are well defined. The absorption at 40 eV appears to be out of phase in the two cases.

Following the calculations of the $FeO_5$ molecule the known R$\bar{3}$m structure was investigated. For the previous calculations the radius of the $FeO_5$ cluster was chosen to be larger than the molecule itself, but due to the periodic nature of the crystal lattice the cluster radius was converged. Convergence series for radii between 2 and 8 Å are shown in Figures 4.7, 4.8, and 4.9 for the three Fermi level scenerios. Inspection of the three plots shows a similar trend that clusters with a radius greater than or equal to 4.5 Å share a similar profile. In the case where the calculation of the Fermi level was skipped and a single iteration of the self consistent method was run the spectra convergence is reached at 5 Å; however, the oscillations labelled *C* and *D* in Figure 3.9 are not reproduced. In the full
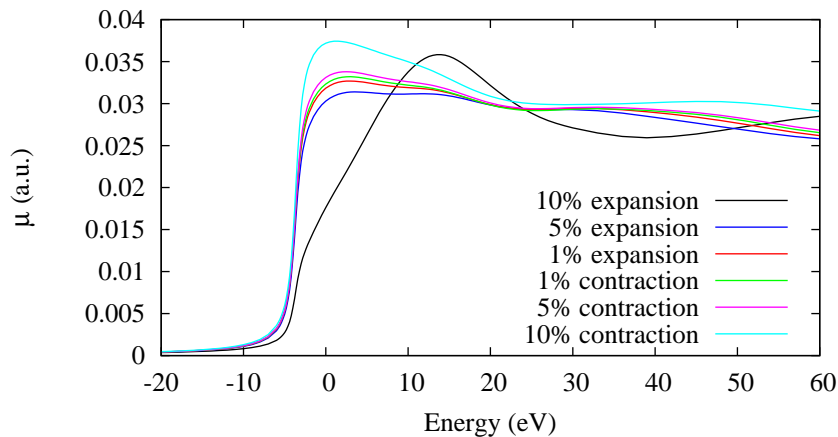
Figure 4.6: XANES spectra calculated using FDMNES for an $FeO_5$ molecule where the neighbouring oxygen cage has been contracted or expanded about its centre. The Greens function method with the muffin-tin potential is shown and quadrupole contributions were included.
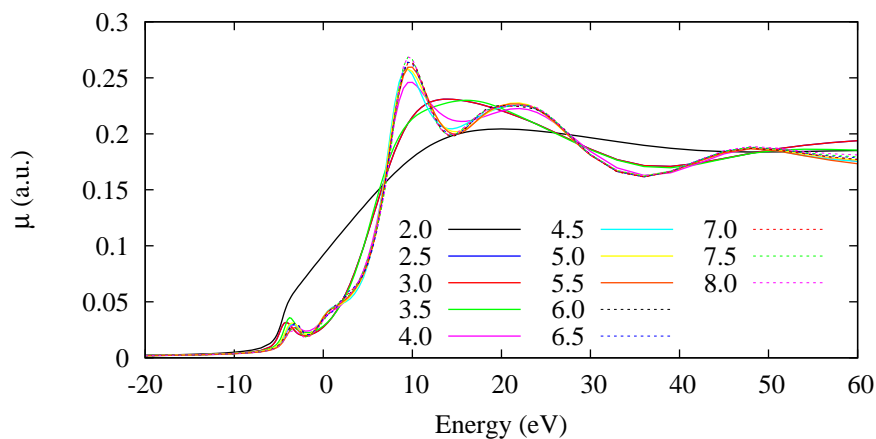


Figure 4.7: XANES spectra calculated using FDMNES for $R\bar{3}m$ structure of $LuFe_2O_4$ where the cluster size is progressively increased; the radius is shown in the legend in Å. The Greens function method with the muffin-tin potential is shown and quadrupole contributions were included. A single iteration of the self consistent method was run.
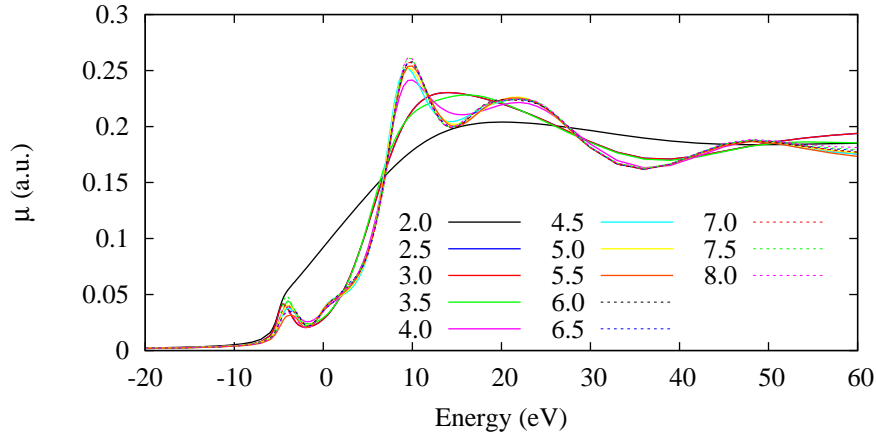
Figure 4.8: XANES spectra calculated using FDMNES for $R\bar{3}m$ structure of $LuFe_2O_4$ where the cluster size is progressively increased; the radius is shown in the legend in Å. The Greens function method with the muffin-tin potential is shown and quadrupole contributions were included. The calculation of the Fermi level was skipped.



Figure 4.9: XANES spectra calculated using FDMNES for $R\bar{3}m$ structure of $LuFe_2O_4$ where the cluster size is progressively increased; the radius is shown in the legend in Å. The Greens function method with the muffin-tin potential is shown and quadrupole contributions were included. The self consistent iterative calculation of the Fermi level was turned on.

SCF case convergence is not reached until 7 Å, but the energy dependence about 20 eV position has flattened out indicating that the unreproduced feature may be effected by the converged electronic structure calculation.

The effect of varying the charge state of the Fe-site was investigated for the $R\bar{3}m$ structure in the same way as described for the $FeO_5$ molecule with the calculation of the Fermi level skipped. The resulting series of XANES spectra is shown in Figure 4.10 where a continuous shift to lower energy and increase in the absorption peak is observed. As was the case with the $FeO_5$ molecule this trend can be explained by the increasing population of unoccupied $3d$ states with increasing charge state. Furthermore, the beginning of a splitting of the maximum at 20 eV is evident in the $Fe^{2.0}$ and $Fe^{3.0}$ spectra and the increased charge state appears to lead to a slight increase in the amplitude of the negative oscillation at 30 eV.

These calculations of the $R\bar{3}m$ structure have been based upon every Fe-site being occupied by the same iron species. Anisotropic charge order is known to be present and this distribution of charge states will be represented in the XANES pattern.

A P1 representation of the structure was constructed and $Fe^{2+}$ and $Fe^{3+}$-type sites were populated following the known charge order structure. A series of calculations were performed with the calculation of the Fermi level skipped where the charge disproportionation and absolute charge of the sites were varied. The results for the cases of $Fe^0/Fe^1$ and $Fe^{1.5}/Fe^{2/5}$ are shown as Figures 4.11 and 4.12 respectively. The sites labelled $Fe_1$ and $Fe_{12}$ correspond to $Fe^{3+}$-like sites in the $Fe^{2+}$-rich and $Fe^{3+}$-rich layers while the $Fe_2$ and $Fe_{10}$ sites correspond to $Fe^{2+}$-like sites in the $Fe^{3+}$-rich and $Fe^{2+}$-rich layers. A difference between each pair of sites is expected due to the differing local environments; however, in this case only the electronic configurations have been varied and negligible changes are observed. More significant changes are expected should anisotropic displacement of the oxygen sites be included as these will differ based upon the population of $Fe^{2+}/Fe^{3+}$ in the local environment. The observed variation in intensity and chemical shift is consistent with the series of calculations on the electronic configuration for the $R\bar{3}m$ and $FeO_5$ systems reported earlier.

Preliminary calculations of anisotropic displacements of the oxygen sublattice have been performed and have an effect on the absorption peak similar to that observed for expansion and contraction in the $FeO_5$ case. Minor changes in the
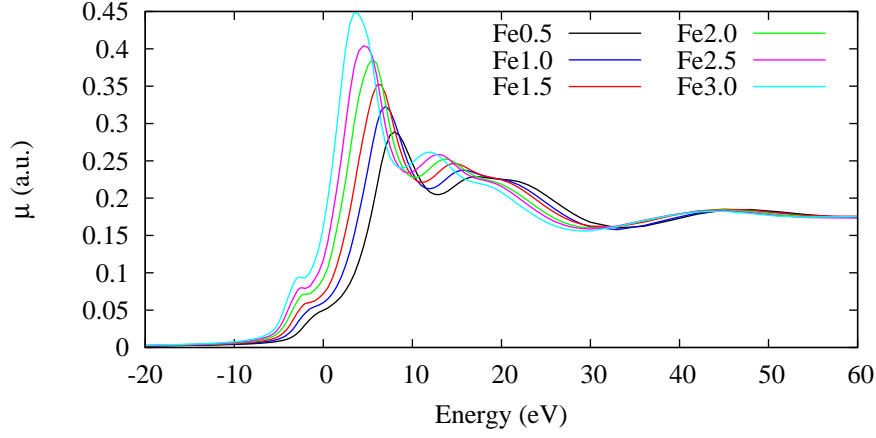
Figure 4.10: XANES spectra calculated using FDMNES for $R\bar{3}m$ structure of $LuFe_2O_4$ where the Fe atom is progressively excited by shifting electron density from the $3d$ to $4p$ states; the effective valence is shown in the legend. The Greens function method with the muffin-tin potential is shown and quadrupole contributions were included. The calculation of the Fermi level was skipped.
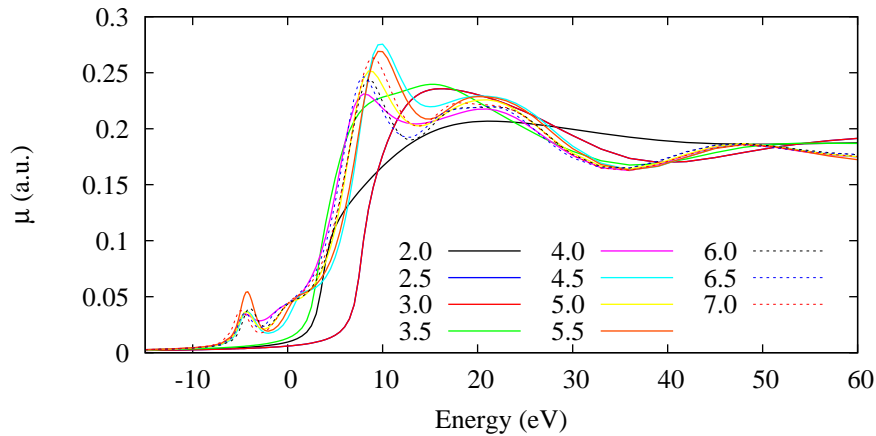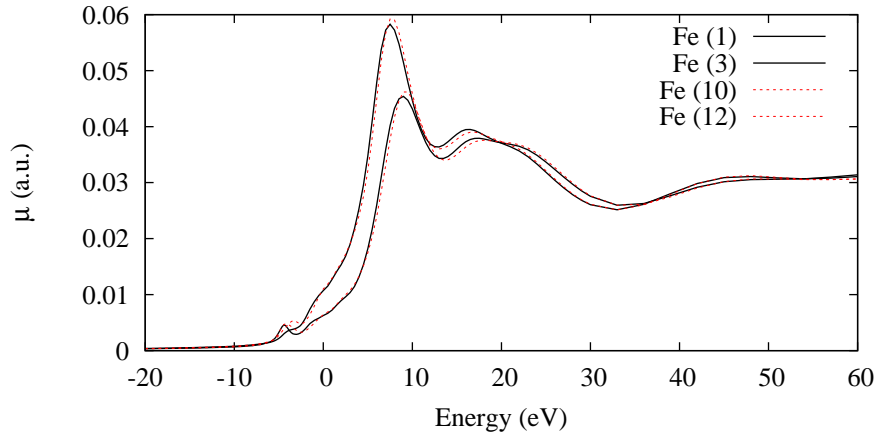


Figure 4.11: XANES spectra calculated using FDMNES for $R\bar{3}m$ structure of $LuFe_2O_4$ expressed in P1 where the Fe-sites have been populated with different charge states as described by the known anisotropic charge order. The Fe sites were populated by $Fe^0/Fe^{1.0}$ electronic configurations respectively. The Greens function method with the muffin-tin potential is shown and quadrupole contributions were included. The calculation of the Fermi level was skipped.
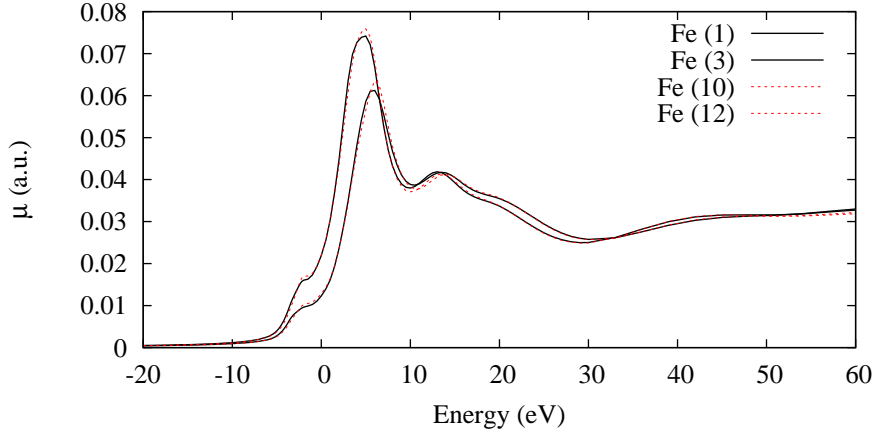
Figure 4.12: XANES spectra calculated using FDMNES for $R\bar{3}m$ structure of $LuFe_2O_4$ expressed in P1 where the Fe-sites have been populated with different charge states as described by the known anisotropic charge order. The Fe sites were populated by $Fe^{1.5}/Fe^{2.5}$ electronic configurations respectively. The Greens function method with the muffin-tin potential is shown and quadrupole contributions were included. The calculation of the Fermi level was skipped.

energy profile are also observed, but they are much smaller than the variation shown in Figure 4.6. The effect of dilation of the oxygen electron density and contraction of the iron density has been investigated, but no clear results have been noted thus far.

The differences between the $Fe^{2+}$ and $Fe^{3+}$ anomalous scattering factors reported in Chapter 3 are supported by these calculations, but further calculations combining the Fe charge, oxygen displacements, and dilation of the electron densities are proposed for the P1 charge ordered configuration in order to reproduce the amplitude of the observed energy dependence.

## 4.4 Discussion & Summary

The aim of these calculations has been to reproduce the energy dependence obtained from the experimental work reported in Chapter 3. The charge series presented in the previous section demonstrate an increase in the intensity of the absorption peak with increasing charge state, which is consistent with the intensity difference between the $Fe^{3+}$ and $Fe^{2+}$ anomalous scattering functions obtained experimentally. However, experimentally the $Fe^{3+}$ edge appears at higher energy while it appears at lower energy in the calculated series.

FDMNES reports its calculations relative to the Fermi level and as the charge state increases previously occupied states become unoccupied and the Fermi energy accordingly decreases. This effect is observed in the calculations presented in the previous section. On the other hand, the chemical shift observed experimentally is due primarily to the increase in the ionisation energy of the ion in the different valence states. It requires more energy to ionise the 1s electron in $Fe^{3+}$ than $Fe^{2+}$ and the edges vary in energy accordingly. Therefore, a relative shift has been applied to the FDMNES calculations in order to compare the shape of the experimentally derived functions with those calculated.

The results presented in the previous section were convoluted by the default function of the program. Examination of the transition probabilities prior to convolution shows that features $C$ and $D$ are reproduced, but are not resolved in the spectra due to the broadening. The width of the broadening as a function of energy was limited significantly and the resulting functions were transformed into anomalous scattering factors and are plotted along with the experimentally determined values in Figures 4.13 and 4.14. The absolute position of the calculated edges was determined such that the corresponding functions matched phase.

The energy dependence of features $B$, $D$, and $E$ match between the functions, but the magnitude of the oscillations do not match. Furthermore, the pre-edge feature $A$ observed experimentally is not reproduced in the calculation and the feature $C$ appears at higher energy in the calculation. The corresponding real part of the anomalous scattering factor was calculated by the Kramers-Kronig transformation and the functions fitted to the experimental data as shown in Figure 4.15.

The fitting is not as good as obtained for the experimentally determined functions, but this is expected as the magnitude of the oscillations was not reproduced. For every reflection shown each energy dependent feature is in phase with the fit. Given that for a purely charge ordered system the phase of the oscillations is a direct result of the interference of the anomalous scattering functions, the reproduction of the phase as shown in Figure 4.15 demonstrates that the data is well represented by the simple charge order model fitted here. As outlined in the previous section, it is expected that further calculations introducing oxygen displacements and other effects will improve the fitting further.
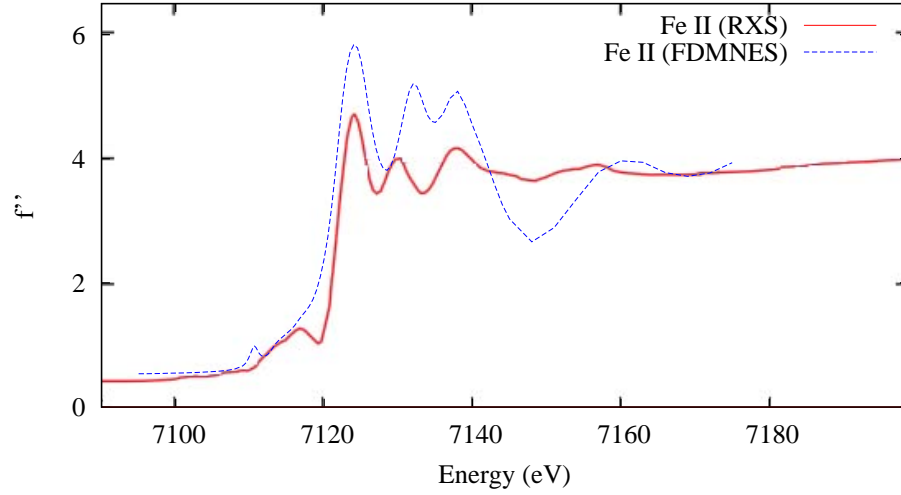
Figure 4.13: The imaginary part of the anomalous scattering factor of $Fe^{2+}$ obtained from the FDMNES calculations (solid) and the RXS experimental work (dashed).
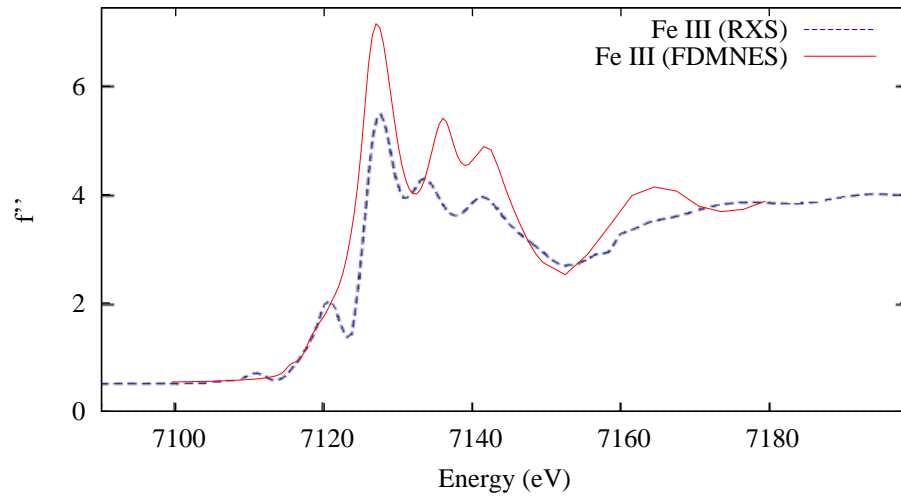
Figure 4.14: The imaginary part of the anomalous scattering factor of $Fe^{3+}$ obtained from the FDMNES calculations (solid) and the RXS experimental work (dashed).
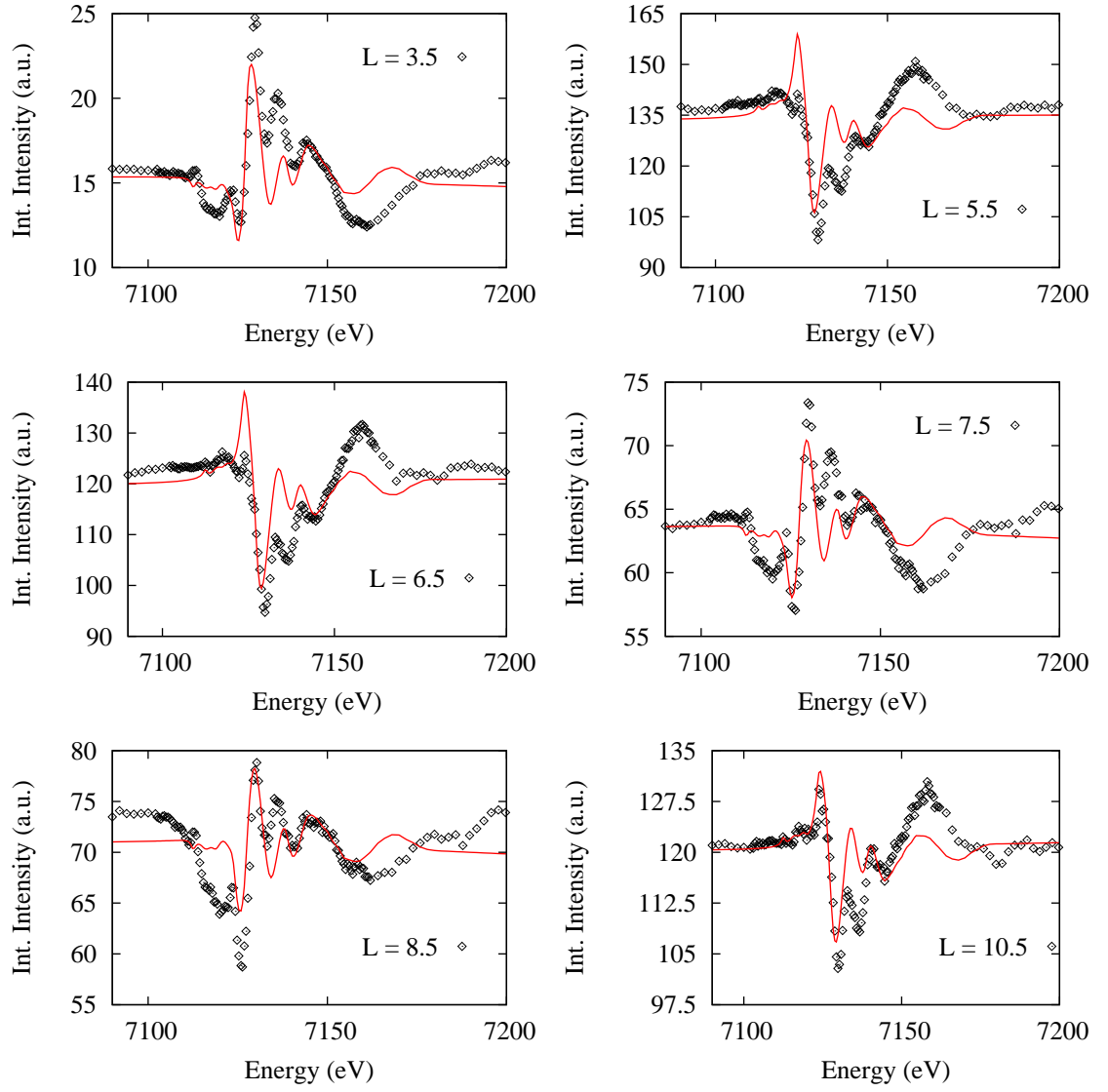
Figure 4.15: Fit following the same procedure as described in Chapter 3 of the anomalous scattering factors obtained from the FDMNES calculations.

Understanding the charge order in $LuFe_2O_4$ is important in order to characterise the ferroelectric component of the multiferroic behaviour of this material; however, direct measurements of the magnetic state are required in order to understand the overall picture. Elastic and inelastic neutron scattering experiments have been performed in order to investigate ferroelectric mode softening, magnetic excitations, and the magnetoelectric coupling in $LuFe_2O_4$ and these results are presented in Chapters 5 and 6.

# Chapter 5

# Inelastic Neutron Scattering

## 5.1 Introduction

The softening of phonon modes is characteristic of a ferroelectric transition as the polarised state stabilises the associated lattice distortions. Furthermore, the transition to a magnetically ordered state is accompanied by critical behaviour which is characterised by the divergence of magnetic correlation length and spin fluctuations. Investigating mode softening and critical magnetic behaviour allows the ferroelectric and ferrimagnetic ordered states of $LuFe_2O_4$ to be better understood.

Inelastic neutron scattering is sensitive to lattice excitations such as phonons and magnons, as well as spin diffusion processes. The energy change ($E$) of the neutron due to its interaction is measured allowing the mapping of the $E$-$\mathbf{Q}$ dispersion corresponding to these processes.

As introduced in Section 1.5, $LuFe_2O_4$ is ferroelectric below 330 K and simultaneously ferrimagnetic below 240 K. A preliminary investigation of phonon dispersion through the ferroelectric ordering temperature and the temperature dependence of ordering fluctuations about the superstructure propagation vector from 30 to 400 K is reported in this chapter.

A brief overview of the experiment is provided in Section 5.2 followed by the data reduction and results in Section 5.3. The discussion of these results is

provided in Section 5.4.

## 5.2   Experimental

A single crystal ingot of $LuFe_2O_4$ was aligned with the $(1\,0\,0)$ and $(0\,1\,0)$ crystallo-graphic directions in the scattering plane on the PUMA Triple Axis Spectrometer at the Helmholtz Zentrum Berlin. The crystal was mounted inside a liquid helium cryostat which was then pressurised with He gas. The flow of liquid He and internal cavity pressure were adjusted to regulate the system temperature. Vertical collimation was chosen in order to maximise the resolution in the *ab*-plane.

Both energy loss and **Q** scans were collected to map out portions of *E*-**Q** space. The temperature dependence of observed phonon dispersion was measured about the ferroelectric transition temperature, and the energy loss and **Q** profiles of diffuse inelastic scattering about the superstructure propagation vector were measured from 30 to 400 K.

The sample used in this experiment was previously shown to be a single crystal by neutron scattering experiments performed by collaborators.

## 5.3   Reduction

The data were provided in ASCII text pre-calibrated in reciprocal space based upon the sample alignment. These files were readily read into SCILAB where preliminary processing was performed. Profile fitting was carried out with custom routines in SCILAB in addition to GNUPLOT using the built-in `voigt` function. As introduced in 2.4.4 the resolution function of the instrument plays an important role in the interpretation of inelastic neutron scattering results. Resolution limited data restricts the analysis, especially in the case of the study of critical phenomena where the peak width in **Q**-space is proportional to the inverse correlation length which must become less than the resolution function as the temperature approaches the magnetic transition temperature. Thus it is critical to deconvolute the resolution function from the measured spectra before drawing quantitative conclusions from the data, and it is important to understand how the resolution function limits qualitative conclusions drawn from uncorrected data.

A quantitative evaluation of the resolution function was not available for the processing of this data, therefore a qualitative analysis of measured temperature dependence is discussed is the following section.

## 5.3.1  Analysis

The $(1\,1\,0)$ dispersion was investigated by collecting energy scans taken at fixed values of $\mathbf{Q}$ between $(1\,1\,0)$ and $(2\,0\,0)$ at both 300 and 400 K. The scans collected at 300 K have been plotted together in Figure 5.1 mapping the $(1\,1\,0)$ dispersion in the $[1\,\text{-}1\,0]$ direction. The plot shows the characteristic shape of the dispersion which appears to be symmetric about the $(1.5\,0.5\,0)$ position with strong elastic signals at both the $(1\,1\,0)$ and $(2\,0\,0)$ positions. Figure 5.2 shows the energy loss cross-section of the dispersion at both temperatures demonstrating no mode softening is observed through the ferroelectric transition temperature as it is only the intensity rather than the curvature of the mode that changes with temperature. The $(2\,0\,0)$ reflection is forbidden by the trigonal symmetry, so the presence of the intensity about the $(2\,0\,0)$ at both 300 and 400 K is not explained by known structural models.

During the experiment, a diffuse inelastic feature around the $\left(\frac{1}{3}\,\frac{1}{3}\,0\right)$-type positions was observed, and the $(1\,1\,0)$ dispersion was mapped in the $[1\,\text{-}2\,0]$ direction in order to observe this feature. This region of $E$-$\mathbf{Q}$ space was mapped at both 300 and 400 K and these maps are provided in Figure 5.3 and Figure 5.4 respectively. The peak profiles of energy loss scans at $\mathbf{Q} = (1.35\,0.3\,0)$ were investigated as a function of temperature, and energy scans as a function of temperature are shown in Figure 5.5. The intensity and $E$-extent of the feature vary, and are at their maximum values in the 240, 255, and 270 K energy loss profiles. An asymmetry about the transition temperature may be noted at this point, as the 150 and 400 K datasets have the same profile.

The energy scans were fitted with a fixed linear background, determined from the high energy loss data of the high temperature scans; a Gaussian profile, fixed at zero energy loss with variable intensity and width; a Lorentzian profile, fixed at zero energy loss with variable intensity and peak width; and Gaussian profiles to fit any excitations ($E \neq 0$) that were observed. A single Gaussian, Lorentzian, or Voigt profile was tested across the temperature range and it was unable to adequately fit the zer-centred spectral profile. As only the tails of these
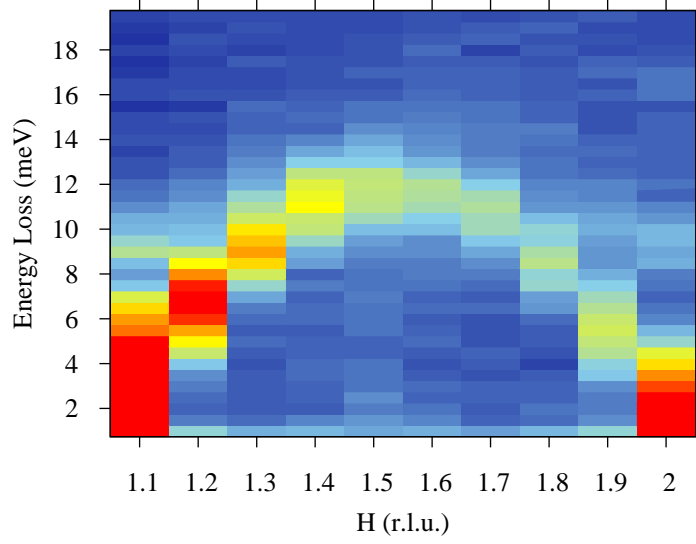
Figure 5.1: $(1\,1\,0)$ dispersion mapped in the $[1\text{-}1\,0]$ direction at 300 K.
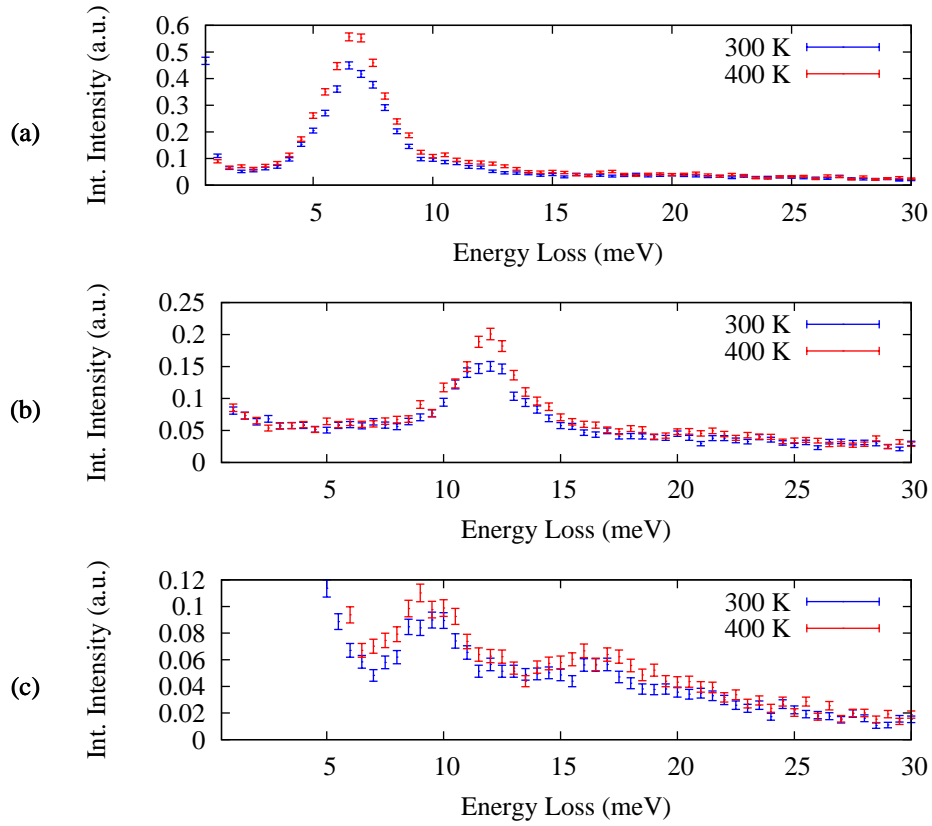


Figure 5.2: Selected energy scans of the $(1\,1\,0)$ dispersion in the $[1\text{-}1\,0]$ direction at both 300 and 400 K. (a) $\mathbf{Q} = (1.2\,0.8\,0)$, (b) $\mathbf{Q} = (1.5\,0.5\,0)$, and (c) $\mathbf{Q} = (2.0\,0.0\,0)$.
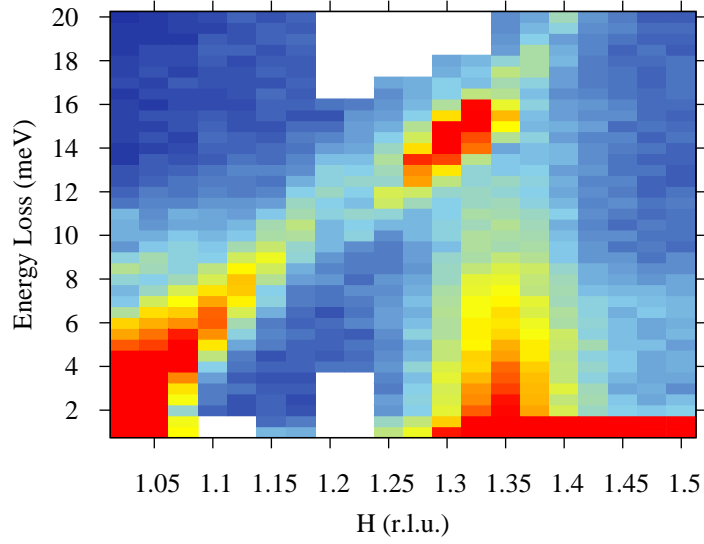
Figure 5.3: $(1\,1\,0)$ dispersion mapped in the $[1\,\text{-}2\,0]$ direction at 300 K. A diffuse feature is noted about the $\left(\frac{4}{3}\,\frac{1}{3}\,0\right)$ position.
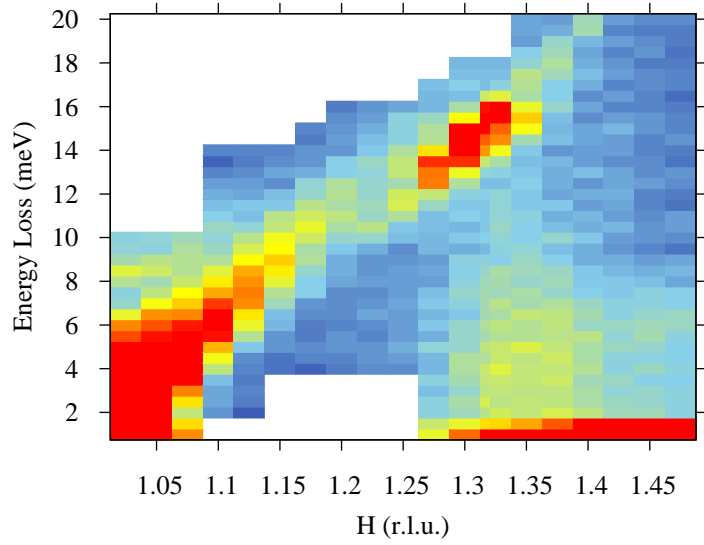


Figure 5.4: $(1\,1\,0)$ dispersion mapped in the $[1\,\text{-}2\,0]$ direction at 400 K. The diffuse feature about $\left(\frac{4}{3}\,\frac{1}{3}\,0\right)$ is weaker at this temperature when compared to Figure 5.3.
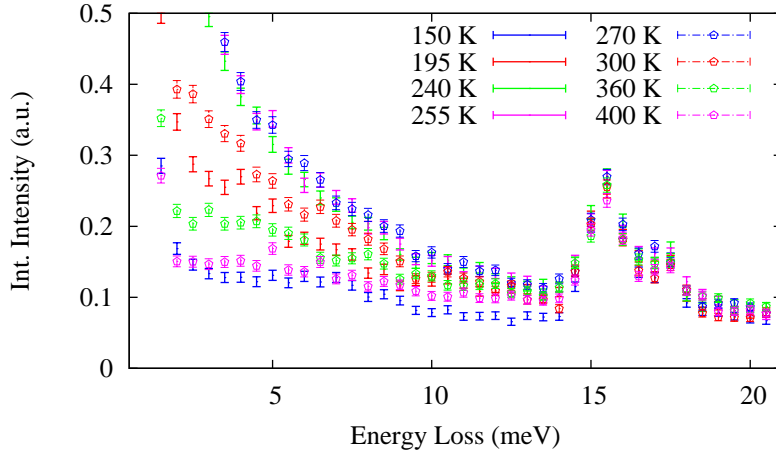
Figure 5.5: Selected energy loss scans taken at $(1.35\,0.3\,0)$ as a function of temperature. The diffuse feature shown in Figures 5.3 and 5.4 is a tail that has a maximum intensity at about 255 K.

peaks have been measured the FWHM and peak height are not "well-behaved" fitting parameters with poor absolute reproducibility; rather, it is the integrated intensity of the profile that is reproducible. The scattering function, $S(\mathbf{Q} = (1.35\,0.3\,0))$, is the integrated area of the energy profile from $E = -\infty \to +\infty$, which is proportional to the sum of the integrated areas of the fitted profiles. The temperature dependence of this integrated intensity is shown in Figure 5.6 where it is observed that the intensity passes through a maximum at the known Néel temperature.

The previously observed asymmetry between the low temperature and high temperature energy profiles shown in Figure 5.5 is further evident in the integrated intensity, indicating significant fluctuations are present in the high temperature ferroelectric phase. The $\left(\frac{1}{3}\,\frac{1}{3}\,0\right)$ reflection is a known magnetic Bragg peak; however, the x-ray scattering results discussed in Chapters 3 and 7 demonstrate the absence of $\left(\frac{1}{3}\,\frac{1}{3}\,0\right)$ satellites in the ferroelectric phase for this sample. Rather, the observation of significant high temperature fluctuations coupled with the previous observation of the $(2\,0\,0)$ (which is also unobserved in other diffraction work) indicates poor $c$-axis resolution and that a portion of the $c^*$-axis is integrated in the observed signal. Accordingly the $(2\,0\,0)$ reflection may be accounted for by the $\left(2\,0\,\bar{1}\right)$ reflection and the Bragg intensity at the $\left(\frac{1}{3}\,\frac{1}{3}\,0\right)$ position results from the sum of the $\left(\frac{1}{3}\,\frac{1}{3}\,0\right)$ and $\left(\frac{1}{3}\,\frac{1}{3}\,\frac{3}{2}\right)$ magnetic reflections and the $\left(\frac{1}{3}\,\frac{1}{3}\,L\right)$ diffuse rod and $\left(\frac{1}{3}+\delta\,\frac{1}{3}+\delta\,\frac{3}{2}\right)$ incommensurate satellites corresponding to the structural distortions of the ferroelectric order. The measurement of both the magnetic and ferroelectric order accounts for the observed asymmetry in the temperature dependence.
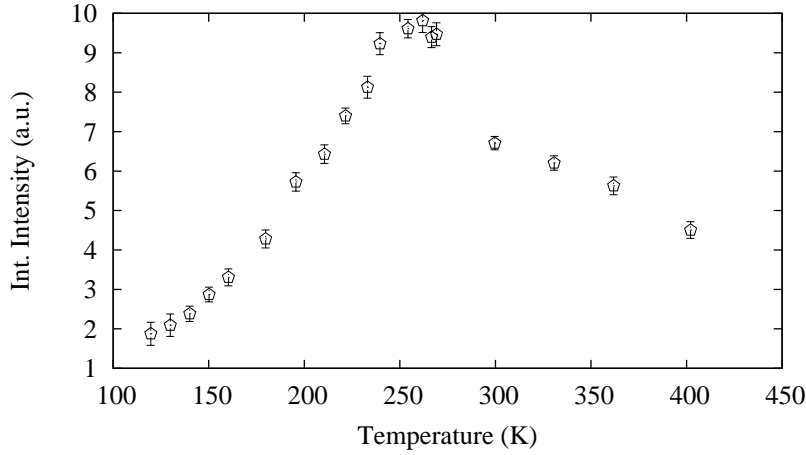
Figure 5.6: Temperature dependence of the integrated intensity which is proportional to $S(\mathbf{Q} = (1.35\,0.3\,0))$.

Through a magnetic transition as $T \to T_C$ (where $T_C$ is the magnetic transition temperature) fluctuations where $\mathbf{Q}$ is the propagation vector of the magnetic ordering dominate and the susceptibility of the ordering field diverges logarithmically about $T_C$. The exponent of this divergence is a critical exponent of the system which describes the universality class of the material. Such behaviour is expected when the correlation length is much longer than the lattice spacing which may be considered to be when the magnitude of the reduced temperature is less than 0.05 for a 3D magnetic system, and less than 0.3 for a 2D system [129]. It can be shown that the scattering function, $S(\mathbf{Q})$, is proportional to this susceptibility through the transition [129, 130] and as LuFe$_2$O$_4$ is a 2D frustrated ferrimagnetic Ising system with spins aligned parallel to the $c$-axis, the observed intensity (which is proportional to $S(\mathbf{Q})$ ) may be expected to diverge logarithmically between approximately 175 K and 325 K. However, a logarithmic divergence is not observed in Figure 5.6; rather, a broad maximum at the magnetic transition is seen. LuFe$_2$O$_4$ is known to be non-stoichiometric with respect to the oxygen content, and the range of oxygen stoichiometries in the sample would produce a distribution of magnetic transition temperatures. Accordingly, this population distribution when convoluted with logarithmic critical divergence would broaden the temperature dependence and produce the observed maximum. The convolution of the temperature dependence of the ferroelectric fluctuactions would also limit the observation of the critical divergence, therefore further experiments with better vertical resolution are required to study this further.

## 5.4 Discussion & Summary

The broadening of the critical divergence observed in this work is supported by a distribution of magnetic transition temperatures resulting from the non-stoichiometry and distribution of oxygen content in the sample; furthermore, the maximum at 250 K is consistent with the Néel temperature. Both the ferroelectric structural modulation and the magnetic ordering are described by satellites and diffuse scattering along the $\left(\frac{1}{3}\,\frac{1}{3}\,L\right)$-type scattering rods and contributions from both the structural distortions and spin ordering are evident in the asymmetry and broadening of the energy loss profiles with strong scattering above the magnetic transition temperature.

During the alignment of the sample the $(1\,1\,0)$ and $(1\,\text{-}1\,0)$ reflections were both observed; however the $(1\,\text{-}1\,0)$ reflection is forbidden. As the *c*-axis unit cell length is 25.28 Å and the instrument was setup for good resolution in the *ab*-plane it is believed that during this experiment the out-of-plane resolution was insufficient and the observed intensity is integrated along at least one unit cell in the $c^*$-direction. This is consistent with the observation of dispersion about the forbidden $(2\,0\,0)$ discussed in the previous section.

This work has shown the temperature dependence the fluctuations in $\text{LuFe}_2\text{O}_4$ is affected by oxygen stoichiometry, and confirmed the Néel point for this sample as 250 K. Further measurements to investigate the full temperature dependence of these features using polarised neutrons at a cold neutron source is proposed, as this would allow the ferroelectric and ferrimagnetic contributions to be separated and provide better out-of-plane resolution. This would also allow the possible stoichiometric effect to be separated from the resolution effect discussed in this chapter.

The multiferroic coupling in $\text{LuFe}_2\text{O}_4$ has been demonstrated by the step in the pyroelectric current reported in the literature [83] which has been measured at approximately 210 K for this sample; however, this does not correspond to the Néel temperature measured in this chapter and also observed in linear susceptibility measurements. Rather, a correspondence with a peak in the linear susceptibility is observed. The nature of the magnetic ordering in this sample has been investigated by elastic neutron scattering and an applied electric field study by magnetic neutron diffraction is reported in Chapter 6.

# Chapter 6

# Single crystal neutron scattering

## 6.1  Introduction

The ferroelectric and ferrimagnetic structures of $LuFe_2O_4$ are complex, as introduced in Sections 1.5.2 and 1.5.3, and these two properties are closely intertwined as they arise from the same lattice sites. As discussed previously, the temperature dependent magnetisation increases rapidly (with decreasing temperature) below the Néel point until a maximum is reached and then a decrease is noted [52] in the zero field cooled case. A step-like increase in the ferroelectric polarisation is observed with a point of inflection below the Néel temperature [83].

The linear susceptibility for the samples used in this thesis was previously collected by Narumi *et al.* and is shown in Figure 6.1. Furthermore, the temperature dependent pyroelectric current for this sample has been measured by Wang of the Hong Kong Polytechnic University after electric field cooling, and a portion of this data is reproduced in Figure 6.2. Comparison of these figures demonstrates that the maximum in the magnetisation occurs below the Néel point at approximately 215 K which coincides with the maximum in the pyroelectric current. The ferroelectric polarisation is the integrated pyroelectric current and as such the maximum observed in Figure 6.2 corresponds to the point of inflection in the step-like increase in the polarisation previously reported [83]. These results suggest that there is a correlation between these two features and indicates a magnetoelectric coupling associated with the peak in the magnetic susceptibility data.
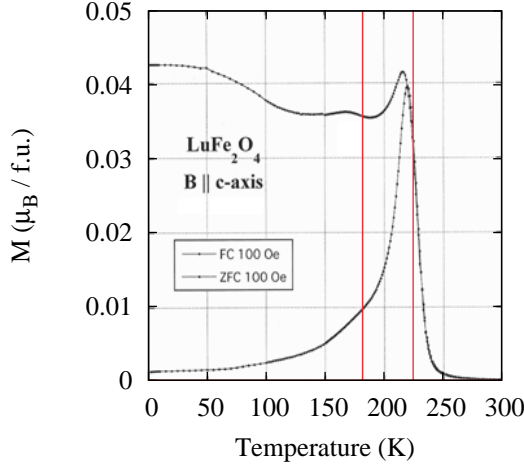
Figure 6.1: Field cooled and zero field cooled temperature dependent magnetisation of $LuFe_2O_4$ measured by Narumi *et al.* [131] on the samples studied in this work. Red lines are drawn to mark 180 and 225 K.
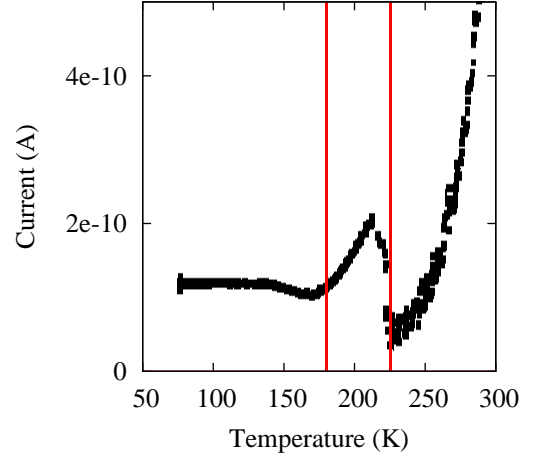
Figure 6.2: A section of the temperature dependent pyroelectric current of $LuFe_2O_4$ measured after electric field cooling; collected by Wang [132] on the samples studied in this work. Red lines are drawn to mark 180 and 225 K.

As reported by Wen *et al.* [105], magnetic-field control of charge order structures in $LuFe_2O_4$ has been demonstrated by magnetic field cooling through the ferroelectric transition temperature. In a similar fashion, electric control of the magnetic structure of $LuFe_2O_4$ has been investigated in this work by electric field cooling not only through the Néel temperature but also through the peak in the zero-field magnetisation data. Magnetic neutron diffraction is an ideal tool to perform this study, and an experimental investigation has been performed at the two temperatures (180 and 225 K) noted by vertical red lines in Figures 6.1 and 6.2.

An introduction to neutron scattering and elastic nuclear and magnetic thermal neutron diffraction was provided in Section 2.4 of Chapter 2; this material provides background for the work presented in this chapter. An outline of the experiment performed is provided in Section 6.2, data reduction and analysis are presented in Section 6.3, and finally the outcomes of this work are discussed in Section 6.4.

## 6.2 Experimental

A segment of the $LuFe_2O_4$ ingot from batch 1 was aligned with the (001) and (110) crystallographic directions of the R$\bar{3}$m structure aligned in the scattering plane on the E2 flat-cone diffractometer at the Helmholtz-Zentrum Berlin (HZB),

in Berlin, Germany. A sample environment was designed and produced at the facility, an outline of which is provided as Figure 6.3. The sample was mounted on the end of the cryostat sample stick between the two electric field plates before being installed into the cryostat. Due to the presence of a strong electric field the internal atmosphere of the cryostat was evacuated (normally it is pressurised with He gas as was done in chapter 5) and conduction from the liquid helium jacket through the sample rod was the primary method of heat transport. The cooling/heating gradient was controlled by adjusting the liquid helium flow and the power output from the heaters. The temperature was monitored by a Pt100 thermocouple mounted in the Teflon block; however, due to the experimental nature of the sample environment an intermediate data logger was not available and the thermocouple resistance was recorded and the temperature determined by use of the available calibration table. A wavelength of 2.39 A was selected based upon the intensity characteristics of the beamline and consideration of the $LuFe_2O_4$ cell parameters.

The sample was heated to 372 K prior to the electric field being switched on with a field strength of 4 kV/cm. The regulator was set to establish thermal equilibrium with the sample at 180 K. When the sample was approximately 235 K the electric field was switched off. The only sample degree of freedom utilised was the sample rotation about an axis perpendicular to the scattering place ($\psi$), while the scattering intensity was measured as a function of the $2\theta$ scattering angle using 4 large area detectors. The instrument-sample configuration is illustrated in Figure 6.4. Scripts were written to drive the sample rotation ($\psi$) and each of the detector positions to produce 3D reciprocal space maps of the $\left(\frac{1}{3}\ \frac{1}{3}\ L\right)$ and $\left(\frac{2}{3}\ \frac{2}{3}\ L\right)$ diffraction rods. Data were collected at first at 180 K and then at 220 K under instantaneous applied fields of $+8$ and $-2.8$ kV/cm after which the sample was electric field cooled back down to 180 K and reciprocal space maps collected without an applied field.

## 6.3   Reduction

Reciprocal space maps about the $\left(\frac{1}{3}\ \frac{1}{3}\ L\right)$ and $\left(\frac{2}{3}\ \frac{2}{3}\ L\right)$ diffraction rods were collected by the method outlined in Section 6.2 and TVNEXUS, the beamline-provided code, was utilised to perform preliminary analysis. As at December, 2008 this code was in constant development and the capability to transform only a selected area of reciprocal space, or alert the user to the presence of empty
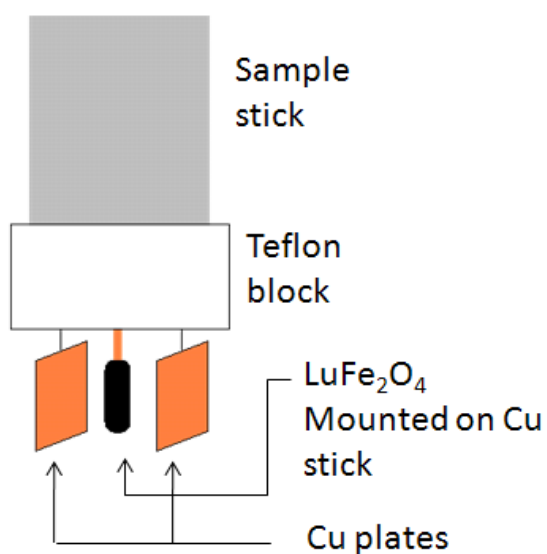
Figure 6.3: Illustration of the sample environment developed by Dr Kiefer and his team at the HZB for an experiment on the E2 instrument as described in text.
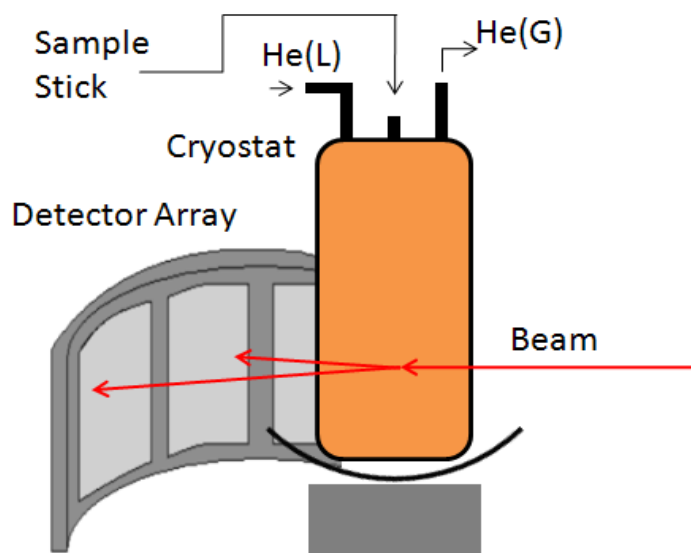


Figure 6.4: Illustration of the sample-instrument configuration utilised on the E2 instrument at the HZB; method described in text.

voxels during high resolution data binning was absent from the code.

The data files were output in the HDF5 file format and therefore the instrument parameters and 2D detector images were readily available. In an effort to address the limitations (as at January, 2009) of TVNexus, local code was written to transform and analyse the data. The computing facilities of iVEC, the Western Australian centre for high performance computing, were utilised in order to perform this analysis.

The SGI Altix located at the iVEC ARRC facility in Technology Park, Western Australia was used to convert coordinates from the raw instrumental space of the detector images into reciprocal space. Code was written and compiled on the supercomputer in C that used the Message Passing Interface (MPI) to take advantage of the processing power of the SGI Altix and divide the dataset up between multiple computing nodes. With a large amount of RAM available to the computing job, the algorithms were designed to convert the data with maximum flexibility to the user allowing specific regions of reciprocal space to be analysed.

A 4D vector, $(q_x, q_y, q_z, I)$, was computed for each detector pixel based upon instrument parameters. Due to the nature of the transformation these voxels are not distributed uniformly in reciprocal space and a 3D grid must be specified by the user. If the grid is defined at too high resolution then there will be elements of the grid in which no observations have been made. If a row or column of the dataset containing one or more of these empty voxels is integrated then the resulting value will be smaller than it should be, and it is impossible to mathematically correct for this; therefore, there is a limiting resolution at which the data can be binned. Each processor records the number of empty cells that it finds within the volume of data it is processing and reports this in the program output. The user must then reduce the number of voxels in the grid until every processor reports zero empty cells. This method ensures accurate integrated profiles are obtained.

Finally the code performs a monitor correction of the 4D dataset based upon histograms generated during the binning process. Assuming that each pixel covers the same solid angle then the integrated intensity of each bin is divided by the number of observations within that voxel. The 4D dataset is then written out in the data format as described in Appendix A. This code is referred to as HDFImport and the execution flow chart is presented in Figure A.1 in Appendix A.

A second program, STACKANALYSIS, was written to integrate this 4D data and output multiple formats that can be readily visualised. The execution flow chart is presented in Figure A.2 in Appendix A. A volume of the data indicated in the input file is integrated and the three XY, XZ and YZ 3D profiles are produced; the 2D profiles xXY, yXY, xXZ, zXZ, yYZ, and zYZ are then calculated from these 3D maps. A series of optional sub-volumes indicated in the input file may be processed in the same way. These profiles are written to disk in a file format as outlined in Appendix A.

These profiles may then be readily visualised by routines prepared for MAT-LAB or SCILAB, or converted into GNUPLOT compatible binary files. 2D and 3D data visualisation and profile fitting was performed using GNUPLOT.

### 6.3.1 Resolution Correction

The E2 flat cone diffractometer is primarily used to study phenomena where the integrated intensity is carefully studied. A result of this is that the instruments resolution function is not well known. Unfortunately no standard was available during the scope of this experiment; however, as noted in Chapter 8 the $LuFe_2O_4$ sample is as sharp as, if not sharper than the instruments $LaB_6$ sample used to calibrate the instrument function and the main structural Bragg peaks are resolution limited in that experiment.

Whilst it is not necessarily the case, in order to resolution correct the data presented in this chapter it has been assumed that the main structural Bragg reflections are also resolution limited - and they have been used in order to characterise the instrument function. The $(0\,0\,3),(0\,0\,6),(0\,0\,9)$ reflections have been fitted and used to determine an instrument correction. These reflections were selected as they have the same orientation as those under study with respect to the instrument optics.

### 6.3.2 Analysis

Each dataset was processed using HDFIMPORT and STACKANALYSIS programs. Regions of the collected reciprocal space volume were selected that had minimum background from the metallic copper used in the sample environment construc-

tion. Furthermore, the sample was found to contain multiple crystallites with some at similar orientations to the main crystallite aligned in the scattering plane. As neutron scattering is performed in transmission, diffracted intensity from every crystallite may be observed and the out-of-plane resolution provided by the 2D detector system was used to separate out the diffracted intensity from the crystallite of interest. A dataset processed with unconstrained axes is presented in Figure 6.5.

After electric field cooling from 370 to 235 K in an applied field of 4kV/cm, reciprocal space maps were collected at 225 K in zero field and *in situ* with applied fields of both polarity. The zero field 3D profile of the $\left(\frac{1}{3}\,\frac{1}{3}\,L\right)$ diffraction rod is plotted in Figure 6.6 and the profile along the *c*-axis in Figure 6.7. Inspection of the *c*-axis profile shows a few discrete peaks on a decaying background. The peak at $\left(\frac{1}{3}\,\frac{1}{3}\,2\right)$ is due to overlap of a Cu powder diffraction ring (from the Cu electrodes) with the diffracted signal from the sample. The other peaks are explained later.

The decaying background shown in Figure 6.7, the integrated $c^*$-profile, is found to be from a diffuse rod of scattering as shown in Figure 6.6 that is centred around the $\left(\frac{1}{3}\,\frac{1}{3}\,L\right)$ direction, as indicated by the $(H\,H\,0)$ integrated profile. As discussed in Section 1.5.2 the magnetic structure of $LuFe_2O_4$ is considered to be an Ising ferrimagnet with the spins oriented parallel to the c-axis and both 2D [48] and 3D [55] magnetic order have been previously observed (in separate cases). In the case of Ising 2D magnetic order the diffracted intensity of such order with no magnetic correlations along the c-axis can be modelled as shown in Equation 6.1. A fit of this model is shown by the red line in Figure 6.7. This function fits the diffuse scattering to within experimental error in agreement with the fitting of the 2D order previously reported [48].

$$\frac{I(\mathbf{Q})}{I_0} = KF(\mathbf{Q})^2(1 - Q_z^2) \tag{6.1}$$

where $I(\mathbf{Q})/I_0$ is the monitor corrected intensity, $K$ is a scaling constant, $F(\mathbf{Q})$ is the magnetic form factor, and $Q_z$ is the z-component of $\mathbf{Q}$.

Diffraction data were also collected at 180 K and the 3D profiles of the $\left(\frac{1}{3}\,\frac{1}{3}\,L\right)$ and $\left(\frac{2}{3}\,\frac{2}{3}\,L\right)$ at this temperature after EFC to 235 K is shown in Figures 6.8 and 6.9. Inspection of Figure 6.8 indicates the data is centred about the $\left(\frac{1}{3}\,\frac{1}{3}\,L\right)$ direction, and the (0 0 L) profile shows a series of discrete diffraction peaks correspond to the $\left(\frac{1}{3}\,\frac{1}{3}\,0\right)$- and $\left(\frac{1}{3}\,\frac{1}{3}\,\frac{1}{2}\right)$-type position reported in the
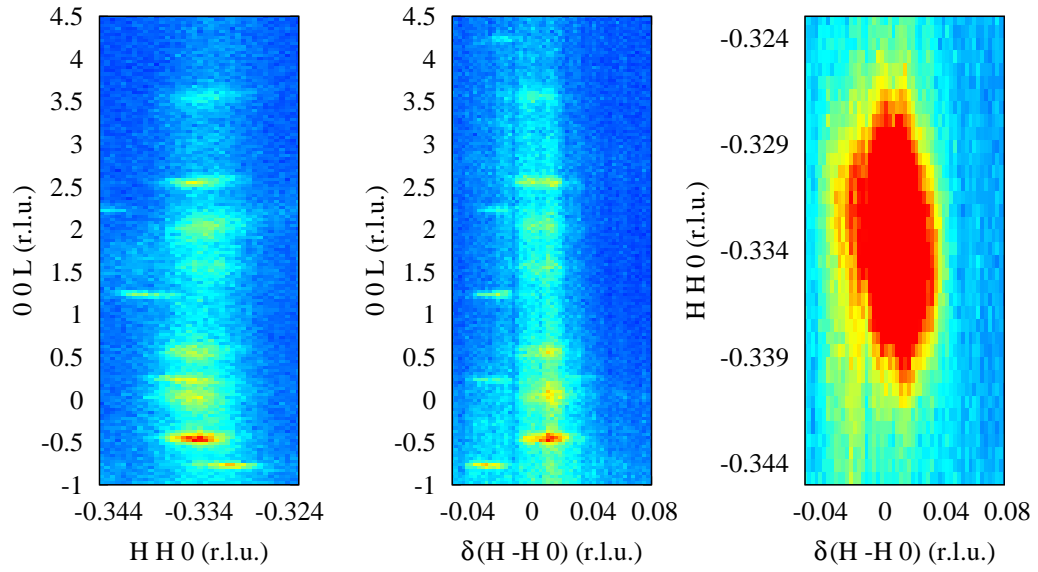
Figure 6.5: The (a) XY, (b) YZ, and (c) XZ integrated profiles of a dataset without limits on the reciprocal space volume collected.
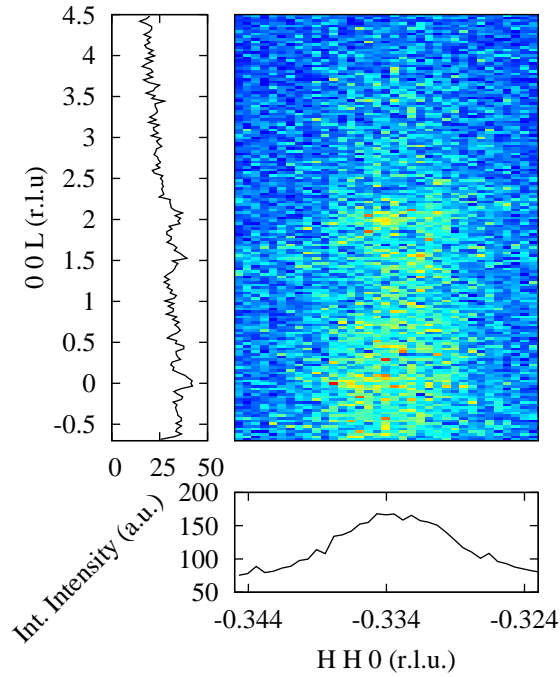


Figure 6.6: 3D profile of the $\left(\frac{1}{3}\ \frac{1}{3}\ L\right)$ rod at 225 K after EFC from 370 to 230 K in an applied field of 4 kV/cm.
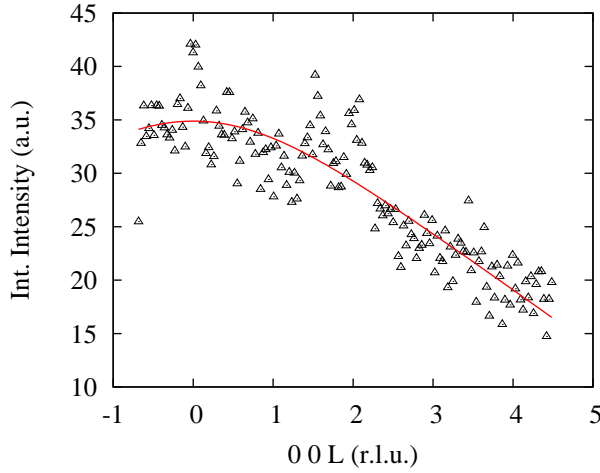
Figure 6.7: Integrated $c^*$-axis profile of the $\left(\frac{1}{3}\,\frac{1}{3}\,L\right)$ rod at 225 K after EFC from 370 to 230 K in an applied field of 4 kV/cm. The red line indicates a fit for a 2D magnetic model with no c-axis correlations, as described in text.

literature [55].

The non-stoichiometric nature of the oxygen content will lead to a distribution of magnetic transition temperatures within the sample and therefore the discrete peaks previously noted in the $c^*$-axis integrated profile shown in Figure 6.7 are attributed to the 3D ordering of a magnetic domain with a higher magnetic transition temperature than the bulk of the sample.

The effect of an applied electric field on the magnetic ordering process was investigated by collecting data after further electric field cooling from 225 to 180 K and also after heating the sample to 360 K and cooling to 180 K in zero field. For comparison the pixel maps of the $\left(\frac{1}{3}\,\frac{1}{3}\,L\right)$ are presented together in Figure 6.10 and the $\left(\frac{2}{3}\,\frac{2}{3}\,L\right)$ in Figure 6.11.

The side-by-side 3D plots of the reciprocal space maps collected after the differing electric field cooling procedures demonstrate that the electric field does have an effect on the magnetic structure of $LuFe_2O_4$ as differences in the satellite intensities are apparent. These differences may be quantified by examining and fitting the 2D integrated profile parallel to the $c^*$-axis. The integrated cross-sections were fitted with Gaussian profiles for the satellites and the diffuse rod was fit using the same uncorrelated 2D Ising model discussed previously and described by Equation 6.1. The profiles and fits of the two EFC situations (labelled "EFC I" and "EFC II") for the $\left(\frac{1}{3}\,\frac{1}{3}\,L\right)$ rod are shown in Figure 6.12 and the integrated intensity and FWHM ($\Gamma$) of each satellite summarised in Tables 6.1 and 6.2.
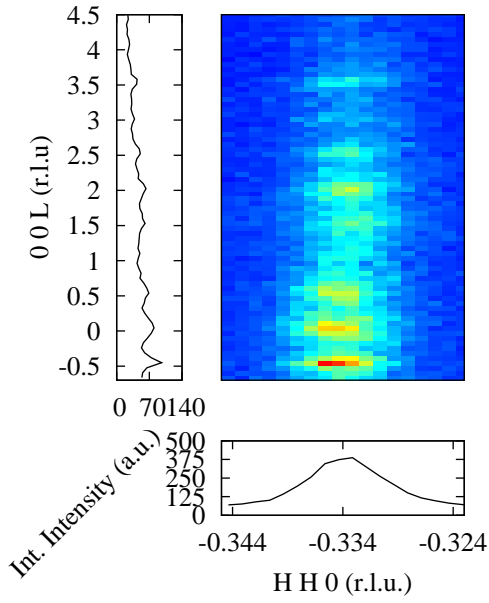
Figure 6.8: Reciprocal space map of the $\left(\frac{1}{3}\,\frac{1}{3}\,L\right)$ diffraction rod collected at 180 K after electric field cooling to 230 K.
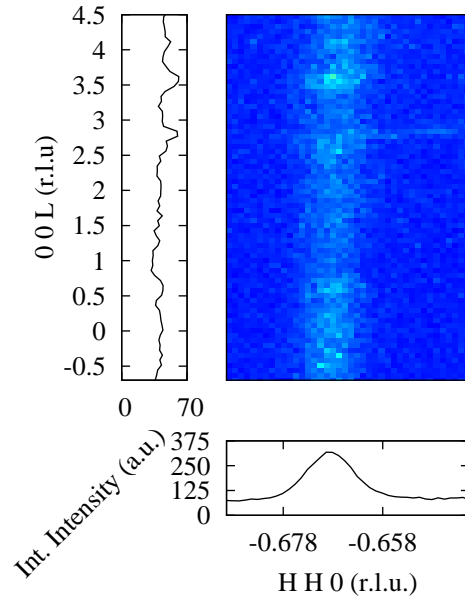
Figure 6.9: Reciprocal space map of the $\left(\frac{2}{3}\,\frac{2}{3}\,L\right)$ diffraction rod collected at 180 K after electric field cooling to 230 K.
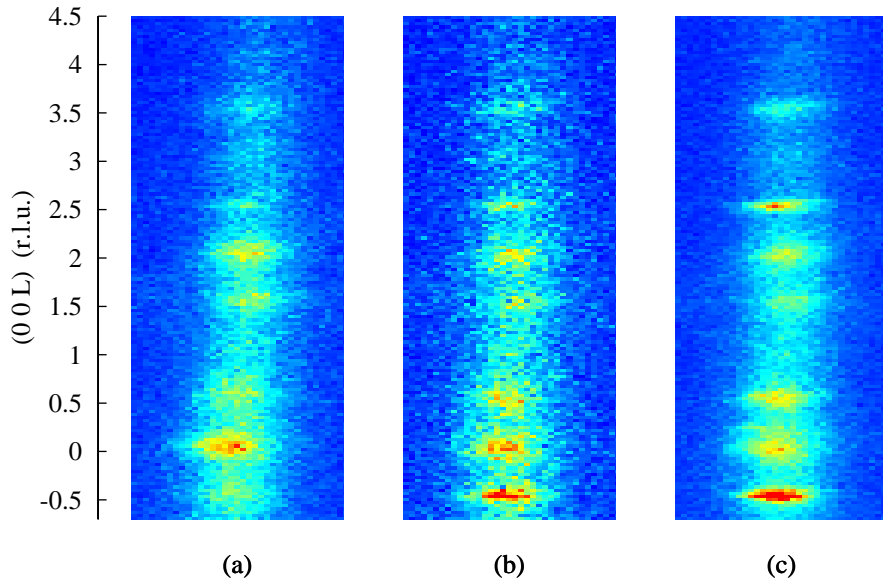


Figure 6.10: Reciprocal space maps of the $\left(\frac{1}{3}\,\frac{1}{3}\,L\right)$ diffraction rod collected at 185 K after (a) cooling with zero electric field, (b) EFC to 230 K in 4 kV/cm, and (c) EFC to 180 K in 4kV/cm.
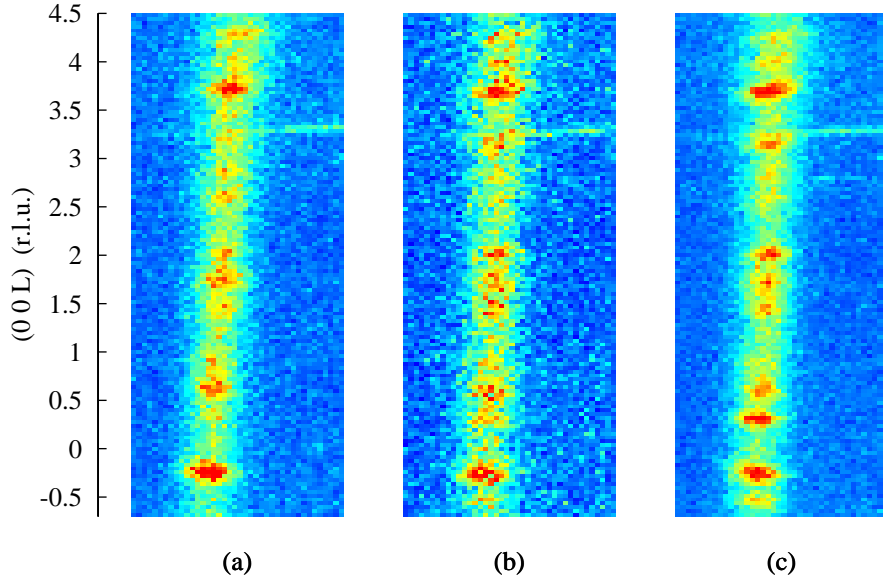
Figure 6.11: Reciprocal space maps of the $\left(\frac{2}{3}\,\frac{2}{3}\,L\right)$ diffraction rod collected at 185 K after (a) cooling with zero electric field, (b) EFC to 230 K in 4 kV/cm, and (c) EFC to 180 K in 4kV/cm.

Similarly, the two three $c^*$-profiles for the $\left(\frac{2}{3}\,\frac{2}{3}\,L\right)$ rod are plotted in Figure 6.13; however, the signal-to-noise ratio is low and the uncertainty in the fitted intensity for these reflections was very high. Accordingly, only the intensities of the $\left(\frac{1}{3}\,\frac{1}{3}\,L\right)$ satellites are discussed.

Comparison of the "ZFC" and "EFC I" sections of Table 6.1 indicates that electric field cooling to 230 K, through the Néel point, has induced some change in the magnetic satellites. There is an increase in the integrated intensity and sharpening (reduction of the FWHM) of the $L = -0.5$ and 2.5 reflections in the $\left(\frac{1}{3}\,\frac{1}{3}\,L\right)$ rod which belong to the same trigonal domain, while no significant

Table 6.1: Fitted parameters of the satellites of the $\left(\frac{1}{3}\,\frac{1}{3}\,L\right)$ scattering rod obtained from the ZFC and EFC I profiles plotted in Figure 6.12. EFC I corresponds to electric field cooling in 4 kV/cm to 235 K. The peak widths shown have been resolution corrected.

| | ZFC | | EFC I | |
|---|---|---|---|---|
| L | Integrated | $\Gamma$ | Integrated | $\Gamma$ |
| (r.l.u.) | Intensity (a.u.) | (r.l.u.) | Intensity (a.u.) | (r.l.u.) |
| -0.5 | $4.35 \pm 0.38$ | $0.279 \pm 0.038$ | $8.56 \pm 0.35$ | $0.108 \pm 0.047$ |
| 0.0 | $13.14 \pm 0.46$ | $0.258 \pm 0.025$ | $13.03 \pm 0.50$ | $0.298 \pm 0.066$ |
| 0.5 | $6.06 \pm 0.42$ | $0.316 \pm 0.045$ | $6.90 \pm 0.43$ | $0.22 \pm 0.13$ |
| 1.5 | $6.25 \pm 0.37$ | $0.192 \pm 0.075$ | $6.37 \pm 0.47$ | $0.30 \pm 0.16$ |
| 2.0 | $9.94 \pm 0.42$ | $0.264 \pm 0.041$ | $7.66 \pm 0.45$ | $0.29 \pm 0.10$ |
| 2.5 | $1.29 \pm 0.21$ | $0.090 \pm 0.036$ | $2.60 \pm 0.25$ | $0.07 \pm 0.27$ |
| 3.5 | $3.10 \pm 0.30$ | $0.212 \pm 0.056$ | $2.52 \pm 0.23$ | $0.134 \pm 0.036$ |
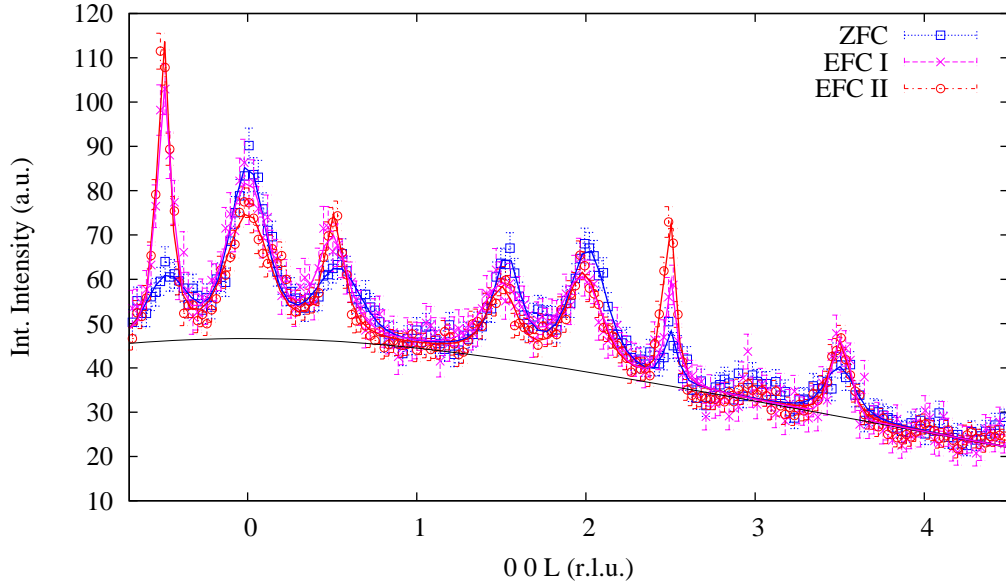
Figure 6.12: Plot of the integrated $c^*$-profile of the $\left(\frac{1}{3}\,\frac{1}{3}\,L\right)$ diffraction rod for the ZFC, EFC I, and EFC II cases. The solid lines are the profile fits matched to each series by the colour shown in the legend; these fits correspond to the values shown in Table 6.1.
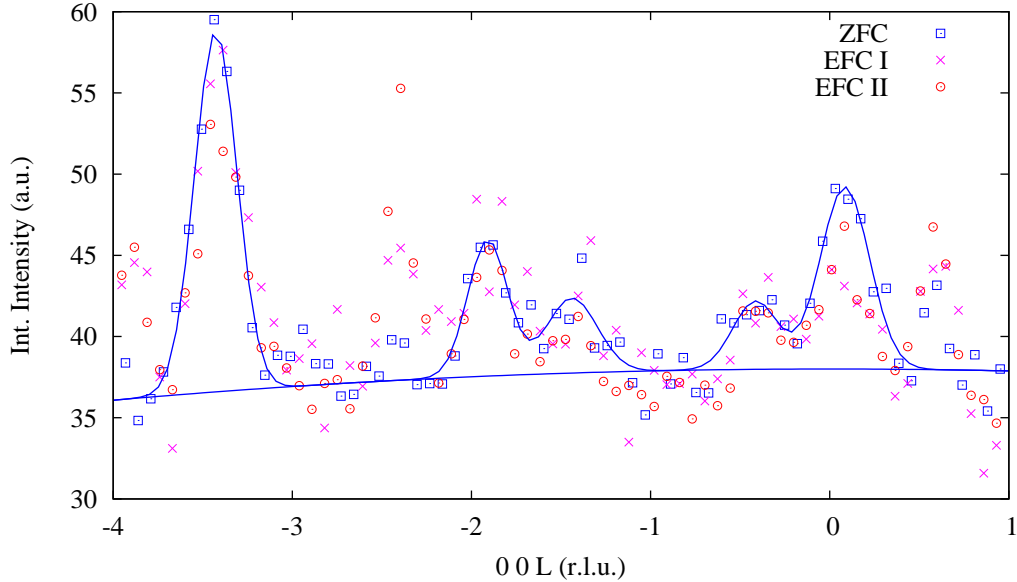


Figure 6.13: Plot of the integrated $c^*$-profile of the $\left(\frac{2}{3}\,\frac{2}{3}\,L\right)$ diffraction rod for the ZFC, EFC I, and EFC II cases. The solid line is a sample profile fit: the uncertainty in the peak intensities was greater than 100% for all satellites other than the $L = -3.5$, so the full series of profile fits are not shown.

Table 6.2: Fitted parameters of the satellites of the $\left(\frac{1}{3}\,\frac{1}{3}\,L\right)$ scattering rod obtained from the EFC I and EFC II profiles plotted in Figure 6.12. EFC I corresponds to electric field cooling in 4 kV/cm to 235 K while EFC II corresponds to further electric field cooling from 220 to 180 K with the same field strength. The peak widths shown have been resolution corrected.

| L | EFC I | | EFC II | |
|---|---|---|---|---|
| (r.l.u.) | Integrated Intensity (a.u.) | $\Gamma$ (r.l.u.) | Integrated Intensity (a.u.) | $\Gamma$ (r.l.u.) |
| -0.5 | 8.56 $\pm$ 0.35 | 0.108 $\pm$ 0.047 | 9.19 $\pm$ 0.34 | 0.089 $\pm$ 0.036 |
| 0.0 | 13.03 $\pm$ 0.50 | 0.298 $\pm$ 0.066 | 10.58 $\pm$ 0.57 | 0.303 $\pm$ 0.025 |
| 0.5 | 6.90 $\pm$ 0.43 | 0.22 $\pm$ 0.13 | 5.78 $\pm$ 0.40 | 0.140 $\pm$ 0.076 |
| 1.5 | 6.37 $\pm$ 0.47 | 0.30 $\pm$ 0.16 | 4.54 $\pm$ 0.48 | 0.210 $\pm$ 0.066 |
| 2.0 | 7.66 $\pm$ 0.45 | 0.29 $\pm$ 0.10 | 7.45 $\pm$ 0.52 | 0.252 $\pm$ 0.038 |
| 2.5 | 2.60 $\pm$ 0.25 | 0.07 $\pm$ 0.27 | 4.12 $\pm$ 0.26 | 0.083 $\pm$ 0.011 |
| 3.5 | 2.52 $\pm$ 0.23 | 0.134 $\pm$ 0.036 | 2.98 $\pm$ 0.28 | 0.142 $\pm$ 0.024 |

changes are observed in the peak intensity or profile of the $\left(\frac{2}{3}\,\frac{2}{3}\,L\right)$ series of satellites. After further electric field cooling to 180 K no further changes are noted as the intensities of the peaks agree to within the fitting uncertainty as shown in Table 6.2.

Peak broadening may arise from a combination of three factors: instrumental broadening, strain, and the correlation length of the electronic ordering. In this case magnetic reflections have been measured and the peak width corresponds to the magnetic correlation length (in addition to instrumental broadening). As noted previously, the applied electric field causes the peaks to sharpen along the $c^*$-axis which corresponds to an increase in the magnetic correlation length parallel to the $c$-axis. The correlation lengths calculated from the resolution corrected peak widths are provided in Table 6.3. The exchange path along the $c$-axis between adjacent Fe bilayers is mediated by O-Lu-O bonds and therefore the $c$-axis correlation length will be a function of stacking faults and the local oxygen stoichiometry. Two correlation lengths are observed: one of approximately 10 nm and the other at approximately 30 nm. The raw detector data has other crystallites and powder rings from the Cu electrodes which intersect with this data, thus the large uncertainty on the L=2.5 result is attributed to noise from another scatterer. There are three symmetry inequivalent $\left(\frac{1}{3}+\delta\,\frac{1}{3}+\delta\,0.5\right)$ type domains in LuFe$_2$O$_4$ which have a periodicity of 3 along the $c$-axis. Therefore 3 different correlation lengths may be expected; however, in the ZFC case it appears the correlation length of the domains is the same.

After electric field cooling the $L = -0.5$ and $L = 2.5$ peaks increase in inten-

Table 6.3: Magnetic correlation lengths calculated from the fitted FWHM of the satellites of the $\left(\frac{1}{3}\,\frac{1}{3}\,L\right)$ diffraction rod.

| L | ZFC | EFC I | EFC II |
|---|---|---|---|
| | $\Gamma$ | $\Gamma$ | $\Gamma$ |
| (r.l.u.) | (nm) | (nm) | (nm) |
| -0.5 | 9.1 $\pm$ 1.2 | 23 $\pm$ 10 | 28 $\pm$ 12 |
| 0.0 | 9.81 $\pm$ 0.95 | 8.5 $\pm$ 1.9 | 8.34 $\pm$ 0.70 |
| 0.5 | 8.0 $\pm$ 1.1 | 11.4 $\pm$ 6.9 | 18.1 $\pm$ 9.9 |
| 1.5 | 13.2 $\pm$ 5.1 | 8.5 $\pm$ 4.5 | 12.0 $\pm$ 3.8 |
| 2.0 | 9.6 $\pm$ 1.5 | 8.7 $\pm$ 3.1 | 10.0 $\pm$ 1.5 |
| 2.5 | 28 $\pm$ 11 | 34.1 $\pm$ 123.6 | 30.4 $\pm$ 4.2 |
| 3.5 | 11.9 $\pm$ 3.1 | 18.8 $\pm$ 5.1 | 17.8 $\pm$ 3.0 |

sity and sharpen with the correlation length increasing to 30 nm and the intensity increasing by a factor of 2. This is direct evidence that electric field cooling through the ferroelectric transition temperature has manipulated the magnetic domains as both the correlation length and domain population of one particular domain have increased. This effect is further explored in the next chapter; however, the reader may immediately note the intensity of the satellites corresponding to the other domains has not decreased indicating that scattering has been created. The non-stoichiometry of the material and presence diffuse scattering indicate the material is not completely ordered, and it is proposed that the presence of the electric field during the cooling process has lead to the ordering of a previously disordered region of the material - possibly through the movement and ordering of oxygen vacancies resulting in longer magnetic exchange paths.

Attempts have been made to model the ZFC and EFC integrated intensities by calculating expected observed intensities using Equation 2.46 (where $\mu$ was set to be the sum of the collinear spin and orbital moments) and combinations of proposed ferroelectric and magnetic structures. The ferroelectric model proposed by Ikeda *et al.* [83] in an antiferroelectric arrangement was combined with the spin models proposed by Christianson *et al.* [55] and Ko *et al.* [122]; however, none of these models were able to describe the observed intensities. Rather, the observed ratio of $\left(\frac{1}{3}\,\frac{1}{3}\,\frac{3}{2}\right)$ satellites to $\left(\frac{1}{3}\,\frac{1}{3}\,0\right)$ is much larger than the proposed models predict. Such a discrepancy may be accounted for by greater magnetic contrast between the $Fe^{2+}$ and $Fe^{3+}$ sites as suggested by Angst *et al.* [56], and this point is revisited in Chapter 7.

## 6.4 Discussion & Summary

Magnetic neutron diffraction has revealed that there exists a progressive magnetic ordering in this sample of $LuFe_2O_4$ with 2D Ising magnetic order observed below the Néel temperature and 3D order observed at lower temperature. Christianson *et al.* have demonstrated 3D order below the Néel temperature [55], and Iida *et al.* have demonstrated 2D order below the Néel point [48]; however, this work is the first report of a progressive ordering between these states.

*In situ* neutron diffraction measurements have demonstrated there is no change in the magnetic diffraction intensity for applied electric fields of either polarity in either the 2D ordered (collected at 225 K) or 3D ordered (collected at 180 K) states. The applied field study has revealed that electric field cooling through the Néel point leads to changes in the magnetic diffraction pattern. One hexagonal domain is preferred in the case of the $\left(\frac{1}{3}\,\frac{1}{3}\,L\right)$ satellites suggesting electric field control of the domain population.

The peak profile of affected peaks sharpens indicating the *c*-axis correlation length increases after electric field cooling through the 3D transition temperature. The ferroelectric distortions stabilised by the applied electric field may stabilise the exchange paths in this direction leading to a longer correlation length, or the magnetic correlation length may be coupled to the ferroelectric correlation length. The ferroelectric correlation length should be established at the ferroelectric ordering temperature (330 K) and therefore if the two domains are coupled spatially then both EFC cases should have the same correlation length which is the case reported here.

The simplest model to describe magnetoelectric coupling in this material is to assume that the applied electric field varies the ferroelectric structure and the $Fe^{2+}/Fe^{3+}$ ordering. The magnetic exchange paths are dependent upon the local structure, and the spin structure depends on the ordering of $Fe^{2+}/Fe^{3+}$. Therefore, ferroelectric distortions of the lattice and variations in the charge ordering are expected to vary the magnetic structure and change the correlation length and satellite intensities accordingly. In such a case, the ferroelectric properties are established at high temperature (330 K) and the magnetic diffraction recorded after EFC to 235 and 180 K should be the same as is reported here.

Glassy dielectric and magnetic behaviour has been reported in the literature

for $LuFe_2O_4$ indicating partial ordering may exist. In such a case, the applied electric field may lead to an ordering of these glassy phases causing additional scattering intensity to be observed. This is explored further in Chapter 7.

In addition to attempting to explain the variations in the intensity and correlation length reported here, it should be noted that the currently accepted models of the magnetic order ascribe the $\left(\frac{1}{3} \frac{1}{3} \frac{3}{2}\right)$ and $\left(\frac{1}{3} \frac{1}{3} 0\right)$-type satellite reflections to the same magnetic structure, but the difference between the correlation lengths of the two types of satellites observed in this work indicates that the electric field only interacts with the $\left(\frac{1}{3} \frac{1}{3} \frac{3}{2}\right)$-type satellites and different correlation lengths result. Christianson *et al.* [55] proposed that the $\left(\frac{1}{3} \frac{1}{3} \frac{3}{2}\right)$-type arise from contrast between the $Fe^{2+}$ and $Fe^{3+}$ on the charge ordered lattice. Such a model is consistent with these results as the ferroelectric correlation length was influenced by the electric field increasing the correlation length of the $Fe^{2+}/Fe^{3+}$ contrast whilst the correlation length of the 2:1 ferrimagnetic spin arrangement remained constant.

$LuFe_2O_4$ is rare in that it is one of the few multiferroic materials to have the ferroelectric phase as the high temperature phase. In this chapter it has been proposed that an applied electric field modifies the magnetic ordering due to its effect on the charge ordered state. In order to further investigate this an *ex situ* electric field study using single crystal x-ray diffraction was performed and the results are reported in Chapter 7.

# Chapter 7

# Non-resonant single crystal x-ray diffraction

## 7.1  Introduction

The neutron scattering experiments presented in Chapters 5 and 6 demonstrate the dynamic properties of the ferroelectric and ferrimagnetic order in $LuFe_2O_4$. The applied electric field study demonstrated that the magnetic order is not influenced by the presence of strong electric fields below the ordering temperature, as demonstrated by *in situ* neutron scattering measurements, yet a difference in the diffraction pattern was noted as a function of electric field cooling procedure that suggests the presence of the electric field at the Néel spin ordering temperature has changed the magnetic structure. A selective effect on one particular hexagonal magnetic domain was noted.

The ferrimagnetic and ferroelectric order arise from the same lattice sites; therefore, in order to understand the magnetoelectric effect reported in Chapter 6 it is important to understand the effect the electric field cooling has on the ferroelectric order. Furthermore, it has been proposed from Landau theory that an applied electric field should favour commensurate charge order [100] and this is also of interest to investigate.

As demonstrated in Chapters 5 and 6, neutrons are sensitive to the magnetic order due to the spin-spin interaction, but also to the ferroelectric order due to

the nuclear scattering cross-section. The potential overlap of these signals was noted in Chapter 5. Non-resonant x-ray scattering on the other hand is not directly sensitive to the magnetic or valence ordering (unlike the resonant x-ray scattering presented in Chapter 3); rather, the observed scattering results only from the atomic positions.

The charge order of $Fe^{2+}/Fe^{3+}$ sites leads to corresponding distortions of the atomic structure that will thereby have the same **Q**-vector. Accordingly, non-resonant x-ray scattering is an ideal tool to indirectly measure the ferroelectric order.

In this chapter the results from an *ex situ* electric field study are reported. An introduction to the principles of x-ray scattering and available software employed in this work was provided in Chapter 2, while an outline of the experimental work is presented as Section 7.2, the data reduction and analysis are presented in Sections 7.3 and 7.4, and finally the discussion and summary are provided in Sections 7.5 and 7.6 respectively.

## 7.2 Experimental

An electric field sample environment was designed and implemented at Curtin University. A hot plate, Teflon mat, two copper electrodes, and a high voltage power supply were used to construct the electric field stage as shown in Figure 7.1. In the initial design, long Teflon blocks were used as weights to orient the Cu electrodes; however, later these were replaced by Teflon coated metal weights. The tip of a 1 mL syringe was removed, and the majority of the plunger handle cut off. The head of the plunger remained adjustable within the remaining plastic cylinder resulting in an insulating adjustable sample stage. A thermocouple was used to monitor the temperature at the sample position, held in place by the handle from the syringe plunger.

A simulation of the electric field produced by such a setup is provided as Figure 7.2. The optimum position within the field is shown to be just above the centre position of the Cu electrodes. The polycrystalline ingot from batch 2 was crushed in an agate mortar and pestle to produce a coarse powder. A portion of this powder was transferred onto the sample stage at the optimum electric field height.
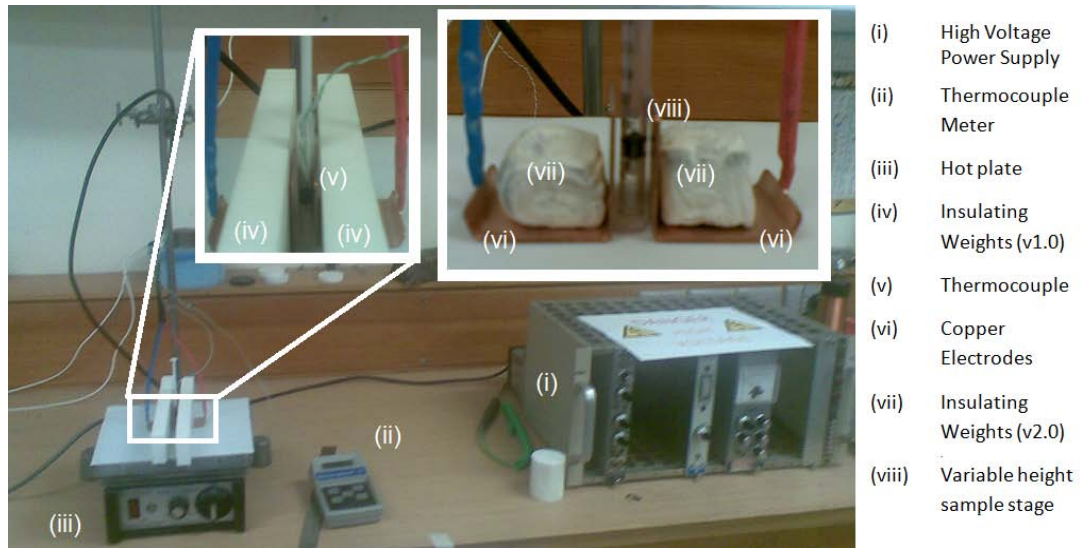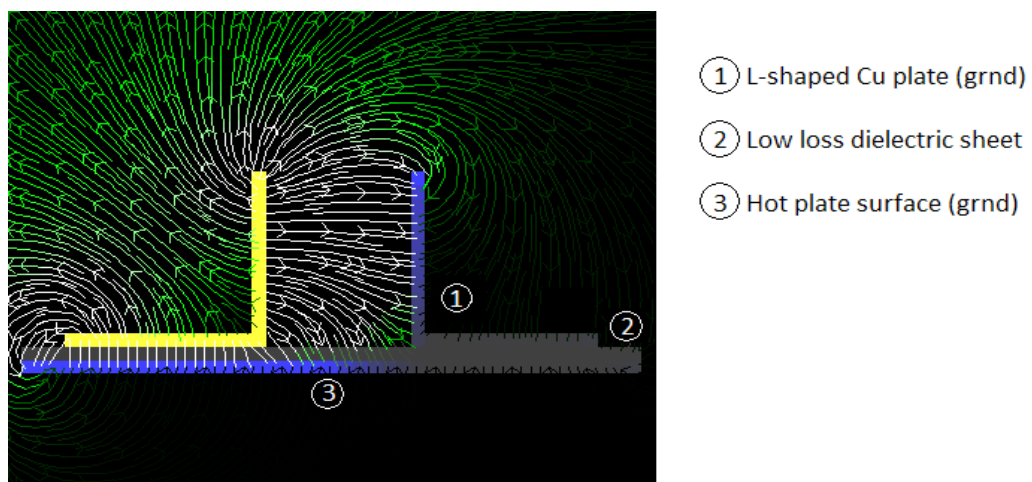
Figure 7.1: Electric field sample environment designed and implemented in the Department of Imaging and Applied Physics at Curtin University with the assistance of Glen Lawson and Mark Winstanley.



Figure 7.2: Electric field simulation for the setup shown in Figure 7.1. The optimum sample position is just above the centre of the copper electrodes.

The sample was heated to 370 K at which point the hot plate was switched off and the thermocouple removed. Immediately, an electric field of approximately 5 kV was applied, and the sample was left for a few hours to cool to room temperature after which the field was removed. A portion of the original powder was put aside for comparison to the electric field cooled (EFC) sample.

The samples were transported to the protein crystallography (PX1) beamline of the Australian synchrotron where *ex situ* non-resonant x-ray scattering experiments were performed. The instrument has one degree of freedom, $\phi$, for sample rotation and a large 2D CCD detector. Multiple fragments from both the electric field cooled and zero field cooled samples, with each dimension approximately less than 5 $\mu$m, were mounted on sample holders. With the beam stop and detector in their minimum sample-distance configuration approximately 55 degrees of $2\theta$ was measured. A wavelength of 0.774887 A was selected to ensure the experiment was conducted away from the Lu and Fe absorption edges.

Initially, multiple runs on each sample were collected with different beam attenuations at 100 K. Three beam attenuation configurations were investigated: open slits with no transmission filter, open slits with maximum transmission attenuation, and closed slits with maximum transmission attenuation. Each run consisted of stepping $\phi$ from $0^o$ to $360^o$ in $0.2^o$ steps. Finally an EFC sample was mounted and variable attenuation runs collected at 100 K with an angular step of $0.5^o$. The temperature dependence was measured by heating the sample to 200, 260, and 360 K and repeating the data collection procedure. Finally the sample was cooled back to 260 K and the set of variable attenuation data collected.

## 7.3    Data reduction

It was determined that with the slits fully closed there was a large uncertainty in the beam intensity; therefore, of the three attenuation modes, only the data collected with open slits and utilising the transmission filter is reported. Furthermore, the results discussed here focus on the final sample measured for which both an electric field cooled (EFC) and zero field cooled (ZFC) dataset exist.

Preliminary data reduction was performed using XDS [125] and DIRAX [133], introduced in Section 2.5.1, on all datasets. The FABLE [134] workbench was used in order to view the raw detector images.

A drawback of XDS is that it is not able to identify incommensurate structures; however, DIRAX [133] applies algorithms that allow for incommensurate propagation vectors. This program requires a list of reflections provided as either instrument angles, or reciprocal space vectors as input. A script was written for SCILAB which converted the reflection list output by XDS (in pixel and frame coordinates) into 3-dimensional reciprocal space coordinates.

In addition to the analysis with XDS and DIRAX code was written, named PX1MAPPER, to make reciprocal space maps calculated using the raw detector images. The code performs the instrument-to-reciprocal space transformation in the same way as the SCILAB script; however, it is performed on a pixel-by-pixel basis for every detector image in the dataset.

PX1MAPPER calculates $\mathbf{Q}$ using the pixel coordinate on the detector $(x, y)$, the optimised beam position $(x_0, y_0)$ and sample distance $(Z)$ obtained from the XDS analysis, and the sample rotation $(\phi)$. Furthermore, two rotations may be defined in the reciprocal space coordinate system to orient the dataset. The rotations are input as a triplet representing the Cartesian vector about which the rotation is made, and the magnitude of the rotation. Each subsequent rotation is applied to the dataset that results from the previous transformation(s).

Reduction of the 4D $(\mathbf{Q}, I)$ dataset into 3D XY, YZ, and XZ integrated cross-sections and 2D x, y, and z integrated profiles was performed using the STACK-ANALYSIS code (introduced in Chapter 6). Visualisation and fitting of these cross-sections and profiles was performed using SCILAB.

A background correction program, BGCORR, was written in C# to background subtract the detector images. The background was calculated starting at the beam centre where a small region was excluded, and then the mean intensities within concentric annuli were calculated. The density of the annuli decreased as the distance from the beam centre increased, and pixels were rejected that were beyond a user provided multiple of the standard deviation. The process was repeated until all pixels remaining in the mask were within this limit, at which point the intensity of every pixel in the annulus was set to the mean value of those in the annular background mask. The result was used as a background map and subtracted from the original detector image. The analysis presented in this work is based upon the raw detector images not processed by BGCORR as the effect on the diffuse scattering could not be quantified.

### 7.3.1 Resolution Correction

The PX1 protein crystallography beamline is primarily used to solve protein crystal structures, so the resolution function of the instrument need not be known by the user. The software inspects peak widths and makes corrections before finally working with just the integrated intensity of the peaks. Unfortunately no standard was available during the scope of this experiment; however, as noted in Chapter 8 the $LuFe_2O_4$ sample is as sharp as, if not sharper than the instruments $LaB_6$ sample used to calibrate the instrument function and the main structural Bragg peaks are resolution limited in that experiment.

Whilst it is not necessarily the case, in order to resolution correct the data presented in this chapter it has been assumed that the main structural Bragg reflections are also resolution limited - and they have been used in order to characterise the instrument function. The $(0\,0\,9)$, $(0\,0\,15)$, $(0\,0\,18)$, and $(0\,0\,24)$ reflections have been fitted and used to determine an instrument correction. These reflections were selected as they span a similar range of $\mathbf{Q}$ and have the same orientation on the detector with respect to the optics of the instrument as the superlattice reflections studied during this experiment.

## 7.4 Analysis

The results obtained by processing the first $180^o$ of rotation data for both the ZFC and EFC datasets with XDS are presented in Table 7.1 and Table 7.2 respectively.

Table 7.1: Fitted cell parameters and instrument values determined from 2048 indexed reflections identified in the first $180^o$ of rotation data of the zero field cooled dataset at 260 K. The detector position, beam position, sample orientation, and cell parameters were all refined during the fit.

| $a$ | $b$ | $c$ | $\alpha$ | $\beta$ | $\gamma$ |
|---|---|---|---|---|---|
| 5.96 $\pm 0.01$ | 5.96 $\pm 0.01$ | 50.6 $\pm 0.1$ | 90.0 $\pm 0.2$ | 90.0 $\pm 0.2$ | 120.0 $\pm 0.3$ |

| | |
|---|---|
| Standard deviation of spot position (pixels) | 2.12 |
| Standard deviation of spindel position (degrees) | 0.18 |
| Sample mosaicity | 0.2 |
| Beam Detector Position X/Y (pixels) | 1038.29  1027.38 |
| Crystal to detector distance (mm) | 83.68 |

Table 7.2: Fitted cell parameters and instrument values determined from 3008 indexed spots identified in the first $180^o$ of rotation data of the electric field cooled dataset at 260 K. The detector position, beam position, sample orientation, and cell parameters were all refined during the fit.

| $a$ | $b$ | $c$ | $\alpha$ | $\beta$ | $\gamma$ |
|---|---|---|---|---|---|
| 5.96 $\pm 0.01$ | 5.96 $\pm 0.01$ | 50.63 $\pm 0.09$ | 90.0 $\pm 0.2$ | 90.0 $\pm 0.2$ | 120.0 $\pm 0.3$ |

| | |
|---|---|
| Standard deviation of spot position (pixels) | 1.73 |
| Standard deviation of spindel position (degrees) | 0.15 |
| Sample mosaicity | 0.2 |
| Beam Detector Position X/Y (pixels) | 1038.33    1027.51 |
| Crystal to detector distance (mm) | 83.67 |

The superstructure reported in the literature is incommensurate with satellites described by the propagation vector $\left(\frac{1}{3}+\delta \ \frac{1}{3}+\delta \ \frac{3}{2}\right)$. The commensurate approximation of the charge order superlattice is described by a $\sqrt{3} \times \sqrt{3} \times 2$ hexagonal cell with $a \approx 5.95$ Å. As demonstrated in Table 7.1 and 7.2, it is this cell that has been identified by XDS.

XDS is unable to distinguish the incommensurate nature of the propagation vectors, therefore the distribution of the spots from their ideal commensurate position is represented in the deviation of the pixel and spindel positions reported in Tables 7.1 and 7.2. The improvement in the number of indexed reflections and deviation of the spot positions in the EFC case may indicate the data have become more commensurate, but it is not possible to distinguish this from the XDS results alone.

Each dataset was processed in DIRAX and as DIRAX works with a maximum of 1000 spots per run chosen at random, the generator was reseeded many times in order to index 98% of the approximately 3200 spots collected. In order to achieve this level of indexing 21 solutions were determined for the ZFC case and 13 solutions for the EFC case of which it was found that the solutions in all cases are equivalent by volume and either related identically, by $60^o$ or $120^o$ rotations inherent to the hexagonal lattice symmetry, or by $180^o$ due to twinning parallel to the $c$-axis ($c' = -c$). The mean values of the cell parameters determined in each case are presented in Table 7.3 and Table 7.4 for the ZFC and EFC cases respectively.

Hexagonal cells were identified in both cases with $a = 5.96$ Å and $c = 50.6$ Å. Analysis with DIRAX did not produce incommensurate solutions as expected, but the uncertainties are also larger than expected for good quality single crystal

Table 7.3: Mean cell parameters obtained by DIRAX analysis of the zero field cooled dataset. Twenty-one solutions were obtained from multiple reseeds of the random number generator used to select the spots for analysis with the fitting parameters Indexfit = 4 and Levelfit = 1500.

| $a$ | $b$ | $c$ | $\alpha$ | $\beta$ | $\gamma$ |
|---|---|---|---|---|---|
| 5.96 $\pm$ 0.01 | 5.96 $\pm$ 0.01 | 50.6 $\pm$ 0.1 | 90.0 $\pm$ 0.2 | 90.0 $\pm$ 0.2 | 120 . $\pm$ 0.3 |

Table 7.4: Mean cell parameters obtained by DIRAX analysis of the electric field cooled dataset. Thirteen solutions were obtained from multiple reseeds of the random number generator used to select the spots for analysis with the fitting parameters Indexfit = 4 and Levelfit = 1500.

| $a$ | $b$ | $c$ | $\alpha$ | $\beta$ | $\gamma$ |
|---|---|---|---|---|---|
| 5.96 $\pm$ 0.01 | 5.97 $\pm$ 0.01 | 50.6 $\pm$ 0.1 | 90.0 $\pm$ 0.2 | 90.0 $\pm$ 0.2 | 120 $\pm$ 0.3 |

data. This may be explained by investigation of the raw detector images.

Selected regions of the detector integrated over 12 consecutive frames showing three scattering rods that arise due to the charge order are presented in Figure 7.3 for the ZFC case, and Figure 7.4 for the EFC case. In Figure 7.3 diffuse scattering is observed between the charge order satellites which do not follow a straight path on the detector; rather, slight deviations about the scattering rod are apparent in the integrated detector images. In Figure 7.4, the EFC case, the intensity of the satellites has increased, in particular the satellites at greater $\mathbf{Q}$.

The peak positions used as input for DIRAX were determined from XDS where the EFC case was shown to have a better quality of fit than the ZFC case. XDS determines the spot location in 3-dimensions by attempting to find the intensity centroid between frames. The diffuse scattering shown in Figure 7.3 will lead to a greater uncertainty in the centroid position and reduce the quality of the fit. The absence of this diffuse scattering in the EFC case will result in more accurate centroid positions, and it is this effect which was previously noted rather than any significant change in the commensurability of the reflections.

In order to analyse the effect of the electric field on the intensity and peak widths of the charge order satellites, reciprocal space mapping was performed by utilising PX1MAPPER, introduced previously in Section 7.3. A $2\theta$-$\phi$ map was produced in order to accurately determine the cell parameters in each case. The peak profiles of the $(0\,0\,9)$ and $(1\,1\,9)$ reflections were used to determine the lattice parameters, and $d_{(1\,1\,0)} = 1.7391304$ Å, $d_{(1\text{-}1\,0)} = 3.01226$ Å, and $d_{(0\,0\,1)} = 25.392347$ Å were used to produce the reciprocal space maps.
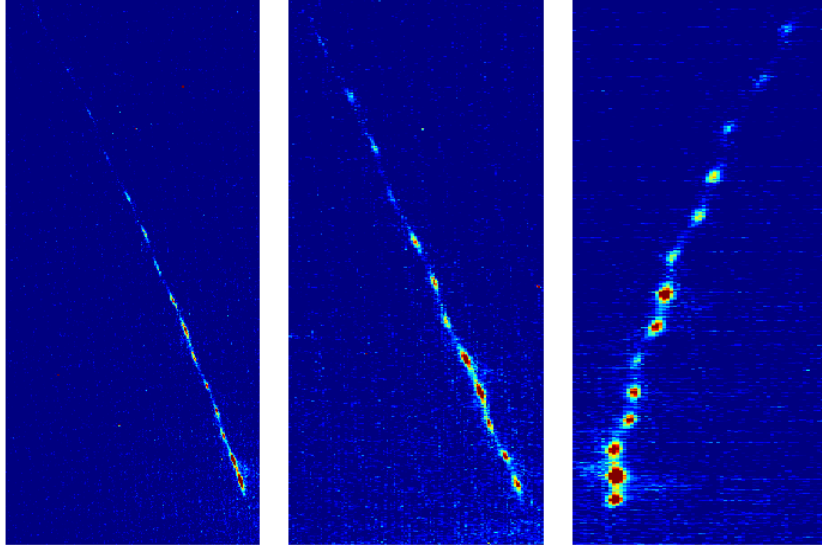
Figure 7.3: Selected regions of the image that results from the integration of 12 consecutive detector frames for the zero field cooled case. Discrete satellites connected by diffuse scattering are shown which result from the charge ordered state. The centre of the detector is located to the bottom right of the first two frames, and the bottom left of the third. The *c*-axis runs parallel to the series of spots shown.
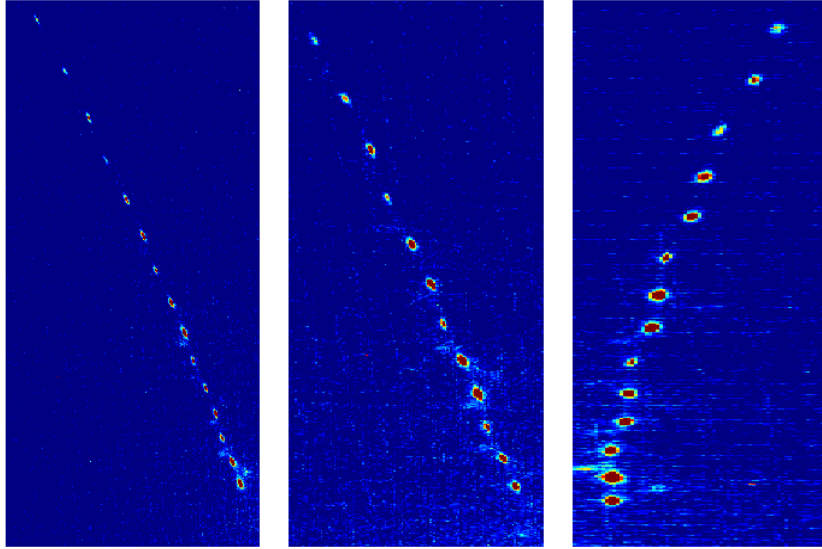


Figure 7.4: Selected regions of the image that results from the integration of 12 consecutive detector frames for the electric field cooled case. Discrete satellites that result from the charge ordered state are observed with an increase in intensity for all satellites compared to Figure 7.3. The centre of the detector is located to the bottom right of the first two frames, and the bottom left of the third. The *c*-axis runs parallel to the series of spots shown.

The reciprocal space map of the *ab*-plane calculated from the ZFC dataset is shown in Figure 7.5. The hexagonal arrangement of the reciprocal lattice is evident, and no changes (beyond slight variations in lattice parameters) are noted in the EFC case. Reciprocal space maps of the $\left(\frac{1}{3} \frac{1}{3} L\right)$ diffraction rod collected at 260 K for the ZFC and EFC cases are presented in Figures 7.6 and 7.7. The incommensurate nature of the charge order structure is evident as the satellites position vary about the $\left(\frac{1}{3} \frac{1}{3}\right)$ position. Three equivalent charge order domains exist, therefore by hexagonal symmetry every third satellite corresponds to the same domain. The three hexagonal propagation vectors are $\left(\frac{1}{3}+\delta \; \frac{1}{3}+\delta \; \frac{3}{2}\right)$, $\left(\frac{1}{3}+\delta \; -\frac{2}{3}-\delta \; \frac{3}{2}\right)$, and $\left(-\frac{2}{3}-\delta \; \frac{1}{3}+\delta \; \frac{3}{2}\right)$. One domain seems inequivalent to the other two due to the offset occurring in the positive direction; however, this is just a result of the propagation vector corresponding to that domain as $\mathbf{G}+\mathbf{q}$, where $\mathbf{G}$ is a reciprocal space point corresponding to a lattice spacing of the ferroelectric prototype and $\mathbf{q}$ is the incommensurate propagation vector, will have differing $\mathbf{G}$ for satellites in the same diffraction rod.

The reciprocal space maps of the $\left(\frac{1}{3} \frac{1}{3} L\right)$ diffraction rod demonstrate the increase in the diffracted intensity of the satellites previously noted from the raw detector images. The changes are summarised by the integrated $c^*$-axis profiles shown in Figure 7.8. The satellite peak profiles were fitted with a Lorentzian profile function in groups of three on a linear background; the resulting integrated intensity and full width at half maximum (FWHM) are provided in Table 7.5.

Comparison of the ZFC and EFC results presented in Table 7.5 shows that the profile of all satellites sharpen in the $c^*$-direction. An increase in the integrated peak intensity is also noted in almost every case, yet despite the increase in height of every peak shown in Figure 7.8 in some cases this is a result of the sharpening of the peak and no increase in intensity is observed.

The incommensurability of the charge ordered superlattice is quantified by $\delta$ and this may be measured from the $(H\,H\,0)$ profiles of the satellites. In order to reduce the error in the measurement of $\delta$, the position of two peaks, one at $\frac{1}{3}+\delta$ and the other at $\frac{1}{3}-\delta$ are measured and $\delta$ taken as half the difference. The the integrated $(H\,H\,0)$ profiles of the reciprocal space map corresponding to the $L = 10.5$ and $11.5$ satellites is shown in Figure 7.9 for both the ZFC and EFC cases. For the ZFC case $\delta$ was determined to be 0.0021, while for the EFC case $\delta$ was found to be 0.0027.
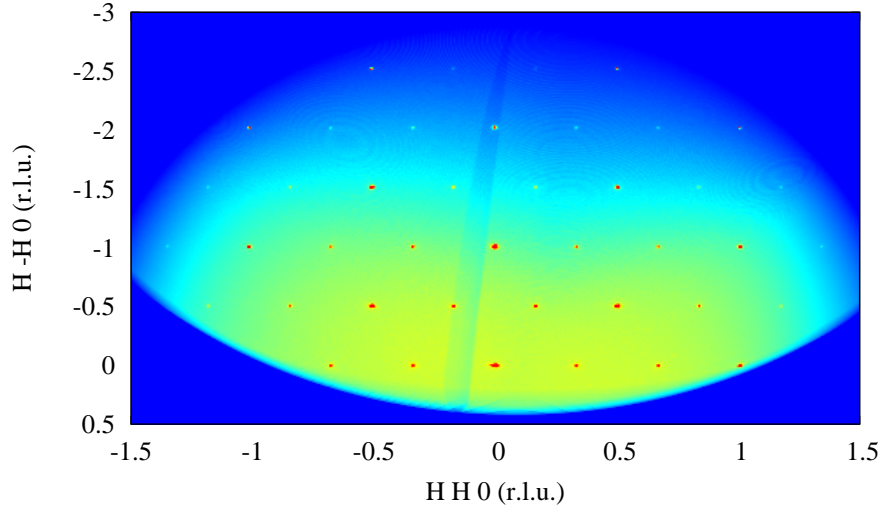
Figure 7.5: Reciprocal space map of the *ab*-plane calculated from the zero field cooled dataset collected at 260 K.
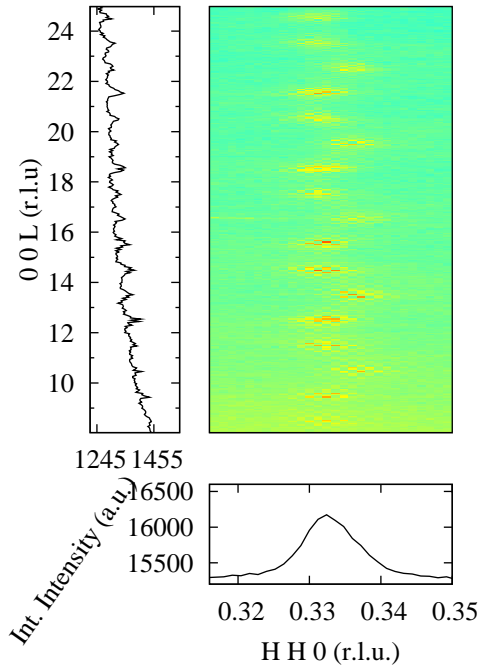


Figure 7.6: Reciprocal space map of the $\left(\frac{1}{3}\,\frac{1}{3}\,L\right)$ diffraction rod collected at 260 K after zero field cooling from 360 K.
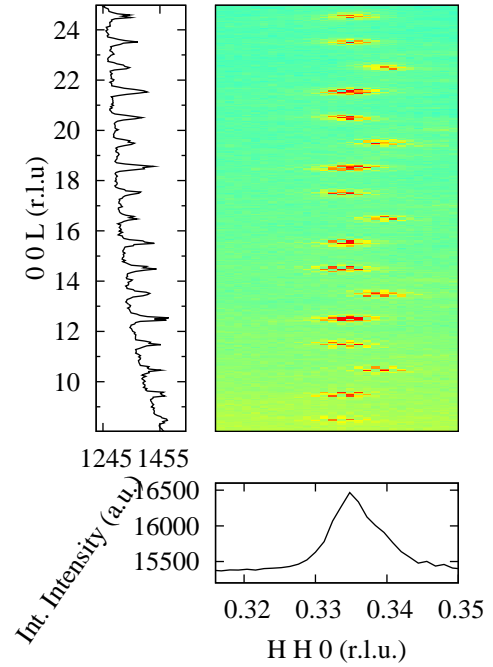


Figure 7.7: Reciprocal space map of the $\left(\frac{1}{3}\,\frac{1}{3}\,L\right)$ diffraction rod collected at 260 K after electric field cooling from 360 K with an applied field of approximately 5 kV/cm.
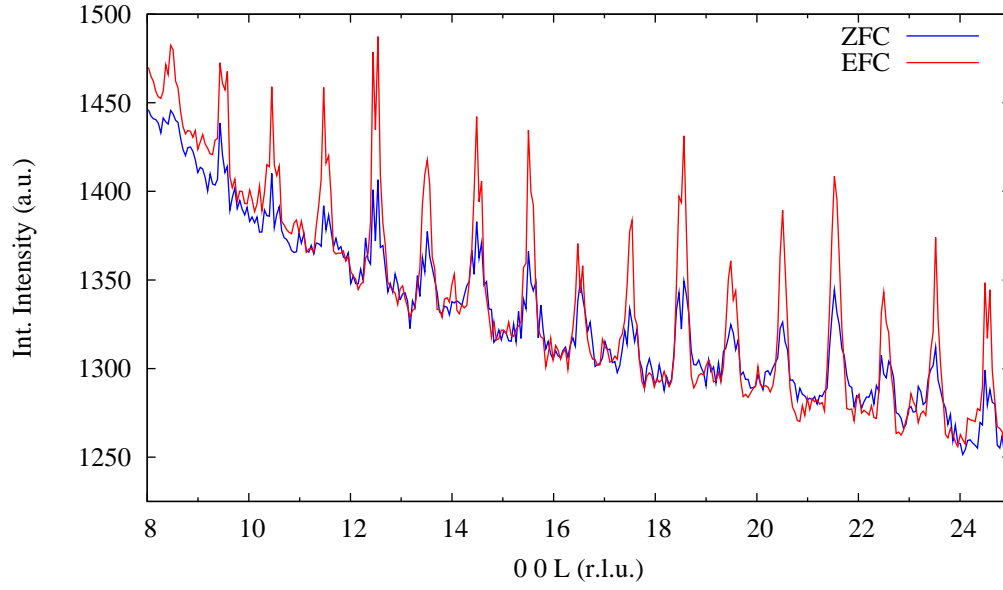
Figure 7.8: Overplot of the c*-axis profiles of the $\left(\frac{1}{3} \frac{1}{3} L\right)$ diffraction data collected at 260 K for the zero field cooled and electric field cooled cases.

Table 7.5: Fitting results for both the zero field cooled and electric field cooled datasets where the $c^*$-axis profile of the satellites has been background subtracted and the peak profiles fitted by Lorentzian profiles. The FWHM ($\Gamma$) provided has been resolution corrected.

| L (r.l.u.) | Int. Intensity (a.u.) | | $\Gamma$ (r.l.u.) | |
|---|---|---|---|---|
| | ZFC | EFC | ZFC | EFC |
| 8.5 | 21.2 $\pm$ 3.0 | 34.5 $\pm$ 3.5 | 0.346 $\pm$ 0.072 | 0.232 $\pm$ 0.037 |
| 9.5 | 29.3 $\pm$ 2.9 | 45.1 $\pm$ 3.3 | 0.280 $\pm$ 0.040 | 0.177 $\pm$ 0.021 |
| 10.5 | 38.9 $\pm$ 3.5 | 45.5 $\pm$ 3.3 | 0.380 $\pm$ 0.048 | 0.170 $\pm$ 0.019 |
| 11.5 | 53.2 $\pm$ 3.6 | 58.1 $\pm$ 3.2 | 0.376 $\pm$ 0.035 | 0.161 $\pm$ 0.014 |
| 12.5 | 66.6 $\pm$ 3.4 | 89.0 $\pm$ 3.4 | 0.323 $\pm$ 0.023 | 0.168 $\pm$ 0.010 |
| 13.5 | 62.9 $\pm$ 3.9 | 63.8 $\pm$ 3.4 | 0.389 $\pm$ 0.033 | 0.173 $\pm$ 0.014 |
| 14.5 | 69.1 $\pm$ 3.7 | 72.7 $\pm$ 3.5 | 0.371 $\pm$ 0.028 | 0.184 $\pm$ 0.014 |
| 15.5 | 46.1 $\pm$ 2.8 | 69.8 $\pm$ 3.2 | 0.213 $\pm$ 0.018 | 0.138 $\pm$ 0.010 |
| 16.5 | 52.7 $\pm$ 4.6 | 43.9 $\pm$ 3.6 | 0.516 $\pm$ 0.061 | 0.194 $\pm$ 0.023 |
| 17.5 | 43.4 $\pm$ 3.4 | 58.9 $\pm$ 3.5 | 0.296 $\pm$ 0.031 | 0.176 $\pm$ 0.015 |
| 18.5 | 63.7 $\pm$ 3.2 | 82.2 $\pm$ 3.2 | 0.285 $\pm$ 0.020 | 0.148 $\pm$ 0.009 |
| 19.5 | 59.2 $\pm$ 3.7 | 55.7 $\pm$ 3.5 | 0.384 $\pm$ 0.034 | 0.180 $\pm$ 0.016 |
| 20.5 | 42.7 $\pm$ 3.3 | 52.8 $\pm$ 3.2 | 0.322 $\pm$ 0.035 | 0.154 $\pm$ 0.014 |
| 21.5 | 50.4 $\pm$ 2.8 | 76.0 $\pm$ 3.2 | 0.259 $\pm$ 0.020 | 0.157 $\pm$ 0.010 |
| 22.5 | 40.2 $\pm$ 3.4 | 39.4 $\pm$ 2.9 | 0.388 $\pm$ 0.046 | 0.146 $\pm$ 0.016 |
| 23.5 | 27.9 $\pm$ 2.6 | 36.6 $\pm$ 2.8 | 0.249 $\pm$ 0.032 | 0.145 $\pm$ 0.016 |
| 24.5 | 18.5 $\pm$ 2.2 | 35.3 $\pm$ 2.7 | 0.214 $\pm$ 0.036 | 0.145 $\pm$ 0.016 |
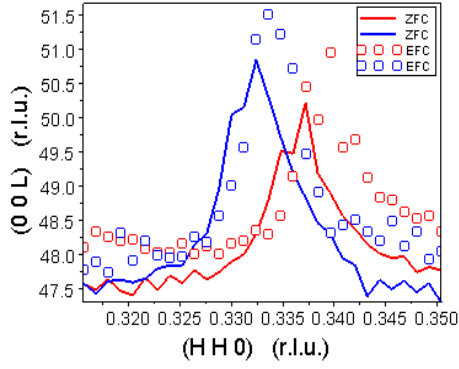
Figure 7.9: Integrated $(H\,H\,0)$ profiles of the satellites of the $L = 10.5$ and 11.5 satellites from the $\left(\frac{1}{3}\,\frac{1}{3}\,L\right)$ diffraction rod collected at 260 K for the zero field cooled (solid) and electric field cooled (open box) datasets.

## 7.5 Discussion

The XDS and DIRAX results indexed the commensurate $\sqrt{3}\times\sqrt{3}\times2$ hexagonal unit cell associated with the charge ordered superstructure; however, the structure is known to be incommensurate and this was shown to be true by the reciprocal space mapping performed using PX1MAPPER. The DIRAX result demonstrated that despite the crushing process and large number of spots collected, 98% of the observed spots could be indexed with equivalent or twinned solutions indicating the sample under examination was a single crystal in that there were no other fragments in the beam.

The satellites are indexed with the propagation vector $\left(\frac{1}{3}+\delta\,\frac{1}{3}+\delta\,\frac{3}{2}\right)$ where $\delta$ was found to equal 0.0021 for the ZFC case and 0.0027 for the electric field cooled case. These results are consistent with the value of 0.0027 reported in the literature [76]. However, the prediction that a commensurate charge ordered state is induced by an applied electric field [100] is not supported by these results. An *in situ* transition to a commensurate state cannot be eliminated by these *ex situ* measurements, thus *in situ* measurements are proposed to fully investigate this result.

It has been inferred from diffraction studies and density functional theory calculations that in the zero field case the antiferroelectric stacking of the dielectric $Fe^{2+}/Fe^{3+}$ double layers results in the half-integer $c^*$-positions of the superlattice reflections and accordingly a zero sample polarisation [56]. It has been proposed that the application of an applied electric field to such a system stabilises the ferroelectric stacking of double layers thereby inducing a polarisation per unit

volume in the sample, increasing the correlation length along the $c$-axis, and causing the intensity of the superlattice reflections to shift to integer $c^*$-positions. The results presented here partially support this proposal in that an increase in the $c$-axis correlation length is observed as indicated by the sharpening of the $c^*$-profile of every satellite; however, the superlattice intensity remains at half-integer $c^*$-positions.

Structure factor calculations readily demonstrate that the ferro- or ferrielectric stacking of the charge ordered layers yields intensity at integer $L$ positions, and the pyroelectric current measurements presented in Section 6.1 demonstrate non-zero polarisation in the electric field cooled case demonstrating ferroelectric, rather than antiferroelectric, order is present. Therefore, the absence of satellites with integer values of $L$ and the presence of satellites with half-integer values in the ferroelectric state demonstrates the $c$-axis periodicity of the structure depends on factors beyond the ferroelectric stacking as ferrielectric or ferroelectric stacking would lead to satellites with integer values of $L$. As a result of this, the assumption that purely antiferroelectric stacking dominates in the ground state on the basis of previously reported diffraction results and structure factor calculations [56] is not valid as these results demonstrates polarised $LuFe_2O_4$ maintains half-integer satellites and therefore further evidence beyond the presence of these satellites is required to determine the polarisation in the ground state.

In addition to an increase in the ferroelectric correlation length, an increase in the diffraction intensity is observed after electric field cooling. The applied electric field may lead to an increase in the polarisation due to increased ferroelectric displacements and accordingly an increase in the scattering intensity; however, the indexing results provide no indication that the trigonal symmetry has been violated. Rather, the increase in the satellite intensity at high $\mathbf{Q}$ indicate that the long range 3-dimensional order is better defined in the electric field cooled case; a result that is supported by the increased correlation length.

Glassy dielectric, spin [60], and orbital [126] behaviour has been observed in $LuFe_2O_4$ and recently a complex magnetic phase diagram has been reported confirming the simultaneous existence of disordered glassy and ordered ferrimagnetic phases [62]. Similarly, both ordered and disordered dielectric phases may exist simultaneously. The complex phase behaviour of this material is attributed to the non-stoichiometric oxygen content, and variation in the local density of oxygen vacancies in this material. In addition to the $Fe^{2+}/Fe^{2+}$ charge order, oxygen vacancies will yield local dielectric anomalies in the lattice. An applied

electric field will not only interact with the dipole moments associated with the charge order, but also stabilise particular configurations of the oxygen vacancies resulting in an overall more ordered state.

The presence of simultaneously disordered and order magnetic states in the sample volume as demonstrated by Phan *et al.* [62], and incomplete charge order as demonstrated here indicate that less than 100% of the sample volume contributes to the x-ray and neutron scattering cross-sections associated with the charge and magnetic order respectively. The ratio of the half-integer to integer magnetic satellites is significantly larger than predicted by the magnetic structure factor of suggested spin models [55, 122] and this has been attributed to unexplained contrast between the $Fe^{2+}$ and $Fe^{3+}$ atomic spins by others [56]. Given that the magnetic and charge order are incomplete an alternative theory is proposed, that this ratio is actually the ratio of the ordered sample volumes rather than the magnetic scattering lengths of the lattice sites.

Independent of the mechanism, the results reported here demonstrate incomplete charge order in $LuFe_2O_4$. The applied electric field stabilises the 3-dimensional ferroelectric order in the material resulting in longer correlation lengths and increasing the extent of the charge order within the material.

## 7.6   Summary

In summary, incomplete charge order in $LuFe_2O_4$ is reported as an outcome of this work. Electric field cooling through the ferroelectric transition temperature results in an increase in the proportion of the sample that is charge ordered in addition to increasing the ferroelectric correlation length. Due to the fact both the ferroelectricity and ferrimagnetic order arise from the same Fe sites it is likely this effect is related to the increase in the magnetic ordering induced by electric field cooling through the 3-dimensional magnetic ordering temperature reported in Chapter 6.

The nature of the incommensurate satellites has been shown to be more complicated than is currently represented in the literature, and the analysis presented here is just the beginning of potential analysis of this dataset. JANA2006 is a program that works with both single crystal and powder data to solve incommensurate structures, and future work involves using this tool to investigate the

data collected here.

In addition to the single crystal diffraction reported here and in Chapter 5, x-ray and neutron powder diffraction experiments were performed on this sample. A temperature dependent study investigating the high temperature ferroelectric prototype ($T > 330$ K), ferroelectric phase ($240 < T < 330$ K), and multiferroic phase ($T < 240$ K) is reported in Chapter 8.

# Chapter 8

# Non-resonant powder x-ray and neutron diffraction

## 8.1 Introduction

The complimentary nature of x-ray and neutron diffraction has been well covered in this work with single crystal x-ray and neutron scattering applied in previous chapters to study aspects of the ferroelectric and magnetic order in multiferroic $LuFe_2O_4$. Single crystal diffraction allows both the intensity and distribution in reciprocal space of observed reflections to be measured providing ready information on the structure to commence refinement. However, it may be impossible to measure a large extent of **Q**-space for practical reasons (such as limited degrees of freedom on the diffractometer), or timing considerations.

Alternatively, powder diffraction allows a large range of |**Q**| to be measured at the expense of direct information on the orientational distribution of the intensity in reciprocal space. A number of programs exist to index powder diffraction data and the material phase composition or structure can be solved by methods such as Rietveld refinement, or direct methods by treating the powder diffraction intensities as single crystal data.

Additionally, the complementary benefits of x-rays and neutrons to the study of light elements, magnetism, and structural disorder may be exploited. In this chapter a temperature dependent powder diffraction study employing both x-ray

and neutron diffraction is presented in order to investigate the ferroelectric and magnetic order and the changes at the ferroelectric and multiferroic transition temperatures.

## 8.2 Experimental

Synchrotron radiation is much brighter than that produced by laboratory sources making it potentially possible to observe variations in intensity or additional peaks that are otherwise too weak to be observed. Accordingly, synchrotron x-ray powder diffraction was performed on the powder diffraction beamline of the Australian Synchrotron in Melbourne, Australia while neutron diffraction was performed on the high resolution powder diffractometer, ECHIDNA, at the OPAL reactor in Sydney, Australia.

### 8.2.1 Synchrotron x-ray powder diffraction

A small portion of the fragmented $LuFe_2O_4$ was ground into a fine powder and loaded to a length of approximately 2 cm within two 0.3 mm glass capillaries. The capillaries were sealed using a flame resulting in a final capillary length of approximately 4 cm.

The x-ray energy was tuned to 15 keV and the beamline calibrated by the beamline scientist. A capillary containing a powder sample of NIST standard reference material 660a (lanthanum hexaboride, $LaB_6$) was loaded and a powder pattern collected between 3.2 to 150.5 degrees $2\theta$. One capillary containing the $LuFe_2O_4$ powder was aligned using the fluorescent screen.

Powder patterns were collected as a function of temperature over the range 3.2 to 83.5 degrees $2\theta$ between 160 K to 360 K in variable increment steps. Powder patterns over the full range of $2\theta$ (3.2 to 150.5 degrees) were collected at $160, 220, 250, 280, 320$ and $360$ K.

## 8.2.2 Neutron powder diffraction

A number of fragments of $LuFe_2O_4$ were ground into a powder and loaded into a vanadium canister to a height of approximately 1 cm. The atmosphere of the canister was exchanged with He in a glovebox bag and then the canister was sealed.

A thermocouple was mounted above the sample and the below-sample thermocouple was removed prior to the sample being mounted onto the cryostat. The cryostat was sealed and pumped to high vacuum and the sample loaded onto the stage of the ECHIDNA high resolution powder neutron diffractometer. The sample height was aligned with the aid of a digital neutron camera. The instrument was rotated to a take-off angle of 140 degrees as this corresponded to a wavelength of approximately 2 Å.

Powder patterns were collected across the full detector range ($4^o$ to $164^o$ in $2\theta$) as a function of temperature between 59 and 382 K. A powder pattern of NIST standard reference material 676 (corundum, $\alpha$-$Al_2O_3$) with the same instrument parameters was collected at the same take-off angle.

## 8.3 Data reduction

The x-ray powder diffraction data were provided in ASCII ($2\theta, I, \sigma_I$) format, with one file per detector position. Each scan utilised two or more detector positions, so the separate files were merged using SCILAB. The adjacent detector positions overlapped slightly, which allowed minor offsets in the detector position to be corrected by adding a $2\theta$-offset to the second (and third and fourth where relevant) detector file determined by the complete overlap of reflections common to each pair of files.

The neutron powder diffraction data were reduced from the raw 2D detector dataset by a fully automated procedure in the beamline software GUMTREE. Each scan was output in a separate ASCII text file with the data in ($2\theta, I, \sigma_I$) format.

Individual peak fitting was performed using SCILAB with a Voigt peak-profile function. Full pattern Rietveld refinement and Le Bail extraction was carried out

in FULLPROF [135], while FOX [136, 137] was utilised for its full pattern indexing and inverse solution methods of crystal structure determination. The crystal structure was also investigated by *direct methods* using GSAS [138] and Marching Cubes ELD [139, 140] allowed the resulting Patterson and Fourier maps to be visualised.

### 8.3.1 Instrument Resolution Correction

The PD power diffraction beamline's $LaB_6$ standard was measured in order to accurately determine the wavelength and characterise the instrument's resolution function. However, after carefully examining the results from the Rietveld refinement discussed later and manually fitting the peak widths it is evident that the $LuFe_2O_4$ sample has peaks that are as sharp as, if not sharper than the $LaB_6$ sample. It is therefore not possible to perform a resolution correction on the widths measured as the sharpest peaks are resolution limited. Rather, a qualitative comparison of peak widths and calculated correlation lengths is provided in the following section.

## 8.4 Analysis

The full pattern profile of a powder diffraction pattern is a result of the instrument and sample scattering functions. The instrument resolution is limited by the beam divergence at the sample and detector, and the distribution of wavelengths in the monochromatic beam. Sample broadening is a result of strain and correlation effects in the sample, such as crystallite size or electronic correlation length. In order to accurately determine the wavelength and instrument profile function a standard is refined under the same instrument setup as the sample of interest.

The powder patterns of NIST standard reference materials 676 and 660a were refined by the Rietveld method using the software package FULLPROF [135]. The resulting wavelength, material and instrument parameters are summarised in Table 8.1 for the synchrotron x-ray experiment and Table 8.2 for the neutron experiment.

Not only do the standard reference materials allow the wavelength to be cali-

Table 8.1: Summary of the parameters refined by the Rietveld method using the FULL-PROF package from a synchrotron x-ray powder diffraction pattern of NIST standard reference material 660a collected on the PD beamline of the Australian Synchrotron.

Instrument parameters

| Wavelength (Å) | 0.82765 |
|---|---|
| $2\theta$-Zero (degrees) | 0.0032 |

Material parameters

| $U$ | 0.000516 | $V$ | 0.000042 | $W$ | 0.00018 | | |
|---|---|---|---|---|---|---|---|
| $X$ | 0.006748 | $Y$ | 0.00 | | | | |
| Asym1 | -0.25238 | Asym2 | -0.03111 | Asym3 | 0.58362 | Asym4 | 0.10022 |

| Atom | $X$ | $Y$ | $Z$ | $B$ |
|---|---|---|---|---|
| La | 0.00 | 0.00 | 0.00 | 0.00 |
| B | 0.19750 | 0.500 | 0.500 | 0.00 |

Table 8.2: Summary of the parameters refined by the Rietveld method using the FULL-PROF package from a neutron powder diffraction pattern of NIST standard reference material 676 collected on the ECHIDNA instrument of the OPAL neutron facility.

Instrument parameters

| Wavelength (Å) | 2.048692 |
|---|---|
| $2\theta$-Zero (degrees) | 0.0092 |

Material parameters

| $U$ | 0.1391 | $V$ | -0.3674 | $W$ | 0.3717 | | |
|---|---|---|---|---|---|---|---|
| $\eta$ | 0.402 | | | | | | |
| Asym1 | 0.7810 | Asym2 | 0.3702 | Asym3 | -1.2128 | Asym4 | -0.6218 |

| Atom | $X$ | $Y$ | $Z$ | $B$ |
|---|---|---|---|---|
| La | 0.00 | 0.00 | 0.00 | 0.00 |
| B | 0.19750 | 0.500 | 0.500 | 0.00 |

brated for the sample measurements, but the high quality of the reference materials allows the peak profile function to be used as an indicator of the instrument broadening.

Synchrotron x-ray and neutron powder diffraction experiments were carried out as described in Section 8.2. The wavelengths calibrated from the refinement of the standard reference materials were used to convert the data to a function of $Q$ rather than $2\theta$ as shown in Figures 8.1 and 8.2 for the neutron and x-ray data respectively. The difference in the data ranges that are shown arises due to the difference in the wavelengths chosen for the two techniques. The wavelength for the synchrotron experiment was chosen to correspond to 15 keV well above the absorption edges of $LuFe_2O_4$. On the other hand, the wavelength for the neutron experiment was selected based upon the predicted ECHIDNA instrument resolution and the spacing between adjacent superlattice reflections as a function of wavelength.

The intensities of the x-ray pattern drop off as a function of $Q$, while this is not the case in the neutron pattern. This effect is due to the x-ray form factor (introduced in Section 2.2) which results from scattering from an electron density, but as neutrons scatter from the nucleus the intensities do not decay in the same fashion.

The x-ray and neutron patterns shown in Figures 8.1 and 8.2 have been overlaid and this is shown in Figure 8.3 where the difference in the peak widths between the two patterns may be noted: broader peaks are observed in the neutron case, which is due to the difference in the instrumental resolution function of the two instruments. Although the ECHIDNA instrument is a state of the art monochromatic high resolution neutron powder diffractometer limited flux (as compared to synchrotron radiation) compromises the resolution. Comparison of identical reflections in each pattern demonstrates that the observed intensities differ for every reflection. As introduced in Sections 2.2 and 2.4, this is a result of the differing scattering lengths of x-rays and neutrons for each atomic species. Each occupied lattice site contributes differently to the observed intensity for each case therefore a combined x-ray/neutron approach to structural solutions allows for complex structures and, in particular, structures with light elements to be solved.

Inspection of the peak profiles of reflections in the x-ray diffraction pattern taken at room temperature prior to any heating or cooling of the sample demon-
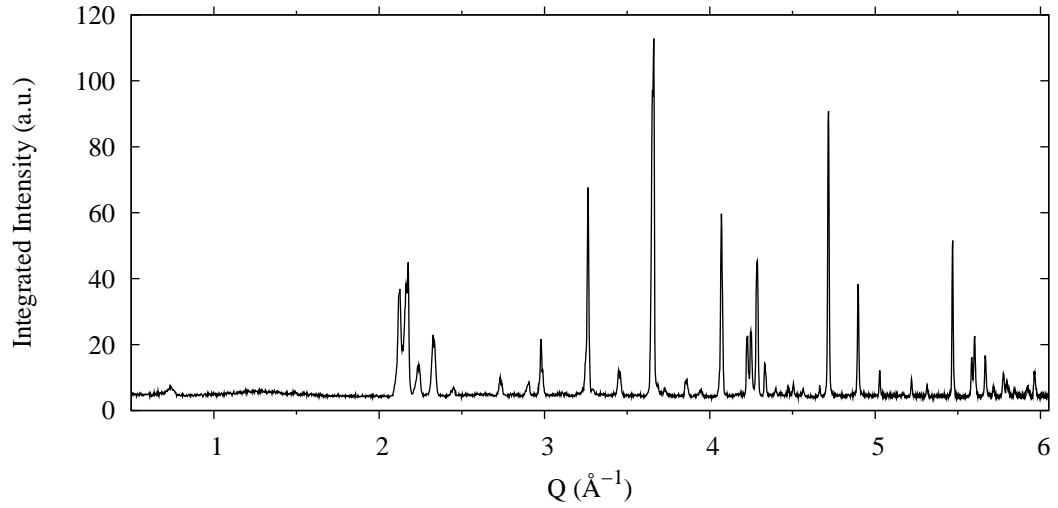
Figure 8.1: Powder neutron diffraction pattern of $LuFe_2O_4$ at 288 K collected on the ECHIDNA instrument of the OPAL reactor in Sydney, Australia.  The full detector range is shown.
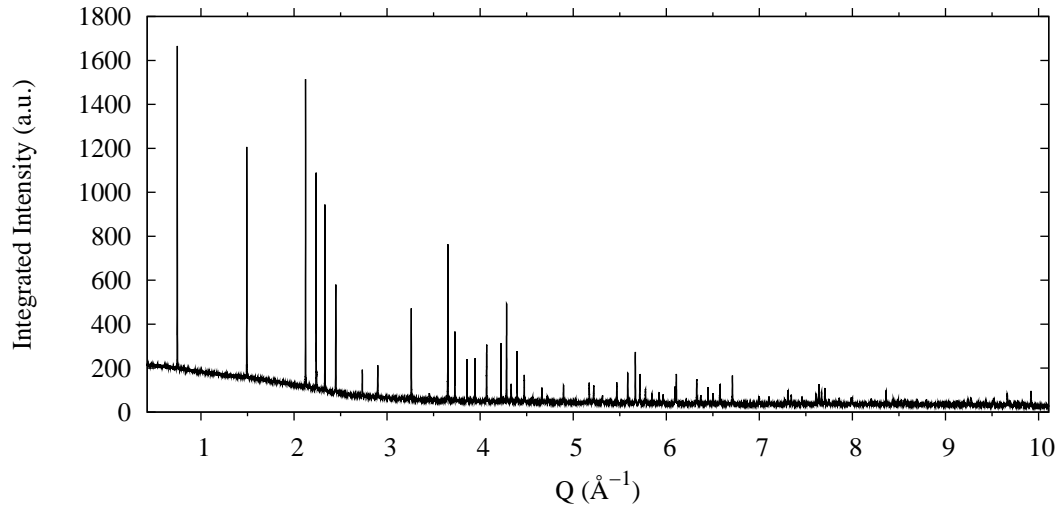


Figure 8.2: Powder synchrotron x-ray diffraction pattern of $LuFe_2O_4$ at 300 K collected on the powder diffraction (PD) beamline of the Australian Synchrotron in Melbourne, Australia.  The full detector range (obtained by merging the data of 4 detector positions) is shown.
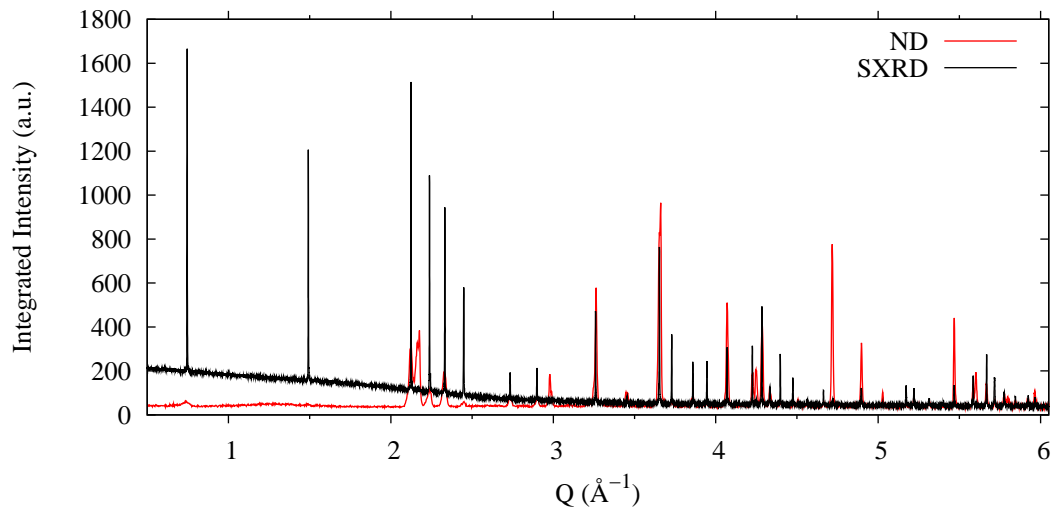
Figure 8.3: Overplot of the neutron and x-ray powder diffraction datasets shown in Figures 8.1 and 8.2 for the range of $Q$ common to both patterns.

strates peak splitting inconsistent with the $R\bar{3}m$ space group at the majority of the peak positions. No peak splitting is observed in the $(0\,0\,3)$, $(0\,0\,6)$, or $(0\,0\,9)$ reflections, but evidence of peak splitting is observed in the $(1\,1\,0)$ reflection and all reflections that are not parallel to the $c^*$-axis; these results are summarised in Figure 8.4.

A similar inspection was made of the neutron diffraction pattern, but due to the difference in the scattering length the $(0\,0\,L)$ reflections are very weak and are unobserved in the pattern. Peak splitting at equivalent $Q$-positions was observed as shown in Figure 8.5; due to the increased peak widths the position of all peaks cannot be accurately determined. The temperature dependence of the pattern was measured from low temperature to values above the ferroelectric transition temperature. As shown in Figure 8.6, magnetic scattering intensity consistent with an Ising system with spins aligned parallel to the $c$-axis was observed as a discontinuous increase in the intensity of the $(1\,1\,0)$ reflection and at superlattice positions below the 3D magnetic ordering temperature. Furthermore, the intensity of the $(1\,1\,0)$ increases slightly and the intensity at super lattice position becomes non-zero below the Néel temperature. There is no discernible change in the intensity of the $(0\,0\,3)$ reflection indicating a negligible component of magnetisation in the $ab$-plane.

Despite the information about the magnetic structure that may be extracted from the neutron diffraction pattern, the increased peak width makes it impossible to accurately determine the position of the split peaks. As the sample was not
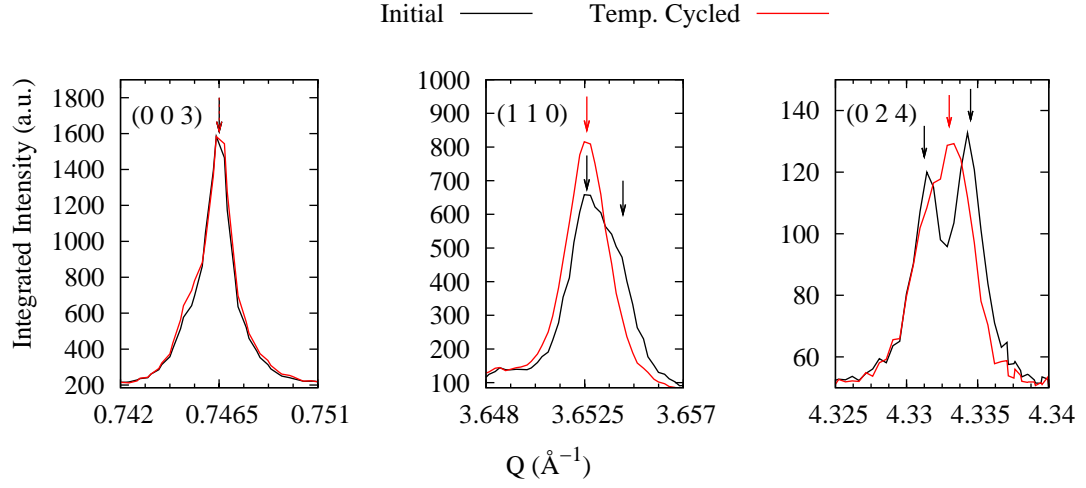
Figure 8.4: Synchrotron x-ray diffraction intensity profiles of the $(0\,0\,3)$, $(1\,1\,0)$, and $(0\,2\,4)$ reflections (as labelled) collected at 300 K after initial sample preparation and then after temperature cycling through the ferroelectric transition temperature.
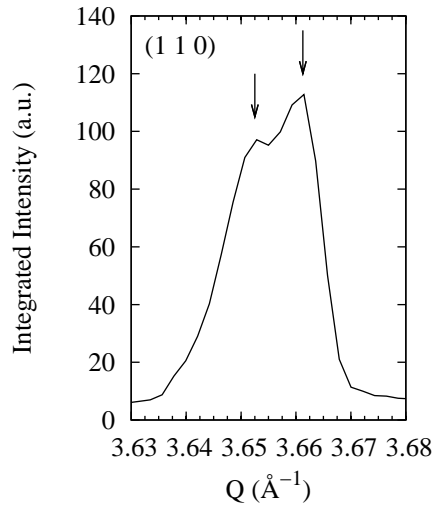


Figure 8.5: Neutron diffraction intensity profile of the $(1\,1\,0)$ reflection collected at 288 K after crushing. Evidence of peak splitting is noted by arrows.
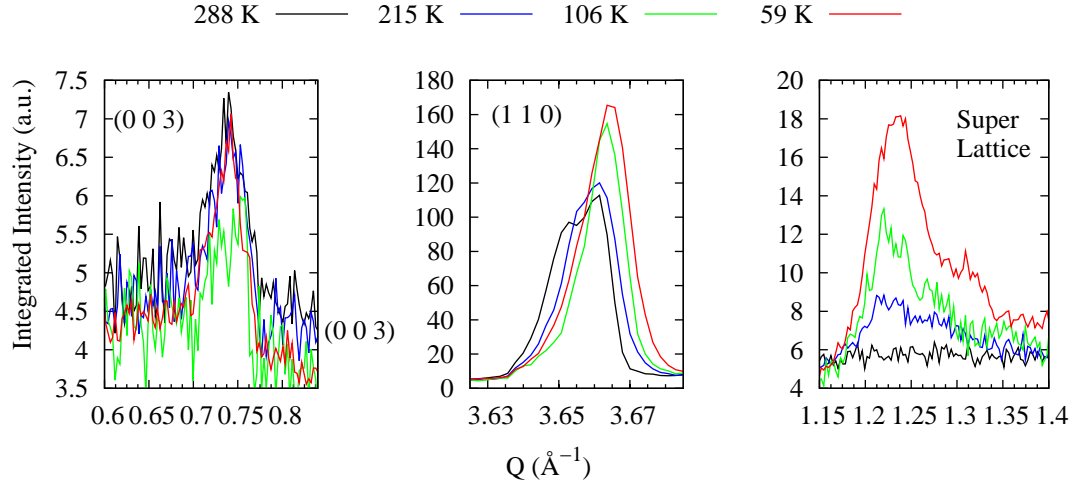
Figure 8.6: Temperature dependence (shown in legend) of the $(0\,0\,3)$, $(1\,1\,0)$, and super-lattice reflections as measured by neutron diffraction through the magnetic transition temperature.

temperature cycled through the ferroelectric transition temperature, this peak splitting is present in all datasets collected below 330 K. Due to this, full analysis of the neutron powder patterns was delayed until a model that could accurately reproduce the pattern was determined from the x-ray data; however, further analysis of the neutron data was beyond the scope of this work as such a model has not yet been obtained.

Individual peak fitting was performed on selected reflections from the x-ray diffraction patterns in order to establish the temperature dependence of material properties. The fitting of the $(0\,0\,3)$, $(0\,0\,6)$, $(0\,0\,9)$, $(1\,1\,0)$, and $(2\,2\,0)$ reflections is summarised here as these reflections correspond to the main crystallographic directions of the hexagonal structure. The peak profiles of the $(0\,0\,3)$ and the $(1\,1\,0)$ reflections are plotted for the temperature series in Figure 8.7.

The peak height of the $(0\,0\,3)$ reflection appears to increase with decreasing temperature, while the $Q$-position of the peak decreases and the peak appears to broaden. On the other hand, the peak height of the $(1\,1\,0)$ reflection decreases with decreasing temperature, while the $Q$-position of the peak increases and the peak width appears to increase. These trends were investigated by fitting the peak profiles with Lorentzian functions in SCILAB.

The integrated intensity and FWHM of the $(0\,0\,3)$ reflection are shown in Figure 8.8 and these results for the $(0\,0\,6)$ reflection are also shown in Figure 8.9 due to the large distribution of points in Figure 8.8 as the low-angle peak asym-
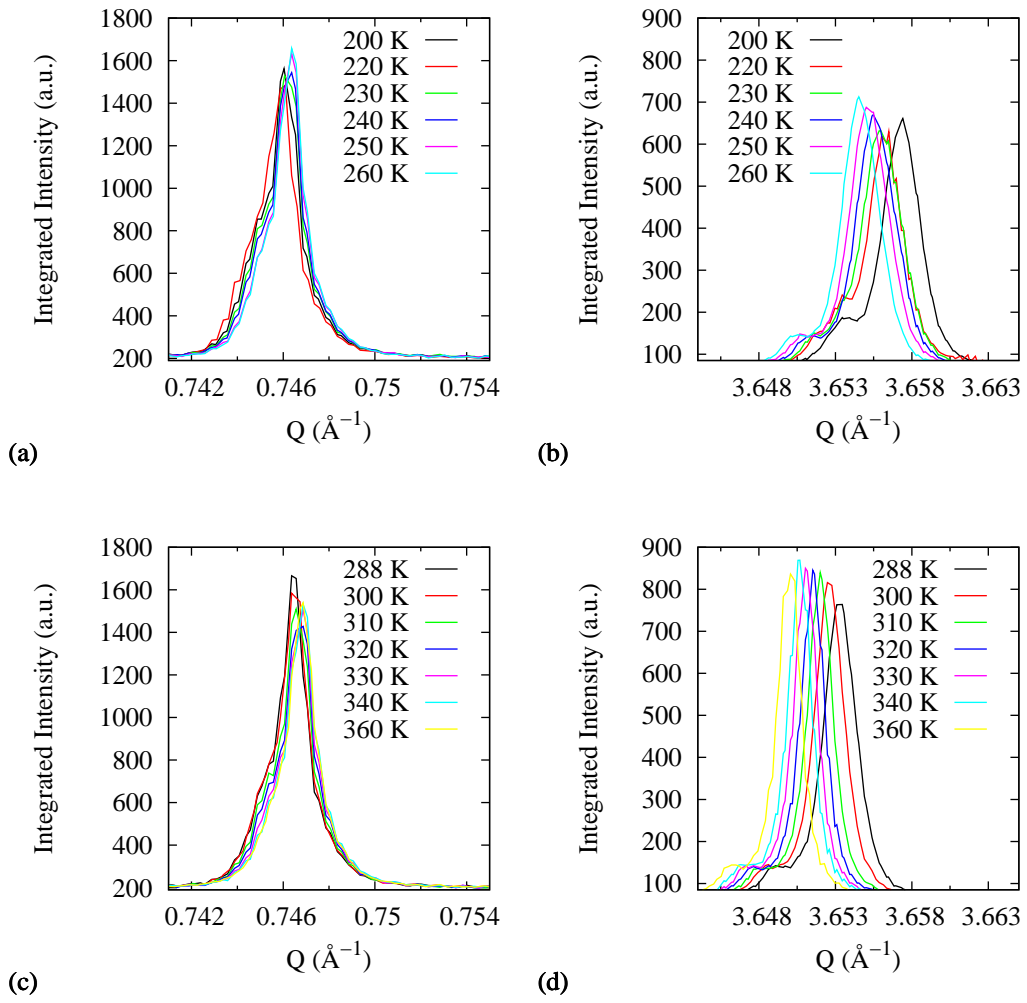
Figure 8.7: Synchrotron x-ray intensity profiles of the (a,c) (0 0 3) and (b,d) (1 1 0) reflections plotted as a function of temperature.

metry of the $(0\,0\,3)$ reflection is not considered in the Lorentzian peak profile function. An increase in the integrated intensity of these reflections is observed with decreasing temperature, with a step corresponding to the ferroelectric transition temperature that has a similar shape to the temperature dependence of the charge ordered superlattice reflections reported in Chapter 3. A sharpening of the $(0\,0\,L)$ reflections is observed through the ferroelectric transition.

The fitted integrated intensity and FWHM of the $(1\,1\,0)$ reflection are shown in Figure 8.11. As temperature decreases the integrated intensity increases, with a step at approximately 310 K. Similar broadening of the $(H\,H\,0)$ reflections is observed below 310 K. This step in the intensity and peak width occurs approximately 20 K below the ferroelectric transition.

The changes in the $Q$-position of the $(0\,0\,3)$ and $(1\,1\,0)$ reflections noted earlier correspond to the expansion (or contraction) of the cell parameters. The cell parameters calculated from the positions of the peaks are shown as a function of temperature in Figure 8.12. Anisotropic thermal expansion is observed, with negative thermal expansion of the $c$-axis.

Both the $(H\,H\,0)$ and $(0\,0\,L)$ sets of reflection have been shown to have a step in the peak width as a function of temperature which corresponds to changes in the strain within the material, the correlation length (crystallite size or ferroelectric domain size), or both. These two properties contribute differently to the peak width as a function of $Q$: the correlation length produces a constant peak broadening, while the broadening from the strain component increases with increasing $Q$. Plotting the FWHM of the peaks as a function of $Q$ allows the two components to be extracted as the inverse correlation length will be the vertical intercept and the strain component the gradient.

The values of the FWHM obtained for the $(0\,0\,3)$, $(0\,0\,6)$ and $(0\,0\,9)$ reflections from the Lorentzian profile fit were fitted with a linear function as a function of temperature and the gradient and vertical intercept noted. The $(0\,0\,3)$ reflection was omitted as the low-angle asymmetry produced inaccurate peak width values. The resulting gradient and correlation length calculated from the vertical intercept (without correcting for instrument broadening) are plotted in Figure 8.13(a) and (b) respectively. Despite the apparent step in the peak width shown in Figure 8.9(b) the trends plotted here demonstrate minimal difference between the correlation length and strain before and after the ferroelectric transition. Rather, the system passes through a maximum in both of these values at the ferroelectric
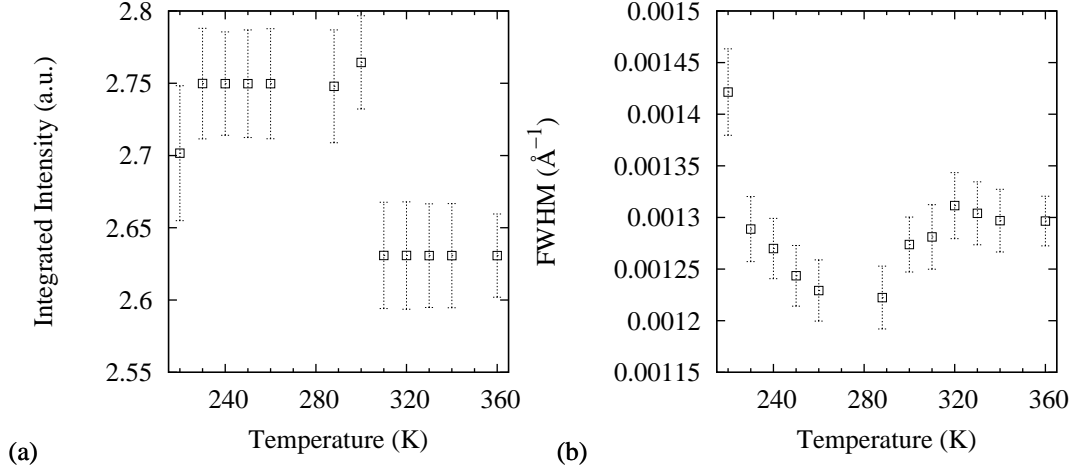
Figure 8.8: Temperature dependence of the (0 0 3) reflection obtained by fitting a Lorentzian profile function: (a) the integrated intensity and (b) the full width at half maximum (FWHM).
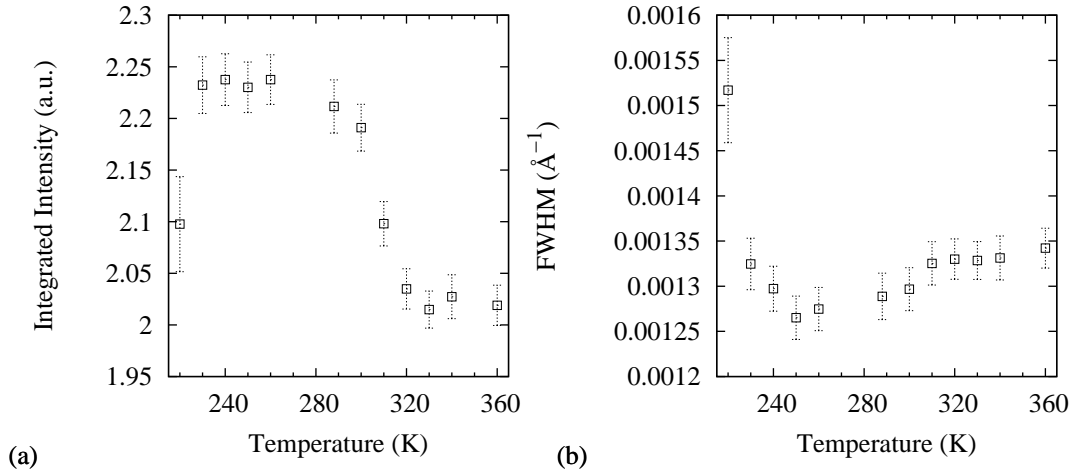


Figure 8.9: Temperature dependence of the (0 0 6) reflection obtained by fitting a Lorentzian profile function: (a) the integrated intensity and (b) the full width at half maximum (FWHM).
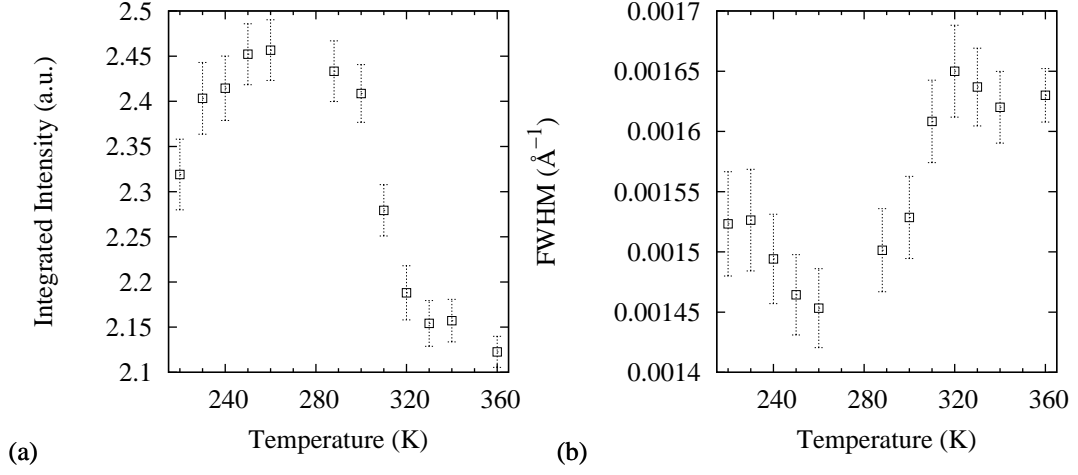
Figure 8.10: Temperature dependence of the $(0\,0\,9)$ reflection obtained by fitting a Lorentzian profile function: (a) the integrated intensity and (b) the full width at half maximum (FWHM).
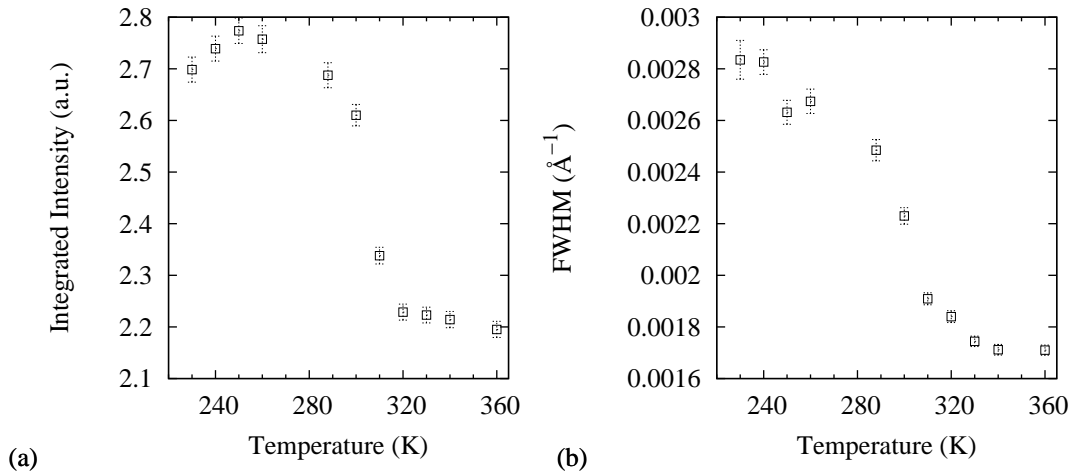


Figure 8.11: Temperature dependence of the $(1\,1\,0)$ reflection obtained by fitting a Lorentzian profile function: (a) the integrated intensity and (b) the full width at half maximum (FWHM).

(a)  (b)
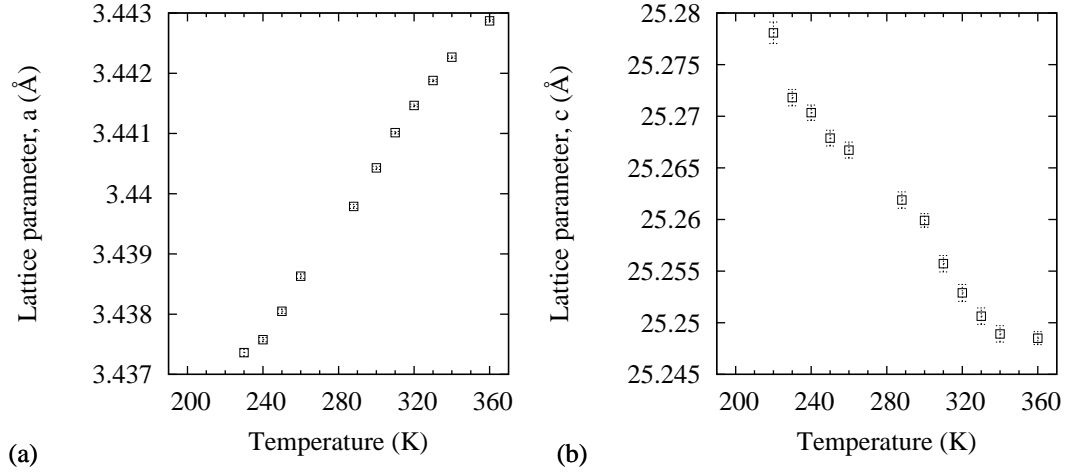
Figure 8.12: Lattice parameters as determined from the Lorentzian profile fitting of the
$(H\,H\,0)$, and $(0\,0\,L)$ type reflections.



(a)  (b)
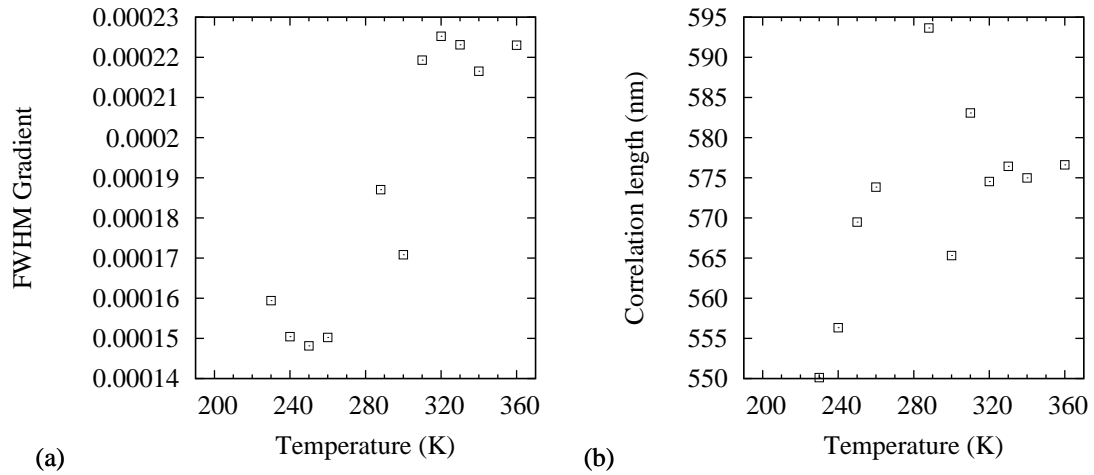
Figure 8.13: Temperature dependence of the gradient (a), and correlation length calcu-
lated from the vertical intercept (b) determined by fitting a linear profile to the FWHM
vs. $Q$ plots of the $(0\,0\,6)$ and $(0\,0\,9)$ reflections.

transition temperature. This behaviour is consistent with the critical behaviour expected through the second order transition, similar to the magnetic critical behaviour characterised in Chapter 5.

Full pattern Rietveld refinement was performed using the FULLPROF package on each x-ray diffraction pattern with a pseudo-Voigt peak profile function. The peak profile parameters, $U$, $V$, $W$, $X$, and $Y$; cell parameters, $a$ and $c$; instrument zero, $2\theta_0$; background, a linear interpolation of points; atom positions, $z$ coordinates of Fe- and O-sites; isotropic thermal parameters, for both O-sites; and anisotropic thermal parameters for the Lu and Fe sites were refined at each temperature. The absorption correction was determined by two methods: it was calculated based upon the density and atomic attenuation lengths obtained from the literature and a 50% packing factor was assumed, and alternatively the absorption correction was progressively increased in steps until positive thermal parameters were obtained in the refinement. Due to the uncertainty in the packing density, the latter value was used in the refinement of the temperature series.

The full pattern refinement of the 360 K pattern is shown in Figure 8.14 and the difference pattern is fairly similar as a function of temperature. The goodness of fit parameters for the Rietveld refinements are presented in Table 8.3 for each temperature. There are a number of weak reflections that are unindexable within the $R\bar{3}m$ space group and these contribute to the error in the full pattern fit; these reflections are addressed in further detail later. Additionally, inspection of the difference plot shown in Figure 8.14 indicates the intensity of a number of reflections are not accurately reproduced by the model. Considering only the data points that contribute to reflections predicted by the $R\bar{3}m$ model (the "Bragg Component") demonstrates an improving trend in the goodness of fit (GoF) and $\chi^2$ increases as temperature decreases until the magnetic transition at which point these parameters increase.

The Rietveld refinements demonstrate that there exists an error in the reproduction of the peak intensities with the R$\bar{3}$m model used. These errors were inspected and it was determined they could not be accounted for by reasonable adjustments to the model, for example the inclusion of preferred orientation. As this was the case, *direct methods* were applied using GSAS in order to try and explain these intensity variations.

Full pattern Rietveld refinement was performed in GSAS after which the intensities were extracted by both the Rietveld and Le Bail methods. The Patterson
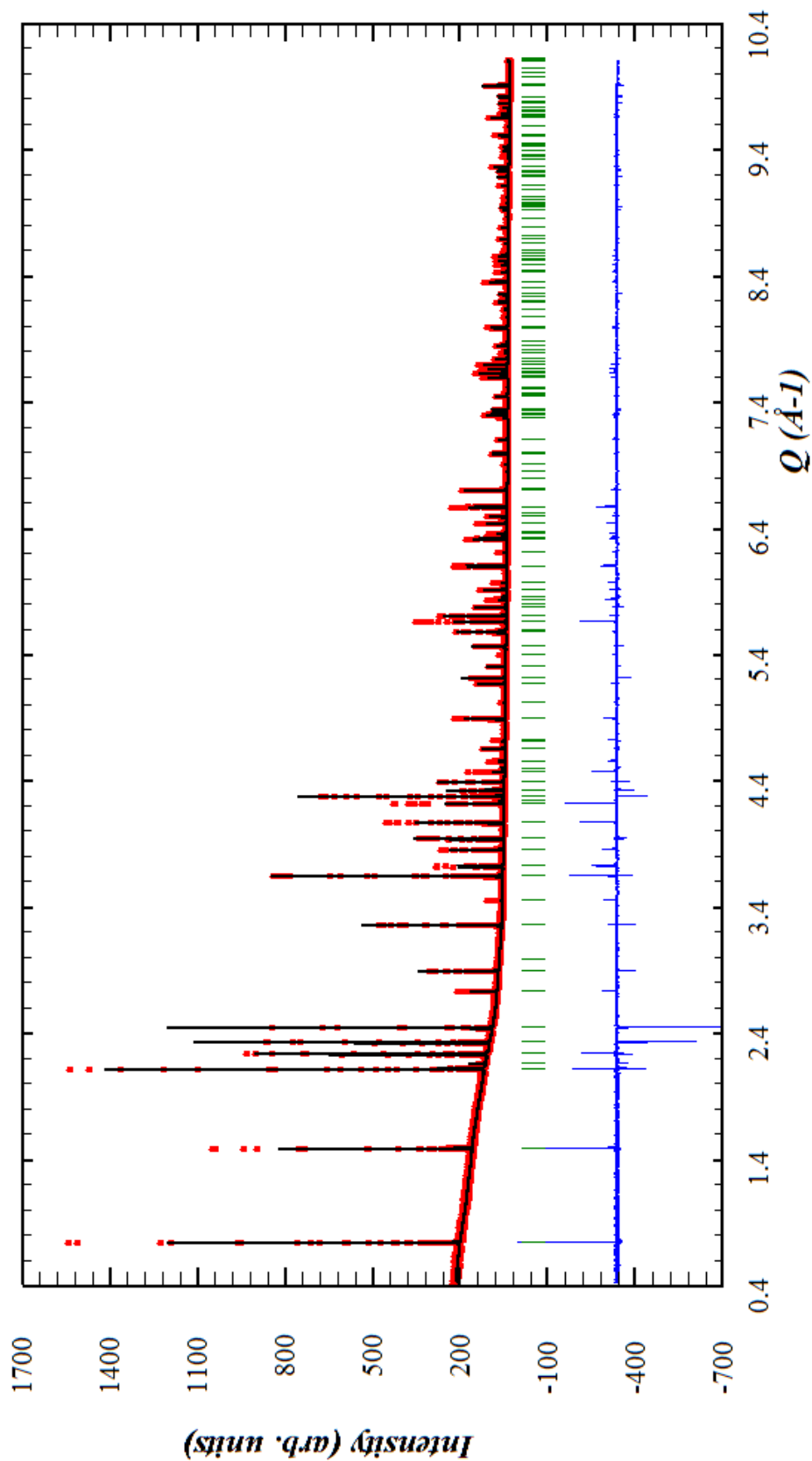
Figure 8.14: Plot of the synchrotron x-ray powder pattern collected at 360 K fitted by Rietveld refinement with the difference and calculated peak positions shown.

Table 8.3: Goodness of fit parameters for the Rietveld refinement of the x-ray temperature series performed using FULLPROF.

| $T$ (K) | Full Pattern | | | | | Bragg Component | | | | |
|---|---|---|---|---|---|---|---|---|---|---|
| | $R_p$ | $R_{wp}$ | $\chi^2$ | $D$ $(\times 10^3)$ | GoF | $R_p$ | $R_{wp}$ | $\chi^2$ | $D$ $(\times 10^3)$ | GoF |
| 360 | 47.8 | 29.1 | 6.542 | 9.31 | 2.6 | 29.9 | 27.5 | 12.09 | 8.4 | 3.5 |
| 340 | 47.8 | 29.2 | 6.649 | 9.50 | 2.6 | 29.8 | 27.7 | 12.26 | 8.57 | 3.5 |
| 330 | 48.6 | 29.5 | 6.516 | 9.57 | 2.6 | 30.3 | 27.9 | 11.97 | 8.64 | 3.5 |
| 320 | 48.3 | 29.6 | 6.482 | 9.71 | 2.5 | 30.8 | 28.1 | 11.70 | 8.82 | 3.4 |
| 310 | 47.9 | 29.8 | 6.580 | 9.88 | 2.6 | 31.1 | 28.4 | 11.35 | 9.02 | 3.4 |
| 300 | 46.0 | 30.5 | 6.896 | 10.7 | 2.6 | 32.1 | 29.3 | 10.71 | 9.97 | 3.3 |
| 287 | 45.7 | 30.8 | 7.271 | 11.1 | 2.7 | 32.5 | 29.7 | 11.01 | 10.3 | 3.3 |
| 260 | 44.8 | 30.4 | 7.247 | 11.0 | 2.7 | 32.2 | 29.3 | 10.75 | 10.2 | 3.3 |
| 250 | 44.5 | 30.4 | 7.297 | 11.1 | 2.7 | 32.2 | 29.4 | 10.78 | 10.3 | 3.3 |
| 240 | 44.2 | 30.7 | 9.239 | 11.0 | 3.0 | 32.3 | 29.8 | 13.64 | 10.4 | 3.7 |
| 230 | 43.6 | 30.6 | 9.096 | 11.0 | 3.0 | 31.9 | 29.7 | 13.40 | 10.4 | 3.7 |

map calculated for the 288 K dataset is shown in Figure 8.15(a) and the set of unique hexagonal vectors that describe the maxima shown in the Patterson map are tabulated in Table 8.4. Each maximum of the Patterson map can be assigned to an interatomic vector of the $R\bar{3}m$ structure indicating there are no missing occupied sites in the given model. The effect varying the Rietveld parameters had on the Fourier map was investigated by generating maps using both the full pattern and full pattern excluding the low angle reflections.

The Fourier map produced by excluding the low angle reflections is shown in Figure 8.15(b) where the lutetium (green), iron (blue), and oxygen (red) are shown with interconnecting bonds. Coloured isosurfaces of constant electron density are shown with green representing negative density ($\rho = -3.5$), blue positive density ($\rho = +3.5$), and red very positive density ($\rho = 5$). Positive density is centred about the Lu sites with 6 negative nodes symmetrically distributed around the site, indicating the refined anisotropic thermal parameters do not correctly

Table 8.4: The maxima of the Patterson map shown in Figure 8.15(a) determined from the GSAS peak search program with $\rho_{min} = 300$.

| $\rho$ | X | Y | Z | Interatomic vector |
|---|---|---|---|---|
| 9274.483 | 0.0000 | 0.0000 | 0.0000 | ALL |
| 3879.705 | 0.6677 | 0.3329 | 0.1225 | Lu-Fe |
| 925.332 | -0.0024 | 0.0024 | 0.1272 | Lu-O |
| 779.1288 | 0.62500 | 0.31250 | 0.03125 | Lu-O |
| 667.286 | 0.0017 | -0.0017 | 0.0842 | Fe-O |
| 499.3241 | 0.31250 | 0.62500 | 0.00781 | Fe-O |
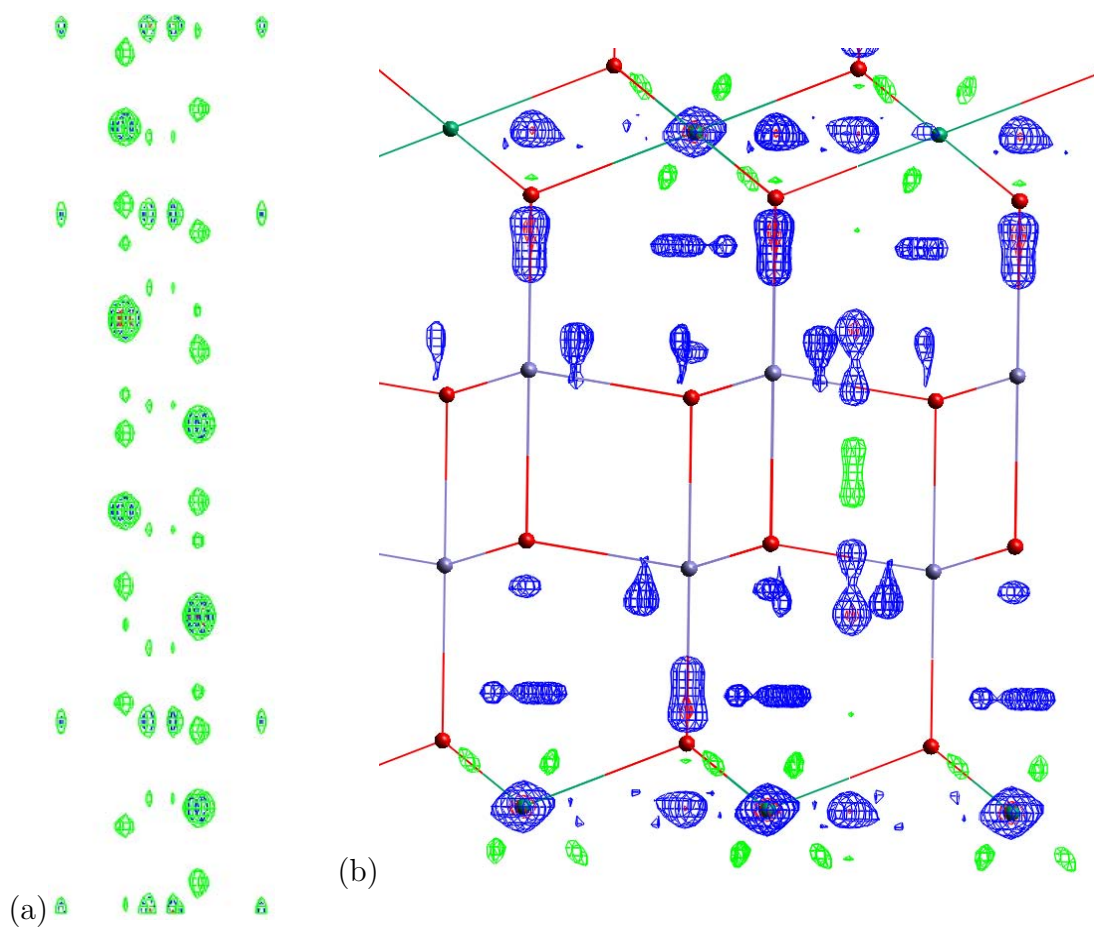
Figure 8.15: (a) The Patterson map calculated from the 288 K synchrotron x-ray diffraction pattern using GSAS and (b) the difference Fourier map calculated from the best Rietveld refinement of the 288 K dataset obtained with the reflections with a $2\theta$ position below $21^o$ excluded. Isosurfaces are shown where green corresponds to negative density ($\rho = -3.5$), blue is positive density ($\rho = +3.5$), and red is very positive density ($\rho = 5$).

model the density calculated from the observations. Anisotropic positive density is shown between the Lu-O-Fe oxygen, between the O and Fe positions. As a small region of negative density is also observed between the Lu and O, the positive density is attributed to disorder of the oxygen site with a slight error in the oxygen position. This is further supported by the negative density, indicating the oxygen should be slightly closer to the iron with a distribution of shorter Fe-O bond lengths in the sample.

Elongated rods of negative density are observed (for example in the middle-right of the image) with two double-node positive regions mirrored about the negative density (above and below). As there are no atoms in the model to contribute electron density at these positions, for they are the interstitial columns of the hexagonal lattice, it is not possible to calculate negative density at these positions. Therefore, these columns of density are attributed to Fourier truncation error. Further small regions of positive density are observed, but these are attributed to maxima in the background of the Fourier map and should be reinvestigated once the lutetium and oxygen densities have been accounted for.

Fixing the scale constant, removing the low-angle exclude region, and further refining all parameters lead to a greater difference between the Fourier maps. This increase in the erroneous electron density associated with the low angle reflections coupled with the extra density around the Lu sites in the Fourier map shown in Figure 8.15(b), indicates the absorption correction is not correct.

Weak unindexed reflections, mentioned earlier, were observed in the synchrotron x-ray powder patterns. Initially, both the possibility that these reflections were from an impurity phase, or alternatively that they were representative of small displacements of the high temperature structure were considered. The peak positions were noted and the full pattern including these values was run compared against the powder diffraction file (PDF) database; however, only the known high temperature structure was found matching the already indexable reflections.

Following this the whole pattern was indexed in FOX from which both monoclinic and orthorhombic solutions were suggested. Parallel tempering methods were applied to two starting scenarios: all atoms at the origin, and the high temperature structure transformed into the coordinates of the new space groups. The atomic positions of the Lu, Fe, and O were allowed to vary with the positions of the other two atoms fixed, and finally the positions of all atoms were allowed to

vary. The number of atoms was divided by the multiplicity of different possible sites within the unit cells, and the result compared against the density in all cases. The unit cells were transformed into P1 and the optimisation procedure repeated. It was determined that sufficient displacement of the Lu or Fe atoms from their hexagonal coordinates to produce adequate intensity at the unindexed positions also produced unobserved intensity at other positions. The oxygen position optimisation runs found that the oxygen formed tight clusters likely representing heavier electron density. FOX is unable to make an absorption correction to the data, so the absorption model was extracted from the FULLPROF refinements and the data manually corrected in SCILAB. The Fourier transforms discussed earlier demonstrated a potential error in the absorption correction which produced extra electron density which could result in the layering and clustering of oxygen observed in FOX.

Following the failure to describe the reflections by modelling the data, the possibility that they resulted from an impurity phase was reinvestigated. The PDF analysis eliminated the starting reagents and other Lu-O, Fe-O, and Lu-Fe-O phases; however, the chemically similar but structurally different $M\mathrm{Fe_2O_4}$ (where $M$ is a transition metal) spinel ferrite was investigated. The structure of this phase is cubic with $a \approx 8$ Å and the indexing of the unexplained reflections based upon this spinel ferrite model is shown in the second column of Table 8.5. Only 5 reflections could be indexed, so a more general approach was taken to look for the $Q$ values corresponding to the reciprocal lattice vectors. The three smallest values of $Q$ were selected and the values of $Q$ calculated for integer miller indices assuming $90^o$ angles between the three vectors. As shown in the third column of Table 8.5, a further 3 reflections were indexed by this model. Furthermore, $(h\,k\,0)$ and $(h\,0\,l)$ reflections were indexed by this method, but no $(0\,k\,l)$ reflections were indexed suggesting that the $(0\,1\,0)$ and $(0\,0\,1)$ reflections are not perpendicular in this model.

Comparison of the intensities of these peaks in the synchrotron and neutron datasets shows a large increase in intensity in the neutron case which indicates the diffracted intensity likely originates from the oxygen sites as it has a weak x-ray scattering length, but a neutron scattering length that is comparable to that of lutetium and iron.

Table 8.5: Indexing results for the reflections observed in the synchrotron x-ray patterns that are unindexable with respect to the high temperature or expected ferroelectric superstructure for (a) a spinel ferrite model and (b) a generic monoclinic model.

| $Q$ (Å$^{-1}$) | Spinel Ferrite | Monoclinic |
|---|---|---|
| 1.49496 | (200) | (100) |
| 2.24201 | (221),(300) | (010) |
| 3.64805 | - | (001) |
| 3.73677 | (430),(500) | (210) |
| 3.86291 | - | - |
| 4.074 | - | - |
| 4.48359 | (600) | (300), (020) |
| 4.89210 | - | - |
| 5.3089 | - | - |
| 5.57757 | - | - |
| 6.3188 | - | - |
| 6.33646 | - | (320) |
| 6.572 | - | - |
| 7.000 | - | (401) |
| 6.705 | - | - |
| 7.112 | - | - |
| 7.29533 | - | (002) |
| 7.98322 | - | - |
| 8.2559 | (11 0 1),(9 5 4) | - |

# 8.5   Discussion & Summary

The synchrotron x-ray and neutron powder diffraction patterns collected following sample preparation by crushing, but prior to temperature cycling, demonstrate a peak splitting consistent with a structural distortion in the *ab*-plane such that $\gamma \neq 120^o$. This effect was shown to be reversible as after heating and cooling through the ferroelectric transition temperature the peak splitting was no longer apparent in the synchrotron data; however, as the low temperature data were collected before the high temperature data in the neutron diffraction experiment the splitting is observed in all datasets. Furthermore, due to the broad peak widths of the neutron data the dataset was put aside until a model consistent with the splitting could be obtained from the high resolution x-ray data.

Ferroelectricity, ferroelasticity, and piezoelectricity are all intrinsically related as the ferroelectric polarisation arises from displacements within the crystal lattice that lead to strain as atoms deviate from their average positions. $LuFe_2O_4$ has a layered structure and it has been shown that strong forces tend to cleave the crystal leaving the $(0\,0\,1)$ surfaces exposed. The force required to cleave in any

other direction is greater, and the force of crushing the sample will both cleave and induce strain into the crystal lattice. Accordingly, through the piezoelectric effect, crushing the sample polarises the material. Upon heating the sample through the ferroelectric transition temperature the material is depolarised and the sample returns to the original structure as observed in this work.

Monoclinic structural distortions of this type in $LuFe_2O_4$ have only been reported in the presence of a strong applied magnetic field, and the data analysis of the single crystal electric field work in Chapter 7 did not indicate any peak splitting. It is possible that due to competing effects in the sample the applied electric field is only able to induce a polarisation in the sample consistent with unobservable atomic displacements; however, the large and rapidly applied forces during crushing cause a greater polarisation associated with observable displacements as the potential energy barrier may be overcome. This hypothesis may be further investigated by comparing the monoclinic distortion reported here with that of the related charge ordered material $Fe_2OBO_3$ [141].

Individual peak fitting of the synchrotron data using a Voigt peak profile function demonstrated that the intensity of the $(H\,H\,0)$ and $(0\,0\,L)$ type reflections increases through the ferroelectric transition temperature and that the peaks sharpen to a minimum value at the transition temperature attributed to critical behaviour. In the magnetic case this behaviour would only be observable in peaks corresponding to the magnetic propagation vector; however, in the case of the ferroelectric transition the polarisation is mediated by strain within the crystal and therefore the reflections analysed here are sensitive to the ferroelectric ordering due to the resulting lattice distortions.

Rietveld refinement, and direct and parallel tempering methods were employed to investigate the differences between the observed intensities and those predicted by the high temperature ferroelectric prototype; however, no clear results were obtained as it was shown the absorption correction has a large impact on the result and is currently insufficient to apply these methods.

Furthermore, weak reflections in the synchrotron data were manually indexed and preliminary results indicate a monoclinic solution. These peaks appear of similar intensity to the normal structural reflections in the neutron data indicating they most likely result from the oxygen sublattice.

The powder diffraction study presented here has demonstrated the unique and

complex properties of this material and further work is proposed. Comparison of the structure observed here with that observed in charge ordered $Fe_2OBO_3$ would allow the relationship between the crushing-induced monoclinic distortion and the polarisation to be investigated, while refinement of the absorption correction and a full analysis of the proposed monoclinic distortion of the oxygen sublattice would provide valuable insights into the role the oxygen anions play in this material.

# Chapter 9

# Conclusion and outlook

In this thesis, neutron and x-ray scattering techniques have been applied to investigate the magnetic and electronic properties of multiferroic $LuFe_2O_4$. Resonant x-ray scattering (RXS) was performed and the electronic and orbital state of the charge ordered Fe-sublattice characterised. Anomalous scattering functions for the $Fe^{2+}$ and $Fe^{3+}$ sites were obtained, and complementary x-ray absorption near edge structure (XANES) calculations were carried out in order to investigate the differences between these functions. An applied field study was performed with both *ex situ* and *in situ* single crystal neutron diffraction and *ex situ* single crystal x-ray diffraction in order to study the magnetoelectric coupling in the multiferroic state. Furthermore, the relationship to the high temperature ferroelectric state was investigated. Finally, synchrotron x-ray and neutron powder diffraction was performed in order to characterise the structural changes associated with the frustrated ferroelectric and ferrimagnetic order.

The RXS experiment, discussed in Chapter 3, was analysed by iterative non-linear regression using a custom Levenberg-Marquadt algorithm. Anomalous scattering functions were obtained for both the $Fe^{2+}$ and $Fe^{3+}$ sites of which the imaginary parts are plotted in Figure 9.1. The energy shift between the two functions was determined to correspond to full $Fe^{2+}/Fe^{3+}$ charge disproportionation by comparison with XANES fingerprinting of these electronic configurations reported in the literature. Furthermore, Nagano *et al.* [97] predicted that not only was the orbital degree of freedom active on the $Fe^{2+}$ sites in this geometry, but that a disordered orbital state exists in $LuFe_2O_4$. RXS is sensitive to the anisotropic electron density associated with orbital ordering with an expected azimuthal and polarisation dependence. The energy dependence of the RXS in-
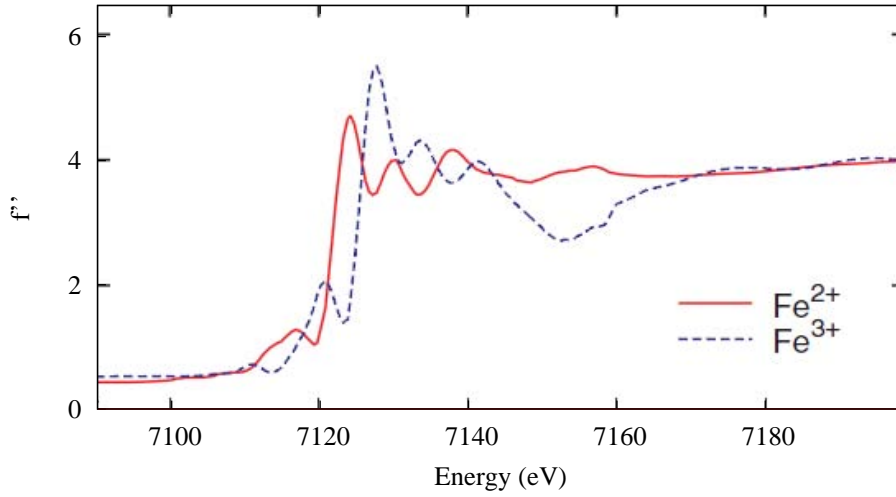
Figure 9.1: The imaginary part of the anomalous scattering factors obtained for the $Fe^{2+}$ and $Fe^{3+}$ sites from the non-linear least squares fitting of resonant x-ray scattering data by the anomalous structure factor about the Fe K-edge. Reported in Chapter 3.

tensity for both the azimuthal angle and polarisation channel was measured and no dependence on either parameter was observed. As a result, the direct observation of a glassy orbital state is reported [126].

XANES calculations using FDMNES and FEFF, reported in Chapter 4, were performed and the physical significance of the anomalous scattering factors obtained in Chapter 3 was investigated. Calculations were performed on an isolated $FeO_5$ molecule, the periodic R$\bar{3}$m structure reported in the literature, and the P1 representation of the charge order super-structure [83]. The charge disproportionation was modelled by shifting electrons from the $3d$ to $4p$ state, and the best result with the charge ordered P1 structure is shown in Figure 9.2. The fits of the anomalous scattering factors obtained from these functions to the resonant x-ray scattering data reported in Chapter 3 showed the energy dependence was reproduced, but further work modelling the anisotropic oxygen displacements is planned in order to better reproduce the magnitude of the oscillations.

Inelastic neutron scattering was carried out on the PUMA beamline of the FRMII, Germany in order to perform a preliminary investigation of phonon mode softening associated with the ferroelectric transition. No mode softening was observed; however, a feature about the $\mathbf{Q} = (1.35\,0.3\,0)$ was observed that was diffuse in $E - \mathbf{Q}$ space. This feature was characterised by collecting both energy loss and $\mathbf{Q}$ scans as a function of temperature from 30 to 400 K. A Lorentzian tail was observed in the energy loss scans, and the temperature dependence of the integrated intensity of this scattering was consistent with critical scattering
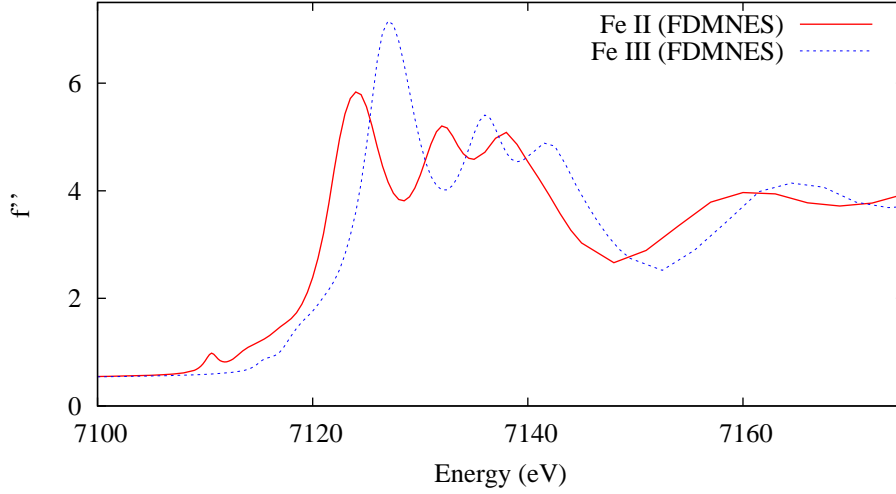
Figure 9.2: The imaginary part of the anomalous scattering factors calculated from the FDMNES XANES calculations of the P1 charge ordered structure reported in Chapter 4.

through the magnetic transition; this is shown in the integrated intensity of the plotted as Figure 9.3. A hyperbolic divergence is expected at the critical temperature which would be characterised by an asymptote, yet a broad maximum was observed which has been attributed to the distribution of oxygen content in the sample and ferroelectric fluctuations measured due to poor *c*-axis resolution. The intensity profile is asymmetric at high temperature and this has been attributed to fluctuations in the ferroelectric phase. Further work is recommended using a polarised cold neutron instrument as this will increase the resolution of the measurements, and allow the magnetic and charge contributions to the scattering to be separated by polarisation analysis.

An applied electric field study was performed using the E2 flat cone diffractometer of the Helmholtz-Zentrum Berlin, Germany in order to study the magnetoelectric coupling. Two-dimensional magnetic order was observed at 235 K characterised by diffuse scattering without any defined Bragg peaks, while well defined three-dimensional order was observed at 180 K. These results provide direct evidence of a 2D-to-3D magnetic ordering process that has only been speculated up until this point in time, as other samples have only been reported to be either 2-or-3 dimensionally ordered. The ordering temperature coincides with a maximum in the linear susceptibility and the step in the polarisation in the multiferroic phase and explains why the step occurs 35 K below the Néel temperature in this sample. Electric field cooling from above the ferroelectric transition temperature to below the Néel temperature was shown to influence the magnetic domain population and it was proposed that the mechanism is the interaction
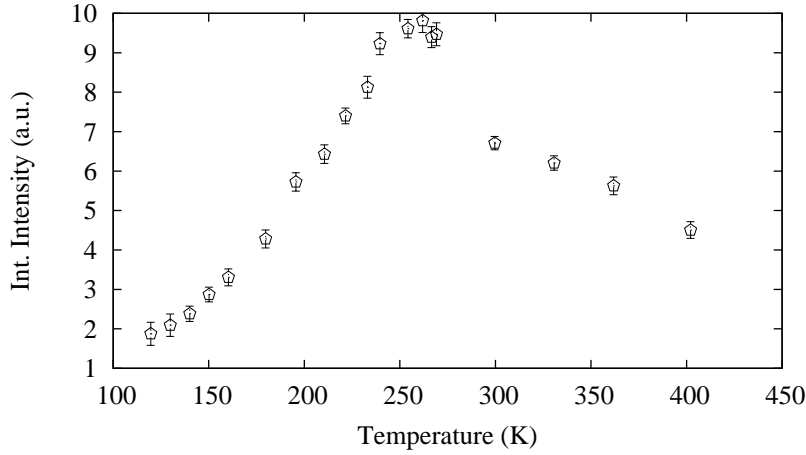
Figure 9.3: The temperature dependence of the integrated intensity of the spectral profile fitted to energy loss scans about $\mathbf{Q} = (1.35\,0.3\,0)$. Reported in Chapter 5.

of the electric field with the charge ordered state as only the $\left(\frac{1}{3}\,\frac{1}{3}\,\frac{3}{2}\right)$-type satellites were affected by the electric field cooling procedure. This result is shown in Figure 9.4 where it is also shown that further electric field cooling through the 3D magnetic ordering temperature does not seem to have any further effect. *In situ* neutron scattering measurements were also performed, but the presence of an applied field was shown to have no effect at either 235 or 180 K.

An *ex situ* x-ray scattering study was performed in order to investigate the nature of the changes to the charge ordered state observed in the magnetic neutron scattering study. Single crystal x-ray scattering was performed using the PX1 protein crystallography beamline of the Australian Synchrotron on previously electrically field cooled (EFC) samples and control samples that were not temperature cycled. Finally, after measuring an EFC sample it was temperature cycled through the ferroelectric transition temperature and the measurement repeated. Reciprocal space maps of the $\left(\frac{1}{3}\,\frac{1}{3}\,L\right)$ diffraction rod for the zero field cooled (ZFC) and EFC cases are shown in Figure 9.5. The EFC process is shown to increase the intensity of all satellite reflections, indicating an increase of the 3D charge order within the sample and an increase in the charge order correlation length. Incomplete charge order is reported and it is proposed that the increase in the charge ordering leads to the observed increase intensity and correlation length reported in Chapter 6. Furthermore, in the neutron study, the ratio of the intensity of the half-integer to integer position satellites was reported to be significantly greater than predicted by spin models of this system. Angst *et al.* [56] explain this as significantly increased contrast between the $Fe^{2+}$ and $Fe^{3+}$ sites as it is believed that the difference between the magnetic moments of these sites leads to the scattering the the half-integer positions. The magnetic ordering of

174
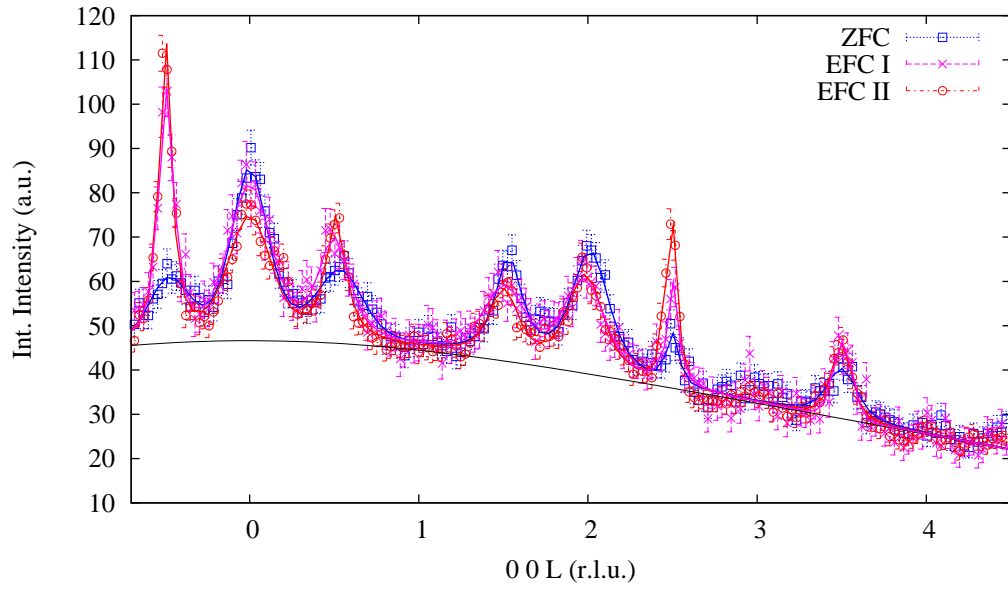
Figure 9.4: The magnetic neutron scattering c* intensity profile of the $\left(\frac{1}{3} \frac{1}{3} L\right)$ diffraction rod for the zero field cooled (ZFC), electrically field cooled to 235 K (EFC I), and further electrically field cooled to 180 K (EFC II) cases; this work was reported in Chapter 6.
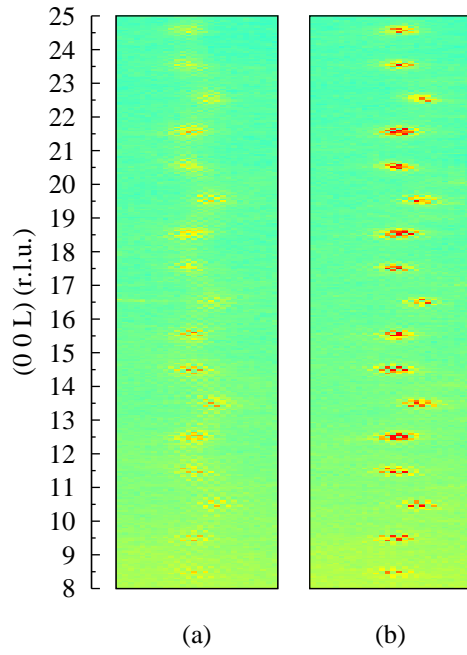


Figure 9.5: Reciprocal space maps of the $\left(\frac{1}{3} \frac{1}{3} L\right)$ diffraction rod collected at 260 K for the (a) zero field cooled and (b) electrically field cooled cases. This work was reported in Chapter 7.

the sample has been shown to be divided between the well ordered ferrimagnetic and other glassy states and here incomplete charge order is reported. Therefore, it is proposed that rather than an unexplained difference between the magnetic moments of the Fe-sites this scaling factor is in fact the difference between the charge and magnetically ordered volumes of the sample.

Powder diffraction experiments were performed in order to conduct a detailed investigation into the temperature dependence of the charge, magnetic, and structural order. Neutron powder diffraction was performed on the ECHIDNA instrument of the OPAL reactor and x-ray powder diffraction was performed on the powder diffraction beamline of the Australian Synchrotron. Peak splitting was shown to be a result of the crushing during sample preparation, but it was fully reversed after temperature cycling through the ferroelectric transition. It is proposed this peak splitting is the result of piezoelectric displacement caused by the crushing process. The patterns were shown to be indexed by the known $R\bar{3}m$ structure; however, the Rietveld refinement demonstrated that the intensities predicted by this model did not agree over the full range measured. No pattern to these intensity variations could be found with respect to the miller indices, nor could they be explained by texture effects such as preferred orientation. Weak reflections that could not be indexed by the known structure were observed in the x-ray data which were found to correspond to a monoclinic structure. The intensity of these reflections was much stronger in the neutron data suggesting they arose from oxygen scattering and accordingly a monoclinic distortion of the oxygen sublattice is reported.

The aim of this thesis was to characterise the electronic and magnetic states of multiferroic $LuFe_2O_4$ through x-ray and neutron scattering techniques. A significant body of other research has been reported by others within the same period of this thesis work, yet as summarised here this work has provided direct evidence of the disordered orbital state of the $Fe^{2+}$ sites in this material and the presence of a progressive 2D-to-3D magnetic ordering process both of which were previously only speculated in the literature. Each study presented here has expanded upon current knowledge in the literature and a number of further experiments are proposed on the foundation of these results. $LuFe_2O_4$ has been shown to be a complex multiferroic material and further studies paying particular attention to the oxygen stoichiometry and using techniques such as polarised neutron scattering which separate the magnetic and electronic contributions will allow this material to be better understood.

# References

[1] Spaldin, N. A., Fiebig, M., and Mostovoy, M. *Journal of Physics: Condensed Matter* **20**, 434203 (2008).

[2] Van Aken, B. B., Rivera, J.-P., Schmid, H., and Fiebig, M. *Nature* **449**, 702–705 (2007).

[3] Hill, N. A. *The Journal of Physical Chemistry B* **104**, 6694–6709 (2000).

[4] Ramesh, R. *Nature* **461**, 1218–1219 (2009).

[5] Fiebig, M. *Journal of Physics D: Applied Physics* **38**, R123–R152 (2005).

[6] Stöhr, J. and Siegmann, H. C. *Magnetism: From Fundamentals to Nanoscale Dynamics.* Springer Series in Sold-State Sciences. Springer, (2006).

[7] Goodenough, J. B. *Physical Review* **100**, 564–573 (1955).

[8] Goodenough, J. B. *Journal of Physics and Chemistry of Solids* **6**, 287–297 (1958).

[9] Kanamori, J. *Journal of Physics and Chemistry of Solids* **10**, 87–98 (1959).

[10] Ramirez, A. P. *Annual Review of Materials Science* **24**, 453–480 (1994).

[11] Hone, D. W. and Richards, P. M. *Annual Review of Materials Science* **4**, 337–363 (1974).

[12] Onsager, L. *Physical Review* **65**, 117–149 (1944).

[13] Collins, M. F. *Magnetic Critical Scattering.* Oxford University Press, (1989).

[14] Navarro, R. and de Jongh, L. *Physica B* **94**, 67–77 (1978).

## REFERENCES

[15] Tannieres, N., Ervard, O., and Aubry, J. *COMPTES RENDUS HEBDO-MADAIRES DES SEANCES DE L ACADEMIE DES SCIENCES SERIE C* **278**, 241–242 January (1974).

[16] Kimizuka, N., Takenaka, A., Sasada, Y., and Katsura, T. *Solid State Communications* **15**, 1321–1323 (1974).

[17] Evrard, O., Malaman, B., Tannières, N., Jeannot, F., and Aubry, J. *COMPTES RENDUS HEBDOMADAIRES DES SEANCES DE L ACADEMIE DES SCIENCES SERIE C* **279**, 1021–1022 (1974).

[18] Evrard, O., Malaman, B., Jeannot, F., Tannieres, N., and Aubry, M. *COMPTES RENDUS HEBDOMADAIRES DES SEANCES DE L ACADEMIE DES SCIENCES SERIE C* **278**, 413–415 (1974).

[19] Kato, K., Kawada, I., and Kimizuka, N. *Zeitschrift für Kristallographie* **141**, 314–320 (1975).

[20] Shindo, I., Kimizuka, N., and Kimura, S. *Material Research Bulletin* **11**, 637–644 (1976).

[21] Iida, J., Takekawa, S., and Kimizuka, N. *Journal of Crystal Growth* **102**, 398–400 (1990).

[22] Isobe, M., Kimizuka, N., Iida, J., and Takekawa, S. *Acta Crystallographica* **C46**, 1917–1918 (1990).

[23] Kimizuka, N. and Katsura, T. *Journal of Solid State Chemistry* **13**, 176–181 (1975).

[24] Kimizuka, N. and Katsura, T. *Journal of Solid State Chemistry* **15**, 151–157 (1975).

[25] Kitayama, K., Sakaguchi, M., Takahara, Y., Endo, H., and Ueki, H. *Journal of Solid State Chemistry* **177**, 1933–1938 (2004).

[26] Kumar, M. S. V., Kuribayashi, K., and Kitazono, K. *Journal of the American Ceramic Society* **92**, 903–910 (2009).

[27] Nakagawa, Y., Inazumi, M., Kimizuka, N., and Siratori, K. *Journal of the Physical Society of Japan* **47**, 1369–1370 (1979).

[28] Sugihara, T., Siratori, K., Shindo, I., and Katsura, T. *Journal of the Physical Society of Japan* **45**, 1191–1198 (1978).

[29] Inazumi, M., Nakagawa, Y., Tanaka, M., Kimizuka, N., and Siratori, K. *Journal of the Physical Society of Japan* **50**, 438–444 (1981).

[30] Tanaka, M., Akimitsu, J., Inada, Y., Kimizuka, N., Shindo, I., and Siratori, K. *Solid State Communications* **44**, 687–690 (1982).

[31] Kishi, M., Miura, S., Nakagawa, Y., Kimizuka, N., Shindo, I., and Siratori, K. *Journal of the Physical Society of Japan* **51**, 2801–2805 (1982).

[32] Kishi, M., Nakagawa, Y., Tanaka, M., Kimizuka, N., and Shindo, I. *Journal of Magnetism and Magnetic Materials* **31-34**, 807–808 (1983).

[33] Iida, J., Tanaka, M., Kito, H., and Akimitsu, J. *Journal of the Physical Society of Japan* **59**, 4190–4191 (1990).

[34] Katano, S., Matsumoto, T., Funahashi, S., Iida, J., Tanaka, M., and Cable, J. W. *Physica B* **213&214**, 218–220 (1995).

[35] Ikeda, N., Mori, R., Kohn, K., Mizumaki, M., and Akao, T. *Ferroelectrics* **272**, 309–314 (2002).

[36] Zhang, Y., Yang, H. X., Guo, Y. Q., Ma, C., Tian, H. F., Luo, J. L., and Li, J. Q. *Physical Review B* **76**, 184105 (2007).

[37] Sugihara, T., Abe, M., and Katsura, T. *Journal of the Physical Society of Japan* **40**, 1211–1212 (1976).

[38] Akimitsu, J., Inada, Y., Siratori, K., Shindo, I., and Kimizuka, N. *Solid State Communications* **32**, 1065–1068 (1979).

[39] Tanaka, M., Kato, M., Kimizuka, N., and Siratori, K. *Journal of the Physical Society of Japan* **47**, 1737–1738 (1979).

[40] Narayanasamy, A., Nagarajan, T., Muthukumarasamy, P., and Kimizuka, N. *Phys. Stat. Sol.* **66**, 377–382 (1981).

[41] Tanaka, M., Iwasaki, H., Siratori, K., and Shindo, I. *Journal of the Physical Society of Japan* **58**, 1433–1440 (1989).

[42] Tanaka, M. *Nuclear Instruments and Methods in Physics Research* **B76**, 149–155 (1993).

[43] Nakamura, S., Kito, H., and Tanaka, M. *Journal of Alloys and Compounds* **272-277**, 574–577 (1998).

[44] Bang, B. K., Kim, S. B., Cheong, S. W., and Kim, C. S. *Physica Status Solidi B* **244**, 4566–4569 (2007).

[45] Bang, B. K., Kouh, T., and Kimizuka, C. S. *Journal of Applied Physics* **103**, 07E307 (2008).

[46] Funahashi, S., Akimitsu, J., Kimizuka, K. S. N., Tanaka, M., and Fujishita, H. *Journal of the Physical Society of Japan* **53**, 2688–2696 (1984).

[47] Funahashi, S., Kito, H., Akimitsu, J., Iida, J., Tanaka, M., and Siratori, K. *Physica B* **174**, 74–76 (1991).

[48] Iida, J., Tanaka, M., Nakagawa, Y., Funahashi, S., Kimizuka, N., and Takekawa, S. *Journal of the Physical Society of Japan* **62**, 1723–1735 (1993).

[49] Kito, H., Akimitsu, J., Nishi, M., Katano, S., Funahashi, S., and Siratori, K. *Physica B* **213 & 214**, 215–217 (1995).

[50] Kito, H., Nishi, M., Katano, S., Akimitsu, J., Funahashi, S., and Siratori, K. *Journal of Magnetism and Magnetic Materials* **140-144**, 1647–1648 (1995).

[51] Iida, J., Nakagawa, Y., and Kimizuka, N. *Journal of the Physical Society of Japan* **55**, 1434–1437 (1986).

[52] Kim, J., Kim, S. B., Jung, C. U., and Lee, B. W. *IEEE Transactions on Magnetics* **45**, 2608–2609 (2009).

[53] Iida, J., Nakagawa, Y., Takekawa, S., and Kimizuka, N. *Journal of the Physical Society of Japan* **56**, 3746–3747 (1987).

[54] Iida, J., Kakugawa, S., Kido, G., Nakagawa, Y., Takekawa, S., and Kimizuka, N. *Physica B* **155**, 307–310 (1989).

[55] Christianson, A. D., Lumsden, M. D., Angst, M., Yamani, Z., Tian, W., Jin, R., Payzant, E. A., Nagler, S. E., Sales, B. C., and Mandrus, D. *Physical Review Letters* **100**, 107601 (2008).

[56] Angst, M., Hermann, R. P., Christianson, A. D., Lumsden, M. D., Lee, C., Whangbo, M. H., Kim, J. W., Ryan, P. J., Nagler, S. E., Tian, W., Jin, R., Sales, B. C., and Mandrus, D. *Physical Review Letters* **101**, 227601 (2008).

[57] Xu, X. S., Angst, M., Brinzari, T., Hermann, R. P., Musfeldt, J. L., Christianson, A. D., Mandrus, D., Sales, B. C., McGill, S., Kim, J.-W., and Islam, Z. *Physical Review Letters* **101**, 227602 (2008).

[58] Wu, W., Kiryukhin, V., Noh, H.-J., Ko, K.-T., Pakrk, J.-H., II, W. R., Sharma, P. A., Harrison, N., Choi, Y., Horibe, Y., Lee, S., Park, S., Yi, H. T., Xhang, C. L., and Cheong, S.-W. *Physical Review Letters* **101**, 137203 (2008).

[59] Park, S., Horibe, Y., Choi, Y. J., Zhang, C. L., Cheong, S.-W., and Wu, W. *Physical Review B* **79**, 180401(R) (2009).

[60] Phan, M. H., Frey, N. A., Srikanth, H., Angst, M., Sales, B. C., and Mandrus, D. *Journal of Applied Physics* **105**, 07E308 (2009).

[61] Wang, F., Kim, J., Kim, Y.-J., and Gu, G. D. *Physical Review B* **80**, 024419 (2009).

[62] Phan, M., Frey, N., Angst, M., de Groot, J., Sales, B., Mandrus, D., and Srikanth, H. *Solid State Communications* **150**, 341–345 (2010).

[63] Michiuchi, T., Yokota, Y., Komatsu, T., Hayakawa, H., Kuroda, T., Maeda, D., Matsuo, Y., Mori, S., Yoshii, K., Kanasaki, N., Kambe, T., and Ikeda, N. *Ferroelectric* **378**, 175–180 (2009).

[64] Park, J. Y., Park, J. H., Jeong, Y. K., and Jang, H. M. *Applied Physics Letters* **91**, 152903 (2007).

[65] Kito, H., Isida, S., Suzuki, M., Akimitsu, J., Takekawa, S., and Siratori, K. *Journal of the Physical Society of Japan* **64**, 2147–2151 (1995).

[66] Enomura, A., Asai, S., Ishiwata, Y., Inabe, T., Sakai, Y., Tsuda, N., Tanaka, M., and Siratori, K. *Journal of the Physical Society of Japan* **52**, 4286–4290 (1983).

[67] Sakai, Y., Kaneda, K., Tsuda, N., Tanaka, M., and Siratori, K. *Journal of the Physical Society of Japan* **54**, 4089–4091 (1985).

[68] oshio Sakai, Kaneda, K., Tsuda, N., and Tanaka, M. *Journal of the Physical Society of Japan* **55**, 3181–3187 (1986).

[69] Tanaka, M., Siratori, K., and Kimizuka, N. *Journal of the Physical Society of Japan* **53**, 760–772 (1984).

[70] Ikeda, N., Kohn, K., Kito, H., Akimitsu, J., and Siratori, K. *Journal of the Physical Society of Japan* **63**, 4556–4564 (1994).

[71] Ikeda, N., Kohn, K., Kito, H., Akimitsu, J., and Siratori, K. *Journal of the Physical Society of Japan* **64**, 1371–1377 (1995).

## REFERENCES

[72] Ikeda, N., Odaka, K., Takahashi, E., Kohn, K., and Siratori, K. *Ferroelectric* **190**, 191–196 (1997).

[73] Yoshii, K., Ikeda, N., and Nakamura, A. *Physica B* **278-380**, 585–586 (2006).

[74] Yoshi, K., Yoneda, Y., Maeda, D., Yokota, Y., Michiuchi, T., Komatsu, T., Ikeda, N., Matsuo, Y., and Mori, S. *Japanese Journal of Applied Physics* **47**, 7599–7602 (2008).

[75] Ikeda, N., Mori, S., and Yoshii, K. *Ferroelectrics* **348**, 38–47 (2007).

[76] Yamada, Y., Nohdo, S., and Ikeda, N. *Journal of the Physical Society of Japan* **66**, 3733–3736 (1997).

[77] Ikeda, N., Yamada, Y., Nohdo, S., Inami, T., and Katano, S. *Physica B* **241-243**, 820–822 (1998).

[78] Ikeda, N., Nohdo, S., and Yamada, Y. *Journal of the Korean Physical Society* **32**, S165–S168 (1998).

[79] Ikeda, N., Tanaka, M., Kito, H., Sasaki, S., and Yamada, Y. *Ferroelectrics* **222**, 227–235 (1999).

[80] Ikeda, N., Ohsumi, H., Mizumaki, M., Mori, S., Horibe, Y., and Kishimoto, K. *Journal of Magnetism and Magnetic Materials* **272-276**, e1037–e1039 (2004).

[81] Ikeda, N., Mori, S., and Kohn, K. *Ferroelectrics* **314**, 41–56 (2005).

[82] Ikeda, N., Kohn, K., Myouga, N., Takahashi, E., Kitoh, K., and Takekawa, S. *Journal of the Physical Society of Japan* **69**, 1526–1532 (2000).

[83] Ikeda, N., Ohsumi, H., Ohwada, K., Ishii, K., Inami, T., Kakurai, K., Murakami, Y., Yoshii, K., Mori, S., Horibe, Y., and Kito, H. *Nature* **436**, 1136–1138 (2005).

[84] Ikeda, N., Mori, R., Mori, S., and Kohn, K. *Ferroelectrics* **286**, 175–184 (2003).

[85] Horibe, Y., Kishimoto, K., Mori, S., and Ikeda, N. *Integrated Ferroelectrics* **67**, 151–157 (2004).

[86] Horibe, Y., Kishimoto, K., and Mori, S. *Journal of the Korean Physical Society* **46**, 192–194 (2005).

## REFERENCES

[87] Mori, S., Shinohara, S., Matsuo, Y., Horibe, Y., Yoshii, K., and Ikeda, N. *Japanese Journal of Applied Physics* **47**, 7597–7598 (2008).

[88] Horibe, Y., Yoshii, K., Ikeda, N., and Mori, S. *Physical Review B* **80**, 092104 (2009).

[89] Ikeda, N., Matsuo, Y., Mori, S., and Yoshii, K. *IEEE Transactions of Ultrasonics, Ferroelectrics, and Frequency Control* **55**, 1043–1045 (2008).

[90] Horibe, Y., Kishimoto, K., Mori, S., and Ikeda, N. *Journal of Electron Micoscopy* **54 (Supplement I)**, i87–i90 (2005).

[91] Murakami, Y., Abe, N., Arima, T., and Shindo, D. *Physical Review B* **76**, 024109 (2007).

[92] Zhang, Y., Yang, H. X., Ma, C., Tian, H. F., and Li, J. Q. *Physical Review Letters* **98**, 247602 (2007).

[93] Li, C.-H., Zhang, X.-Q., Cheng, Z.-H., and Sun, Y. *Applied Physics Letters* **92**, 182903 (2008).

[94] Li, C., Xiangqun, Z., Cheng, Z., and Sun, Y. *Applied Physics Letters* **93**, 152103 (2008).

[95] Zeng, L. J., Yang, H. X., Zhang, Y., F., T. H., Ma, C., Qin, B., Zhao, Y. G., and Li, J. Q. *Europhysics Letters* **84**, 57011 (2008).

[96] Nagano, A. and Ishihara, S. *Journal of Physics: Condensed Matter* **19**, 145263 (2007).

[97] Nagano, A., Naka, M., Nasu, J., and Ishihara, S. *Physical Review Letters* **99**, 217202 (2007).

[98] Nasu, J., Nagano, A., Naka, M., and Ishihara, S. *Physical Review B* **78**, 024416 (2008).

[99] Xiang, H. J. and Whangbo, M. H. *Physical Review Letters* **98**, 246403 (2007).

[100] Harris, A. B. and Yildirim, T. *arXiv:0812.3575v1* (2008).

[101] Li, S., Luo, S., Fu, R., Wang, B. J. K., Liu, J.-M., Ding, J., and Li, X. *Applied Physics A* **96**, 893–898 (2009).

[102] Subramanian, M. A., He, T., Chen, J., Rogadi, N. S., Calvarese, T. G., and Sleight, A. W. *Advanced Materials* **18**, 1737–1739 (2006).

## REFERENCES

[103] Serrao, C. R., Sahu, J. R., Ramesha, K., and Rao, C. N. R. *Journal of Applied Physics* **104**, 016102 (2008).

[104] Naka, M., Nagano, A., and Ishihara, S. *Physical Review B* **77**, 224441 (2008).

[105] Wen, J., Xu, G., Gu, G., and Shapiro, S. M. *Physical Review B* **80**, 020403 (2009).

[106] Li, C.-H., Wang, F., Liu, Y., Zhang, X.-Q., Cheng, Z.-H., and Sun, Y. *Physical Review B* **79**, 172412 (2009).

[107] Wen, J., Xu, G., Gu, G., and Shapiro, S. M. *arXiv:1001.3611v1 [cond-mat.mtrl-sci]* (2010).

[108] Squires, G. L. *Introduction to the theory of thermal neutron scattering.* Dover Publications, Inc., New Ork, (1996).

[109] Kittel, C. *Introduction to Solid State Physics.* John Wiley & Sons, Inc, 8th edition, (2005).

[110] Cromer, D. T. and Liberman, D. *Journal of Chemical Physics* **53**, 1891 (1970).

[111] Cromer, D. T. and Liberman, D. A. *Acta Crystallographica A* **37**, 267 (1981).

[112] Hahn, T. *International tables for crystallography.* Springer, (2005).

[113] Ravel, B. and Newville, M. *Journal of Synchrotron Radiation* **12**, 537–541 (2005).

[114] Newville, M. *Journal of Synchrotron Radiation* **8**, 332 (2001).

[115] Ohta, K. and Ishida, H. *Applied Spectroscopy* **42**, 952–957 (1988).

[116] Cross, J. O., Newville, M., Rehr, J. J., Sorensen, L. B., Bouldin, C. E., Watson, G., Gouder, T., Lander, G. H., and Bell, M. I. *Physical Review B* **58**, 11215 (1998).

[117] Lucarini, V., Saarinen, J., Peiponen, K.-E., and Vartiainen, E. *Kramers-Kronig Relations in Optical Materials Research.* Springer, Heidelberg, (2005).

[118] Als-Nielsen, J. and McMorrow, D. *Elements of Modern X-Ray Physics.* John Wiley & Sons, Inc., (2001).

[119] Koningsberger, D. C. and Prins, R. *X-ray Absorption: Principles, Applications, Techniques of EXAFS, SEXAFS and XANES.* Chemical Analysis. John Wiley & Sons, Inc., New York, (1988).

[120] Joly, Y. *Physical Review B* **63**, 125120 (2001).

[121] Ankudinov, A., Ravel, B., Rehr, J., and Conradson, S. *Physical Review B* **58**, 7565 (1998).

[122] Ko, K.-T., Noh, H.-J., Kim, J.-Y., Park, B.-G., Park, J.-H., Tanaka, A., Kim, S. B., Zhang, C. L., and Cheong, S.-W. *Physical Review Letters* **103**, 207202 (2009).

[123] Kuepper, K., Raekers, M., C.Taubitz, Prinz, M., Derks, C., Newmann, M., Postnikov, A. V., de Groot, F. M. F., Piamonteze, C., Prabhakaran, D., and Blundell, S. J. *Physical Review B* **80**, 220409(R) (2009).

[124] Cooper, M. and Nathans, R. *Acta Crystallographica* **23**, 357 (1967).

[125] Kabsch, W. *Journal of Applied Crystallography* **26**, 795–800 (1993).

[126] Mulders, A., Lawrence, S., Staub, U., García-Fernández, M., Scagnoli, V., Mazzoli, C., Pomjakushina, E., Conder, K., and Wang, Y. *Physical Review Letters* **103**, 077602 (2009).

[127] Ide-Ektessabi, A., Kawakami, T., and Watt, F. *Nuclear Instruments and Methods in Physics Research B* **213**, 590–594 (2004).

[128] Benfatto, M., Solera, J. A., Ruiz, J. G., and Chaboy, J. *Chemical Physics* **282**, 441–450 (2002).

[129] Cowley, R. A. *Methods of Experimental Physics*, volume 23, Part C, chapter 18 'Phase Transitions'. Academic Press Inc. (1987).

[130] Shirane, G., Shapiro, S. M., and Tranquada, J. M. *Neutron Scattering with a Triple-Axis Spectrometer.* Cambridge University Press, (2002).

[131] Narumi, Y. and Kindo, K. Magnetometry study of $LuFe_2O_4$ (*Unpublished*).

[132] Wang. DC study of the polarisation in multiferroic $LuFe_2O_4$ (*Unpublished*).

[133] Duisenberg, A. J. *Journal of Applied Crystallography* **25**, 92–96 (1992).

[134] FABLE Workbench. *http://wiki.fable.sourceforge.net/* (2010).

[135] Rodríguez-Carvajal, J. *Satellite Meeting on Powder Diffraction of the XV IUCr Congress* , 127 (1990).

[136] Favre-Nicolin, V. and Cerny, R. *Journal of Applied Crystallography* **35**, 734–743 (2002).

[137] FOX: Free Objects for Crystallography. *http://objcryst.sourceforge.net/* (2010).

[138] Larson, A. and Dreele, R. V. *Los Alamos National Laboratory Report* , LAUR 86–748 (2000).

[139] Husak, M. and Rohlicek, J. *Journal of Applied Crystallography* **40**, 600 (2007).

[140] Marching Cubes ELD. *http://www.vscht.cz/min/mce/index.html* (2010).

[141] Angst, M., Khalifah, P., Hermann, R., Xiang, H., Whangbo, M., Varadarajan, V., Brill, J., Sales, B., and Mandrus, D. *Physical Review Letters* **99**, 086403 (2007).

# Appendix A

# Single Crystal Neutron Diffraction Supplement

This appendix provides supplementary information on the programs written to perform the data reduction and reciprocal space mapping in Chapters 6 and 7.

Figure A.1: HDFIMPORT flow chart.

Figure A.1: continued from previous page.

Figure A.2: STACKANALYSIS flow chart.



**StackAnalysis** – an MPI C program written, compiled and run on the iVEC (http://www.ivec.org) ARRC HPC facility at Technology Park, Western Australia.
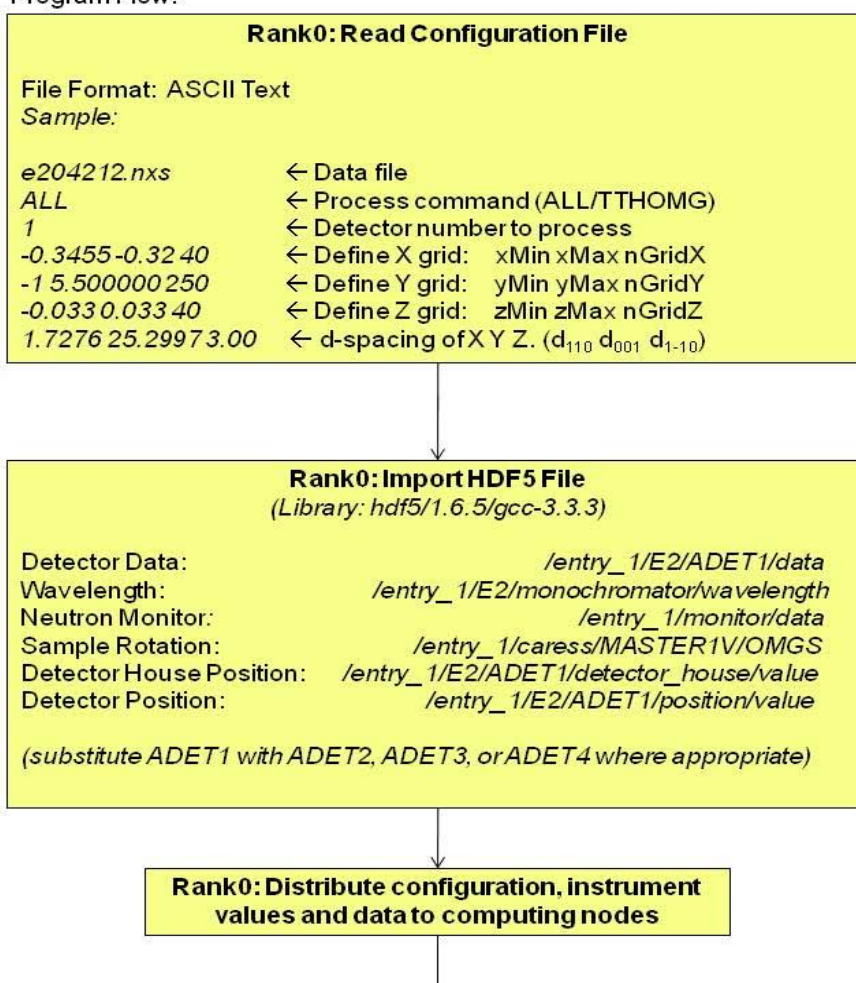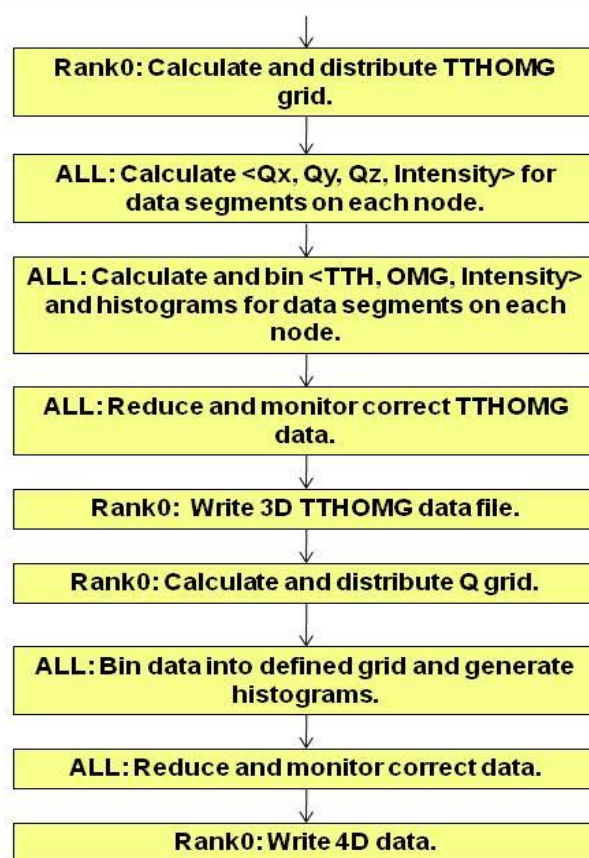
Program Flow:

**Rank0: Read Configuration File**

File Format:  ASCII Text
*Sample:*

| | |
|---|---|
| *PIX* | ← Mode (only PIX implemented) |
| *-1 -1 -1* | ← Starting (bottom left) coordinate of data volume to analyse; units depend on mode. (PIX = voxels) |
| *0 0 79* | ← Ending (top right) coordinate of data volume to analyse. |
| *2* | ← Number of sub-stacks. |
| *33 46 0 98 85 50*
*33 66 0 98 158 50* | ← List of start and end coordinates of substacks. |

**Rank0: Read 4D data file (./outputXYZ.dat)**

**Rank0: Distribute data to nodes.**

**ALL: Integrate and reduce XY, XZ and YZ 3D datasets.**

**ALL: Iterate over all substacks and produce all 2D and 3D datasets.**

**Rank0: Write all datasets to disk.**